

FLORIDA INTERNATIONAL UNIVERSITY

Miami, Florida

SPARK PLASMA SINTERING OF 2D NITRIDE AND CARBIDE BASED CERAMICS

A dissertation submitted in partial fulfillment of

the requirements for the degree of

DOCTOR OF PHILOSOPHY

in

MATERIALS SCIENCE AND ENGINEERING

by

Archana Loganathan

2019

To: Dean John L. Volakis
College of Engineering and Computing

This dissertation, written by Archana Loganathan, and entitled Spark Plasma Sintering of 2D Nitride and Carbide based Ceramics, having been approved in respect to style and intellectual content, is referred to you for judgment.

We have read this dissertation and recommend that it be approved.

Zhe Cheng

Wenzhi Li

Benjamin Boesl, Co-Major Professor

Arvind Agarwal, Co-Major Professor

Date of Defense: June 17, 2019

The dissertation of Archana Loganathan is approved.

Dean John L. Volakis
College of Engineering and Computing

Andrés G. Gill
Vice President for Research and Economic Development
and Dean of the University Graduate School

Florida International University, 2019

DEDICATION

“கற\$ கக ம& அள) கலராத\$ உலகள)” – Avvaiyar, Tamil Poet

Meaning: What you have learnt is only a handful and what you have not is the size of

the world

To make something special, you just have to believe it's

special - (Mr. Ping, Kung Fu Panda)

ACKNOWLEDGMENT

I would like to express my sincere and deepest sense of gratitude to my major advisor Professor Arvind Agarwal for accepting and giving me this opportunity to pursue my Ph.D in his research group. I thank you for being patient, constantly supporting with his valuable and critical guidance during the course of my Ph.D research. The basic discussions starting from organizing the results to time management to networking and multi-tasking with different projects has helped me to establish myself as a better researcher. My sincere and heartfelt thanks for all the time and dedication you have invested for your students. I am fortunate to have the best and the most inspiring professor as my advisor. I am grateful for all the financial support and encouraging me to participate in different conference presentations. Special thanks for continuously supporting and encouraging me to develop the leadership skills by being the delegate in the President's Council for Student Advisors (PCSA) and represent FIU in the American Ceramic Society.

My special thanks to my co-major advisor, Dr. Benjamin Boesl for his extensive support throughout my Ph.D research. At the lowest phase of my research even, Dr. BB was always open to discussions, suggesting different ways to approach the problem, always felt positive and energized walking out of your office. I would really like to thank you for the patience, discussions and allowing me to use the in-situ indentation facility.

Also, I take this opportunity to thank my previous mentors from my undergraduate school, Prof. R. Subramanian, Dr. J. Krishnamoorthi and Prof. P.C. Angelo. Special thanks to Prof. Ashutosh S. Gandhi, who always encouraged me to question and think critically during scientific discussions. I would like to thank my mentors Dr. Vimal and Rajesh from Nissan, who encouraged me to pursue research career.

I would like to thank my committee members, Dr. Zhe Cheng, Dr. Yu Zhong and Dr. Wenzhi Li for accepting to serve my dissertation committee. Thank you for supporting and providing suggestions throughout my research.

My heartfelt thanks to Dr. Lidia Kos from University Graduate School, FIU, for giving me the second opportunity to pursue my dream of Ph.D and giving me the office space in UGS for completing my thesis. I will never forget this timely help and the second chance to breathe. Thank you so much Dr. Kos. Karla Ortega and Ashley Mendez from UGS, thank you so much for constantly checking and motivating me in the thesis writing process. Special thanks to Dr. Anuradha Godavarty, for sharing her experience in US, for feeding me indian home food, encouraging, caring and giving me a lot of confidence whenever I was low mentally or physically. Thank you all for being my family and in each of you, I saw my late mother pushing me to reach my dream.

I am thankful for the help from Dr. Satyam Suwas, Indian Institute of Science (IISc), Bengaluru, India for the texture and transmission electron microscopy studies, which provided detailed insights about the interface of sintered nanosheets. Thanks to Amit Sharma for coordinating and performing experiments on the BNNS and BCN sintered compacts. Amit was always available for scientific discussions and which helped us to analyze our results in more detail.

Also, I am thankful to Dr. Chunlei Wang, FIU for the FTIR studies. Many thanks to Richa Agrawal for coordinating with us for experiments and sharing her expertise on FTIR analysis. I would like to sincerely thank Dr. Surendra Saxena and Dr. Jiahua Chen from FIU, for allowing me to use the Raman spectroscopy facility in their lab.

I would like to thank and acknowledge University Graduate School, FIU for supporting me through Dissertation Evidence Acquisition (DEA) and Dissertation Year Fellowship (DYF)

awards. I would also like to acknowledge the financial support from Army Research Laboratory grant (ARL W911NF-15-2-0106) and US DOE (DE-FE0026325).

I am extremely thankful to the support of the Advanced Materials Engineering Research Institute (AMERI) at FIU for providing research facilities. I would like to appreciate and thank Dr. Alex Franco for the training, advice and support to provide the solution of instruments in AMERI whenever needed.

I am extremely grateful to Tiziana Leoni, Mabel Fernandez, Mariam Barrueco and Beatriz from the Department of Mechanical and Materials Engineering, always ready to help me with administrative work whenever I am in need.

I would like to thank and acknowledge the support from all the plasma forming group members. I would never forget the coffee/lunch breaks, potluck, boba tea, Miami beach, birthday celebrations, barbeques, fun during conferences and the list is endless. The past four years with all the PFL members is the most memorable part of my life. I would like to thank my lab seniors (as per PJ's request), Dr. Christopher Rudolf, Dr. Cheng Zhang and Pranjali Nautiyal (PJ) for training me on different equipment and sharing your expertise during scientific discussions. Special thanks to my PFL friends Luiza, Pranjali, Jennifer, Sadhana, Sara, Leslie, Tony, Cat, Kazu, Lu and Tanaji. Thanks to Luiza and Sadhana for their kindness to invite me for casual dinner, lot of tips for what to buy in supermarkets. Also, thanks to Luiza, Pranjali and Sadhana for being patient and listening to all my cry baby stories in the past four years.

I thank Vennila mam, Nishi, Ashwini, Monica, Krithi, Shilpa, Linda, Madhu for all the good times we had during different occasions. The motivation of my dream was alive in the past four years by long phone calls with my close friends – Pragna, Srinivas, Gowri (12 am friends).

Above all, I am indebted to my dad and late mother for their unwavering faith in me, constant love, support and encouragement without which it would have been difficult for me to complete my research successfully. I want to thank my sister for being my mother and always being by my side without any second thought. Surendra has been the biggest support for my existence to pursue my dream in this land of opportunities. Thank you would be such a small phrase to mention. I owe my thesis and graduation to my father, mother, sister and Surendra.

- Archana Loganathan

ABSTRACT OF THE DISSERTATION

SPARK PLASMA SINTERING OF 2D NITRIDE AND CARBIDE BASED CERAMICS

by

Archana Loganathan

Florida International University, 2019

Miami, Florida

Professor Arvind Agarwal, Co-Major Professor

Professor Benjamin Boesl, Co-Major Professor

Two-dimensional (2D) nanomaterials have stimulated significant interest among the materials community due to a wide variety of applications ranging from functional to structural properties. Boron nitride nanosheets (BNNS), boron-carbon-nitride (BCN), and MXene ($M_{n+1}X_n$, transition metal carbides, nitrides or carbonitrides) belongs to the 2D materials family with van der Waals bonding between the layers. The research on synthesis and properties of BNNS, BCN and MXene has been predominantly explored for single- or multi-layered 2D nanosheets. In this study, the focus is to synthesize bulk layered BNNS and BCN, using single or multilayered 2D nanomaterials by spark plasma sintering (SPS). The rapid processing conditions of SPS allow retention of nanoscale structure in the bulk form.

Monolithic BNNS with 92% dense structure was prepared by SPS. The monolithic BNNS with h-BN structure displayed a preferred orientation of basal plane (0002) along the top-surface and this is ascribed to BNNS high aspect ratio. During high-load indentation, the total energy dissipation along the top-surface was 50% higher than the cross-section of the BNNS pellet. Ternary BCN phase was synthesized from 2D graphene nanoplatelet (GNP) and BNNS using reactive SPS technique from temperature range of 1650 - 1750 °C. Hexagonal BCN phase with minor cubic BCN phase was formed in the reactive sintered pellets.

Tribological behavior of sintered BNNS and BCN was studied at room temperature and 600 °C. The coefficient of friction (COF) increased with the formation of cubic BCN at room temperature but reduced at 600 °C due to a graphitized transfer layer. Room temperature wear rate of BCN synthesized at 1750 °C increased compared to BCN synthesized at 1650 °C due to higher level of densification.

In this study, the other van der Waals 2D material MXenes multi-scale damping properties were explored for the first time. Multiscale damping behavior of MXene showed high loss tangent ($\tan \delta$) of 0.37 and it was 200% higher than pure MAX. It has been hypothesized that the bond contraction operates within a single MXene layer, compression and sliding/shearing of MXene sheets operates between MXene layers. After 50,000 long cycle test, MXene layers exhibit highly stable damping behavior suggesting its suitability as a dampener.

TABLE OF CONTENTS

CHAPTER	PAGE
Chapter I: Introduction	1
1.1. Two-dimensional Nanostructured Materials	1
1.2. Significance of Two-dimensional Materials	3
1.2.1. Boron Nitride Nanosheets (BNNS)	4
1.2.2. Boron-Carbon-Nitride System (BCN)	5
1.2.3. MXene	5
1.3. Importance of Understanding the Mechanical and Tribological Properties of 2D Materials	6
1.4. Research Objectives	7
1.5. References	9
Chapter II: Literature Review	14
2.1. Two-dimensional Materials	14
2.2. Hexagonal Boron Nitride Nanosheets	14
2.2.1. Synthesis of BNNS	15
2.2.2. Consolidation Methods for h-BNNS	18
2.2.3. Structural and Anisotropic Properties of BNNS	19
2.2.4. Physical Properties of BNNS	21
2.2.5. Mechanical and Tribological Properties of BNNS	22
2.2.6. Application of BNNS	23
2.3. Boron-Carbon-Nitride System	24
2.3.1. Synthesis of BCN	25
2.3.1.1. Solid-State Reactive Sintering Method	29
2.3.2. Different Structure and Bonding Nature of BCN	30
2.3.3. Mechanical and Tribological Properties of BCN	33

2.3.4. Applications of BCN	36
2.4. MXene	37
2.4.1. Synthesis of MXene	39
2.4.2. Functionalization of MXene	43
2.4.3. Structural and Physical Properties of MXene	44
2.4.4. Electronic Properties of MXene	48
2.4.5. Mechanical and Tribological Properties of MXene	49
2.4.6 Applications of MXene	55
2.5. Scope on Exploring the Properties of Bulk Structured 2D Nanomaterials (BNNS, BCN) and Damping Properties of MXene Nanosheets	58
2.6. References	60
Chapter III: Experimental Procedure	78
3.1. Monolithic BNNS Preparation – Spark Plasma Sintering	78
3.2. Synthesis of BCN System	79
3.2.1. BNNS and GNP Mixing – Ball Milling	79
3.2.2. Reaction Synthesis of BNNS and GNP - Spark Plasma Sintering	80
3.3. Synthesis of MXene – Hydrofluoric Acid Treatment	81
3.4. Structural Characterization	81
3.4.1. X-ray Diffraction – Phase Analysis	81
3.4.2. Raman Spectroscopy and Fourier Transform Infrared Spectroscopy	82
3.4.3. Crystallographic Texture Analysis	82
3.5. Microstructural Characterization	83
3.5.1. Scanning Electron Microscopy – Fracture Characteristics of Bulk 2D Material	83
3.5.2. Transmission Electron Microscopy – Interface Analysis of Bulk 2D Material	84
3.6. Mechanical Properties	85

3.6.1. Microhardness	85
3.6.2. Nanoindentation – Hardness and Elastic Modulus	85
3.6.3. In-situ High Load Indentation – Deformation Behavior of Bulk 2D Material	86
3.6.4. Micro- and Nano-scale Damping Studies	87
3.7. Tribological Behavior of Bulk 2D Materials	89
3.7.1. Ball-On-Disk: Macroscale Friction and Wear	89
3.7.2. Scratch: Micro- scale Wear	90
3.8. References	91
 Chapter IV: Results and Discussion	 92
4.1. Monolithic BNNS Consolidated by Spark Plasma Sintering	92
4.1.1. As-received BNNS Characterization – Structural and Microstructural Evaluation	92
4.1.2. Monolithic BNNS – Density, Structural and Microstructural Evaluation	94
4.1.3. Fracture Mechanism of Monolithic BNNS	98
4.1.4. Effect of Texture Orientation of Spark Plasma Sintered BNNS	99
4.1.5. Mechanical Properties of Monolithic BNNS	101
4.1.5.1. Microhardness of Monolithic BNNS	101
4.1.5.2. Nanomechanical Properties: Elastic Modulus and Hardness of Monolithic BNNS	102
4.1.6. Tribological Behavior of Monolithic BNNS	103
4.1.7. High Load In-situ Indentation Behavior of Monolithic BNNS	106
4.1.7.1. Deformation along Monolithic BNNS Top Surface	107
4.1.7.2. Deformation along Monolithic BNNS Cross-section	111
4.1.7.3. Deformation Mechanism of Monolithic BNNS Pellet Respect to Different Orientations	114

4.1.8. Conclusion of Monolithic BNNS Consolidated by Spark Plasma Sintering	117
4.2. Monolithic BCN Consolidated by Spark Plasma Sintering	118
4.2.1. High Energy Ball Milled BNNS and GNP Characterization	118
4.2.2. Reaction Synthesis BCN System – SPS Parameters	120
4.2.2.1. Reactive Sintering Mechanism – BCN Phase Formation	121
4.2.3. Monolithic BCN – Density, Structure and Microstructure	123
4.2.4. Fracture Mechanism of Monolithic BCN	137
4.2.5. Effect of Texture Orientation of Spark Plasma Sintered BCN	140
4.2.6. Mechanical Properties of Monolithic BCN	144
4.2.6.1. Microhardness of Monolithic BCN	144
4.2.6.2. Nanomechanical Properties: Reduced Elastic Modulus and Hardness of Monolithic BCN	145
4.2.7. Tribological Behavior of Monolithic BCN	146
4.2.8. High Load In-situ Indentation Behavior of Monolithic BCN	158
4.2.9. Conclusion of Reaction Synthesized BCN Phase	165
4.3. Synthesis and Property Evaluation of 2D MXene	166
4.3.1. MXene Synthesis – HF Acid Treatment	166
4.3.2. Phase Evolution with HF Acid Treatment	166
4.3.3. Microstructural Evolution with HF Acid Treatment	168
4.3.4. Electrical Resistivity of HF Treated MXene	169
4.3.5. Tribological Behavior of HF Treated MXene	170
4.3.6. Multiscale Damping Behavior of HF Treated MXene	172
4.3.6.1. Damping Mechanisms in MAX and MXene	177
4.3.7. Conclusion of 2D MXene Synthesis and Damping Behavior	185
4.4. References	185
Chapter V: Conclusion	193

Chapter VI: Recommendations for Future Work	199
VITA	203

LIST OF TABLES

TABLE	PAGE
Table 1.1: Classification and list of 2D materials	3
Table 2.1: Structural parameter of hexagonal boron nitride nanosheet	20
Table 2.2: List of different bonds present in BCN and their corresponding bond energy	32
Table 2.3: Mechanical properties of ternary B-C-N system	35
Table 2.4: Synthesis conditions for MXene using HF acid	40
Table 2.5: Synthesis conditions for MXene using fluoride salt (HCl – LiF)	42
Table 2.6: Calculated elastic constant ‘ c_{11} ’ of MXene and the MAX phase values are the one in brackets	51
Table 2.7: Calculated mechanical and electronic properties for pristine and functionalized MXene	51
Table 2.8: Tribological properties of MXene	54
Table 3.1: Reactive spark plasma sintering conditions for BCN phase	80
Table 4.1: Deformation mechanism observed during top surface indentation with respect to the slope and the corresponding time duration from the video	108
Table 4.2: Deformation mechanism observed during cross-section indentation with respect to the slope and the corresponding time duration from the video	112
Table 4.3: Reaction synthesis conditions for SPS and the measured density of reaction synthesized pellets	124
Table 4.4: Microhardness of the reaction sintered BCN pellets	145

Table 4.5:	Nanohardness and reduced elastic modulus of the reaction sintered BCN pellets	146
Table 4.6:	Wear volume loss and wear rate of reactive sintered BCN pellets tested at room temperature	149
Table 4.7:	Wear volume loss and wear rate of reactive sintered BCN pellets tested at high temperature	155
Table 4.8:	Reactive sintered BCN 3 deformation mechanisms, normalized associated energy and the time range in video observed during the top surface indentation	160
Table 4.9:	Length of the diagonals from the indent of the BCN high load indentation	164
Table 4.10:	Interlayer spacing and FWHM for MAX and HF treated MXene samples	167
Table 4.11:	Calculated energy for bond contracting of pure and functionalized Ti_2C	169
Table 4.12:	Total number of layers interacted during damping, calculated from the monolayer thickness and average displacement measured during nanoDMA for HF-treated samples	181

LIST OF FIGURES

FIGURE	PAGE
Figure 1.1: Schematic representation of nanostructured materials	2
Figure 1.2: Work plan of the present research	9
Figure 2.1: Scanning tunneling microscope image of monolayer boron nitride grown on Rh(111) surface by high temperature CVD	15
Figure 2.2: Transmission electron microscope image of exfoliated BNNS by (a) mechanical exfoliation, (b) chemical exfoliation. Scanning electron microscope image of (c, d) exfoliation from the edge of h-BN particle and (e, f) peeling off thin sheet from the top surface of h-BN particle, (g) vertical aligned BNNS synthesized by CVD at 900 -1200 °C for 30 and 60 min	18
Figure 2.3: (a) Crystal structure of BNNS and (b) model of monolayer 2D BNNS	20
Figure 2.4: STEM image of BCN with the composition distribution of B, C, N and O elements	26
Figure 2.5: TEM image of BCN with the composition distribution of B, C, and N elements	26
Figure 2.6: Cross-sectional SEM micrographs of (a) BC1, (b) BC2, (c) BC3 and (d) BC4 demonstrating microstructural changes of BCN films with increasing N ₂ content	27
Figure 2.7: Schematic representation of BCN nanosheet synthesis	27
Figure 2.8: Ternary phase diagram of the B-C-N system	30
Figure 2.9: Different structural arrangement of hexagonal BCN	32
Figure 2.10: Different structural arrangement of hexagonal BC ₂ N	33
Figure 2.11: Different structural arrangement of cubic BC ₂ N	33
Figure 2.12: Different type of MXene structure and their corresponding compositions	38
Figure 2.13: SEM images of (a) Ti ₃ AlC ₂ before HF treatment and (b) Ti ₃ AlC ₂ after HF treatment forms Ti ₃ C ₂	40

Figure 2.14:	SEM images of powders of, a) $\text{Mo}_2\text{Ga}_2\text{C}$, b) Mo_2CT_x etched in HF for 160h c) $\text{Mo}_2\text{CT}_x\text{-Li}$ etched in LiF/HCl for 6 days and, d) $\text{Mo}_2\text{CT}_x\text{-Li}$ etched for 16 days	42
Figure 2.15:	Schematic of MXene monolayer with and without surface terminations	43
Figure 2.16:	Schematic representation of MXene structure synthesized from MAX phase	45
Figure 2.17:	SEM image of (a) as-synthesized $\text{Ti}_3\text{C}_2\text{T}_x$ MXene and (b) after oxidation of $\text{Ti}_3\text{C}_2\text{T}_x$ MXene	46
Figure 2.18:	Schematic illustration of oxidation under different conditions	47
Figure 2.19:	Computed mechanical properties of oxygen functionalized MXenes compared with the other 2D materials	52
Figure 2.20:	Theoretical capacities of Li- and non-Li-ion batteries with oxygen terminated MXene nanosheets	56
Figure 3.1:	SEM image of the as-received BNNS	78
Figure 3.2:	SEM image of the as-received GNP	80
Figure 3.3:	SEM image of the as-received MAX (Ti_2AlC) powder	81
Figure 3.4:	Schematic representation of sintered 2D materials, showing the region of interest for texture studies	83
Figure 3.5:	Schematic representation of TEM sample preparation of sintered pellet	84
Figure 3.6:	In-situ high load indentation micro-load frame (a) Schematic diagram and (b) image of it inside the SEM chamber	87
Figure 3.7:	Height-time profile of HF treated MXene	88
Figure 3.8:	Optical image of the dispersed powder particles on the metallic stub. The particles were identified and resolved under the optical microscope to perform dynamic nanoindentations to capture the damping properties of pure MAX and etched particles	89
Figure 4.1:	(a) X-ray diffraction pattern and (b) SEM image of as-received BNNS powder	93

Figure 4.2:	X-ray diffraction pattern of sintered BNNS pellet (Inset shows the XRD pattern of sintered BNNS pellet at lower intensity)	94
Figure 4.3:	Raman spectra of the sintered BNNS from the (a) top surface and (b) cross-section	96
Figure 4.4:	SEM image of top surface of sintered BNNS pellet	96
Figure 4.5:	HRTEM image of the sintered BNNS showing (a-b) bright field image showing nano-sized grains and twins, (c-d) lattice planes with the inset showing corresponding diffraction pattern	98
Figure 4.6:	SEM images of BNNS pellet (a) fractured surface indicating the lamellar structure and (b) zig-zag fractured surface (yellow dotted arrows indicate the zig-zag edges)	99
Figure 4.7:	Schematic drawing of the sintered BNNS SPS pellet top surface indicating the region of texture studies along with the pole figures of (0002) plane, $(11\bar{2}0)$ plane and $(01\bar{1}1)$ plane. The directions with reference to sample coordinates are defined as normal direction (ND, normal to the sample surface), transverse direction (TD, Y-axis) and reference direction (RD, X-axis)	100
Figure 4.8:	Schematic drawing of the sintered BNNS SPS pellet cross-section indicating the region of texture studies along with the pole figures of (0002) plane, $(11\bar{2}0)$ plane and $(01\bar{1}1)$ plane. The directions with reference to sample coordinates are defined as normal direction (ND, normal to the sample surface), transverse direction (TD, Y-axis) and reference direction (RD, X-axis)	101
Figure 4.9:	Load vs displacement curve of nanoindentations performed on the polished top surface and cross-section of sintered BNNS pellet	103
Figure 4.10:	Coefficient of friction at 3 N load for the BNNS SPS pellet at room temperature and high temperature for a track radius of 2 mm	104
Figure 4.11:	SEM images of the wear track for the room temperature test shows (a) direction of the wear track, (b) multiple BNNS layer at the edges of wear track, (c) pit formation and (d) bending of nanosheets	105
Figure 4.12:	SEM images of the wear track at the high temperature indicating (a) smooth wear track, (b) material pile up and (c) delamination and crack propagation	106

Figure 4.13:	Top surface indent load-displacement curve and SEM images of deformation event at different stage of loading	107
Figure 4.14:	SEM images of the top indented surface after the tip removal, (a) lower magnification of the indented surface indicating the regions from where the SEM images b, c and d, were imaged, (b) layered fractured surface, (c) bending of sheets, and (d) crack propagation at the bottom of the indent surface	110
Figure 4.15:	Cross-section indent load-displacement curve and SEM images of deformation event at different stage of loading	111
Figure 4.16:	SEM images of the cross-section indented surface after the tip removal, (a) low magnification image indicating the regions from where the SEM images b, c and d, were imaged, (b) delaminated of the sheets, (c) crack propagation from indentation, and (d) fine cracks below the indent surface	113
Figure 4.17:	(a) Schematic drawing showing the simple hexagonal system marked with the basal plane (0002), prismatic plane (11 $\bar{2}$ 0), pyramidal plane (01 $\bar{1}$ 1) and the schematic of layered BNNS. Also, the loading direction along the top surface and cross-section are marked. (b) Combined load-displacement curve along the top surface and cross-section of sintered BNNS	115
Figure 4.18:	SEM images of as-received (a) graphene nanoplatelets and (b) boron nitride nanosheets	118
Figure 4.19:	SEM image of the ball milled BNNS and GNP	119
Figure 4.20:	XRD patterns of the as-received GNP, as-received BNNS and ball milled BCN powder	120
Figure 4.21:	BCN phase formation mechanism during reactive spark plasma sintering	121
Figure 4.22:	XRD patterns of the reaction sintered (a) BCN 1, BCN 2 and BCN 3, (b) and (c) shows the scans in the 2 θ range of 23-32° and 40-45° respectively	125
Figure 4.23:	FTIR spectra of the ball milled powder and reaction sintered BCN 1, BCN 2 and BCN 3 respectively	127

Figure 4.24:	Raman spectra of reaction synthesized (a) BCN 1, (b) BCN 2, (c) BCN 3 and (d) change in I_D/I_G value with respect to reactive sintering conditions	129
Figure 4.25:	HRTEM image of the reaction sintered BCN 1 showing (a-b) bright field image showing GNP/BNNS, (c-d) lattice resolved TEM images with the inset showing corresponding diffraction pattern	130
Figure 4.26:	HRTEM image of the reaction sintered BCN 2 showing (a-b) bright field image showing GNP/BNNS and reacted BCN region, (c-d) lattice resolved TEM images with the inset showing corresponding diffraction pattern	132
Figure 4.27:	HAADF STEM image of reaction synthesized BCN 2	134
Figure 4.28:	HRTEM image of the reaction sintered BCN 3 showing (a-b) bright field image showing GNP/BNNS and reacted BCN region, (c-d) lattice resolved TEM images with the inset showing corresponding fast Fourier transform (FFT) pattern	136
Figure 4.29:	HAADF STEM image of reaction synthesized BCN 3	137
Figure 4.30:	SEM images of BCN1 pellet fracture surface indicating (a) unreacted GNP, porosity, (b) unreacted BNNS, zig-zag fracture surface and (c) kinking	138
Figure 4.31:	SEM images of BCN 2 pellet fracture surface showing (a) dense regions and (b) large reacted regions with few unreacted BNNS and GNP	139
Figure 4.32:	SEM images of BCN 3 pellet fracture surface indicating (a) dense regions with lamellar structure, (b) large reacted regions with few unreacted BNNS and GNP and (c) multiple nanosheets reaction sintered	140
Figure 4.33:	Texture studies of reactive sintered BCN 1 (002), (101), (100) pole figures along the (a) top surface and (b) cross-section of the pellet	142
Figure 4.34:	Texture studies of reactive sintered BCN 2 (002), (101), (100) pole figures along the (a) top surface and (b) cross-section of the pellet	143

Figure 4.35:	Texture studies of reactive sintered BCN 3 (002), (101), (100) pole figures along the (a) top surface and (b) cross-section of the pellet	143
Figure 4.36:	Schematic drawing of the sintered BCN pellet indicating the region of texture along top surface and cross-section. Simple hexagonal system is marked with the basal plane (0002) and pyramidal plane (101 $\bar{1}$)	144
Figure 4.37:	Relative volume fraction of textured components for the reactive sintered BCN pellets	144
Figure 4.38:	Coefficient of friction vs reactive sintering conditions for the bulk BCN pellets at room temperature	147
Figure 4.39:	Optical profilometer 3D wear track profiles of (a) BCN 1, (b) BCN 2, (c) BCN 3 and (d) two-dimensional line profiles displaying the wear track depth and width of BCN pellets tested at room temperature	148
Figure 4.40:	SEM micrographs of BCN 1 wear track formed after the wear test at room temperature	149
Figure 4.41:	SEM micrographs of BCN 2 wear track formed after wear test at room temperature	151
Figure 4.42:	SEM micrographs of BCN 3 wear track formed after wear test at room temperature	152
Figure 4.43:	Coefficient of friction vs reactive sintering conditions for the bulk BCN pellets at high temperature	153
Figure 4.44:	Optical profilometer 3D wear track profiles of (a) BCN 1, (b) BCN 2, (c) BCN 3 and (d) two-dimensional line profiles displaying the wear track depth and width of BCN pellets tested at high temperature	154
Figure 4.45:	SEM micrographs of BCN 1 wear track formed after wear test at high temperature	155
Figure 4.46:	SEM micrographs of BCN 2 wear track formed after wear test at high temperature	156
Figure 4.47:	SEM micrographs of BCN 3 wear track formed after wear test at high temperature	157

Figure 4.48:	Top surface indent load-displacement (a) combined BCN curves, and the individual (b) BCN 1, (c) BCN 2, (c) BCN 3 curves	159
Figure 4.49:	SEM images of deformation at different stages of loading from the real-time video	161
Figure 4.50:	SEM images of the reaction sintered BCN 1 top surface indent after the tip removal	162
Figure 4.51:	SEM images of the reaction sintered BCN 2 top surface indent after the tip removal	163
Figure 4.52:	SEM images of the reaction sintered BCN 3 top surface indent after the tip removal	164
Figure 4.53:	X-ray diffraction patterns of MAX and HF-treated MXene powders	168
Figure 4.54:	SEM images of (a) MAX, (b) 1 h, (c) 2 h and (d) 4 h HF treated MXene powder	169
Figure 4.55:	Schematic diagram showing the tribological test and shearing of MXene layers	170
Figure 4.56:	Wear track of steel substrate lubricated with pure MAX (Ti_2AlC) powder showing (a) low magnification, (b) pressed MAX powder, (c) lamellar structure and kinking	171
Figure 4.57:	Wear track of steel substrate lubricated with 1 h HF treated MXene (Ti_2C) powder showing (a) low magnification, (b) separated MXene layers populated along the track, (c) shearing of MXene layer	172
Figure 4.58:	Loss tangent values of MAX and HF treated samples at 1 mN and 5 mN load	174
Figure 4.59:	(a) damping height-time profiles at 5 mN load and (b) damping constant for pure MAX and HF-treated samples	175
Figure 4.60:	Damping behavior of MAX and HF-treated samples at a dynamic loading of (d) 1 μN and (e) 10 μN in the frequency range of 10-250 Hz	176
Figure 4.61:	Long cycle test for HF-treated samples at loads of 1 μN and 10 μN for a frequency of 150 Hz	177
Figure 4.62:	Schematic describing the intralayer deformation mechanism	178

Figure 4.63:	Schematic describing the compression between the sheets	179
Figure 4.64:	Change in displacement with varying frequency upon mechanical loading of (a) 1 μN and (b) 10 μN . Energy change with varying frequency upon mechanical loading of (c) 1 μN and (d) 10 μN	182
Figure 4.65:	Schematic describing the shearing/sliding between the sheets	184

Chapter I: Introduction

Graphene was the first 2D material discovered in the 2D materials paradigm. Beyond graphene, two-dimensional (2D) carbide and nitride based ceramics have attracted immense attention for their intriguing mechanical properties. The purpose of this study is to unravel the mechanical and tribological behavior of sintered two-dimensional (2D) carbide and nitride based ceramics with respect to their orientation. Monolayer 2D materials have been widely studied due to their unique properties and investigated primarily. In this study, multilayered two-dimensional materials are developed by spark plasma sintering and detailed analysis on the in-plane and out-of-plane deformation mechanisms are investigated in the sintered 2D materials. Mechanical and multiscale tribological properties of multilayered 2D material with respect to their orientation are investigated and this study will enable the wide range of novel applications.

1.1. Two-dimensional Nanostructured Materials

Nanostructured materials are low-dimensional materials in relation to their size, shape or layer thickness varying in the range of 1-100 nm. Nanostructured materials are classified based on their size and structure as zero-dimensional (0D), one-dimensional (1D), two-dimensional (2D) and three-dimensional (3D) [1]. Schematic representation of nanostructured materials are shown in Figure 1.1 [2]. Nanostructured materials exhibit unique mechanical, electrical, optical or magnetic properties due to their nanosize range and large surface area.

Two-dimensional materials are layered structure (two dimensions – length and thickness) with high aspect ratio and thickness in nanometer range [3]. The 2D materials vary from monolayer - single atomic layer, to multilayer – multiple atomic layers. They have strong in-plane chemical bond (covalent or ionic) and weak out-of-plane bond between the layers [4].

Due to this weak bonding between the layers, 2D materials can be cleaved into individual nanosheets. They can be synthesized by several methods such as hydrothermal synthesis, mechanical exfoliation, liquid exfoliation, chemical vapor deposition [5-8]. The different type of 2D nanostructure materials are nanoplates, nanosheets, nanowalls, nanodisks, nanoprisms and branched structures [9-13]. The properties of 2D materials vary with respect to their number of layers (single or multilayer) and they exhibit different electronic transport, mechanical, chemical, optical, thermal and magnetic properties [4]. Also, 2D materials are classified as (i) graphene family (van der Waals solids), (ii) 2D transition metal dichalcogenides (TMDs), (iii) 2D oxides, and series of 2D materials in each family are listed in Table 1.1 [14]. Recently, a new system has emerged in the 2D family, which is a structural analogue of graphene, known as MXene ($M_{n+1}X_n$) [15]. The most promising applications of 2D materials are electronic devices (sensors, superconductors), optoelectronic devices (photodiode), energy storage systems (supercapacitors, battery, and fuel cells), photocatalysts, inert coatings and reinforcements in nanocomposites [4, 16, 17]. Since the discovery of graphene [6], the interest in 2D materials has been rekindled and the family of 2D materials have received great attention. Unraveling the novel properties of a monolayer to multilayer and hybrid 2D systems will instigate further research and innovative applications.

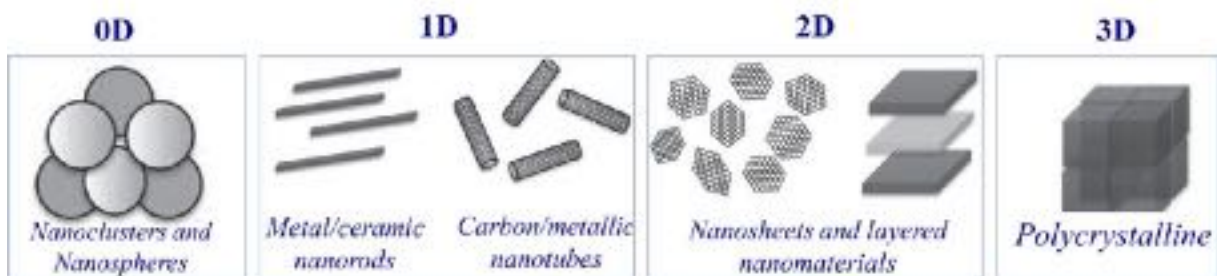


Figure 1.1: Schematic representation of nanostructured materials [2]

Table 1.1: Classification and list of 2D materials [4]

Graphene family	Graphene		hBN "white graphene"	BCN	Fluorographene	Graphene oxide
2D chalcogenides	MoS ₂ , WS ₂ , MoSe ₂ , WSe ₂		Semiconducting dichalcogenides: MoTe ₂ , WTe ₂ , ZrS ₃ , ZrSe ₃ , and so on		Metallic dichalcogenides: NbSe ₂ , NbS ₂ , TaS ₂ , TiS ₂ , NiSe ₂ , and so on	
					Layered Semiconductors: GaSe, GaTe, InSe, Bi ₂ Se ₃ , and so on	
2D oxides	Micas, BSCCO	MnO ₂ , WO ₃	Perovskite-type: LaNiO ₃ , (Ca,Sr) ₂ Nb ₂ O ₁₀ , Bi ₂ Ti ₂ O ₁₂ , Cu ₂ Ta ₂ TiO ₈ and so on		Hydroxides: Ni(OH) ₂ , Eu(OH) ₂ and so on	
	Layered Cu oxides	TiO ₂ , MnO ₂ , V ₂ O ₅ , TaO ₃ , RuO ₄ and so on			others	

1.2. Significance of Two-dimensional Materials

The growing interest in 2D materials in the recent years arises from their quantum size effect (nanometer-scale thickness) and high surface area. The monolayer or few layers of 2D material exhibit unique physical, chemical, electronic and optical characteristics. In terms of optical properties, 2D materials vary over a wide range of electromagnetic spectrum from ultraviolet (UV) to infrared (IR) because of zero band gap nature [18]. This distinct feature has significant role in modern device applications, such as photodetectors, solar cells, electronic semiconductor devices and optical coatings. The 2D materials broadly comprises of various compositions covering several elements from the periodic table and this results in fabrication of electronic devices from metals, semimetals, semiconductors to insulators. Heterostructures can be constructed by stacking different layered 2D materials, as their surface are smooth, passivated which results in excellent interface and these layers are bonded by weak van der Waals force [19]. In addition, for certain applications, the surface nature of 2D materials are custom tailored (ligand-surface interactions) by surface treatments [20]. Layers of 2D nanosheets have weak interactions between the sheets as they are bonded by weak van der Waals force, these 2D layered materials can be used as lubricants and additives for lubricating oils. Graphene, BNNS, WS₂, MoS₂, graphene oxide and MXene are few example of lubricants.

Monolayer graphene has exhibited high Young's modulus and tensile strength [21, 22]. So, this study suggests, it is possible to use 2D materials as reinforcements in composites to enhance their mechanical properties. This emphasizes the mechanical properties of 2D materials are equally interesting and will result in new avenue of potential applications. In the present research, mechanical and tribological properties of multi-layered van der Waals solids such as (i) boron nitride nanosheets, (ii) boron-carbon-nitride system and (iii) MXene are studied.

1.2.1. Boron Nitride Nanosheets (BNNS)

Hexagonal boron nitride (h-BN) are present in the 2D form as boron nitride nanosheets (BNNS), also called as white graphene, it is a structural analog of graphene [23]. They are generally found in stable form as a single monolayer or few layers of thin sheets of h-BN. The boron and nitrogen atoms within the plane have strong covalent bonding, and thus have superior thermal, chemical and mechanical properties. The weak van der Waals bond between BN layers facilitates gliding of layers against each other which enables them to be used as an excellent solid lubricant. It has been previously reported that functionalized BN nanosheets dispersed in various oils, exhibited enhanced lubrication compared to h-BN powder [24]. BNNS have also been used as a reinforcement in composite materials for improved mechanical properties [25-28]. BNNS have wide range of additional applications including deep ultraviolet emitter, functional composites, self-cleaning coatings, optoelectronic and nanoelectronic devices [24, 29-31]. Though 2D-BNNS are finding applications as reinforcement in composites, still their orientation effect on the mechanical and tribological properties are of great interest.

1.2.2. Boron-Carbon-Nitride System (BCN)

Layered boron carbon nitride (BCN) is a ternary system comprising of boron, carbon, nitrogen atoms arranged in graphene structure. 2D-BCN system has varying atomic arrangements and stoichiometry. Layered BCN system are mostly synthesized by chemical vapor deposition (CVD), physical vapor deposition (PVD), magnetron sputtering, chemical doping of graphene with B and N, mechanical alloying, high pressure high temperature methods [32-36]. Most of the synthesized BCN system comprises of graphene and h-BN phases, where it is difficult to identify the real BCN as X-ray diffraction patterns (h-BCN, graphene, h-BN) overlap with each other. So, it has been challenging to synthesize single phase BCN. The BCN system have shown good electronic and magnetic properties, these properties can be tailored by varying the arrangement or concentration of B, C, and N atoms. The BCN system have interesting applications in electronic devices, nano-devices, field emission, wear protective coatings.

1.2.3. MXene

The recent addition to the family of 2D materials are layered transition metal carbides, nitrides or carbonitrides called as MXene. They are synthesized by chemically etching out 'A' layers from MAX ($M_{n+1}AX_n$) phases, where M is the transition metal, A is from A-group element, X could be either nitrogen or carbon, n - 1, 2 or 3 [37-39]. This results in the formation of multilayer 2D MXene ($M_{n+1}C_n$), which is a structural analogue of graphene. For example, Ti_3C_2 MXene was formed by chemical etching of metallic Al layer from Ti_3AlC_2 by aqueous hydrofluoric acid (HF) at room temperature [40]. Newly synthesized MXene has very high surface energy, so it is susceptible to surface functionalization of -OH, -F or -O groups. MXene layers are easily separable after synthesis, as it weakens the interactions between MXene layers after the Al layers have been etched. MXene has exceptional electronic properties, good

magnetic, optical and thermal properties, these properties can be customized by controlling and modifying MXene surface terminations. MXene has been studied for wide range of applications, such as batteries, supercapacitors, sensors, electromagnetic shielding and hydrogen storage [41-45]. Theoretical studies on MXene has shown good mechanical properties, especially the functionalized MXene display enhanced mechanical properties [40]. So, MXene are further explored for other potential properties and applications, such as reinforcements for structural applications, flexible devices and lubricants.

1.3. Importance of Understanding the Mechanical and Tribological Properties of 2D Materials

In general, there are only few reports on mechanical properties of bulk 2D materials. Experimental study on mechanical properties of monolayer graphene has shown excellent in-plane stiffness and strength [21, 22]. The understanding of mechanical properties of monolayer or multilayer 2D materials are vital in improving their functionality of potential applications. Elastic properties of most monolayer 2D materials are primarily studied, as the atomically thin 2D materials can be deformed by in-plane stretching or out-of-plane bending. Based on first principle calculations, 2D materials elastic properties are predicted. The strength and toughness of 2D materials are imperative in the research of their mechanical properties, as the major concern in device applications of 2D materials is the fracture behavior. Concurrently, it is important to discern the fundamental fracture mechanisms of both monolayer, multilayer and bulk 2D materials. Recognizing these fundamental mechanical properties of 2D materials will lead to novel applications.

Layered 2D materials as lubricants are widely used, due to its unique frictional and wear properties. Most of the lubricants are from graphene family and metal dichalcogenides. As the layered materials have smooth surface and weak van der Waals interactions between the layers, it offers easy interlayer sliding, resulting in excellent tribological behavior. During

tribological studies, layered materials have the ability to separate as single layer and form protective film on worn surface, thereby enhancing the lubrication. In addition, surface treatments of 2D materials enables homogeneous dispersion of layered materials in oil or liquid medium, indicating layered materials can be used as additive in typical lubricants [46, 47]. Monolayer or multilayered 2D materials can be used in engine components, reinforcement in coatings for joint implants, micro (or nano) electromechanical systems (MEMS/NEMS) to reduce the friction and simultaneously improve the wear resistance. These properties and developments have fostered further research on layered 2D materials for tribological applications.

In the previous studies, the research was focused mostly on mechanical properties of monolayer 2D materials and tribological properties of mono/multilayer 2D materials as additives. In the present study, we emphasize the mechanical properties, deformation mechanisms and tribological properties with respect to their orientation of multilayered bulk 2D materials sintered by spark plasma sintering.

1.4. Research Objectives

The *overall objective* of the proposed work is to understand the bulk behavior of sintered 2D nitride and carbide based ceramics with respect to their orientation. The overall objective will be achieved through following specific aims:

- Spark plasma sintering (SPS) of 2D boron nitride nanoplatelets (BNNS)
- *Reaction synthesis* of BNNS and graphene nanoplatelets (GNP) using SPS to form the ternary boron carbon nitride (BCN) system
- Exploring the *friction and wear properties* of the sintered BNNS pellets along the in-plane and out-of-plane direction

- Exploring the friction and wear properties of the sintered BCN pellets along the out-of-plane direction
- *In-situ* high load indentation studies on the sintered BNNS and BCN pellets along the in-plane and out-of-plane direction – in order to *identify the deformation with respect to their orientation*
- Synthesizing *2D MXene from MAX phase*, and understanding their basic mechanical and tribological properties

Figure 1.2 shows the summary of the research carried out in this study.

The dissertation has been organized in the following chapters, Chapter 2 presents the detailed literature review of BNNS, BCN and MXene, highlights the motivation for this research study. The experimental procedure and characterization methods used for this research are discussed in Chapter 3. The results and detailed scientific analysis based on the objective of this research are presented and discussed in Chapter 4. The key findings and conclusions are summarized in Chapter 5. The thesis ends with Chapter 6 comprising of recommendations for future research.

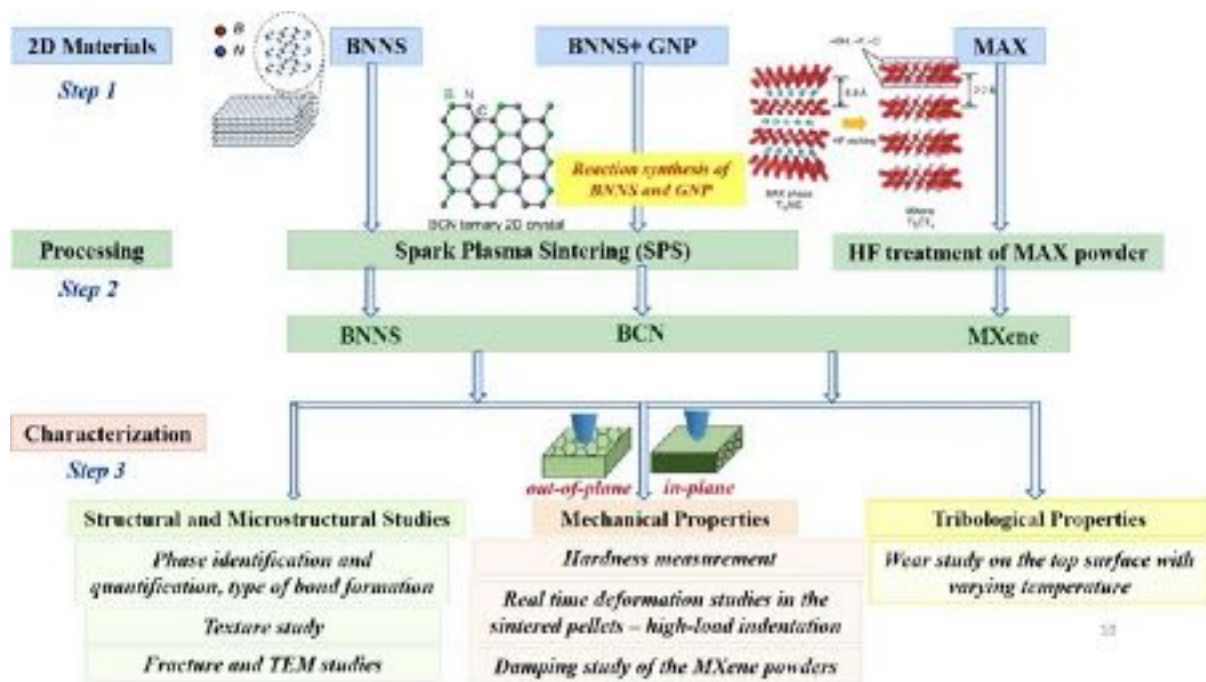


Figure 1.2: Work plan of the present research

1.5. References

1. V.V. Pokropivny, V.V. Skorokhod. Classification of nanostructures by dimensionality and concept of surface forms engineering in nanomaterial science. *Material Science Engineering C* 27 (2007) 990-993.
2. P.R. Sajanlal, T.S. Sreepasad, A.K. Samal, T. Pradeep. Anisotropic nanomaterials: Structure, growth, assembly, and functions. *Nano Reviews* 2 (2011) 1-62.
3. J.M. Hamm, O. Hess, Two two-dimensional materials are better than one. *Science* 340 (2013) 1298-1299.
4. A. Gupta, T. Sakhivel, S. Seal. Recent development in 2D materials beyond graphene. *Progress in Materials Science* 73 (2015) 44–126.
5. Y. Peng, Z. Meng, C. Zhong, J. Lu, W. Yu, Y. Jia, Y. Qian. Hydrothermal synthesis and characterization of single-molecular-layer MoS₂ and MoSe₂. *Chemistry Letters* 30 (2001) 772–773.
6. K.S. Novoselov, A.K. Geim, S.V. Morozov, D. Jiang, Y. Zhang, S.V. Dubonos, I. V. Grigorieva, A.A. Firsov. Electric field effect in atomically thin carbon films. *Science* 306 (2004) 666–669.
7. V. Nicolosi, M. Chhowalla, M.G. Kanatzidis, M.S. Strano, J.N. Coleman. Liquid exfoliation of layered materials. *Science* 340 (2013) 1226-1229.

8. Y. Zhan, Z. Liu, S. Najmaei, P.M. Ajayan, J. Lou. Large-area vapor-phase growth and characterization of MoS₂ atomic layers on a SiO₂ substrate. *Small* 8 (2012) 966–971.
9. A.K.P. Mann, S.E. Skrabalak. Synthesis of single crystalline nanoplates by spray pyrolysis: A metathesis route to Bi₂O₆. *Chemistry of Materials* 23 (2011) 1017–1022.
10. P.F. Siril, L. Ramos, P. Beaunier, P. Archirel, A. Etcheberry, H. Remita. Synthesis of ultrathin hexagonal palladium nanosheets. *Chemistry of Materials* 21 (2009) 5170–5175.
11. S. Vizireanu, S.D. Stoica, C. Luculescu, L.C. Nistor, B. Mitu, G. Dinescu. Plasma techniques for nanostructured carbon materials synthesis. A case study: carbon nanowall growth by low pressure expanding RF plasma. *Plasma Sources Science and Technology* 19 (2010) 034016-1-034016-10.
12. S.H. Jung, E. Oh, K.H. Lee, Y. Yang, C.G. Park, W. Park, S.H. Jeong. Sonochemical preparation of shape-selective ZnO nanostructures. *Crystal Growth and Design* 8 (2008) 265–269.
13. B.B. Nayak, D. Behera, B.K. Mishra. Synthesis of silicon carbide dendrite by the arc plasma process and observation of nanorod bundles in the dendrite arm. *Journal of American Ceramic Society* 93 (2010) 3080-3083.
14. A. Geim, I. Grigorieva. Van der Waals heterostructures. *Nature* 499 (2013) 419–425.
15. M. Naguib, Y. Gogotsi. Synthesis of two-dimensional materials by selective extraction. *Accounts of Chemical Research* 48 (2015) 128-135.
16. S.Z. Butler, S.M. Hollen, L. Cao, Y. Cui, J.A. Gupta, H.R. Gutiérrez, T.F. Heinz, S.S. Hong, J. Huang, A.F. Ismach, E. Johnston-Halperin, M. Kuno, V.V. Plashnitsa, R.D. Robinson, R.S. Ruoff, S. Salahuddin, J. Shan, L. Shi, M.G. Spencer, M. Terrones, W. Windl, J.E. Goldberger. Progress, challenges, and opportunities in two dimensional materials beyond graphene. *ACS Nano* 7 (2013) 2898-2926.
17. J.N. Tiwari, R.N. Tiwari, K.S. Kim. Zero-dimensional, one-dimensional, two-dimensional and three-dimensional nanostructured materials for advanced electrochemical energy devices. *Progress in Material Science* 57 (2012) 724–803.
18. F. Bonaccorso, Z. Sun, T. Hasan, A.C. Ferrari. Graphene photonics and optoelectronics. *Nature Photonics* 4 (2010) 611-622.
19. A.K. Geim, I.V. Grigorieva. Van der Waals heterostructures. *Nature* 499 (2013) 419–425.
20. Y. Xu, Z. Liu, X. Zhang, Y. Wang, J. Tian, Y. Huang, Y. Ma, X. Zhang, Y. Cheng. A graphene hybrid material covalently functionalized with porphyrin: synthesis and optical limiting property. *Advanced Materials* 21 (2009) 1275–1279.

21. I. Frank, D.M. Tanenbaum, A. Van der Zande, P.L. McEuen. Mechanical properties of suspended graphene sheets. *Journal of Vacuum Science and Technology B* 25 (2007) 2558-2561.
22. C. Lee, X. Wei, J.W. Kysar, J. Hone. Measurement of the elastic properties and intrinsic strength of monolayer graphene. *Science* 321 (2008) 385-388.
23. M. Corso, W. Auwarter, M. Muntwiler, A. Tamai, T. Greber, J. Osterwalder. Boron nitride nanomesh. *Science* 303 (2004) 217–220.
24. S. Kumari, O.P. Sharma, R. Gusain, H.P. Mungse, A. Kukrety, N. Kumar, H. Sugimura, O.P. Khatri. Alkyl-chain-grafted hexagonal boron nitride nanoplatelets as oil dispersible additives for friction and wear reduction. *ACS Applied Materials and Interfaces* 7 (2015) 3708-3716.
25. R. Saggar, H. Porwal, P. Tatarko, I. Dlouhy, M.J. Reece. Boron nitride nanosheets reinforced glass matrix composites. *Advances in Applied Ceramics* 114 (2015) S26-S33.
26. A. Kovalcikova, J. Balko, C. Balazsi, P. Hvizdos, J. Disza. Influence of h-BN content on mechanical and tribological properties of Si₃N₄/BN ceramic composites. *Journal of European Ceramic Society* 34 (2014) 3319–332.
27. D. Cai, Z. Yang, X. Duan, B. Liang, Q. Li, D. Jia, Y. Zhou. A Novel BN–MAS system composite ceramics with greatly improved mechanical properties prepared by low temperature hot-pressing. *Material Science Engineering A* 633 (2015) 194–199.
28. W. Sun, L. Wang, T. Wu, Y. Pan, G. Liu. Communication—multi-layer boron nitride nanosheets as corrosion-protective coating fillers. *Journal of Electrochemical Society* 163 (2016) C16-C18.
29. K. Watanabe, T. Taniguchi, H. Kanda. Direct-bandgap properties and evidence for ultraviolet lasing of hexagonal boron nitride single crystal. *Nature Materials* 3 (2004) 404–409.
30. A.G.F. Garcia, M. Neumann, F. Amet, J.R. Williams, K. Watanabe, T. Taniguchi, D. Goldhaber Gordon. Effective cleaning of hexagonal boron nitride for graphene devices. *Nano Letters* 12 (2012) 4449–4454.
31. J. Li, G. Gui, J. Zhong. Tunable bandgap structures of two dimensional boron nitride. *Journal of Applied Physics* 104 (2008) 094311.
32. C. Popov, K. Saito, B. Ivanov, Y. Koga, S. Fujiwara, V. Shanov. Chemical vapor deposition of BC₂N films and their laser induced etching with SF₆. *Thin Solid Films* 312 (1998) 99.
33. V. Linssa, S.E. Rodilb, P. Reinkec, M.G. Garnierd, P. Oelhafend, U. Kreissige, F. Richter. Bonding characteristics of DC magnetron sputtered B-C-N thin films investigated by Fourier-transformed infrared spectroscopy and X-ray photoelectron spectroscopy. *Thin Solid Films* 467 (2004) 76-87.

34. W. Wang, Y. Bando, C. Zhi, W. Fu, E. Wang, D. Golberg. Aqueous noncovalent functionalization and controlled near-surface carbon doping of multiwalled boron nitride nanotubes. *Journal of American Chemical Society* 130 (2008) 8144.
35. R. Torres, I. Caretti, R. Gago, Z. Martín, I. Jiménez. Bonding structure of BCN nanopowders prepared by ball milling. *Diamond and Related Materials* 16 (2007) 1450-1454.
36. Y.J. Tian, J.L. He, D.L. Yu, D.C. Li, G.T. Zou, X.P. Jia, L.X. Chen, O. Yanagisawa. B–C–N compound synthesized under high temperature and high pressure. *Radiation Effects and Defects Solid* 157 (2002) 245-251.
37. M. Naguib, V.N. Mochalin, M.W. Barsoum, Y. Gogotsi. Y. 25th anniversary article: MXenes: a new family of two-dimensional materials. *Advanced Materials* 26 (2014) 992-1005.
38. M.W. Barsoum. The $M_{N+1}AX_N$ phases: A new class of solids: Thermodynamically stable nanolaminates. *Progress in Solid State Chemistry* 28 (2000) 201-281.
39. M.W. Barsoum, in *Encyclopedia of Materials Science and Technology*, (Eds: K. H. J. Buschow, R. W. Cahn, M. C. Flemings, E. J. Kramer, S. Mahajan, P. Veysiere), Elsevier, Amsterdam, 2006.
40. M. Naguib, M. Kurtoglu, V. Presser, J. Lu, J.J. Niu, M. Heon, L. Hultman, Y. Gogotsi, M.W. Barsoum. Two-dimensional nanocrystals produced by exfoliation of Ti_3AlC_2 . *Advanced Materials* 23 (2011) 4248-4253.
41. M. Naguib, J. Come, B. Dyatkin, V. Presser, P.L. Taberna, P. Simon, M.W. Barsoum, Y. Gogotsi. MXene: a promising transition metal carbide anode for lithium-ion batteries. *Electrochemistry Communications* 16 (2012) 61-64.
42. Y.Y. Peng, B. Akuzum, N. Kurra, M.Q. Zhao, M. Alhabeab, B. Anasori, E.C. Kumbur, H.N. Alshareef, M. D. Ger, Y. Gogotsi. All-MXene (2D titanium carbide) solid-state micro supercapacitors for on-chip energy storage. *Energy and Environmental Science* 9 (2016) 2847-2854.
43. F. Wang, C. Yang, C. Duan, D. Xiao, Y. Tang, J. Zhu. An organ-like titanium carbide material (MXene) with multilayer structure encapsulating hemoglobin for a mediator-free biosensor. *Journal of Electrochemical Society* 162 (2015) B16–B21.
44. F. Shahzad, M. Alhabeab, C.B. Hatter, B. Anasori, S. Man Hong, C.M. Koo, Y. Gogotsi, Electromagnetic interference shielding with 2D transition metal carbides (MXenes). *Science* 353 (2016) 1137-1140.
45. Q. Hu, D. Sun, Q. Wu, H. Wang, L. Wang, B. Liu, A. Zhou, J. He, MXene: A new family of promising hydrogen storage medium, *J. Phys. Chem. A* 117 (2013) 14253-14260.

46. M.E. Uddin, T. Kuila, G.C. Nayak, N.H. Kim, B.C. Ku, J.H. Lee. Effects of various surfactants on the dispersion stability and electrical conductivity of surface modified graphene. *Journal of Alloys and Compound* 562 (2013) 134-142.
47. H.J. Song, X.H. Jia, N. Li, X.F. Yang, H. Tang. Synthesis of Fe₂O₃ nanorod/graphene oxide composites and their tribological properties. *Journal of Material Chemistry* 22 (2011) 895-902.

Chapter II – Literature Review

2.1. Two-dimensional Materials

Since the discovery of graphene, two-dimensional (2D) materials have garnered significant attention in the research world. The 2D materials are layered crystalline materials. Graphene has excellent electrical, mechanical and thermal properties, they are used in various applications from energy storage, photovoltaics, electronics, and light-weight composite materials to lubrication application. Similarly, there are other 2D materials existing with diverse physical and chemical properties. The 2D materials will unravel the new generation of applications in energy, electronic and optoelectronic devices. Most of the 2D materials can be synthesized as monolayer or multilayered materials with varying atomic thickness. The varying atomic thickness of 2D materials can influence the physical, mechanical and chemical properties. In this chapter, the synthesis, structure, physical, mechanical properties and applications of boron nitride nanosheet, 2D ternary boron-carbon-nitride system and MXene are discussed. Finally, the literature review leads us to the scope of exploring certain properties of bulk nanostructured 2D materials are presented.

2.2. Hexagonal Boron Nitride Nanosheets

Boron nitride nanosheets (BNNS) are two-dimensional layered materials comprising of single or multilayered h-BN. They are structurally similar to graphene. In each layer of BNNS, boron and nitrogen atoms are arranged alternate to each other in a honeycomb lattice. The sp^2 hybridized alternating B-N atoms comprises of partial covalent and ionic bonding, unlike pure covalent C-C bonding in graphene and the layers are held by weak van der Waals force. So, BNNS are distinct from graphene and they have unique properties, like electrically insulating, wide band gap, high mechanical strength (monolayer BNNS), high thermal conductivity, high

temperature stability, low dielectric constant, good chemical stability and good lubrication. BNNS are synthesized by top-down exfoliation (mechanical exfoliation, ball milling) and bottom-up (CVD, PVD) growths. BNNS are used in wide range of diverse applications, deep ultraviolet photodetectors, solid lubricants, protective coatings, dielectric gates, thermal fillers, anti-oxidant lubricants, cosmetics, light emitting diodes, insulators, neutron captures, catalyst, capacitors and flexible electronics.

2.2.1. Synthesis of BNNS

In the initial days, monolayer boron nitride nanosheet was grown epitaxially on single crystalline metal surface (Ni, Pd, Pt, Rh) by thermal decomposition and high temperature chemical vapor deposition (CVD) of borazine [1, 2]. This monolayer boron nitride was observed by scanning tunneling microscope as displayed in Fig. 2.1. With the discovery of graphene, free-standing monolayer hexagonal boron nitride was discovered by micromechanical cleavage technique [3]. So, BNNS can be prepared by several methods such as, mechanical exfoliation, chemical exfoliation (sonication), ball-milling, high-energy electron beam irradiation, chemical vapor deposition (CVD), physical vapor deposition (PVD), and wet chemical reaction of urea and boric acid [4-10].

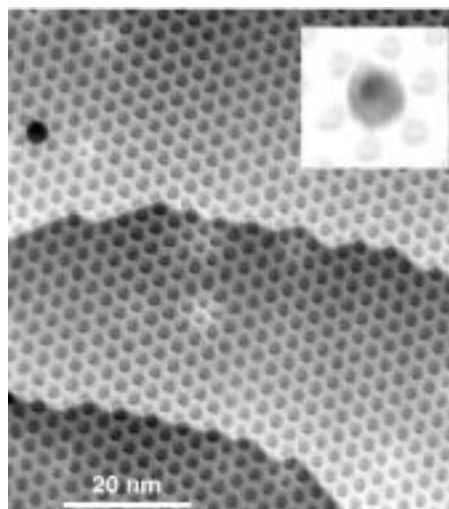
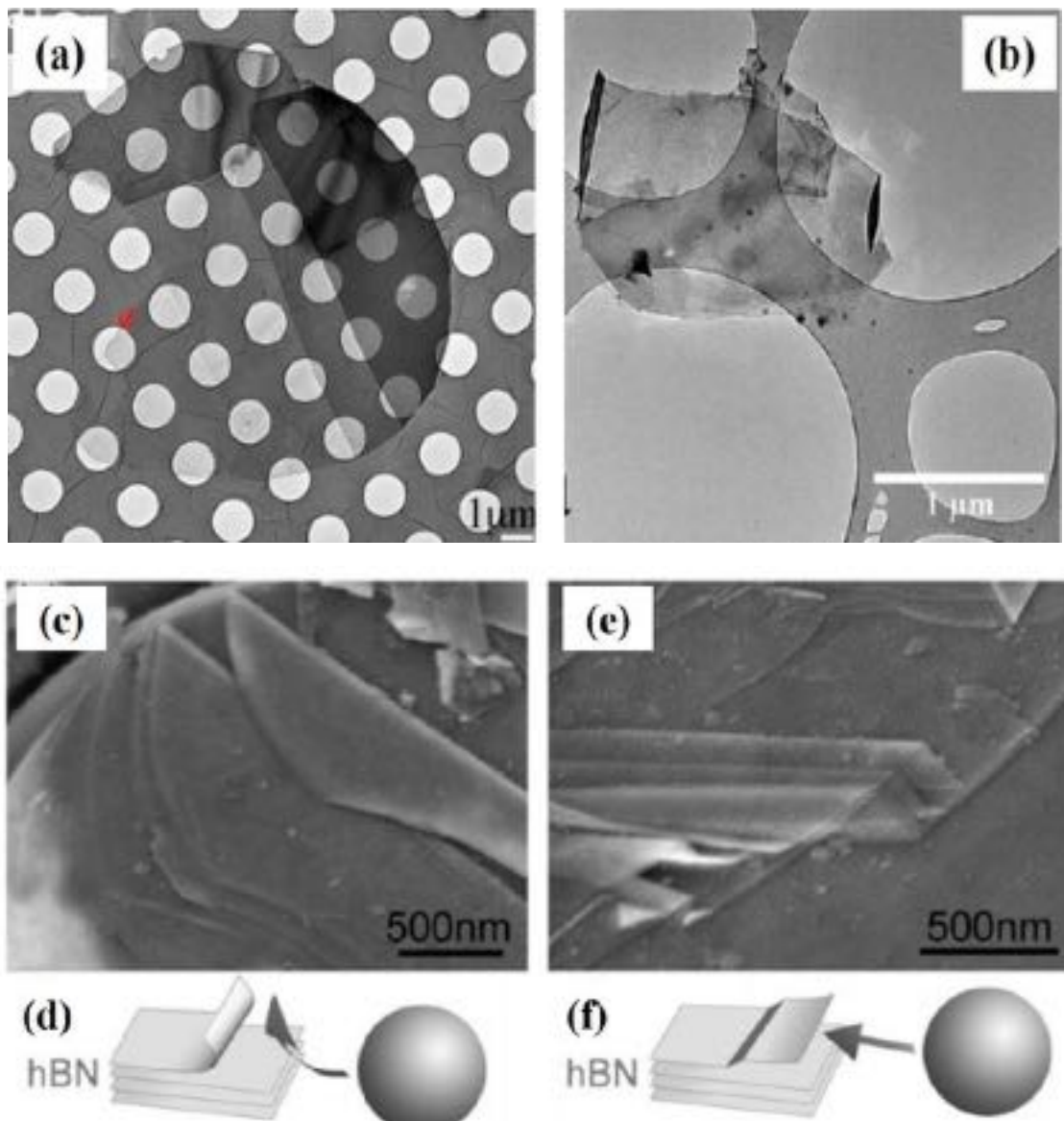


Figure 2.1: Scanning tunneling microscope image of monolayer boron nitride grown on Rh(111) surface by high temperature CVD [2]

- (a) Mechanical Exfoliation - This technique is one of the easiest way to synthesize high-quality BNNS. The layers of boron nitride were peeled off from h-BN powders using an adhesive tape. Average crystallite size of peeled BNNS was about 10 μm with the thickness of BNNS varying between 3.5 nm to 80 nm as shown in Fig. 2.2(a) [4]. The drawback of this technique is the lateral size of BNNS.
- (b) Chemical Exfoliation – This technique is also referred as sonication by ultrasonic energy. Monolayer and multilayer BNNS can be exfoliated by this method. Han *et al.* for the first time synthesized mono/few-layered nanosheets from the single crystalline h-BN through ultrasonication in an organic solution (Fig. 2.2(b)) [5]. Various solvents were used in this technique for chemical exfoliation of BNNS and the solvents were required to be with similar surface energy as h-BN [11, 12]. BNNS with thickness of 2-10 nm was exfoliated and this technique is scalable.
- (c) Ball Milling - The h-BN powders was ball milled under a controlled nitrogen atmosphere to obtain thin BNNS [6]. High quality nanosheets were produced by optimizing ball milling conditions, so the BNNS shear more gently. Further, the ball milled h-BN were sonicated in liquid medium for a shorter duration (0.5 h) to achieve thin BNNS as shown in Fig. 2.2(c). Advantage of this technique is to produce high yield BNNS.
- (d) Chemical Vapor Deposition (CVD) - Large area and large quantity BNNS were produced by CVD. By catalyst free CVD technique, thick BNNS can be produced [13]. Deposition temperature was low, adjusted from 1100 to 1300 $^{\circ}\text{C}$ and BNNS in the size range of 25-50 nm were produced. In certain CVD methods, thin BNNS can be synthesized by combination of different precursors such as BF_3/NH_3 , BCl_3/NH_3 , $\text{B}_2\text{H}_6/\text{NH}_3$ or single precursor such as ammonia borane, borazane, and borazine [14-17]. Using thermal CVD

method, vertically aligned BNNS were produced on Si/SiO₂ substrates by using B, MgO and FeO precursors under NH₃ flow in furnace as shown in Fig. 2.2(g) [18]. The major disadvantage of CVD technique was the contamination, where mostly it has metal or metal oxide impurities.

(e) Wet Chemical Reaction – Multilayered BNNS were synthesized by chemical reaction at 900 °C between boric acid and urea in nitrogen atmosphere [10]. Varying the concentration of boric acid and urea, the number of BNNS layers were regulated and for example with increase in urea concentration, the nanosheet thickness decreases.



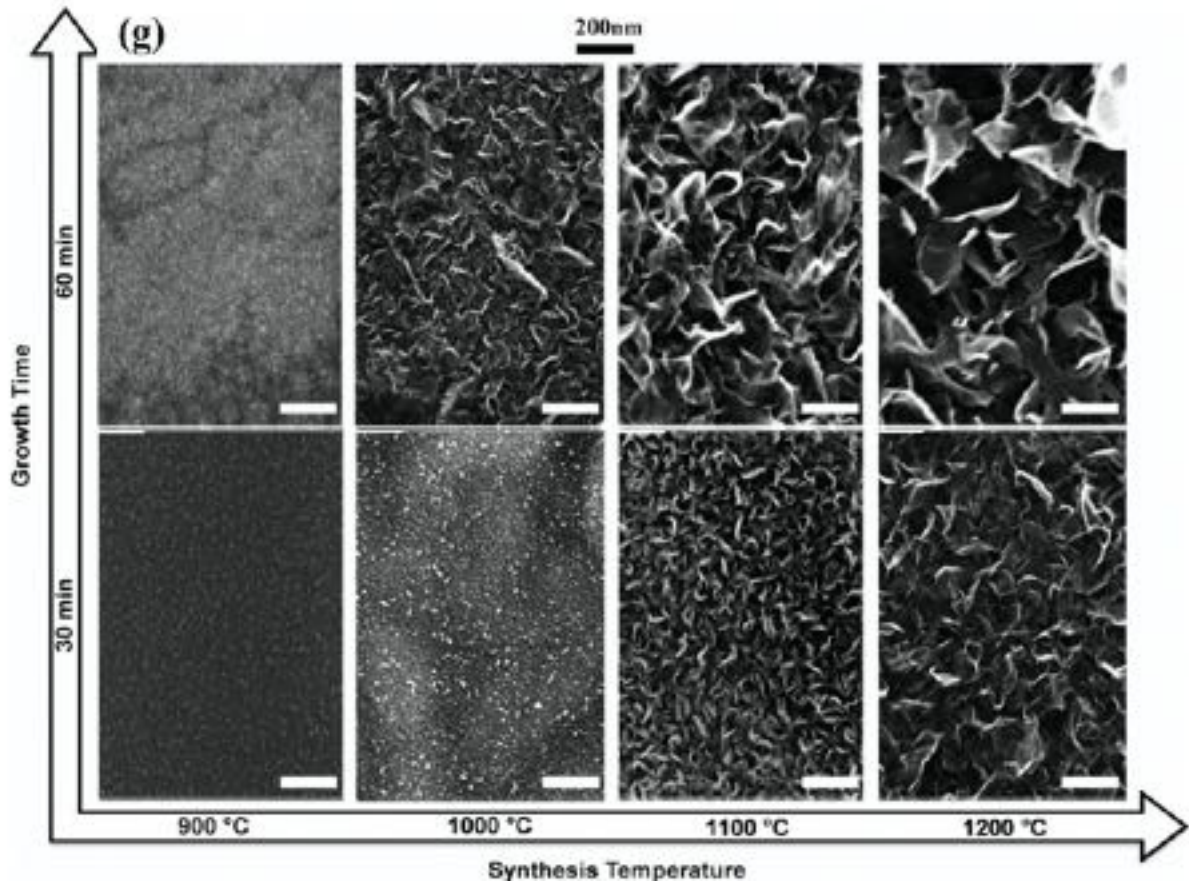


Figure 2.2: Transmission electron microscope image of exfoliated BNNS by (a) mechanical exfoliation [4], (b) chemical exfoliation. Scanning electron microscope image of (c, d) exfoliation from the edge of h-BN particle and (e, f) peeling off thin sheet from the top surface of h-BN particle [6], (g) vertical aligned BNNS synthesized by CVD at 900 -1200 °C for 30 and 60 min [18]

2.2.2. Consolidation Methods for h-BNNS

Consolidation of 2D BNNS in the bulk form have not been studied till date. Mostly BNNS were used in the consolidation process as reinforcement in composite materials for suppressing grain growth, improving the strength and toughness. Various consolidation process for BNNS as reinforcement, includes pressureless sintering, spark plasma sintering (SPS), plasma spraying, hot isostatic pressing and hot pressing [19-23]. In case of conventional h-BN powders consolidation, they were mostly sintered using sintering aid by hot pressing, pressureless sintering or spark plasma sintering [24-26]. The densification of monolithic compact depends on heating rate, cooling rate, sintering temperature, holding time and the applied pressure. Compared to different consolidation methods, spark plasma sintering will be

an effective method for densification of h-BNNS without losing their 2D nature. This can be accomplished by faster heating of the die and sample with shorter dwell times during sintering, which results in minimum grain growth of sintered BNNS.

2.2.3. Structural and Anisotropic Properties of BNNS

Monolayer hexagonal BNNS is a structural analogue of graphene and they are often referred as white graphene. BNNS has a honeycomb structure, in a 2D lattice plane the sp^2 bonded B and N atoms are arranged alternatively, where each hexagonal ring comprises of 3 boron and 3 nitrogen atoms. Unlike graphene, the layers are stacked in a peculiar way, where the hexagonal rings are superposed and along the c-axis, B and N atoms are in series. Typical BNNS structure is shown in Fig. 2.3. The BNNS interlayers are held together by weak van der Waals forces. Boron and nitrogen atoms within the plane exhibit a strong covalent (σ) bonding. In addition, the insulating nature of BNNS arises from partial ionic bonding observed because of the electronegativity difference between B-N atoms [27]. The interlayer distance between two BNNS layers is 0.334 nm and structural parameters are summarized in Table 2.1 [28]. Due to the large interlayer spacing and weak bonding between the layers, sliding of layers occurs easily against each other. The edges of BNNS can be either zig-zag B/N or BN paired armchair edge [29]. Most of the properties of monolayer BNNS are similar to graphene because of their structural similarity. BNNS layers shows AA' stacking - along the c-axis, hexagonal rings are stacked with B and N atoms alternate to each other, whereas graphene displays AB stacking sequence – each layer is shifted by half a hexagon. So compared to graphene, BNNS AA' stacking sequence has a strong interlayer interaction which results in poor exfoliation or functionalization.

Table 2.1: Structural parameter of hexagonal boron nitride nanosheet [28]

Type of material	h-BN
Crystal structure	Hexagonal
B-N bond length	0.144 nm
Lattice parameter	a = 0.250 nm c = 0.666 nm

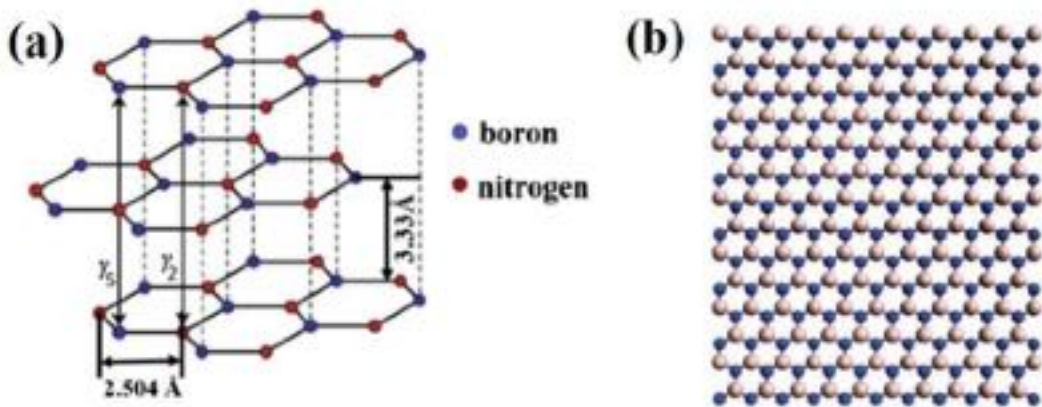


Figure 2.3: (a) Crystal structure of BNNS and (b) model of monolayer 2D BNNS [29]

One of the prominent physical property of hexagonal boron nitride nanosheet is the ability to exhibit highly oriented structure. This arises from the symmetry of h-BN itself as-per the law of crystal physics [30]. BNNS anisotropy results from the bonding nature difference along the in-plane (strong covalent bonding within the hexagonal planes) and out-of-plane (weak van der Waals forces between the planes). Additionally, anisotropic nature of the BNNS are instigated by the synthesis and processing techniques. For example, BNNS coating on Si/SiO₂ substrate at 1000 °C by CVD technique displayed partially vertically aligned BNNS [18]. Similarly, hot pressing of h-BN under uniaxial pressure allows the particles to rearrange, where the particles were arranged perpendicular to the pressing direction [31]. The anisotropic nature has a significant role on the physical and mechanical properties of hexagonal boron

nitride nanosheet. Sometimes, this textured nature may contribute in better electrical, mechanical, thermal or optical properties compared to isotropic BNNS.

2.2.4. Physical Properties of BNNS

The h-BN has high thermal conductivity, theoretical calculations on thermal conductivity (κ) of 2D BNNS showed the values in the range of 300 – 2000 $\text{Wm}^{-1}\text{K}^{-1}$ [32-35]. BNNS thermal conductivity value was mostly higher than certain metals and ceramic materials, but their value was comparatively lesser than graphene thermal conductivity, 1500 – 2500 $\text{Wm}^{-1}\text{K}^{-1}$. Though graphene and BNNS exhibit similar crystal structure and lattice constants, the difference in thermal conductivity arises from the atomic mass differences of the B-N atoms and BNNS softer phonon dispersions [32]. As graphene is thermally and electrically conductive, they cannot be used for certain applications such as high speed dielectronics and electronics [36]. For these applications, they require a material with quick heat conducting and electrically insulating in nature. Single layer BNNS has higher thermal conductivity compared to multilayer BNNS, this is attributed to the decreased interlayer phonon scattering. BNNS has good oxidation resistance and chemical stability up to 850 °C compared to graphene [37]. BNNS have wide band gaps of 5.0-6.0 eV and they are electrical insulators [38, 39]. In BNNS, the wide band gap exist along the thickness and lateral direction of the layer. Similarly, h-BNNS have wide optical band gap of 5.7 eV to 6 eV [40-42]. BNNS has good absorption in the ultraviolet range and for the visible range it has no absorption. BNNS has considerable photoluminescence property. Hexagonal BNNS in infrared and visible range is transparent. In terms of magnetic properties, pristine 2D BNNS is a non-magnetic in nature, by introducing defects or adding dopants to 2D BNNS structure, will results in spontaneous magnetization [43, 44]. Si *et al.* showed spontaneous magnetization of h-BNNS, by creating vacancy defects of B or N atoms in the h-BN structure [45]. In terms of wetting properties, Pakdel *et al.* showed

the vertically aligned BNNS on Si substrates has good water repellency [18]. So the contact angle for water on BNNS surface increased from 51° to 150° . Thus, the BNNS surface changed from hydrophobic surface to super-hydrophobic surface. Also, the change in pH of water will not affect the wetting properties of BNNS because of its chemical inertness [18, 46]. The surface roughness of BNNS has a significant effect on the wetting nature. Simulation studies on wetting of wrinkled monolayer BNNS has shown smaller contact angle, this was due to the difference in B-N polarity and this initiates the interaction with polar water molecules [47].

2.2.5. Mechanical and Tribological Properties of BNNS

Monolayer graphene has shown exceptional mechanical properties, as BNNS is structural analogue of graphene, monolayer BNNS is expected to be stronger [48-50]. Compared to most of the 2D materials, BNNS remains to be stronger [51]. First principle calculations on monolayer BNNS showed the in-plane strength to be 267 N/m [51]. Experimentally, the mechanical properties of multilayered BNNS has been studied by nanoindentation and atomic force microscope [52]. The breaking stress and modulus of free standing BNNS were measured by indenting at the center of BNNS layer using diamond tip. The thickness of BNNS was 1-2 nm, the resulting breaking stress was 8-16 N/m and modulus was 220-510 N/m. The reported modulus was less than the modulus of monolayer BNNS (270 N/m) measured by first principle calculation. This difference in modulus with respect to experimentation is attributed to the defects in BNNS (intrinsic vacancy). Similarly, single crystalline BNNS by sonication method varied in thickness from 25 nm to 300 nm [53]. Bending modulus of single crystalline BNNS was measured by three-point bending test using atomic force microscope. The flexibility of BNNS enhances with decrease in thickness of nanosheet, this was due to the layer distribution of stacking faults.

Two dimensional BNNS has excellent friction and wear properties similar to graphene. This behavior was observed in bulk h-BN and graphite. The weak van der Waals bond between BN layers facilitates gliding of layers against each other which enables them to be used as an excellent solid lubricant. In addition, BNNS has outstanding chemical inertness, good strength and smooth surface, these properties further enhance the tribological properties. Recent study revealed the frictional properties of 2D BNNS depends on the thickness of the layer [54]. BN nanosheets dispersed in various lube oils exhibited enhanced lubrication properties compared to h-BN powder [55].

2.2.6. Application of BNNS

BNNS has wide range of applications because of its various physical and mechanical properties.

(a) Electronic application – BNNS is an outstanding dielectric material and used in electronic devices as field-effect tunneling transistor, where BNNS separated two graphene layers and acts as a gate insulator [56]. They can also be used in future as field emitters or catalyst.

(b) Optical application – BNNS exhibit excellent optical properties (i.e) ultraviolet (UV) luminescence emissions. BNNS are promising candidates for optoelectronic applications. Deep UV photodetectors were used for optical storage, pollution monitoring, water purification, photocatalysis, space communications, light emitting diodes and optical sensor [57].

(c) Thermal application – BNNS thermal conductivity and specific heat are substantially good. So, BNNS can be used as thermal fillers in composite and thermal rectifiers for microelectronic processor, calorimeters and refrigerators [58, 59].

(d) Mechanical applications – BNNS has excellent mechanical properties, they are used widely as reinforcement material in ceramic and polymer composites. For example, Si_3N_4 with boron nitride nanosheets were prepared by hot isostatic pressing. Compared to monolithic Si_3N_4 , ceramic composites ($\text{Si}_3\text{N}_4/\text{BNNS}$) displayed an increase in fracture toughness especially with an addition of 5 wt% of BNNS [60]. BN nanosheets were also employed in PMMA as reinforcement, which showed 22% improvement in elastic modulus and 11% increase in strength of PMMA with significant improvement in thermal conductivity of the composite [61].

(e) Wetting application – Hydroxyl functionalized BNNS surface change in their wetting behavior, by hydrophobic or super-hydrophobic compared to smooth BNNS film [62]. Hence, BNNS films can be used in self-cleaning coatings, water-repellency coatings, anti-corrosion and anti-fouling systems.

(f) Tribological application – Two dimensional h-BNNS has excellent friction and wear properties, which is due to the weak van der Waals forces between the layers. BNNS can be used as lubricating oil additive, high temperature lubricant, solid-state lubricant and as lubricating additive in ceramic, polymers and metals.

(g) Cosmetic application – BNNS is transparent in nature, has high oil absorption and good moisture binding effect. BNNS are used in cosmetics as raw powder in small quantity range from 0.1 wt% to 70 wt%. They are used in eye-shadow, foundation, lipsticks, shampoos and skincare creams.

2.3. Boron-Carbon-Nitride System

Ternary boron-carbon-nitride (BCN) system can typically form cubic BCN structure and 2D layered BCN structure comprising of B, C, N atoms arrange themselves in graphene structure. In addition, the B-C-N system has varying compositions. The 2D BCN and cubic

BCN systems can be synthesized by different techniques such as pulsed laser deposition (PLD), chemical doping of graphene with B and N, magnetron sputtering, high pressure high temperature methods, chemical vapor deposition (CVD), by mechanical alloying [63-67]. The synthesized BCN system mostly after synthesis, undergoes phase separation, in the 2D BCN systems after synthesis it comprises of h-BN and graphene. This results in the major difficulty of BCN phase identification, as the strongest peak of h-BCN, graphene and h-BN overlap with each other. Hence, the major challenge is to synthesize single phase BCN. The properties of BCN system can be tailored by optimizing the composition and structural arrangement of B, C, and N atoms in the layered structure. Also, the 2D layered BCN nanosheets have been held by weak van der Waals forces and they are part of the layered van der Waals 2D nanomaterials along with graphene, BNNS and graphene oxide. The 2D BCN system have wide range of application from wear protective coatings, electronic devices, nano-devices and field emitters.

2.3.1. Synthesis of BCN

In two-dimensional materials, one of the important ternary system is hexagonal BCN (h-BCN). The major drawback of BCN system is the phase separation and homogeneous synthesis [68]. Similar to other 2D materials, BCN can be synthesized as single or multilayered BCN nanosheets. The h-BCN nanosheets are structurally similar to graphene. The most widely used method for synthesis of BCN is the chemical vapor deposition (CVD) technique. Using B, C, N sources, large area atomic layer of h-BNC was synthesized with compositions varying from h-BN to graphene [69]. Jin *et al.* synthesized crumpled h-BCN nanosheets by catalyst free bottom-up CVD method and thermally decomposing the precursors (urea, boric acid and polyethylene glycol (PEG)) with the tunable B and N bond [70]. Figure 2.4 shows the scanning transmission electron microscopy (STEM) image of synthesized BCN. In another study, conducting graphene was used for direct controlled chemical conversion to ternary high quality

semiconducting h-BNC. The synthesized h-BNC films were highly crystalline without compromising the electronic properties and the original structure of graphene [71]. Another technique used for BCN synthesis was the pulsed laser deposition (PLD). Using this technique, thin films with controlled composition and structure can be synthesized. BCN thin film was synthesized by PLD technique using BN and C dual targets in vacuum and nitrogen atmosphere [72].

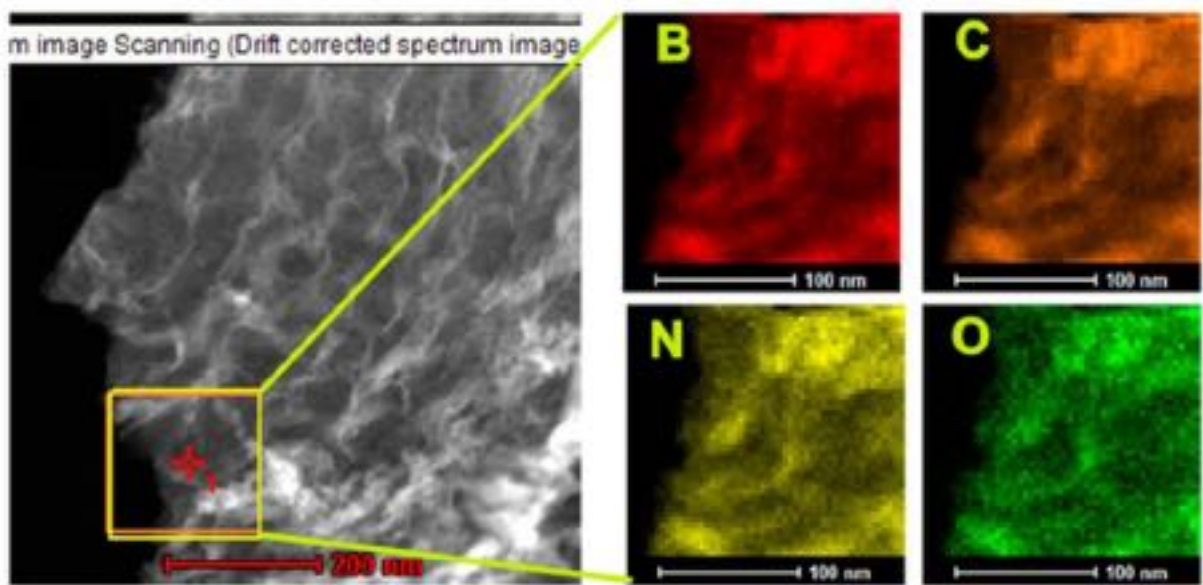


Figure 2.4: STEM image of BCN with composition distribution of B, C, N, O elements [70]

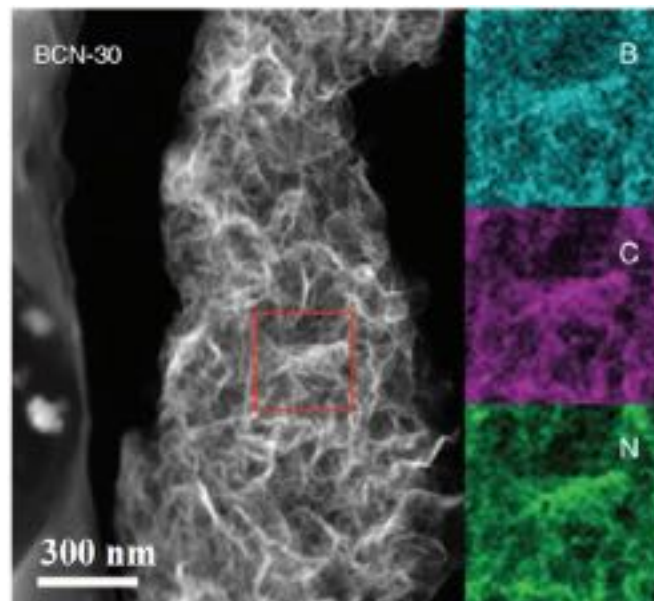


Figure 2.5: TEM image of BCN with the composition distribution of B, C, and N elements [73]

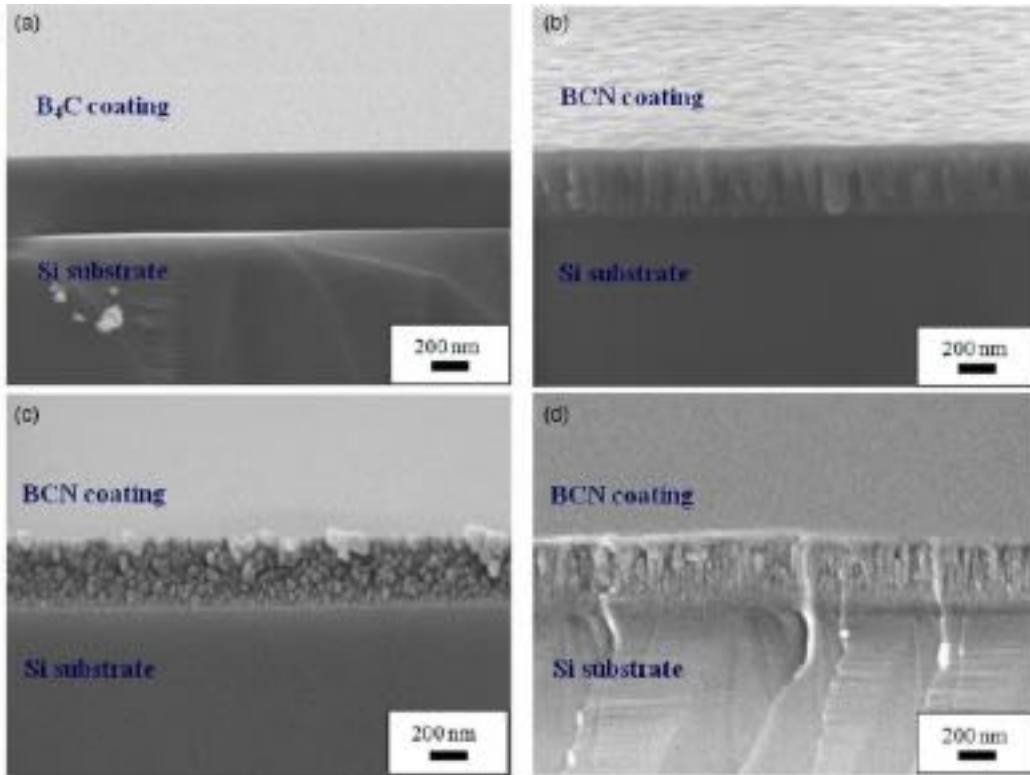


Figure 2.6: Cross-sectional SEM micrographs of (a) BC1, (b) BC2, (c) BC3 and (d) BC4 demonstrating microstructural changes of BCN films with increasing N₂ content [78]

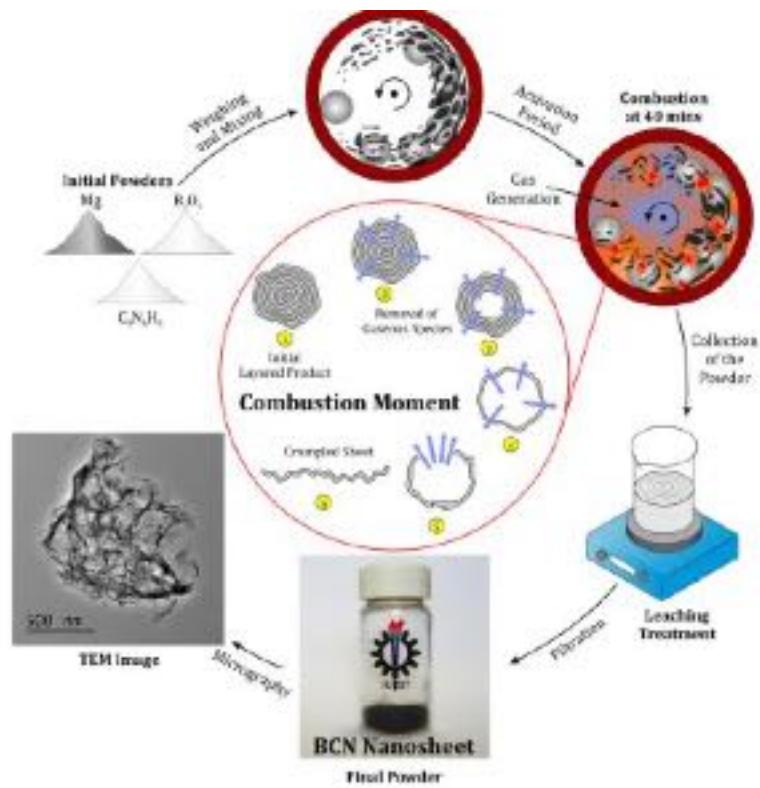


Figure 2.7: Schematic representation of BCN nanosheet synthesis [79]

Pyrolysis method was used to synthesize the BCN nanosheets by carbon doping of h-BN nanosheets (Fig. 2.5). Glucose percentage was varied in a mixture containing boron oxide and urea. These mixtures were kept in tube furnace for 5 h at 1250 °C in a controlled ammonia atmosphere [73]. Ternary BCN in bulk form was synthesized by in-vacuum thermolysis method at high temperature around ~1000 °C, by decomposition of ethane 1,2-diamineborane on Cu foil. This study was carried out in ultra-high vacuum environment to reduce the presence of oxides on BCN surface. Chemically homogeneous BCN ternary system was synthesized by this technique [74]. The ternary h-BCN was also synthesized by thermal substitutional method through substitutional carbon doping of h-BNNS at 850 °C. This method was favorable to adjust the band-gap of h-BCN by controlling the amount of C in h-BN nanosheets and this 2D BCN showed an excellent non-linear optical performance [75, 76]. Thick h-BCN films can be prepared by magnetron sputtering [77, 78]. On steel and Si substrates thick h-BCN film of 400 nm (Fig. 2.6) was deposited by reactive DC magnetron sputtering, using sintered B₄C as target by varying the proportion of N₂ (precursor) and Ar (reactive gas) sputtering gas. Ternary h-BCN nanosheets of few layer was synthesized by solid-state combustion reaction method. Initially the magnesium, boron trioxide and melamine were mixed by ball milling and then by combustion for 40 min, magnesium in the presence of melamine reduces boron trioxide to form BCN nanosheets as shown in Fig. 2.7 [79]. Huang *et al.* synthesized amorphous BCN [(BN)_{0.5}C_{0.5}] by ball milling of h-BN and graphite. The amorphous BCN was treated at 7.7 GPa and 2300 °C by high-pressure high-temperature (HPHT) conditions, it resulted in phase segregation of amorphous C, BN and turbostratic graphite [80]. Graphene and boron nitride nanosheets have been used to prepare the covalently bonded BCN composites [81]. This BN_{1-x}G_x (x – 0.25, 0.5, 0.75) composite was synthesized by carbodiimide reaction where it uses covalent cross-linking with organic linkers. So, the h-BCN system can be synthesized by several chemical and mechanical routes.

2.3.1.1. Solid-State Reactive Sintering Method

The solid-state reactive sintering method has been generally performed using spark plasma sintering (SPS). This method has also been referred as reactive spark plasma sintering. This technique has been generally used for synthesizing nanostructured materials and consolidation of nanopowders. The reactive sintering technique was carried out in vacuum atmosphere by protecting the nanomaterials from oxidation. In the meantime, chemical reactions for the synthesis of new phase can be performed in SPS with simultaneous densification of nanomaterials. The initial sample preparation, involves by placing the mixed solid reactants in graphite die, and the nanomaterials in dies were subjected to uniaxial pressure with pulsed electric current. In addition, initial characteristics of reactant materials like grain size, uniform mixture with minimum agglomeration and initial chemical properties will dictate the successful synthesis of new nanostructured material by reactive SPS. The chemical reaction will be initiated at different contact points of the reactant mixture, resulting in the synthesis of new phase nanostructured materials. So the interfacial reaction between the nanostructured materials happens majorly at the point of contact between the materials and it is good to create more contact points for effective chemical reaction during SPS. To improve the number of nucleation sites for the chemical reaction to occur, it has been important to prepare the starting materials with good interfaces. This could be achieved with fine particle size and thorough mixture of particles without any agglomeration. So, mechanical milling would be a good sample preparation technique before reactive SPS. In this milling process, there will be grain size reduction, defect formation, uniform mixing with increased interfacial area between the starting materials. This will create multiple nucleation sites and will be favorable for chemical reaction during reactive SPS. Hence, reactive SPS will be a successful synthesis technique for synthesizing BCN bulk nanostructured material.

2.3.2. Different Structure and Bonding Nature of BCN

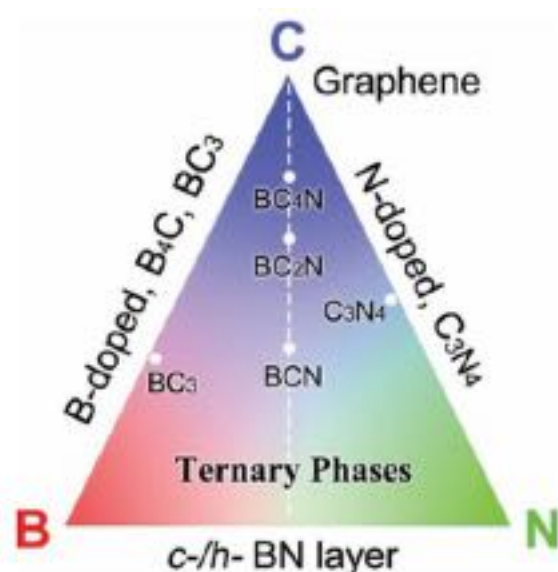


Figure 2.8: Ternary phase diagram of the B-C-N system [82]

The boron-carbon-nitride ternary system can form cubic boron-carbon-nitride (c-BCN), which has been considered to be one of the superhard material with high hardness or layered hexagonal boron-carbon-nitride system (h-BCN) which have semiconducting and lubricating properties [82]. The 2D graphitic B-C-N ternary system comprises of sp^2 bonding, where the coordination is trigonal in nature and structurally similar to h-BN or graphite. The hexagonal B-C-N ternary system can form different layered phases as shown in the white dashed line of the BCN phase diagram (Fig. 2.8) [82]. In the 2D BCN nanosheet, the graphenic sites will be filled with the boron, nitrogen, carbon atoms as their atomic parameters have been identical, their stacking sequence was ABAB... and they have different composition, resulting in various number of hexagonal $B_xC_yN_z$ compounds [83-85]. The different layered hexagonal structures of B-C-N ternary systems have been h-BCN, h-BC₂N and h-BC₄N. In this ternary h-BCN system, boron, carbon, nitrogen atoms can be arranged in three different ways as shown in Figure 2.9. Three different chemically ordered structures of h-BCN, basically conserve the primary three bonds - B-C, C-N and B-N. Based on DFT calculations, the h-BCN were

metastable in nature due to the strong bonding nature between the atoms (B, C and N) and high energy was required to break these bonds [86]. In the Figure 2.9 for h-BCN structure, the coordination of (B/C/N) atoms in all the three structures were different around the boron, carbon, and nitrogen atoms. The stability of the BCN structure were dictated by the nature of bonds formed between B-C-N atoms and they form different bonds such as B-N, C-C, N-N, B-B, B-C, N-C. Each bond has different bond energy as listed in Table 2.2 [87]. The bonds with highest bond energy will contribute to the stabilization of crystal structure with specific arrangement. Based on Table 2.2, the B-N and C-C bonds have highest bond energy compared to other bonds. So, in the BCN structure, the upsurge in the count of B-N and C-C bonds will be the most stable structure. In some structures, the atomic arrangement can have equal number of B-N and C-C bonds. On such conditions the dictating factor for structure stability will be based on the stress between the layers. Also, the three atoms (B, C, N) have different electronegativity and based on their electronegativity, there will electrostatic attraction or repulsion, this dictates the type of bond formed and stability of the structure. Depending on the above mentioned factors, among the three different arrangements in h-BCN structure (Fig. 2.9), v3 was the most stable structure with maximum B-N/C-C bonds compared to v1/v2 and v1 was stable compared to v2 structure [86, 88]. Similarly, Figure 2.10 shows the different arrangement present in the h-BC₂N structure [87, 89]. The h-BC₂N structure has five different atomic arrangement and the most stable structure was type II compared to the rest four structures.

In the ternary BCN system, the other common structure has been the cubic BCN with sp³ bonding and tetrahedral coordination. The cubic BCN has been structurally similar to cubic boron nitride (c-BN) or diamond. Similar like hexagonal B-C-N, the cubic B_xC_yN_z has different chemical compositions and the compounds are namely – c-BCN, c-BC₂N and c-BC₄N [90-92]. Among all the cubic BCN compounds, c-BC₂N has been mostly widely studied and

its hardness has been comparable to diamond [90, 93]. The $c\text{-BC}_2\text{N}$ compound has different arrangement of boron, carbon and nitrogen as shown in Fig. 2.11 [93]. Stability of the cubic BC_2N has been dictated by the nature of bonds formed between the boron-carbon-nitrogen atoms, the favored atomic arrangement will have maximum C-C and B-N bonds. Among the seven different possible arrangements, the stable structures have been the type (i) and (ii) compared to the rest 5 arrangements. The N-N and B-B bond was not found in type (i) and (ii) structure, and the formation energy for both these structure were the lowest. The other five structure have positive formation energy, leading them to be metastable in nature with $c\text{-BC}_2\text{N}$ transforming to cubic boron nitride and diamond. Thus, structural stability was best observed for type (i) and type (ii) structure in $c\text{-BC}_2\text{N}$.

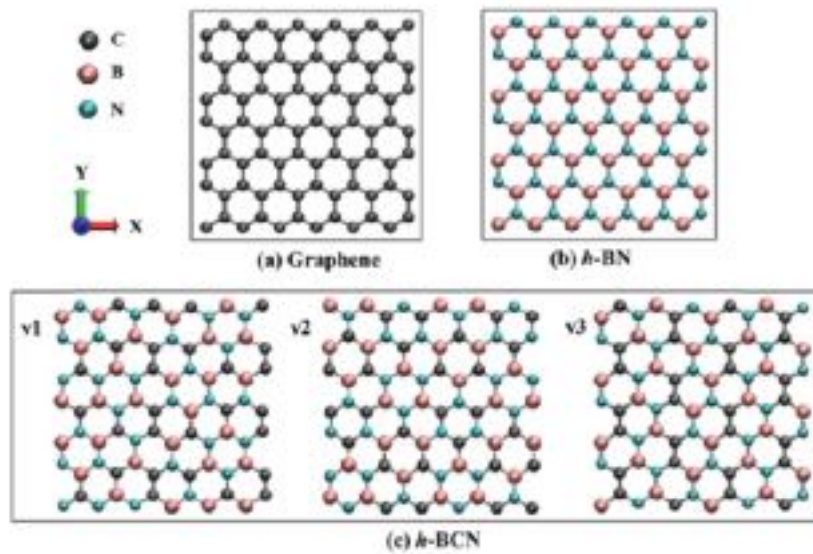


Figure 2.9: Different structural arrangement of hexagonal BCN [86]

Table 2.2: List of different bonds present in BCN and their corresponding bond energy[87]

Bond	Bond energy (eV)
B-B	2.32
C-C	3.71
N-N	2.11
B-C	2.59
B-N	4.00
C-N	2.83

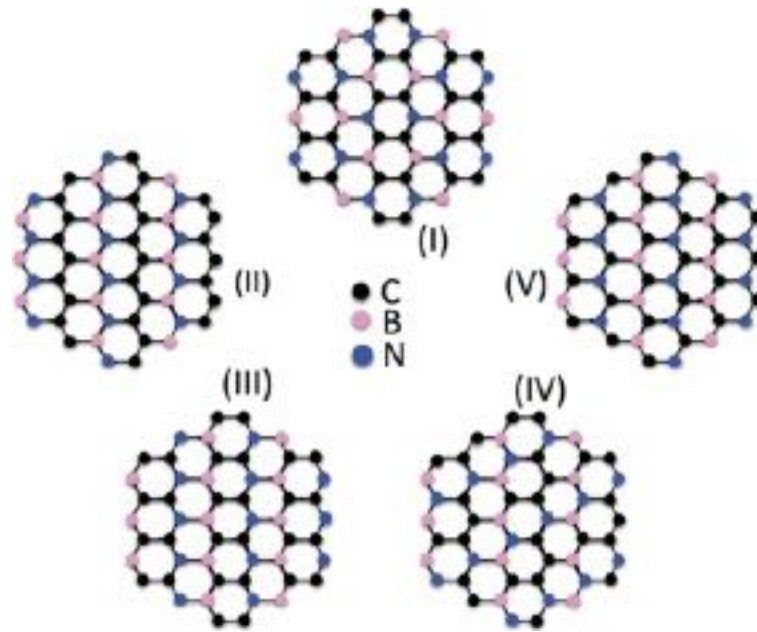


Figure 2.10: Different structural arrangement of hexagonal BC_2N [87, 89]

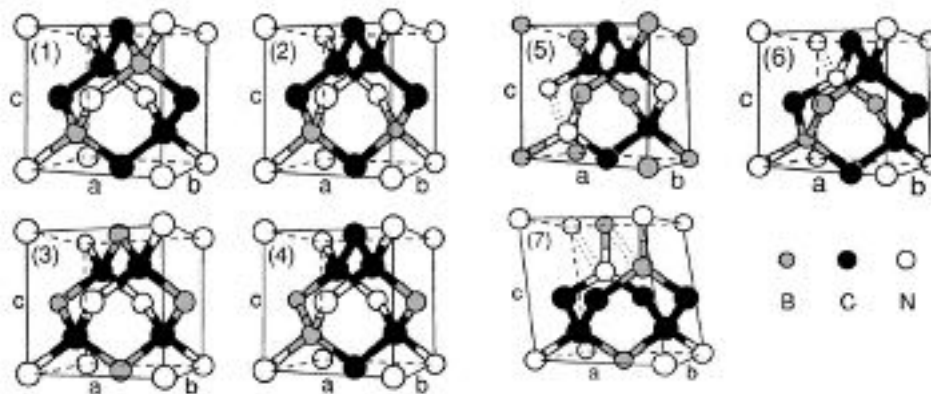


Figure 2.11: Different structural arrangement of cubic BC_2N [93]

2.3.3. Mechanical and Tribological Properties of BCN

The mechanical properties (hardness, elastic modulus) of the ternary B-C-N system vary depending on the synthesis technique (powder, pellet, or coating), the crystal structure it forms, and the hardness measurement technique. The mechanical properties of ternary BCN system are listed in Table 2.3. The ternary cubic BCN system has been considered as one of the potential superhard material after diamond. Among the different compounds of cubic B-C-N system, the BC_2N compound has high hardness of 76 GPa due to the sp^3 type of atomic

bonding and it is considered as the second hardest material [91]. The cubic BC₂N was prepared by diamond anvil cell compression of graphitic-BN-C at high pressure and temperature. In addition, the cubic BC₂N system is stable and ductile in nature. The hardness and Young's modulus values of cubic BC₂N are higher than cubic boron nitride and lower than diamond. Zhao *et al.* prepared cubic BC₂N and BC₄N by sintering the ball milled mixture of graphite/h-BN. In addition to the ternary BCN phase formation, diamond and cubic BN phase were also observed [92]. The hardness of both cubic BC₂N/BC₄N (Table 2.3) phase were higher than cubic BN. First principle calculations of cubic BC₄N revealed the estimated theoretical hardness to be 84.3 GPa by Vicker's method [94]. In another study, cubic BC₂N synthesized by self-propagating high temperature synthesis showed 95 GPa nanohardness and 600 GPa elastic modulus, these values were comparable to diamond [95]. High pressure and high temperature technique was used to synthesize bulk cubic BCN pellet and the cubic BCN hardness measured by Knoop indentation method was 52 GPa [96]. Sun *et al.* predicted the cubic BC₂N hardness by ab-initio pseudopotential DFT and the theoretical Vicker's hardness was 72 GPa [97]. Overall, based on Table 2.3, it is evident that cubic BC₂N is one of the superhard material and the hardness is higher than cubic BN. For the hexagonal BCN, mostly they were studied as coatings for electronic applications. Mannan *et al.* synthesized hexagonal BCN (h-BCN) films on silicon substrate by microwave plasma chemical vapor deposition [98]. The microhardness of 2 μm thick h-BCN film varied between 3.8 GPa to 4.4 GPa. The mechanical properties of 2D hexagonal B-C-N system (2D B-C-N) was theoretically explored so far, especially in terms of their elastic properties. Jiao *et al.* studied the elastic properties of monolayer BC₂N theoretically by first-principle DFT calculations. The Young's modulus (309 GPa/m), shear modulus (128 GPa/m), and bulk modulus (195 GPa/m) were calculated for the monolayer BC₂N [99]. These calculated Young's modulus of monolayer BC₂N was higher than hexagonal boron nitride elastic property and lower than graphene elastic property. Recently,

the elastic properties of monolayer h-BCN was studied by classical molecular dynamics [100]. At zero kelvin, the calculated Young's modulus of monolayer h-BCN along the 'x' direction was 786 GPa and 'y' direction was 830 GPa. Theoretical calculations using first-principle DFT on graphene like BC₄N revealed their elastic modulus to be 157 Pa [101]. Mostly the mechanical properties of 2D h-BCN were calculated for monolayer and by theoretical approach.

Table 2.3: Mechanical properties of ternary B-C-N system

Composition and Phase	Hardness (GPa)	Young Modulus (GPa)	Technique	References
c-BC ₂ N	76	-	Vicker's indentation	[91]
	75	980 ± 40	Nanoindentation	
c-BC ₂ N	62	-	Vicker's indentation	[92]
c-BC ₄ N	68	-	Vicker's indentation	[92]
c-BC ₄ N	84.3 (Theoretical Vicker's hardness)	-	Theoretical – First principle calculations	[94]
c-BC ₂ N	95	600	Nanoindentation	[95]
c-BCN	52	412 (Bulk modulus)	Knoop Indentation	[96]
c-BC ₂ N	72 (Calculated Vicker's hardness)	-	Ab-initio pseudopotential density functional method	[97]
h-BCN	3.8 – 4.4	-	Nanoindentation	[98]

Ternary B-C-N system has been considered as one of the potential lubricating coatings. Deng *et al.* studied the tribological properties of ternary BCN coatings deposited by ion beam assisted deposition (IBAD) at room temperature and high temperature (300 °C) [102]. The coefficient of friction (COF) at room temperature of the BCN coating was 0.2 - 0.3 and it decreased to ~0.1 at high temperature test (300 °C). This decrease in COF was attributed to the transfer layer (graphitized carbon) formed at high temperature. BC_xN stoichiometry films prepared by IBAD method had a hexagonal structure and with larger carbon content, the BC_xN

was diamond-like structure [103]. The COF with varying carbon content was in the range of ~0.18-0.35. The wear rate decreased with increasing carbon content due to the formation of sp^3 bond in BC_xN system. The tribological properties of cubic BCN [104-108] coatings has been studied extensively compared to hexagonal BCN or 2D h-BCN. So, the tribological properties of hexagonal B-C-N nanosheets remain elusive and has to be probed in the future.

2.3.4. Applications of BCN

BCN nanosheets have a band gap of 0 – 5.5 eV and it can be tuned by varying the concentration of boron, carbon or nitrogen. The photo luminescent BCN nanostructure can be used for biomedical applications and optoelectronics [109]. BCN Monolayers with tunable elemental compositions can be used for carbon based energy applications [110, 111]. BCN nanosheets are used in wide variety of energy applications from supercapacitors to lithium-ion batteries to fuel cells, due to their heteropolar bonding nature which triggers their electrochemical behaviors [112-114]. BCN nanosheets and bulk BCN have been studied for lithium storage properties, where they have achieved good capacity and cyclability as anode materials for Li-ion batteries [115-118]. Lie *et al.*, synthesized BCN nanosheets of large surface area with 2-6 atomic layers and they were used as anode for lithium half cells. Compared to bulk BCN, nanosheets showed good storage capability for lithium batteries. After 5000 cycles, they showed stable capacity (100 mAh/g at 2 A/g) [118]. The 2D BCN nanosheets as a catalyst have been highly efficient in oxygen reduction reactions (ORR) in polymer electrolyte fuel cells [119]. In addition, 2D BCN exhibited good tolerance with methanol compared to platinum/carbon catalyst. Graphene like BCN can be also used as ORR catalyst for metal-air batteries [120]. They are relatively stable and cost effective compared to commercial platinum/carbon catalyst. Also, 2D BCN has the potential to be next generation ORR catalyst for fuel cells and metal-air batteries. In hydrogen evolution reaction (HER), BCN has displayed

excellent electrocatalytic activity for hydrogen generation [121]. Theoretical studies on this metal free BCN catalyst showed a good stability and HER activity. BCN as electrodes in supercapacitors, have displayed good capacitance and stability [112, 122]. In supercapacitors, compared to un-doped graphene, BCN graphene electrode materials have displayed superior rate capability and good capacitance, due to their high surface area and conductivity [123]. For gas adsorption, BCN have been used and they have the ability to selectively uptake CO₂ higher compared to CH₄, N₂, and H₂ [111, 124]. Especially, BC₂N has shown good gas absorption nature due to their high surface area and with increase in surface area their gas uptake increases. In addition, BCN tunable band gap and conducting nature allows them to be used as good microwave absorbers [125]. BCN has the ability to sense the uric acid and dopamine, where they are used as electrochemical sensors [126]. Their ability to selectively detect (uric acid and dopamine) in electrochemical sensors, where the effective electron transfer happens because of their high surface area nature with good electronic conductivity and the edges available in their structure. The semiconducting nature of BCN with their energy gap, allows them to be used in field effect transistors (FET) [127]. The boron enriched BCN films can also be employed for solid-state neutron detectors as the boron isotope has the ability to capture high-neutrons [128]. Hexagonal BCN has good frictional and wear properties because of their interlayer sliding nature. So the h-BCN systems has been studied for tribological applications, where they can be used for MEMS, NEMS, automotive lubrications and adhesive contacts [129].

2.4. MXene

MXene is the emerging new class of 2D layered material and they are 2D transition metal carbides, nitrides or carbonitrides. MXenes are synthesized by etching away ‘A’ atomic layer from the layered MAX phase. Since 2011 with the discovery of Ti₃C₂, MXenes research

has been growing fast [130]. After that 19 new compositions have been synthesized experimentally and theoretically some more compositions have been predicted as shown in Fig 2.12 [131-134]. The general formula of MXene are of three different type, M_2X , M_3X_2 and M_4X_3 (M - early transition metal, X - C and/or N). The early transition metal in the MXene general formula are of three different forms, (i) one M element, (ii) two M elements exist to form solid solution and (iii) two M elements exist to form ordered phases. Compared to solid-solution MXenes, ordered MXenes are energetically stable. Further, the X site forms solid solution carbonitrides. So far, 50-60 MXene compositions have been synthesized [135, 136]. The 2D layered MXene displays unique physical, electrical, chemical and mechanical properties. So, they can be used in wide range of applications, including energy storage devices, catalysis, hydrogen storage, supercapacitor, biosensors, absorption studies, structural composites and electromagnetic interference shielding.

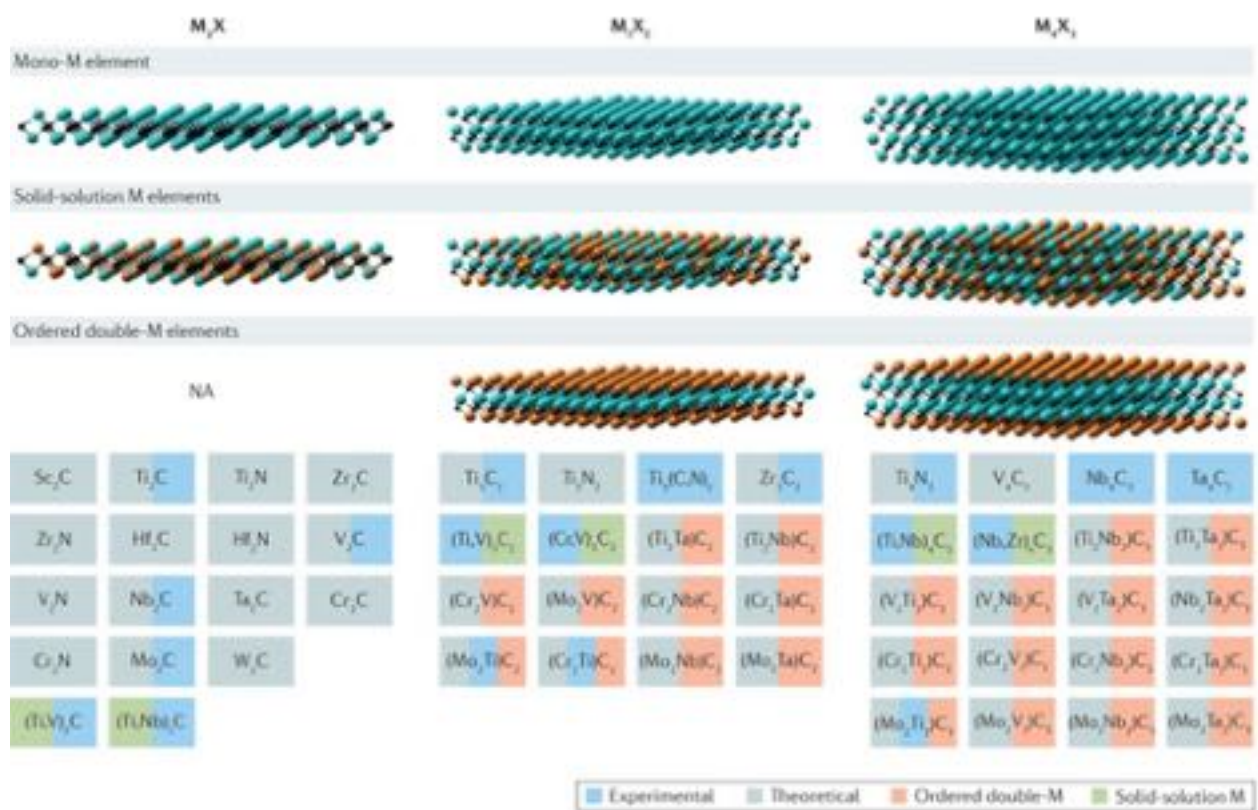


Figure 2.12: Different type of MXene structure and their corresponding compositions [132]

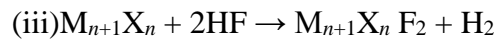
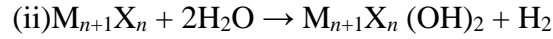
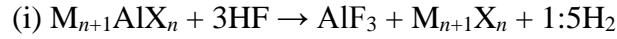
2.4.1. Synthesis of MXene

MXenes ($M_{n+1}X_n$) are mostly synthesized by selective etching of 'A' layer from the MAX ($M_{n+1}AX_n$), where M is early transition metal, A is the element from group 13 and 14 of the periodic table, X is C and/or N. The M-X bond is strong bonding of covalent or ionic nature and M-A bond is purely metallic in nature. Due to weak bonding nature of M-A bond, it's easy to selectively etch 'A' element layers from MAX phase. Acid solutions comprising of aqueous fluoride was used mostly for selective etching of A-elements. The acid solutions generally used are hydrofluoric acid (HF) or ammonium fluoride with ammonium hydrogen bifluoride or hydrochloric acid with fluoride reacts internally to form HF [135, 137, 138]. Among the different 'A-element', Al was the only one element to be successfully etched from MAX phases. Recently, MXene was synthesized from different precursor other than MAX. From Mo_2Ga_2C composition, Ga layered were etched to form Mo_2CT_x and $Zr_3C_2T_x$ MXene was obtained by etching of Al_2C_3 layers from $Zr_3Al_3C_5$ [139, 140]. At high temperature around 550 °C, Ti_4N_3 MXene synthesis from Ti_4AlN_3 MAX phase was achieved by selectively etching Al layer using molten fluoride salt mixture in argon atmosphere [141]. Monolayer MXene was synthesized by bottom up synthesis approach, Mo_2C MXene was grown by chemical vapor deposition on Mo foils and it was few nanometers thick with 100 μm in size [142]. Different synthesis technique of MXene are presented in the following subsections.

(a) Selective Etching using Hydrofluoric Acid

Different types of MXenes ($M_{n+1}X_n - M_2X, M_3X_2, M_4X_3$) are synthesized using hydrofluoric acid. The major synthesis parameters are HF concentration, reaction time and temperature [135, 137, 143]. Typical example of MAX phase before and after HF treatment is shown in Fig. 2.13 [136]. Based on the early transition metal (M) in MAX phase, the selective etching conditions differ, also it relies on the nature of bonding, type of structure and initial

particle size of MAX phase. Table 2.4 summarizes some of the etching conditions for different MXene synthesis [136, 140, 144-148]. Simple reaction steps in the etching process of MXene (M_3X_2) from MAX (M_3AlX_2) phase at room temperature with 50% hydrofluoric acid for 2 h are as follows,



The key finding from most of the synthesis with HF clearly indicate, as the atomic number of M increases – the acid concentration has to be increased with longer reaction time as the M-Al bonding becomes stronger (since M has larger valence electrons) [135]. Similarly, MAX ($M_{n+1}AX_n$) phase with larger ‘n’ value, needs a stronger acid concentration for etching and longer reaction time to form desired MXene. These observations show that MXene synthesis with selective etching using HF acid is a kinetically driven process.

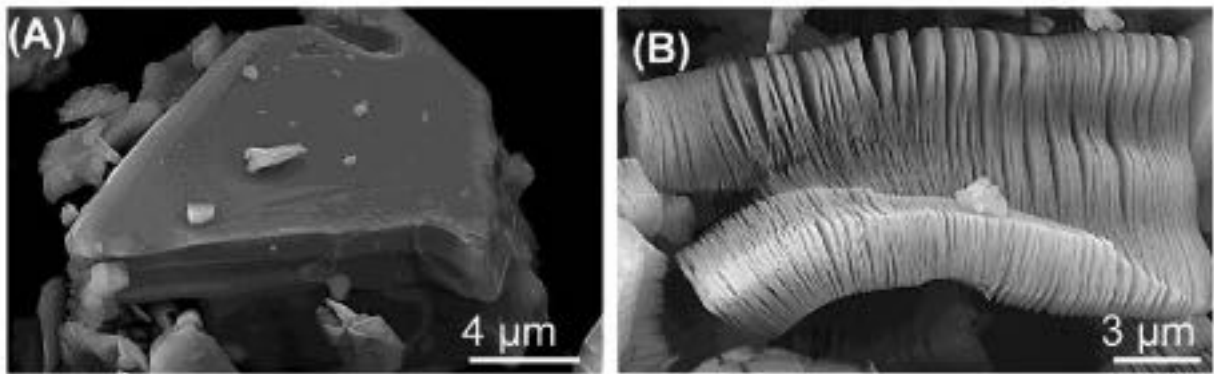


Figure 2.13: SEM images of (a) Ti_3AlC_2 before HF treatment and (b) Ti_3AlC_2 after HF treatment forms Ti_3C_2 [136]

Table 2.4: Synthesis conditions for MXene using HF acid

MXene Type	MXene	Precursor	Concentration (wt%)	Duration and Temperature	Reference
M_2X	Ti_2CT_x	Ti_2AlC	10	10 h, Room temperature	[136]
	Ti_2CT_x	Ti_2AlC	40	2.5 h, Room temperature	[144]

	V_2CT_x	V_2AlC	50	90 h, Room temperature	[145]
	Nb_2CT_x	Nb_2AlC	50	90 h, Room temperature	[145]
	$(Ti,Nb)_2CT_x$	$(Ti,Nb)_2AlC$	50	28 h, Room temperature	[136]
M_3X_2	$Ti_3C_2T_x$	Ti_3AlC_2	50	2 h, Room temperature	[136]
	$(Ti,V)_3C_2T_x$	$(Ti,V)_3AlC_2$	50	18 h, Room temperature	[146]
	$Zr_3C_2T_x$	$Zr_3Al_3C_2$	50	72 h, Room temperature	[140]
M_4X_3	$Nb_4C_3T_x$	Nb_4AlC_3	50	90 h, Room temperature	[147]
	$(Nb,Ti)_4C_3T_x$	$(Nb,Ti)_4AlC_3$	50	90 h, 50 °C	[148]
	$Ta_4C_3T_x$	Ta_4AlC_3	50	72 h, Room temperature	[136]

(b) Selective Etching using Fluoride Salt

MXenes ($M_{n+1}X_n - M_2X, M_3X_2, M_4X_3$) are synthesized using fluoride salt and strong acid in this method [138, 149-151]. For example, HCl acid with LiF salt are used for MXene synthesis, where the acid and salt react to form HF acid for selective etching of A layer. Table 2.5 summarizes the selective etching conditions using fluoride salt for different MXene synthesis. Similarly for MXene synthesis, HF acid with LiCl salt are used for etching away of A atoms [152]. The main advantage of the salt method is easy delamination of MXene with no further processing, as the etching of A layers occurs with metal halide formation and Li^+ ions with water intercalate the MXene layers, resulting in weak interaction and increased spacing with MXene layers. Figure 2.14 shows the typical example of MAX phase before and after etching with HCl acid/LiF salt.

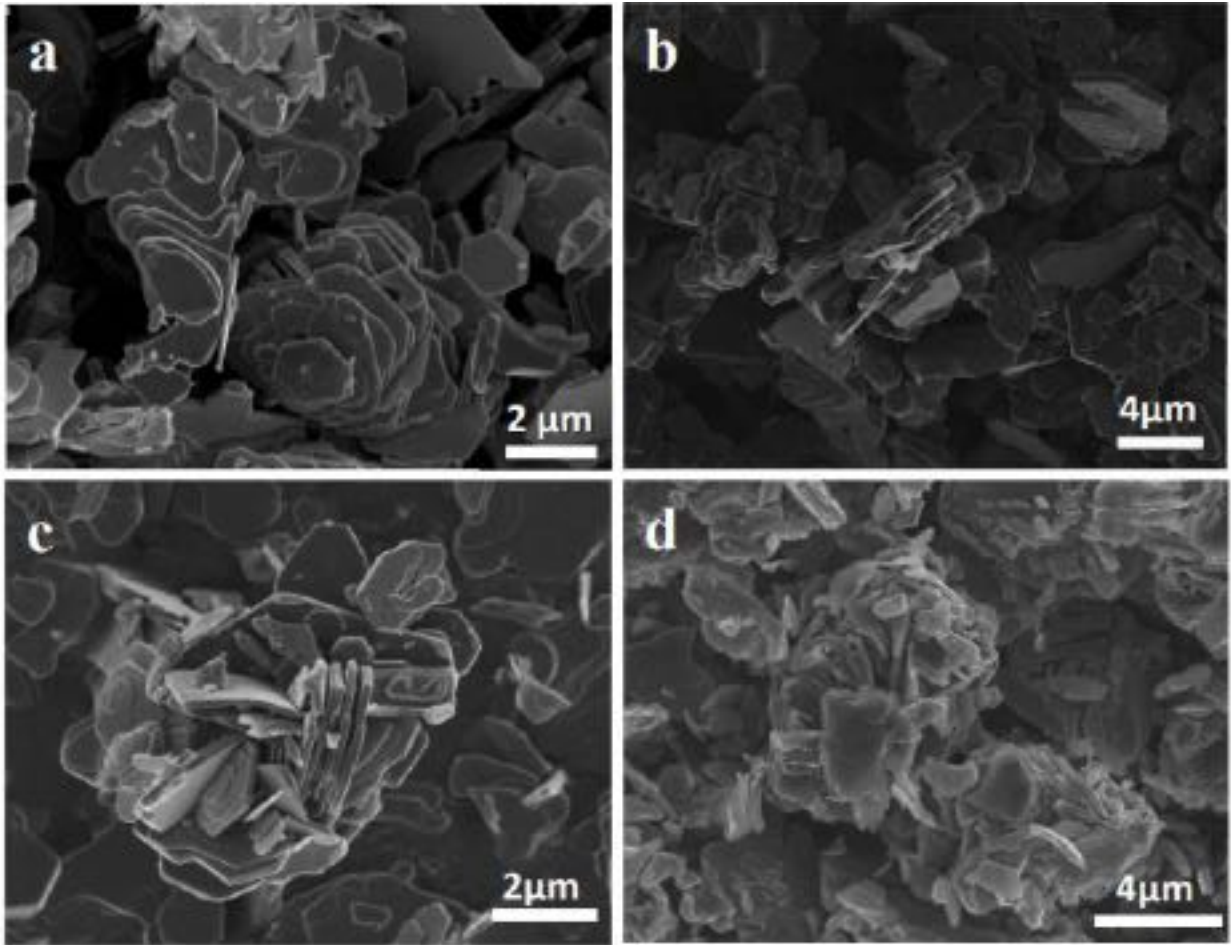


Figure 2.14: SEM images of powders of, a) $\text{Mo}_2\text{Ga}_2\text{C}$, b) Mo_2CT_x etched in HF for 160h c) $\text{Mo}_2\text{CT}_x\text{-Li}$ etched in LiF/HCl for 6 days and, d) $\text{Mo}_2\text{CT}_x\text{-Li}$ etched for 16 days [149]

Table 2.5: Synthesis conditions for MXene using fluoride salt (HCl –LiF)

MXene Type	MXene	Precursor	Concentration (wt%)	Duration and Temperature	Reference
M_2X	Mo_2CT_x	$\text{Mo}_2\text{Ga}_2\text{C}$	9M HCl- 15 mol LiF	72 h, 35 °C	[149]
M_3X_2	$\text{Ti}_3\text{C}_2\text{T}_x$	Ti_3AlC_2	9M HCl- 5 mol LiF	24 h, 35 °C	[150]
	$\text{Cr}_2\text{TiC}_2\text{T}_x$	$\text{Cr}_2\text{TiAlC}_2$	6M HCl- 5 mol LiF	42 h, 55 °C	[132]
M_4X_3	$(\text{Nb, Zr})_4\text{C}_3\text{T}_x$	$(\text{Nb, Zr})_4\text{AlC}_3$	12M HCl- 10 mol LiF	168 h, 50 °C	[148]
	$\text{Ti}_4\text{N}_3\text{T}_x$	Ti_4AlN_3	Molten salt LiF, NaF, KF	0.5 h, 550 °C	[141]

2.4.2. Functionalization of MXene

MXene are mostly synthesized by selective etching of A layers from MAX phase with aqueous hydrofluoric (HF) acid or fluoride based acid solutions. MXene have a mixture of surface terminations and the functional groups are -OH, -O or -F. The general formula of MXene with surface termination are $M_{n+1}X_nT_x$, where T is the surface terminations. The schematic representation of MXene with surface termination is shown in Fig. 2.15 [153]. The MXenes synthesized so far have surface terminations. Computational studies on pristine MXenes and MXenes with surface terminations are considered for their property evaluation [133, 154, 155]. For computational studies, MXenes with mixed surface functionalization or specific surface functionalization are taken into account [131, 156-159]. The MXene surface terminations have an important role on the electronic, mechanical and charge transport properties. For example, in terms of electronic properties, pristine MXene (Ti_3C_2) is metallic in nature, with surface terminations certain MXenes ($Ti_3C_2F_2$, $Ti_3C_2OH_2$) are semiconducting in nature [131, 135]. Also, the surface termination ordering with M and X atoms determines their stability and properties. The most stable stacking sequence with surface termination is ABCABC for M, X, and T respectively.

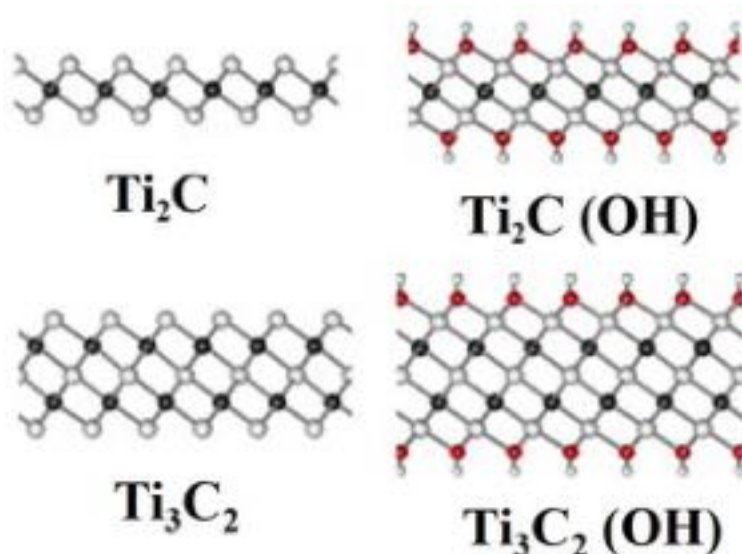


Figure 2.15: Schematic of MXene monolayer with and without surface terminations [153]

2.4.3. Structural and Physical Properties of MXene

Mostly MXenes are synthesized by selective etching of particular atomic layers from the MAX phase material. The precursor MAX phase is hexagonal layered close packed (hcp) structure with P63/mmc space group. The general formula for MAX phase is $M_{n+1}AX_n$, d block early transition metals are M (e.g. M = Ti, V, Cr, Mo, Hf, Zr), the main-group sp elements are A (III A or IV A), and C or N or C/N are X in MAX [160-162]. The M atoms are structured based on hexagonal close packing and X atoms occupy the octahedral interstitial sites, where the A layer of atoms are between the $M_{n+1}X_n$ layer. In MAX phase, the M-X bond is a mixture of strong covalent/ionic bonding and M-A bond is a pure metallic bond. During chemical etching, it's easier to extract A layer from MAX phase (M-A bond is weaker than M-X bond) and this results in the formation MXene layers ($M_{n+1}X_nT_x$). The newly formed MXene layers are stable with T_x the surface functional groups -O (oxygen), -OH (hydroxyl), -F (fluorine) and the value of 'n' dictates the thickness of MXene layers [160, 135, 163]. Based on the formula, MXene are of three different type M_2X , M_3X_2 and M_4X_3 . Figure 2.16 shows the schematic illustration of MXene synthesis from MAX phase. Most 2D materials such as graphite or BNNS are synthesized by mechanical exfoliation or sonication methods due to their weak van der Waals interactions between the layers, while MXene cannot be synthesized by such methods due to their relatively strong bonding nature of M-A bond [164]. The pristine MXene ($M_{n+1}X_n$) is hexagonal close packed structure with P63/mmc symmetry. The MXene, MX layers are in general held together by weak bonds (hydrogen bond and van der Waals forces). At high temperatures, the MXene layers forms the rocksalt like 3D $M_{n+1}X_n$ structure [132]. The ordering of M atoms changes for the different MXenes (M_2X , M_3X_2 and M_4X_3). For M_2X structure, ABABAB is the preferred stacking sequence for M atoms (hcp stacking). For M_3X_2 and M_4X_3 , ABCABC is the preferred stacking sequence for M atoms (face centered cubic (FCC) stacking). The synthesized MXene layers can delaminated to single layer by sonication

methods. During the process of washing and sonication, the surface functional groups can be replaced, where MXene functionalized with $-O/-OH$ are comparatively stable than $-F$ (washing MXene in water replaces the $-F$ with $-OH$ surface group). Similarly, at high temperature exposure or metal adsorption process, the $-OH$ terminations in MXene are changed to $-O$ surface groups [165, 166]. Pristine MXene can be synthesized by decomposition of $-O$ terminated MXene while it's in contact with metals (Al, Mg, Ca).

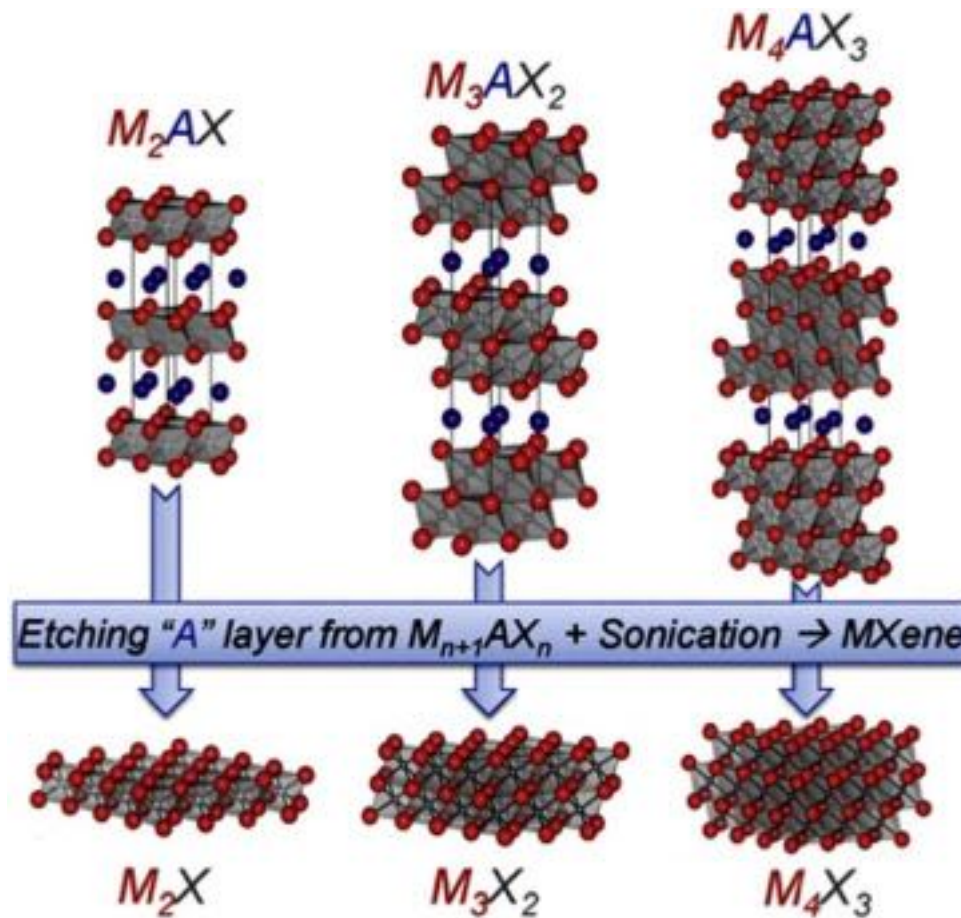


Figure 2.16: Schematic representation of MXene structure synthesized from MAX phase [135]

In $M_{n+1}X_nT_x$ MXene, each element M, X, surface terminations (T) and n, the number of layers have significant effect on their physical, chemical, mechanical and thermal properties. In terms of chemical properties, the titanium based MXenes ($Ti_3C_2T_x$) react with oxygen in air or pressurized water or CO_2 and the MXene layers oxidize to form anatase TiO_2 (Fig. 2.17). After oxidation, TiO_2 particles adhere to the surface of amorphous carbon sheets [167, 168]. In

another study, in-situ TEM studies revealed, anatase TiO_2 nanoparticles formed during the flash oxidation of MXene layers and with longer oxidation time, anatase TiO_2 nanoparticles transformed to thin sheets of nanocrystalline rutile [169]. Figure 2.18 shows the schematic of anatase and rutile TiO_2 formation based on flash and slow oxidation conditions. The same trend of anatase TiO_2 to rutile TiO_2 phase transformation was observed for Ti_2CT_x MXene at high temperature [144].

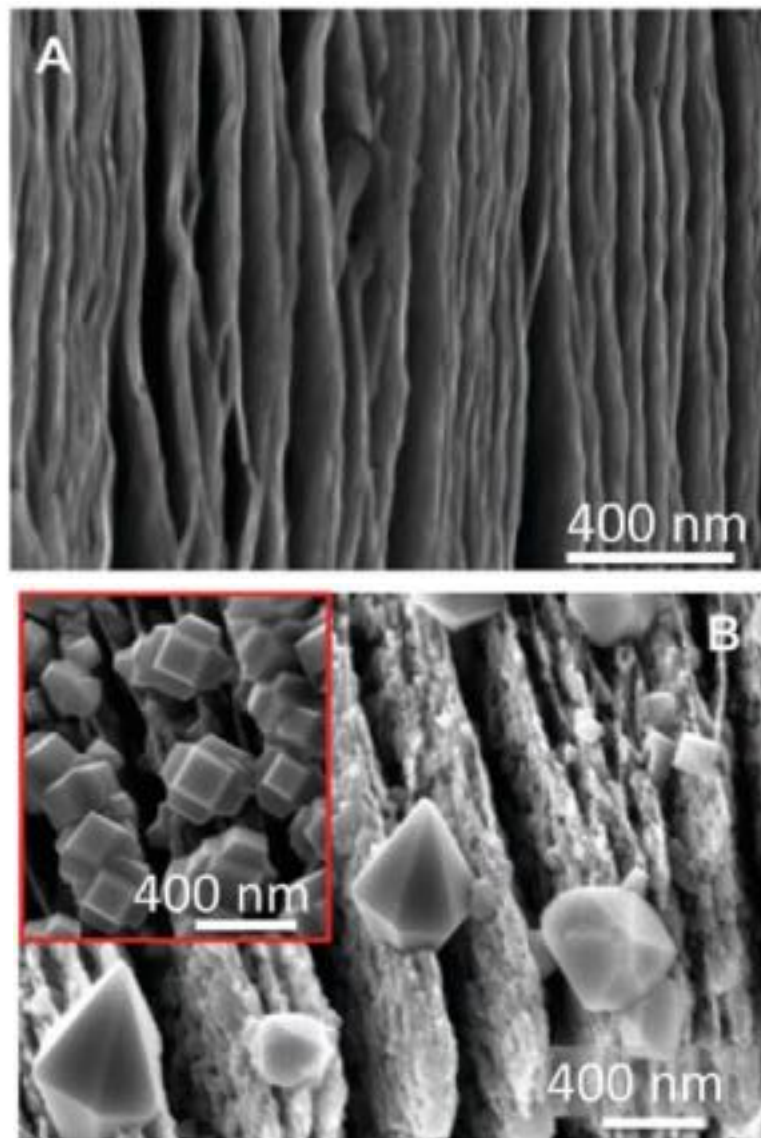


Figure 2.17: SEM image of (a) as-synthesized $\text{Ti}_3\text{C}_2\text{T}_x$ MXene and (b) after oxidation of $\text{Ti}_3\text{C}_2\text{T}_x$ MXene [167]

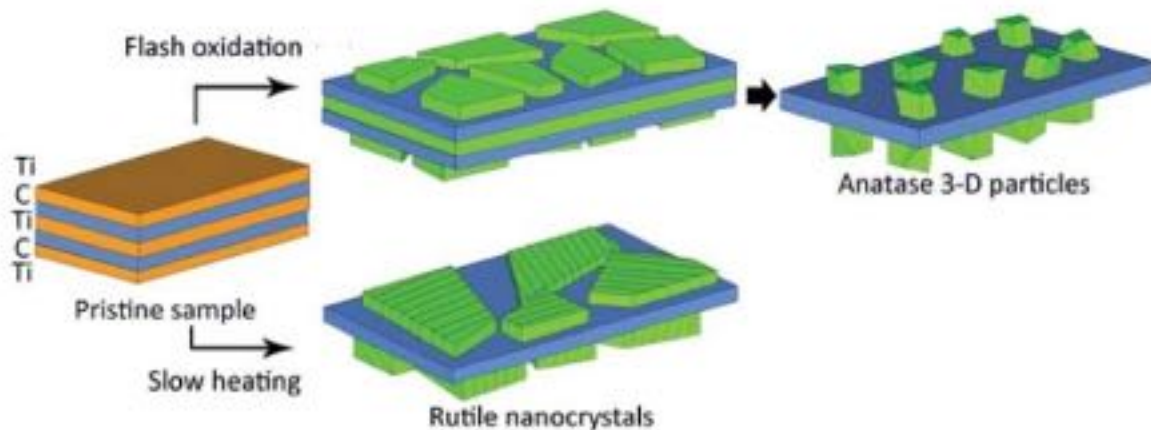


Figure 2.18: Schematic illustration of oxidation under different conditions [144]

Magnetic behavior of pristine MXene have been studied, especially the ferromagnetic and antiferromagnetic properties [131, 154, 170, 171]. Theoretical studies on titanium based MXenes (Ti_2X (C, N)) revealed the possible defects such as vacancies (single-type and Shottky-type double) present in the systems and such system were magnetic in nature because the 3d-orbitals have unpaired electrons [172]. The layered MXene magnetic properties are useful for application like spintronic. Using density functional theory, Cr_2CT_x and Cr_2NT_x are identified to have magnetic moments, however these MXene are yet to be studied experimentally [170]. In terms of chemical properties, surface functional groups present in the MXene systems play a significant role. The contact angle with most MXene surface are small and they are hydrophilic in nature [136]. The $Ti_3C_2T_x$ with OH and O surface groups contribute in creating strong bond to the water molecules present in solvent solutions and with different semiconductors [173]. Redox reactions are stronger in the MXene metal sites (example – Ti, V, Nb) and in the sulfuric acid solution, MXenes are stable [138]. The optical properties of MXenes depend on the type of functional groups terminated along their surface. Among the three surface functional groups (O-, OH-, F-), the Ti_3C_2 with O- termination has the ability to absorb light in the visible light spectrum. Compared to pure Ti_3C_2 MXene or the OH-/F-terminated Ti_3C_2 , the O- terminated Ti_3C_2 has higher optical properties, due to the O- density of states formed near the fermi energy [174, 175]. The layer thickness, out-of-plane and in-

plane anisotropic nature of MXene, will dictate MXenes ability to absorb light [176]. Based on the optical properties of MXene, they can be used in photovoltaic devices especially the polarized light driven type, conductive MXene film as transport electrodes in optical device, and broadband optical switch in photonic device [177-179]. The surface properties of pristine MXenes and functionalized MXenes (O-, F-, OH-) are different. The surface functionalization of MXene results in the modification of the surface dipole moments due to the polarity of the surface functional groups, and charge redistribution within the MXene surface and surface functional groups [180]. The OH-terminated MXenes in half occupied nearly free electron states can act as absorbents, so certain gas sensors based applications can use this surface terminated MXenes [181].

2.4.4. Electronic Properties of MXene

The electronic properties of MXene are mostly widely studied and researched. First principle calculations on pristine MXene ($M_{n+1}X_n$) shows them as good electrical conductors [133]. Similar to MAX phases, MXenes is metallic in nature which arises from their similar high density of states (DOS) at the fermi level and electron density distribution. Naguib *et al.* cold pressed MXene disks have good electrical conductivity and they are comparable to multilayer graphene [136]. So, the monolayer MXene can be postulated to have higher conductivity. The metallic property of titanium nitride MXene is higher than titanium carbide MXene, as the nitrogen atom has one extra electron than the carbon atom and the density of states at fermi level decreases as the thickness of MXene layer increases because of the Ti-C or Ti-N bond formation [182]. MXene layers with surface terminations -O, -F or -OH functional groups have a predominant effect on electronic properties. Thus, functionalized MXene are semiconducting in nature with narrow band gap, it relies on the MXene composition and the surface terminations orientation [131, 135, 183, 184]. Few examples of surface

terminated MXenes have band gaps like Sc_2CO_2 , Sc_2CF_2 , Ti_2CO_2 , Hf_2CO_2 , $\text{Sc}_2\text{C}(\text{OH})_2$ and Zr_2CO_2 [131, 185-187]. Similarly, pristine Ti_3C_2 MXene is a metal and functionalized $\text{Ti}_3\text{C}_2\text{F}_2/\text{Ti}_3\text{C}_2\text{OH}_2$ are semiconductors. In pristine MXene (M_{n+1}X_n), d bands of M and below it is the p bands of X are separated by narrow band gap. With surface functionalization of MXene, there is hybridization between the functional groups p bands and d bands of M, resulting in the generation of new bands below the fermi level. The semiconducting nature in functionalized MXene arises from the lower electronegativity, where M donates the electrons to X and T (surface functional groups), and M becomes positively charged. In addition, phase transition between the T- and H-phases (MXene) arises from the atomic stacking order of transition metal M layer, this causes the semiconducting and metallic phase transition [188].

2.4.5. Mechanical and Tribological Properties of MXene

The mechanical properties of MXene have been studied theoretically by first-principle DFT approach. By this approach, the mechanical properties of pristine and functionalized MXene have been predicted. Kurtoglu *et al.* primarily studied the elastic properties of pristine MXene by first-principle DFT [133]. The basal plane of pristine MXene was subjected to a uniform tensile and compressive deformations, till 0.003 of maximum strain. The elastic constant ' c_{11} ' values are summarized in Table 2.6. This study revealed an impressive elastic modulus of most pristine MXene (along the basal plane) system exceeding 600 GPa. Wang *et al.* carried out the DFT calculations on the mechanical properties of Ti_2C monolayer, where their elastic constant was 137 N/m, Young's modulus was 130 N/m and Poisson's ratio was 0.23 [189]. It is revealed monolayer Ti_2C to be weaker than graphene and BNNS but stronger than MoS_2 . Guo *et al.* used first-principle calculations to evaluate the stress-strain curves and Young's modulus of the pristine and oxygen functionalized 2D $\text{Ti}_{n+1}\text{C}_n$ ($n = 1, 2, 3$) [190]. This study demonstrated that Ti_2C functionalized with O can withstand up to 28% strain due to their

enhanced mechanical flexibility and MXene in the future can be used for flexible device applications. Yorulmaz *et al.* used first-principle calculations to study the mechanical properties of pristine and functionalized MXene, M_2XT_2 with $M = \text{Ti, Hf, Sc, Zr, Mo}$, $X = \text{C/N}$ and $T = \text{-O/-F}$ [155]. The computed lattice constant (a , Å), band gap (E_g , eV), elastic constant (c_{11} , c_{12} , N/m) and Young's modulus (Y , N/m) values are summarized in Table 2.7. This study has demonstrated the mechanical and electronic properties for different type MXene, these findings will contribute in the synthesis of new 2D MXene materials. Borysiuk *et al.* employed classical molecular dynamics (MD) for estimating the Young's modulus from the stress-strain curves upon tensile loading [191]. The estimated Young's modulus values by molecular dynamics for Ti_2C , Ti_3C_2 , and Ti_4C_3 MXenes were close to the values reported earlier by DFT approach. This study suggests that the molecular dynamics method can be used to explore the properties of MXene. Lipatov *et al.* measured the elastic properties using atomic force microscopy by indentation method for the mono- and bi-layer $\text{Ti}_3\text{C}_2\text{T}_x$ MXene [192]. The bi-layered $\text{Ti}_3\text{C}_2\text{T}_x$ MXene expanded upon indentation, while the Young's modulus measured on monolayer $\text{Ti}_3\text{C}_2\text{T}_x$ was ~ 0.33 TPa. The DFT calculations predicted the MXene functionalized with oxygen to have excellent mechanical strength compared to pristine and -F/-OH functionalized MXene [193-197]. Figure 2.19 summarizes the oxygen functionalized $M_2\text{C}$ MXene ($M_2\text{CO}_2$) having excellent mechanical properties compared to other 2D materials [196]. This is due to the electron charge transfer after functionalization from the M-C inner bonds to M-O outer bonds. However, oxygen functionalized MXene has lower electrical conductivity compared to fluorine and hydroxyl functionalized MXene, while the other two have high electrical conductivity [193, 198]. The authors report this to be the highest modulus among other 'solution-processed' 2D materials. MXene is also found to exhibit pseudo-negative compressibility, as it undergoes expansion along its crystallographic c direction when subjected to compression in the presence of water. This is accomplished by extensive slipping

between the individual layers [199]. Based on these studies on mechanical properties of MXene, researchers have attempted to use it as a promising reinforcement candidate for developing nanocomposites [200, 201]. Ling and co-workers demonstrated the addition of 40 wt.% $Ti_3C_2T_x$ to polyvinyl alcohol (PVA) matrix film by vacuum assisted filtration resulted in a 200% increase in stiffness and tensile strength due to functionalization by -OH group which improved the interfacial bonding between the MXene sheets and PVA [200]. Despite these theoretical studies, the mechanical properties of MXene experimentally remain unexplored. This gives us the opportunity to explore the mechanical properties of MXene experimentally.

Table 2.6: Calculated elastic constant ‘ c_{11} ’ of MXene and the MAX phase values are the one in brackets [133]

Layer	c_{11} (GPa)	Layer	c_{11} (GPa)
M_2AC		M_2AC_2	
Ti_2C	636 (312)	Ti_2C_2	523 (368)
V_2C	718 (338)	Ta_2C_2	575 (417)
Cr_2C	690 (340)	M_3AC_3	
Zr_2C	594 (261)	Ti_3C_3	512 (403)
Hf_2C	658 (291)	Ta_3C_3	633 (437)
Ta_2C	788 (334)		

Table 2.7: Calculated mechanical and electronic properties for pristine and functionalized MXene [155]

Carbides	Sc_2C	Ti_2C	Zr_2C	Mo_2C	Hf_2C	MD	α	E_g	C_{11}	C_{12}	γ	MD	α	E_g	C_{11}	C_{12}	γ		
a (Å)	3.308	3.039	3.280	2.995	3.211	Sc_2CF_2	2	3.278	0.79	177	42	167	Sc_2NF_2	2	3.183	nil	175	44	164
E_g (eV)	nil	nil	nil	nil	nil	Sc_2CF_2	3	3.028	0.98	172	52	156	Sc_2NF_2	3	3.157	nil	181	51	167
C_{11} (Nm^{-1})	94	135	143	145	154	Sc_2CF_2	4	2.986	0.84	168	68	140	Sc_2NF_2	4	3.117	nil	190	66	167
C_{12} (Nm^{-1})	16	37	45	-9	50	Ti_2CF_2	2	3.060	nil	183	68	159	Ti_2NF_2	2	3.070	nil	173	64	150
γ (Nm^{-1})	92	125	129	145	154	Ti_2CF_2	3	3.026	nil	205	52	191	Ti_2NF_2	4	2.910	nil	231	71	209
Nitrides	Sc_2N	Ti_2N	Zr_2N	Mo_2N	Hf_2N	Ti_2CF_2	4	2.980	nil	229	66	210	Zr_2NF_2	2	3.294	nil	166	65	140
a (Å)	3.177	2.985	3.246	2.802	3.171	Zr_2CF_2	2	3.311	nil	166	65	141	Zr_2NF_2	4	3.147	nil	227	64	209
E_g (eV)	nil	nil	nil	nil	nil	Zr_2CF_2	3	3.280	0.24	193	45	182	Hf_2NF_2	2	3.252	nil	129	72	88
C_{11} (Nm^{-1})	117	154	140	130	178	Mo_2CF_2	1	3.354	nil	132	48	114	Hf_2NF_2	4	3.100	nil	288	54	170
C_{12} (Nm^{-1})	23	41	38	37	54	Mo_2CF_2	4	2.986	nil	230	48	220	Sc_2NO_2	2	3.236	nil	177	79	142
γ (Nm^{-1})	112	143	130	120	161	Hf_2CF_2	2	3.264	nil	181	64	157	Hf_2NO_2	4	3.134	nil	289	144	217
						Hf_2CF_2	3	3.232	0.31	207	40	199	Mo_2NO_2	4	3.014	nil	175	98	120
						Hf_2CF_2	4	3.179	nil	280	60	225							
						Sc_2CO_2	3	3.445	1.76	168	88	121							
						Ti_2CO_2	2	3.035	0.26	266	85	238							
						Ti_2CO_2	3	3.010	0.69	257	87	227							
						Zr_2CO_2	2	3.319	0.90	266	82	240							
						Zr_2CO_2	3	3.284	1.05	252	93	218							
						Mo_2CO_2	1	3.337	nil	87	24	80							
						Mo_2CO_2	4	2.884	nil	361	145	302							
						Hf_2CO_2	2	3.265	1.02	293	80	271							
						Hf_2CO_2	3	3.228	1.10	285	95	253							

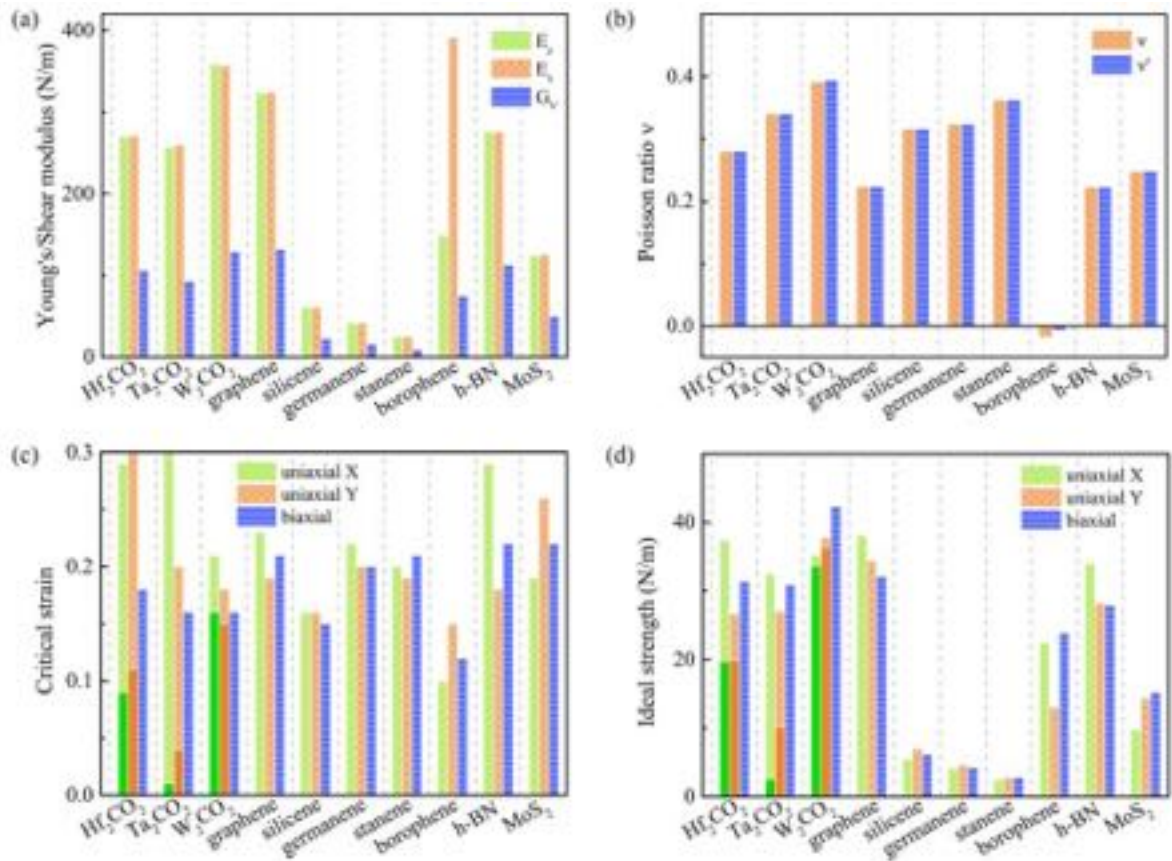


Figure 2.19: Computed mechanical properties of oxygen functionalized MXenes compared with the other 2D materials [196]

The layered structure of MXene with weak van der Waals bond between the MXene sheets are similar to graphene, this nature of MXene, makes it a potential candidate for tribological applications. This property is advantageous for enhancing the frictional and wear properties of MXene based composites as additives [202-205]. In the conventional lubricating solutions such as base oil, solvents such as ethanol, MXene can be used as additives [206-209]. The tribological studies of MXene sheets from the literature are listed in Table 2.8. In addition, theoretically by first-principle DFT calculations, the frictional properties of MXene have been studied [210, 211]. The frictional properties of all three different type titanium based MXene system ($Ti_{n+1}C_n$ ($n=1, 2, 3$)) were studied by computational DFT approach [210]. This study revealed the pristine MXene systems with oxygen vacancy defect on the surface will have the coefficient of friction less than 0.31. The functionalized (-OH, -OCH₃) Titanium based MXene systems will have coefficient of friction in the range of 0.10 to 0.14. Zhang *et al.* studied the

frictional properties of pristine M_2C ($M = Ti, Ta, Zr, Hf, Nb, W,$ and Mo) and oxygen functionalized M_2C by DFT [211]. The pristine MXene like Ti_2C will have larger resistance to sliding compared to oxygen functionalized Ti_2C . The larger lattice constant of the oxygen functionalized M_2C will reduce the resistance to sliding. Experimentally the tribological property of MXene was explored by Yang *et al.* for the Ti_3C_2 MXene [209]. The as-synthesized Ti_3C_2 MXene was added to lubricating base oil as additive and the concentration of MXene in the base oil was varied from 0 wt.% to 1.0 wt.%. The coefficient of friction decreased from 0.125 (pure base oil) to 0.063 with addition of Ti_3C_2 MXene to base oil. The tribological properties of functionalized $Ti_3C_2(OH)_2$ MXene in base oil as additive was studied by ball-on-disc tribology test [206]. The coefficient of friction decreased to less than ~ 0.09 for 1 wt.% MXene + base oil compared to base oil under the load of 15 N and 200 rpm. MXene is a potential filler for polymer-based nanocomposites and metal-matrix nanocomposites due to the lamellar structure [202-204]. $Ti_3C_2T_x$ MXene – epoxy nanocomposite displayed a superior frictional properties compared to pure epoxy [203]. The coefficient of friction for the 2.0 wt.% $Ti_3C_2T_x$ MXene – epoxy nanocomposite (0.228) was twice lower than pure epoxy (0.673) at 0.3 m/s of sliding velocity and smooth wear track surface without any damage was observed for the MXene-epoxy nanocomposite. Mai *et al.* studied the tribological properties of Ti_3C_2 /copper composite coating prepared by electrodeposition technique [204]. The COF of Ti_3C_2 /copper composite coating reduced by 0.27-0.3 (40-46%) compared to COF (0.5) of pure copper coating. Also, the wear rate decreased by 8 to 19 times for the copper coating with Ti_3C_2 nanosheets. The above studies support MXene to be a promising candidate for solid lubricant additive in lubricating oil and lubricating nanofillers for polymer- or metal- based nanocomposites.

Table 2.8: Tribological properties of MXene

Composition	Coefficient of friction	Comments	References
$Ti_{n+1}C_n$ (n=1, 2, 3)	Less than ~0.31	Computational study (DFT)	[210]
$Ti_{n+1}C_n$ (n=1, 2, 3) with -OH, -OCH ₃	0.10-0.14	Computational study (DFT)	[210]
Ti ₃ C ₂	0.063-0.07	1.0 wt.% Ti ₃ C ₂ MXene added as additive to base oil	[209]
Ti ₃ C ₂ (OH) ₂	Less than ~0.10	1.0 wt.% Ti ₃ C ₂ (OH) ₂ MXene added as additive to base oil	[206]
Ti ₃ C ₂ T _x	0.114	0.8 wt.% Ti ₃ C ₂ T _x MXene added as additive to PAO8 base oil	[208]
TiO ₂ /Ti ₃ C ₂ T _x	0.073	1.0 wt.% TiO ₂ /Ti ₃ C ₂ T _x hybrid nanocomposite in base oil under 20 N load and 150 rpm	[205]
Ti ₃ C ₂ coating	0.15 (0.5 N load) 0.19 (1 N load)	Ti ₃ C ₂ coating on copper plate	[207]
Ti ₂ CT _x -Epoxy	0.228	2.0 wt.% Ti ₂ CT _x – epoxy nanocomposite under 98 N load and sliding velocity of 0.3 m/s	[203]
Ti ₃ C ₂ -UHMWPE (ultrahigh molecular weight polyethylene)	0.13	2.0 wt.% Ti ₃ C ₂ – UHMWPE nanocomposite under 200 N load and 200 rpm	[202]
Ti ₃ C ₂ -Copper coating	Less than ~0.3	26-40-Ti ₃ C ₂ – copper coating under 1 N load and 200 rpm	[204]

2.4.6. Applications of MXene

The 2D layered MXene have unique electrical, chemical, physical, ion-transportation, mechanical and tribological properties. These properties would lead to a variety of potential applications in several fields, from batteries, catalysis, fuel cells, sensors, adsorption devices, and supercapacitors.

(a) Li-ion batteries – MXene is being examined as the new electrode material (anode) for Li-ion battery application by replacing the current anode material (graphite). Since graphite has moderate specific capacity and poor rate capability. Theoretical storage capacity of $\text{Ti}_3\text{C}_2\text{Li}_2$ was comparable to graphite and pristine Ti_3C_2 has outstanding rate performances. In general, surface terminated MXenes have lower performance, while $-\text{O}$ terminated MXenes have higher capacity [165, 166, 183, 212]. Experimental studies at 1C rate, revealed reversible capacities of Ti_2CT_x (110 mAh/g), V_2CT_x (260 mAh/g), and Nb_2CT_x (170 mAh/g) [144, 145, 213]. Computational studies of MXene as anode have shown good stability of MXene structure and good rate capability. For example, Ti_2C MXene under the influence of strain has shown Li absorption properties [214].

(b) Na-ion batteries – MXene is being studied for sodium-ion batteries (NIB) electrode materials. $\text{Ti}_3\text{C}_2\text{T}_x$ MXene was used as anode in NIB study, during sodium-ion intercalation and de-intercalation, there was expansion of interlayer space. Also, during electrochemical reaction there was no structural change, it exhibited good rate capability and capacity after 100 cycles [215]. Similarly, good capacity and rate capability was achieved for Ti_2CT_x and V_2CT_x MXene materials [135, 216]. Ti_3C_2 with CNT was used as composite anode material for sodium-ion battery. The composite electrode material showed a good cyclability after 500 cycles and good capacity [217].

(c) MXene based electrodes, as cathode were also studied for Li-S batteries [218, 219]. For Li-S battery, Ti_2C MXene phase was used as cathode and it exhibited very good 2D electron

conductivity and terminal Ti sites formed strong Ti-S interaction. Due to this interaction, they showed good discharge capacity and stable cycle life [220]. In addition, MXenes can be used as anode for Al-, K-, Ca- and Mg-ion batteries because they have the capability to accommodate different ions between the $M_{n+1}X_nT_x$ layers [166]. Figure 2.20 shows the theoretical capacities of Li-ion and post Li-ions for surface terminated MXene sheets with oxygen.

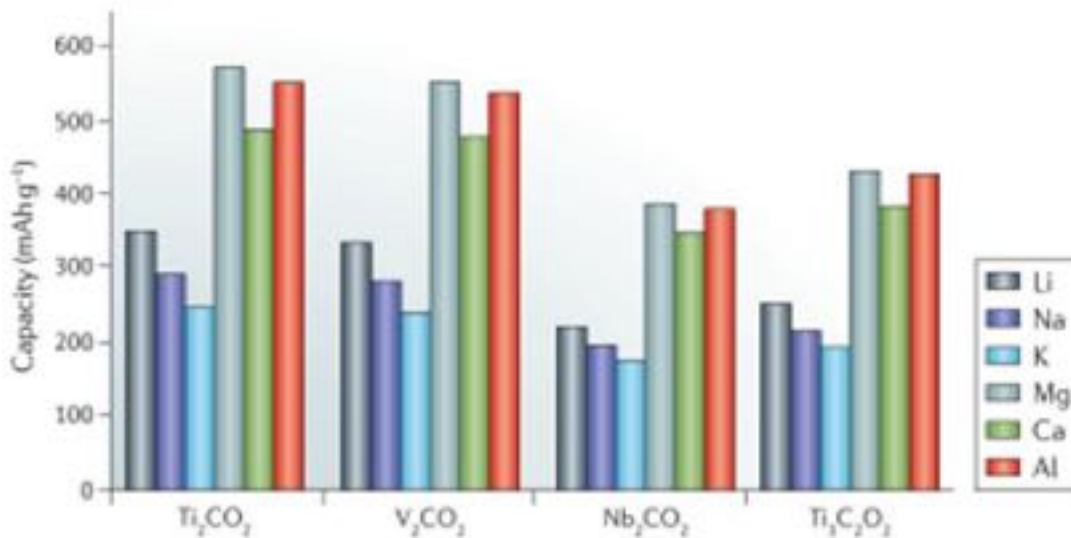


Figure 2.20: Theoretical capacities of Li- and non-Li-ion batteries with oxygen terminated MXene nanosheets [166]

(d) Supercapacitors – Similarly to batteries, MXenes are promising electrode material for supercapacitors. MXene are preferred as electrodes for supercapacitors because of their surface area and morphological nature. $Ti_3C_2T_x$ has been widely used for supercapacitor electrodes [200, 221-223]. The $Ti_3C_2T_x$ MXene has been fabricated as pure films and in few other studies, they were used as MXene-based composite films such as MXene-carbon nanotube and MXene-polymer (polyvinyl alcohol – PVA). In the cyclic test of about 10,000 cycles, the volumetric capacitance of MXene based electrodes remained stable without any degradation [138, 200, 221-223].

(e) MXene have been widely studied for different variety of sensors from electrochemical sensors, solid state gas adsorptive sensors, piezo resistive wearable sensors, photo-luminescent

sensors, terahertz sensor, bio-sensors and based on MXene, surface enhanced Raman spectroscopy with advanced sensing system has also been developed [224]. Among the different properties of MXene, bio-compatibility of MXene has been one of the important properties, where they are used as matrix material for bio-sensing applications.

(f) Microwave absorbers – Near the fermi level, the single layer MXene which are metallic in nature will have high density of electrons, which contributes to MXene dielectric properties and electrical conductivity [135]. Based on these properties, MXene can be used in microwave absorbers as additives to polymer-based composites. Ti_3C_2 MXene has shown absorption greater than 92% in a wide frequency range and they have demonstrated to be a potential filler to composites for microwave absorbers [225].

(g) Hydrogen storage – MXene is a potential and new material for hydrogen storage. Initially, Ti_2C , Sc_2C and V_2C materials hydrogen storage potential was investigated theoretically by first-principle pseudopotential calculations [226]. In case of Ti_2C MXene, hydrides are formed by dissociation of molecular hydrogen absorbed on the surface and the consecutive MXene layers below the surface absorbs the hydrogen in molecular form. The reversible capacity of molecular hydrogen is higher and the reversible hydrogen storage will occur in Ti_2C MXene. An important prediction reveal the ability of 2D Ti_2C to store hydrogen from liquid nitrogen temperature, room temperature to high temperature. Experimentally the hydrogen storage performance was improved by adding Ti_3C_2 MXene to the $4\text{MgH}_2\text{-LiAlH}_4$ composite [227]. The re-hydrogenation kinetics was significantly enhanced for the $4\text{MgH}_2\text{-LiAlH}_4$ composite.

(h) The Sc_2C with oxygen (O-) functionalization (Sc_2CO_2) on the surface can be used for ferroelectric and piezoelectric applications [178, 228]. By applying electric field in a ferroelectric MXene semiconductors, the polarity of the material will be reversed. As Sc_2CO_2 MXene are 2D material, their polarizations are different along the in-plane and out-of-plane directions.

(i) Thermoelectric performance of MXene materials with surface functionalization are promising due to the enhanced Seebeck coefficient and electrical conductivity [134]. The potential MXene materials for thermoelectric applications are the O-functionalized M_2C ($M = Ti, Hf, Zr$) and Sc_2CT_2 ($T = O, OH, F$) [229-231].

(j) MXene has been a promising material for electromagnetic interference (EMI) shielding. $Ti_3C_2T_x$ exhibits a superior EMI shielding performance, due to their high electrical conductivity and low reflections [232]. The flexibility of the MXene allows them to be used for EMI shielding applications of different shapes and MXene based composites are also used for EMI shielding [232, 233].

2.5. Scope on Exploring the Properties of Bulk Structured 2D Nanomaterials (BNNS, BCN) and Damping Properties of MXene Nanosheets

The literature review on the layered van der Waals nanomaterials, namely the 2D BNNS, B-C-N ternary system and MXene, indicate the extensive research experimentally and theoretically on single layered or multilayered 2D materials, and as additives in polymer or metal based nanocomposites. Despite these studies, there are hardly any research reported so far on the properties of bulk nanostructured 2D (BNNS, BCN) materials and on multilayered MXene damping properties. Based on the above literature review, the research will focus on experimental investigation of bulk nanostructured 2D (BNNS and BCN) materials mechanical/tribological properties and MXene damping properties. This study will result in the exploration of new avenue of applications in future.

2D BNNS

- So far there have been reports of BNNS used as filler material in composite and those composite materials were sintered by spark plasma sintering. This study will explore

the sintering of purely 2D BNNS into a bulk nanostructured material by spark plasma sintering, without addition of any sintering aid.

- Due to the high temperature exposure during SPS, detailed study on phase formation, microstructural change, interfacial bonding between the nanosheets and texturing of BNNS in the bulk form will be performed. In addition, the bulk nanostructured 2D BNNS mechanical and tribological properties will be explored and the aim is to understand the deformation of mechanisms of BNNS in bulk form.

2D BCN

- Using 2D nanomaterials (BNNS and GNP) as starting material to form the layered BCN system by reactive spark plasma sintering has not been reported so far. During this high temperature synthesis by reactive SPS process, it can transform some of the layered BCN phase formed to cubic BCN phase. Understanding the possible phases formed during this reactive spark plasma sintering will be interesting.
- After reactive SPS process, the interfacial bonding between the nanosheets, mechanical properties, tribological properties and deformation mechanisms for the layered BCN system are studied in this work. Can the small fraction of cubic BCN phase present in the bulk nanostructure, affect the mechanical and tribological properties!

2D MXene

- Mechanical properties of MXene have been extensively studied by theoretical approaches such as first-principle DFT and molecular dynamics. This gives us the scope to explore the mechanical properties of HF treated MXene particles.
- In addition, the 2D MXene sheets morphology and structure is analogous to graphene, suggesting the possibility of damping behavior in MXene. Also, in MXene the intralayer bonding is different from graphene due to heteroatomic Ti-C bonds as opposed to sp^2 hybridized C-C bonding in graphene. Hence, unique deformation could

be expected from MXene and those could be different from the deformation of graphene nanosheets. In this study, the dynamic deformation characteristics of multi-layer MXene will be explored.

2.6. References

1. A. Nagashima, N. Tejima, Y. Gamou, T. Kawai, C. Oshima. Electronic-structure of monolayer hexagonal boron-nitride physisorbed on metal-surfaces. *Physical Review Letters* 75 (1995) 3918-3921.
2. M. Corso, W. Auwarter, M. Muntwiler, A. Tamai, T. Greber, J. Osterwalder. Boron nitride nanomesh. *Science*, 303 (2004) 217-220.
3. K.S. Novoselov, D. Jiang, F. Schedin, T.J. Booth, V.V. Khotkevich, S.V. Morozov, A.K. Geim. Two-dimensional atomic crystals. *Proceedings of the National Academy of Sciences of the United States of America* 102 (2005) 10451-10453.
4. D. Pacile, J.C. Meyer, C.O. Girit, A. Zettl. The two-dimensional phase of boron nitride: Few-atomic-layer sheets and suspended membranes. *Applied Physics Letters* 92(13) (2008) 133107- 133113.
5. W. Q. Han, L. Wu, Y. Zhu and K. Watanabe. Structure of chemically derived mono- and few-atomic-layer boron nitride sheets. *Applied Physics Letters* 93(22) (2008) 23103.
6. L.H. Li, Y. Chen, G. Behan, H. Zhang, M. Petracic, A.M. Glushenkov. Large-scale mechanical peeling of boron nitride nanosheets by low-energy ball milling. *Journal of Material Chemistry* 21 (2011) 11862-11866.
7. C. Jin, F. Lin, K. Suenaga, S. Iijima. Fabrication of a freestanding boron nitride single layer and its defect assignments. *Physical Review Letters* 102(19) (2009) 195505.
8. L. Song, L. Ci, H. Lu, P.B. Sorokin, C. Jin, J. Ni, A.G. Kvashnin, D.G. Kvashnin, J. Lou, B.I. Yakobson. Large scale growth and characterization of atomic hexagonal boron nitride layers. *Nano Letters* 10(8) (2010) 3209-3215.
9. B. BenMoussa, J.D. Haen, C. Borschel, J. Barjon, V.M. Soltani, C. Ronning, M.D. Olieslaeger, H.-G. Boyen, K. Haenen. Hexagonal boron nitride nanowalls: physical vapor deposition, 2D/3D morphology and spectroscopic analysis. *Journal of Physics D: Applied Physics* 45 (2012) 135302-135311.
10. A. Nag, K. Raidongia, K.P.S.S. Hembram, R. Datta, U.V. Waghmare, C.N.R. Rao. Graphene analogues of BN: novel synthesis and properties. *ACS Nano* 4 (3) (2010) 1539-1544.

11. J.H. Warner, M.H. Rummeli, A. Bachmatiuk, B. Buchner. Atomic resolution imaging and topography of boron nitride sheets produced by chemical exfoliation. *ACS Nano* 4(3) (2010) 1299-1304.
12. Y. Wang, Z. Shi, J. Yin. Boron nitride nanosheets: large-scale exfoliation in methanesulfonic acid and their composites with polybenzimidazole. *Journal of Materials Chemistry* 21(30) (2011) 11371-11377.
13. R. Gao, L. Yin, C. Wang, Y. Qi, N. Lun, L. Zhang, Y.X. Liu, L. Kang, X. Wang. High-yield synthesis of boron nitride nanosheets with strong ultraviolet cathodoluminescence emission. *Journal of Physical Chemistry C* 113 (2009) 15160-15165.
14. X.F. Jiang, Q.W., X.B. Wang, X. Li, J. Zhang, D. Golberg, Y. Bando. Recent progress on fabrications and applications of boron nitride nanomaterials: A review. *Journal of Material Science Technology* 31(6) (2015) 589-598.
15. W. Auwärter, H.U. Suter, H. Sachdev, T. Greber. Synthesis of one monolayer of hexagonal boron nitride on Ni(111) from B-Trichloroborazine (CIBNH)₃. *Chemistry of Materials* 16(2) (2004) 343-345.
16. Y. Ye, U. Graupner, R. Krüger. Hexagonal boron nitride from a borazine precursor for coating of SiBNC fibers using a continuous atmospheric pressure CVD process. *Chemical Vapor Deposition* 17 (7-9) (2011) 221-227.
17. Y.M. Shi, C. Hamsen, X.T. Jia, K.K. Kim, A. Reina, M. Hofmann, A.L. Hsu, K. Zhang, H.N. Li, Z.-Y. Juang, M.S. Dresselhaus, L.J. Li, J. Kong. Synthesis of few-layer hexagonal boron nitride thin film by chemical vapor deposition. *Nano Letters* 10 (2010) 4134-4139.
18. A. Pakdel, C. Zhi, Y. Bando, T. Nakayama, D. Golberg. Boron nitride nanosheet coatings with controllable water repellency. *ACS Nano* 5 (2011) 6507-6515.
19. S. Nam, K. Chang, W. Lee, M. Kim, J. Hwang, H. Choi. Structural effect of two-dimensional BNNS on grain growth suppressing behaviors in Al-matrix nanocomposites. *Scientific Reports* 8 (2018) 1614.
20. R. Sagar, H. Porwal, P. Tatarko, I. Dlouhy, M.J. Reece. Boron nitride nanosheets reinforced glass matrix composites. *Advanced Applied Ceramic* 114 (2015) S26-S33.
21. J. Zhu, Y. Chen, J. Ren, D. Zhao, W. Liu. Boron nitride nanoplatelets induced synergetic strengthening and toughening effects on splats and their boundaries of plasma sprayed hydroxyapatite coatings. *Ceramic International* 44 (2018) 10604-10610.
22. A. Kovalcikova, J. Balko, C. Balazsi, P. Hvizdos, J. Disza. Influence of h-BN content on mechanical and tribological properties of Si₃N₄/BN ceramic composites. *Journal of European Ceramic Society* 34 (2014) 3319-3328.
23. D. Cai, Z. Yang, X. Duan, B. Liang, Q. Li, D. Jia, Y. Zhou. A Novel BN–MAS system composite ceramics with greatly improved mechanical properties prepared by low temperature hot-pressing. *Materials Science and Engineering A* 633 (2015) 194-199.

24. X.M. Duan, D.C. Jia, Z.L. Wu, Z. Tian, Z.H. Yang, S.J. Wang, Y. Zhou. Effect of sintering pressure on the texture of hot-press sintered hexagonal boron nitride composite ceramics. *Scripta Materialia* 68 (2013) 104-107.
25. B. Wang, C.C. Jin, J. Yang, C.F. Hu, T. Qiu. Physical and mechanical properties of hexagonal boron nitride ceramic fabricated by pressureless sintering without additive. *Advances in Applied Ceramics* 114 (2015) 273-276.
26. D.W. Ni, G.J. Zhang, Y.M. Kan, Y. Sakka. Textured h-BN ceramics prepared by slip casting. *Journal of American Chemical Society* 94 (2011) 1397-1404.
27. D. Pacile, J.C. Meyer, C.O. Girit, A. Zettl. The two dimensional phase of boron nitride: few-atomic-layer sheets and suspended membranes. *Applied Physics Letters* 92 (2008) 133107-1-133107-3.
28. D. Golberg, Y. Bando, Y. Huang, T. Terao, M. Mitome, C. Tang, C. Zhi. Boron nitride nanotubes and nanosheets. *ACS Nano* 4 (2010) 2979–2993.
29. Y. Lin, J.W. Connell. Advances in 2D boron nitride nanostructures: nanosheets, nanoribbons, nanomeses, and hybrids with graphene. *Nanoscale* 4 (2012) 6908-6939.
30. J. Ney, *Physical Properties of Crystals* [Russian translation], Mir, Moscow (1967).
31. X.M. Duan, D.C. Jia, Z.L. Wu, Z. Tian, Z.H. Yang, S.J. Wang, Y. Zhou. Effect of sintering pressure on the texture of hot-press sintered hexagonal boron nitride composite ceramics. *Scripta Materialia* 68 (2) (2013) 104-107.
32. C. Sevik, A. Kinaci, J.B. Haskins, T. Cagin. Characterization of thermal transport in low-dimensional boron nitride nanostructures. *Physical Review B* 84 (2011) 085409.
33. L. Lindsay, D.A. Broido, Enhanced thermal conductivity and isotope effect in single-layer hexagonal boron nitride. *Physical Review B* 84 (2011) 155421.
34. L. Lindsay, D.A. Broido, Theory of thermal transport in multilayer hexagonal boron nitride and nanotubes. *Physical Review B* 85 (2012) 035436.
35. T. Ouyang, Y. Chen, Y. Xie, K. Yang, Z. Bao, J. Zhong. Thermal transport in hexagonal boron nitride nanoribbons. *Nanotechnology* 21 (2010) 245701.
36. H.L. Zhu, Y.Y. Li, Z.Q. Fang, J.J. Xu, F.Y. Cao, J.Y. Wan, C. Preston, B. Yang, L.B. Hu. Highly thermally conductive papers with percolative layered boron nitride nanosheets. *ACS Nano* 8 (2014) 3606-3613.
37. L.H. Li, J. Cervenka, K. Watanabe, T. Taniguchi, Y. Chen. Strong oxidation resistance of atomically thin boron nitride nanosheets. *Nano Letters* 2 (2014) 1457-1462.
38. K. Watanabe, T. Taniguchi, T. Niiyama, K. Miya, M. Taniguchi. Far-ultraviolet plane-emission hand held device based on hexagonal boron nitride. *Nature Photonics* 3 (2009) 591–594.

39. K. Watanabe, T. Taniguchi, H. Kanda. Direct-bandgap properties and evidence for ultraviolet lasing of hexagonal boron nitride single crystal. *Nature Materials* 3 (2004) 404-409.
40. C.H. Lee, M. Xie, V. Kayastha, J. Wang, Y.K. Yap. Patterned growth of boron nitride nanotubes by catalytic chemical vapor deposition. *Chemistry of Materials* 22 (2010) 1782-1787.
41. A. Pakdel, X. Wang, C. Zhi, Y. Bando, K. Watanabe, T. Sekiguchi, T. Nakayama, D. Golberg. Facile synthesis of vertically aligned hexagonal boron nitride nanosheets hybridized with graphitic domains. *Journal of Material Chemistry* 22 (2012) 4818-4824.
42. V. Barone, J.E. Peralta. Magnetic boron nitride nanoribbons with tunable electronic properties. *Nano Letters* 8 (2008) 2210–2214.
43. R.Q. Wu, L. Liu, G.W. Peng, Y.P. Feng. Magnetism in BN nanotubes induced by carbon doping. *Applied Physics Letters* 86 (2005) 122510–122513.
44. R.Q. Wu, G.W. Peng, L. Liu, Y.P. Feng. Possible graphitic-boron-nitride-based metal-free molecular magnets from first principles study. *Journal of Physics: Condensed Matter* 18 (2006) 569–576.
45. M.S. Si, D.S. Xue. Magnetic properties of vacancies in a graphitic boron nitride sheet by first-principles pseudopotential calculation. *Physical Review B*: 75 (2007) 193409.
46. C.H. Lee, J. Drelich, Y.K. Yap. Super hydrophobicity of boron nitride nanotubes grown on silicon substrates. *Langmuir* 25 (2009) 4853-4860.
47. G.X. Li, Y. Liu, B. Wang, X.M. Song, E. Li, H. Ya. Preparation of transparent BN films with super hydrophobic surface. *Applied Surface Science* 254 (2008) 5299-5303.
48. C. Lee, X. Wei, J.W. Kysar, J. Hone. Measurement of the elastic properties and intrinsic strength of monolayer graphene. *Science* 321 (2008) 385-388.
49. A. Bosak, J. Serrano, M. Krisch, K. Watanabe, T. Taniguchi, H. Kanda. Elasticity of hexagonal boron nitride: Inelastic X-ray scattering measurements. *Physical review B* 73 (2006) 041402.
50. K. Michel, B. Verberck. Theory of elastic and piezoelectric effects in two-dimensional hexagonal boron nitride. *Physical review B* 80 (2009) 224301.
51. H. Sahin, S. Cahangirov, M. Topsakal, E. Bekaroglu, E. Akturk, R.T. Senger, S. Ciraci. Monolayer honeycomb structures of group-IV elements and III-V binary compounds: First principle calculations. *Physical Review B* 80 (2009)155453.
52. L. Song, L.J. Ci, H. Lu, P.B. Sorokin, C.H. Jin, J. Ni, A.G. Kvashnin, D.G. Kvashnin, J. Lou, B.I. Yakobson, P.M. Ajayan. Large scale growth and characterization of atomic hexagonal boron nitride layers. *Nano Letters* 10 (2010) 3209-3215.

53. C. Li, Y. Bando, C. Zhi, Y. Huang, D. Golberg. Thickness-dependent bending modulus of hexagonal boron nitride nanosheets. *Nanotechnology* 20 (2009) 385707.
54. C. Lee, Q. Li, W. Kalb, X.Z. Liu, H. Berger, R.W. Carpick, J. Hone. Frictional characteristics of atomically thin sheets. *Science* 328 (2010) 76-80.
55. S. Kumari, O.P. Sharma, R. Gusain, H.P. Mungse, A. Kukrety, N. Kumar, H. Sugimura, O.P. Khatri. Alkyl-chain-grafted hexagonal boron nitride nanoplatelets as oil dispersible additives for friction and wear reduction. *ACS Applied Materials and Interfaces* 7 (2015) 3708-3716.
56. L. Britnell, R.V. Gorbachev, R. Jalil, B.D. Belle, F. Schedin, A. Mishchenko, T. Georgio, M.I.Katsnelson, L. Eaves, S.V. Morozov, N.M.R. Peres, J. Leist, A.K. Geim, K.S. Novoselov, L.A. Ponomarenko. Field-Effect Tunneling Transistor Based on Vertical Graphene Heterostructures. *Science* 335 (2012) 947-950.
57. A. Gupta, T. Sakhivel, S. Seal. Recent development in 2D materials beyond graphene. *Progress in Materials Science* 73 (2015) 44–126.
58. X. Wang, P. Wu. Preparation of highly thermally conductive polymer composite at low filler content via a self-assembly process between polystyrene microspheres and boron nitride nanosheets. *ACS Applied Materials and Interfaces* 9 (2017) 19934-19944.
59. X. K. Chen, J.W. Hu, X.J. Wu, P. Jia, Z.H. Peng, K.Q. Chen. Tunable thermal rectification in graphene/hexagonal boron nitride hybrid structures. *Journal of Physics D: Applied Physics* 51 (2018) 085103.
60. A. Kovalcikova, J. Balko, C. Balazsi, P. Hvizdos, J. Disza. Influence of hBN content on mechanical and tribological properties of Si₃N₄/BN ceramic composites. *Journal of European Ceramic Society* 34 (2014) 3319-3328.
61. C. Zhi, Y. Bando, C. Tang, H. Kuwahara, D. Golberg. Largescale fabrication of boron nitride nanosheets and their utilization in polymeric composites with improved thermal and mechanical properties. *Advanced Materials* 21 (2009) 2889-2893.
62. A. Pakdel, Y. Bando, D. Golberg. Plasma-Assisted Interface Engineering of Boron Nitride Nanostructure Films. *ACS Nano* 8 (2014) 10631-10639.
63. C. Popov, K. Saito, B. Ivanov, Y. Koga, S. Fujiwara, V. Shanov. Chemical vapor deposition of BC₂N films and their laser induced etching with SF₆. *Thin Solid Films* 312 (1998) 99.
64. V. Linssa, S.E. Rodilb, P. Reinkec, M.G. Garnierd, P. Oelhafend, U. Kreissige, F. Richtera. Bonding characteristics of DC magnetron sputtered B-C-N thin films investigated by Fourier-transformed infrared spectroscopy and X-ray photoelectron spectroscopy. *Thin Solid Films* 467 (2004) 76-87.
65. W. Wang, Y. Bando, C. Zhi, W. Fu, E. Wang, D. Golberg. Aqueous noncovalent functionalization and controlled near-surface carbon doping of multiwalled boron nitride nanotubes. *Journal of American Chemical Society* 130 (2008) 8144.

66. R. Torres, I. Caretti, R. Gago, Z. Martín, I. Jiménez. Bonding structure of BCN nanopowders prepared by ball milling. *Diamond and Related Materials* 16 (2007) 1450-1454.
67. Y.J. Tian, J.L. He, D.L. Yu, D.C. Li, G.T. Zou, X.P. Jia, L.X. Chen, O. Yanagisawa. B–C–N compound synthesized under high temperature and high pressure. *Radiation Effects and Defects Solid* 157 (2002) 245-251.
68. Q.S. Zeng, H. Wang, W. Fu, Y.J. Gong, W. Zhou, P.M. Ajayan, J. Lou, Z. Liu. Band engineering for novel two-dimensional atomic layers. *Small* 11 (2015) 1868–1884.
69. L. Ci, L. Song, C.H. Jin, D. Jariwala, D. Wu, Y. J. Li, A. Srivastava, Z.F. Wang, K. Storr, L. Balicas, F. Liu, P.M. Ajayan. Atomic layers of hybridized boron nitride and graphene domains. *Nature Materials* 9 (2010) 430–435.
70. J. T. Jin, F. P. Pan, L.H. Jiang, X.G. Fu, A.M. Liang, Z.Y. Wei, J.Y. Zhang, G.Q. Sun. Catalyst-free synthesis of crumpled boron and nitrogen co-doped graphite layers with tunable bond structure for oxygen reduction reaction. *ACS Nano* 8 (2014) 3313–3321.
71. Y. J. Gong, G. Shi, Z. H. Zhang, W. Zhou, J. Jung, W. L. Gao, L. L. Ma, Y. Yang, S. B. Yang, G. You, R. Vajtai, Q. F. Xu, A. H. MacDonald, B. I. Yakobson, J. Lou, Z. Liu, P. M. Ajayan. Direct chemical conversion of graphene to boron- and nitrogen- and carbon-containing atomic layers. *Nature Communications* 5 (2014) 3193.
72. S. Zhang, J. Wu, Q. Yang, R. Tu, C.B. Wang, Q. Shen, L.M. Zhang. Stoichiometric controlling of boroncarbonitride thin films with using BN-C dual-targets. *AIP Advances* 5 (2015) 047125.
73. C. J. Huang, C. Chen, M. W. Zhang, L. H. Lin, X. X. Ye, S. Lin, M. Antonietti, X. C. Wang. Carbon-doped BN nanosheets for metal-free photoredox catalysis. *Nature Communications* 6 (2015) 7698.
74. L. Massimi, M. G. Betti, S. Caramazza, P. Postorino, C. Mariani, A. Latini, F. Leardini. In-vacuum thermolysis of ethane 1,2-diamineborane for the synthesis of ternary borocarbonitrides. *Nanotechnology* 27 (2016) 435601.
75. F. K. Ma, M. X. Wang, Y. L. Shao, L. J. Wang, Y. Z. Wu, Z. P. Wang, X. P. Hao. 'Thermal substitution' for preparing ternary BCN nanosheets with enhanced and controllable nonlinear optical performance. *Journal of Material Chemistry C* 5 (2017) 2559–2565.
76. T. Zhang, S. Zeng, G. Wen. A simple precursor pyrolysis route to BCN nanoflakes. *Materials Letters* 132 (2014) 277– 280.
77. Z. Han, G. Li, J. Tian, M. Gu. Microstructure and mechanical properties of boron carbide thin films. *Materials Letters* 57 (2002) 899– 903.
78. T. Tavsanoğlu, M. Jeandin, O. Addemir. Synthesis and characterisation of thin films in the B–C–N triangle. *Surface Engineering* 32 (2016) 755–760.

79. M. Jalaly, F.J. Gotor, M. Semnan, M.J Sayagués. A novel, simple and rapid route to the synthesis of boron carbonitride nanosheets: combustive gaseous unfolding. *Scientific Reports* 7 (2017) 3453.
80. J. Huang, Y.T. Zhu, H. Mori. Structure and phase characteristics of amorphous boron–carbon–nitrogen under high pressure and high temperature. *Journal of Materials Research* 16 (2001) 1178–1184.
81. R. Kumar, K. Gopalakrishnan, I. Ahmad, C.N.R. Rao. BN– Graphene composites generated by covalent cross-linking with organic linkers. *Advanced Functional Materials* 25 (2015) 5910–5917.
82. L. Song, Z. Liu, A.L.M. Reddy, N.T. Narayanan, J.T. Tijerina, J. Peng, G. Gao, J. Lou, R. Vajtai, P.M. Ajayan. Binary and ternary atomic layers built from carbon, boron and nitrogen. *Advanced Materials* 24 (2012) 4878-4895.
83. A. Rubio. Hybridized graphene: nanoscale patchworks. *Nature Materials* 9 (2010) 379-380.
84. A. Rubio, J.L. Corkill, M.L. Cohen. Theory of graphitic boron nitride nanotubes. *Physical Review B* 49 (1994) R5081–R5084.
85. Y. Miyamoto, A. Rubio, M.L. Cohen, S.G. Louie. Chiral tubules of hexagonal BC₂N. *Physical Review B* 50 (1994) 4976–4979.
86. S. Beniwal, J. Hooper, D.P. Miller, P.S. Costa, G. Chen, S.Y. Liu, P.A. Dowben, E.C.H. Sykes, E. Zurek, A. Enders. Graphene-like boron–carbon–nitrogen monolayers. *ACS Nano* 11 (2017) 2486-2493.
87. H. Nozaki, S. Itoh. Structural stability of BC₂N. *Journal of Physical and Chemistry of Solids* 57 (1) (1996) 41-49.
88. Y.Y. Zhang, Q.X. Pei, H.Y. Liu, N. Wei. Thermal conductivity of a h-BCN monolayer. *Physical Chemistry Chemical Physics* 19 (2017) 27326-27331.
89. S. Bhandary, B. Sanyal. Graphene-Boron Nitride Composite: A Material With Advanced Functionalities, In *Composites and Their Properties.*, 1st ed.; Hu, N., Ed.; InTech: Rijeka, Croatia
90. V.L. Solozhenko, D. Andrault, G. Fiquet, M. Mezouar, D.C. Rubie. Synthesis of superhard cubic BC₂N. *Applied Physics Letter* 78(10) (2001) 1385–1387.
91. V.L. Solozhenko. Synthesis of novel superhard phases in the B–C–N system. *International Journal of High-Pressure Research* 22(3–4) (2002) 519–524.
92. Y. Zhao, D.W. He, L.L. Daemen, T.D. Shen, R.B. Schwarz, Y. Zhu, D.L. Bish, J. Huang, J.Zhang, G. Shen, J. Qian, T.W. Zerda. Superhard B-C-N materials synthesized in nanostructured bulks. *Journal of Material Research* 17 (2002) 3139-3145.
93. H. Sun, S.H. Jhi, D. Roundy, M.L. Cohen, S.G. Louie. Structural form of cubic BC₂N. *Physical Review B* 64 (2001) 094108.

94. X. Luo, X.-F. Zhou, Z. Liu, J. He, B. Xu, D. Yu, H.T. Wang, Y. Tian. Refined crystal structure and mechanical properties of superhard BC₄N crystal: first-principles calculations. *Journal of Physical Chemistry C* 112 (2008) 9516-9519.
95. L. Kommel, R. Metsvahi, M. Viljus, E. Kimmari, K. Kolju, R. Traksmäa. Design of superhard c-BC₂N-precipitates in B₄C/Al-composites through SHS and heat treatment. In: *Proceedings of 8th international DAAAM baltic conference "Industrial Engineering"* 19–21 April 2012, Tallinn, Estonia.
96. V.L. Solozhenko, E. Gregoryanz. Synthesis of superhard materials. *Materials Today* 8 (2005) 44-51.
97. J. Sun, X. Zhou, G. Qian, J. Chen, Y. Fan, H. Wang, X. Guo, J. He, Z. Liu, Y. Tian. Chalcopyrite polymorph for superhard BC₂N. *Applied Physics Letter* 89 (2006) 151911.
98. M.A. Mannan, H. Noguchi, T. Kida, M. Nagano, N. Hirao, Y. Baba. Chemical bonding states and local structures of the oriented hexagonal BCN films synthesized by microwave plasma CVD. *Materials Science in Semiconductor Processing* 11 (2008) 100-105.
99. L. Jiao, M. Hu, Y. Peng, Y. Luo, C. Li, Z. Chen. Electronic, elastic, and optical properties of monolayer BC₂N. *Journal of Solid State Chemistry* 244 (2016) 120-128.
100. S. Thomas, S.U. Lee. Atomistic insights into the anisotropic mechanical properties and role of ripples on the thermal expansion of h-BCN monolayers. *RSC Advances* 9 (2019) 1238-1246.
101. K. Raidongia, A. Nag, K.P.S.S. Hembram, U.V. Waghmare, R. Datta, C.N.R. Rao. BCN: a graphene analogue with remarkable adsorptive properties. *Chemistry A European Journal* 16 (1) (2010) 149-157.
102. X. Deng, H. Kousaka, T. Tokoroyama, N. Umehara. Deposition and tribological behaviors of ternary BCN coatings at elevated temperatures. *Surface and Coatings Technology* 259 (2014) 2-6.
103. I. Caretti, I. Jiménez, R. Gago, D. Cáceres, B. Abendroth, J.M. Albella. Tribological properties of ternary BCN films with controlled composition and bonding structure. *Diamond and Related Materials* 13 (2004) 1532-1537.
104. Y.M. Chen, Z.X. Zeng, S.R. Yang, J.Y. Zhang. The tribological performance of BCN films under ionic liquids lubrication. *Diamond and Related Materials* 18 (2009) 20-26.
105. S. Miyake, M. Wang, T. Saitoh, S. Watanabe. Micro-tribological properties of B-C-N extremely thin protective films deposited on plasma pretreated magnetic layers. *Surface and Coatings Technology* 195 (2005) 214-226.
106. S. Xu, X. Ma, G. Tang, Q. Zhang. Air annealing effect on scratch behavior of BCN films. *Surface Engineering* 31(7) (2015) 1–7.
107. Y. Kusano, J.E. Evetts, I.M. Hutchings. Deposition of boron carbon nitride films by dual cathode magnetron sputtering. *Thin Solid Films* 343–344 (1999) 250-253.

108. F. Zhou, Q.Z. Wang, B. Yue, X.M. Wu, L.J. Zhuge, X.N. Cheng. Mechanical properties and bonding structure of boron carbon nitride films synthesized by dual ion beam sputtering. *Material Chemistry and Physics* 138 (1) (2013) 215-224.
109. W. Lei, D. Portehault, R. Dimova, M. Antonietti. Boron carbon nitride nanostructures from salt melts: tunable water-soluble phosphors. *Journal of American Chemical Society* 133 (2011) 7121–7127.
110. J. Wu, M.F. Rodrigues, R. Vajtai, P.M. Ajayan. M. Tuning the electrochemical reactivity of boron- and nitrogen-substituted graphene. *Advanced Materials* 28 (2016) 6239–6246.
111. N. Kumar, K. Moses, K. Pramoda, S.N. Shirodkar, A.K. Mishra, U.V. Waghmare, A. Sundaresan, C.N. Rao. Borocarbonitrides, $B_xC_yN_z$. *Journal of Material Chemistry A* 1 (2013) 5806–5813.
112. Z. Wu, W. Ren, L. Xu, F. Li, H. Cheng. Doped graphene sheets as anode materials with super high rate and large capacity for lithium ion batteries. *ACS Nano* 5 (2011) 5463–5471.
113. H. Guo, Q. Gao. Boron and nitrogen co-doped porous carbon and its enhanced properties as supercapacitor. *Journal of Power Sources* 556 (2009) 551–556.
114. H. Konno, T. Ito, M. Ushiro, K. Fushimi, K. Azumi. High capacitance B/C/N composites for capacitor electrodes synthesized by a simple method. *Journal of Power Sources* 195 (2010) 1739–1746.
115. W. Lei, S. Qin, D. Liu, D. Portehault, Z. Liu, Y. Chen. Large scale boron carbon nitride nanosheets with enhanced lithium storage capabilities. *Chemical Communications* 49 (2013) 352–354.
116. S. Bhat, P.V.W. Sasikumar, L. Molina-Luna, M.J. Graczyk-Zajac, J.H. Kleebe, R. Riedel. Electrochemical Li Storage Properties of Carbon-Rich B–C–N Ceramics. *Journal of Carbon Research C* 2 (2016) 1-10.
117. M. Ishikawa, T. Nakamura, M. Morita, Y. Matsuda, S. Tsujioka, T. Kawashima. Boron-carbon-nitrogen compounds as negative electrode matrices for rechargeable lithium battery systems. *Journal of Power Sources* 55 (1995) 127–130.
118. M. Kawaguchi, Y. Imai, N. Kadowaki. Intercalation chemistry of graphite-like layered material BC₆N for anode of li ion battery. *Journal of Physics and Chemistry of Solids* 67 (2006) 1084–1090.
119. K. Moses, V. Kiran, S. Sampath, CNR Rao. Few-layer boron carbon nitride nanosheets: Platinum-free catalyst for the oxygen reduction reaction. *Chemistry - An Asian Journal* 9 (2014) 838-843.
120. Y. Zheng, Y. Jiao, L. Ge, M. Jaroniec, S.Z. Qiao. Two-step boron and nitrogen doping in graphene for enhanced synergistic catalysis. *Angewandte Chemie* 152 (2013) 3110-3116.

121. M. Chhetri, S. Maitra, H. Chakraborty, U.V. Waghmare, C.N.R. Rao. Superior performance of borocarbonitrides, $B_xC_yN_z$, as stable, low-cost metal-free electrocatalysts for the hydrogen evolution reaction. *Energy and Environmental Sciences* 9 (2016) 95-101.
122. Z. Ling, Z. Wang, M. Zhang, C. Yu, G. Wang, Y. Dong, Y. Wang, J. Qiu. Sustainable synthesis and assembly of biomass-derived B/N co-doped carbon nanosheets with ultrahigh aspect ratio for high-performance supercapacitors. *Advanced Functional Materials* 26 (2016) 111-119.
123. S. Dou, X. Huang, Z. Ma, J. Wu, S. Wang. A simple approach to the synthesis of BCN graphene with high capacitance. *Nanotechnology* 26 (2015) 045402.
124. N. Kumar, K.S. Subrahmanyam, P. Chaturbedy, K. Raidongia, A. Govindaraj, K.P.S.S. Hembram, A.K. Mishra, U.V. Waghmare, C.N.R. Rao. Remarkable uptake of CO_2 and CH_4 by graphene like borocarbonitrides, $B_xC_yN_z$. *ChemSusChem* 4 (2011) 1662– 1670.
125. Y. Kang, Z. Chu, D. Zhang, G. Li, Z. Jiang, H. Cheng, X. Li. Incorporate boron and nitrogen into Graphene to make BCN hybrid nanosheets with enhanced microwave absorbing properties. *Carbon* 61 (2013) 200–208.
126. K. Pramoda, K. Moses, U. Maitra, C.N.R. Rao. Superior performance of a MoS_2 -RGO composite and a borocarbonitride in the electrochemical detection of dopamine, uric acid and adenine. *Electroanalysis* 27 (2015) 1892–1898.
127. M.B. Sreedhara, K. Gopalakrishnan, B. Bharath, R. Kumar, G.U. Kulkarni, C.N.R. Rao. Properties of nanosheets of 2D borocarbonitrides related to energy devices, transistors and other areas. *Chemical Physics Letters* 657 (2016) 124–130.
128. E. Salas, R.J. Jiménez Ribóo, J. Sánchez-Marcos, F. Jiménez-Villacorta, A. Muñoz-Martín, J.E. Prieto, V. Joco, C. Prieto. Elastic properties of B–C–N films grown by N_2 -reactive sputtering from boron carbide targets. *Journal of Applied Physics* 114 (2013) 213508-213514.
129. N. Ansari, F. Nazari, F. Illas. Theoretical study of electronic and tribological properties of h-BNC₂/graphene, h-BNC₂/h-BN and h-BNC₂/h-BNC₂ bilayers. *Physical Chemistry Chemical Physics* 17 (2015) 12908-12918.
130. M. Naguib, M. Kurtoglu, V. Presser, J. Lu, J.J. Niu, M. Heon, L. Hultman, Y. Gogotsi, M.W. Barsoum. Two-dimensional nanocrystals produced by exfoliation of Ti_3AlC_2 . *Advanced Materials* 23 (2011) 4248-4253.
131. M. Khazaei, M. Arai, T. Sasaki, C.Y. Chung, N.S. Venkataramanan, M. Estili, Y. Sakka, Y. Kawazoe. Novel electronic and magnetic properties of two-dimensional transition metal carbides and nitrides. *Advanced Functional Materials* 23 (2013) 2185-2192.
132. B. Anasori, Y. Xie, M. Beidaghi, J. Lu, B.C. Hosler, L. Hultman, P.R.C. Kent, Y. Gogotsi, M.W. Barsoum. Two dimensional, ordered, double transition metals carbides (MXenes). *ACS Nano* 9 (2015) 9507-9516.

133. M. Kurtoglu, M. Naguib, Y. Gogotsi, M.W. Barsoum. First principles study of two-dimensional early transition metal carbides. *MRS Communications* 2 (2012) 133-137.
134. M. Khazaei, M. Arai, T. Sasaki, M. Estili, Y. Sakka. Two-dimensional molybdenum carbides: potential thermoelectric materials of the MXene family. *Physical Chemistry Chemical Physics* 16 (2014) 7841-7849.
135. M. Naguib, V.N. Mochalin, M.W. Barsoum, Y. Gogotsi. 25th anniversary article: MXenes: a new family of two-dimensional materials. *Advanced Materials* 26 (2014) 992-1005.
136. M. Naguib, O. Mashtalir, J. Carle, V. Presser, J. Lu, L. Hultman, Y. Gogotsi, M.W. Barsoum. Two dimensional transition metal carbides. *ACS Nano* 6 (2012) 1322-1331.
137. L. Wang, H. Zhang, B. Wang, C. Shen, C. Zhang, Q. Hu, A. Zhou, B. Liu. Synthesis and electrochemical performance of $Ti_3C_2T_x$ with hydrothermal process. *Electronic Materials Letters* 12 (2016) 702-710.
138. M. Ghidui, M.R. Lukatskaya, M.Q. Zhao, Y. Gogotsi, M.W. Barsoum. Conductive two-dimensional titanium carbide 'clay' with high volumetric capacitance. *Nature* 516 (2014) 78-81.
139. R. Meshkian, L.Å. Näslund, J. Halim, J. Lu, M.W. Barsoum, J. Rosen. Synthesis of two-dimensional molybdenum carbide, Mo_2C , from the gallium based atomic laminate Mo_2Ga_2C . *Scripta Materialia* 108 (2015) 147-150.
140. J. Zhou, X.H. Zha, F.Y. Chen, Q. Ye, P. Eklund, S.Y. Du, Q. Huang. Two-dimensional zirconium carbide by selective etching of Al_3C_3 from nanolaminated $Zr_3Al_3C_5$. *Angewandte Chemie International Edition* 128 (2016) 5092-5097.
141. P. Urbankowski, B. Anasori, T. Makaryan, D. Er, S. Kota, P.L. Walsh, M.Q. Zhao, V.B. Shenoy, M.W. Barsoum, Y. Gogotsi. Synthesis of two-dimensional titanium nitride Ti_4N_3 (MXene). *Nanoscale* 8 (2016) 11385-11391.
142. C. Xu, L. Wang, Z. Liu, L. Chen, J. Guo, N. Kang, X.L. Ma, H.M. Cheng, W. Ren. Large-area high-quality 2D ultrathin Mo_2C superconducting crystals. *Nature Materials* 14 (2015) 1135-1141.
143. O. Mashtalir, M. Naguib, B. Dyatkin, Y. Gogotsi, M.W. Barsoum. Kinetics of aluminum extraction from Ti_3AlC_2 in hydrofluoric acid. *Materials Chemistry and Physics* 139 (2013) 147-152.
144. J. X. Li, Y. L. Du, C. X. Huo, S. Wang, C. Cui. Thermal stability of two-dimensional Ti_2C nanosheets. *Ceramic International* 41 (2015) 2631-2635.
145. M. Naguib, J. Halim, J. Lu, K. M. Cook, L. Hultman, Y. Gogotsi, M. W. Barsoum. New two-dimensional niobium and vanadium carbides as promising materials for Li-ion batteries. *Journal of American Chemical Society*. 135 (2013) 15966.

146. M. Naguib. MXenes: A new family of two-dimensional materials and its application as electrodes for Li-ion batteries. PhD Thesis, Drexel University (2014).
147. M. Ghidui, M. Naguib, C. Shi, O. Mashtalir, L.M. Pan, B. Zhang, J. Yang, Y. Gogotsi, S. J. Billinge, M.W. Barsoum. Synthesis and characterization of two-dimensional Nb₄C₃ (MXene). *Chemical Communications* 50 (2014) 9517-9520.
148. J. Yang, M. Naguib, M. Ghidui, L.M. Pan, J. Gu, J. Nanda, J. Halim, Y. Gogotsi, M.W. Barsoum. Two-dimensional Nb-based M₄C₃ solid solutions (MXenes). *Journal of American Ceramic Society* 99 (2015) 660-666.
149. Z.W. Seh, K.D. Fredrickson, B. Anasori, J. Kibsgaard, A.L. Strickler, M.R. Lukatskaya, Y. Gogotsi, T.F. Jaramillo, A. Vojvodic. Two-dimensional molybdenum carbide (MXene) as an efficient electrocatalyst for hydrogen evolution. *ACS Energy Letters* 1 (2016) 589-594.
150. A. Lipatov, M. Alhabej, M.R. Lukatskaya, A. Boson, Y. Gogotsi, A. Sinitskii. Effect of Synthesis on quality, electronic properties and environmental stability of individual monolayer Ti₃C₂ MXene flakes. *Advanced Electronic Materials* 2 (2016) 1600255.
151. J. Halim, S. Kota, M.R. Lukatskaya, M. Naguib, M.Q. Zhao, E.J. Moon, J. Pitock, J. Nanda, S.J. May, Y. Gogotsi, M.W. Barsoum. Synthesis and characterization of 2D molybdenum carbide (MXene). *Advanced Functional Materials* 26 (2016) 3118-3127.
152. M. Ghidui, J. Halim, S. Kota, D. Bish, Y. Gogotsi, M.W. Barsoum. Ion-exchange and cation solvation reactions in Ti₃C₂ MXene. *Chemistry of Materials* 28 (2016) 3507-3514.
153. A. Enyashin, A. Ivanovskii. Atomic structure, comparative stability and electronic properties of hydroxylated Ti₂C and Ti₃C₂ nanotubes. *Computational and Theoretical Chemistry* 989 (2012) 27-32.
154. I.R. Shein, A.L. Ivanovskii. Graphene-like titanium carbides and nitrides Ti_{n+1}C_n, Ti_{n+1}N_n (n = 1, 2, and 3) from de-intercalated MAX phases: First-principles probing of their structural, electronic properties and relative stability. *Computational Material Science* 65 (2012) 104-114.
155. U. Yorulmaz, A. Özden, N.K. Perkgöz, F. Ay, C. Sevik. Vibrational and mechanical properties of single layer MXene structures: a first-principles investigation. *Nanotechnology* 27 (2016) 335702.
156. X. Zhang, Z. Ma, X. Zhao, Q. Tang, Z. Zhou. Computational studies on structural and electronic properties of functionalized MXene monolayers and nanotubes. *Journal of Material Chemistry A* 3 (2015) 4960-4966.
157. L.Y. Gan, Y.J. Zhao, D. Huang, U. Schwingenschlögl. First-principles analysis of MoS₂/Ti₂C and MoS₂/Ti₂CY₂ (Y = F and OH) all-2D semiconductor/metal contacts. *Physical Review B* 87 (2013) 245307.

158. G.R. Berdiyrov, M.E. Madjet, K.A. Mahmoud. Ionic sieving through $\text{Ti}_3\text{C}_2(\text{OH})_2$ MXene: first-principles calculations. *Applied Physics Letters* 108 (2016) 113110.
159. B. Anasori, C. Shi, E.J. Moon, Y. Xie, C.A. Voigt, P.R.C. Kent, S.J. May, S.J.L. Billinge, M.W. Barsoum, Y. Gogotsi. Control of electronic properties of 2D carbides (MXenes) by manipulating their transition metal layers. *Nanoscale Horizons* 1 (2016) 227-234.
160. M. W. Barsoum. The $\text{M}_{\text{N}+1}\text{AX}_\text{N}$ phases: A new class of solids: Thermodynamically stable nanolaminates. *Progress in Solid State Chemistry* 28 (2000) 201-281.
161. M.W. Barsoum, D. Brodtkin, T. El-Raghy. Layered machinable ceramics for high temperature applications. *Scripta Materialia* 36 (1997) 535-541.
162. M.W. Barsoum, T. El-Raghy. The MAX phase: unique new carbide and nitride materials. *American Scientist* 89 (2001) 333-343.
163. V.M.H. Ng, H. Huang, K. Zhou, P.S. Lee, W. Que, J.Z. Xu, L.B. Kong. Recent progress in layered transition metal carbides and/or nitrides (MXenes) and their composites: synthesis and applications. *Journal of Material Chemistry A* 5 (2017) 3039-3068.
164. Q. Tang, Z. Zhou. Graphene analogous low dimensional materials. *Progress in Material Science* 58 (2013) 1244-1315.
165. Y. Xie, M. Naguib, V. N. Mochalin, M.W. Barsoum, Y. Gogotsi, X. Q. Yu, K.W. Nam, X. Q. Yang, A.I. Kolesnikov, P.R.C. Kent. Role of surface structure on li-ion energy storage capacity of two-dimensional transition-metal carbides. *Journal of American Chemical Society* 136 (2014) 6385.
166. Y. Xie, Y. Dall'Agnese, M. Naguib, Y. Gogotsi, M.W. Barsoum, H.L.L. Zhuang, P.R.C. Kent. Prediction and characterization of MXene nanosheet anodes for non-lithium-ion batteries. *ACS Nano* 8 (2014) 9606.
167. M. Naguib, O. Mashtalir, M. R. Lukatskaya, B. Dyatkin, C. Zhang, V. Presser, Y. Gogotsi, M. W. Barsoum. One step synthesis of nanocrystalline transition metal oxides on thin sheets of disordered graphitic carbon by oxidation of MXenes. *Chemical Communications* 50 (2014) 7420-7423.
168. Z. Y. Li, L. B. Wang, D. D. Sun, Y. D. Zhang, B. Z. Liu, Q. K. Hu, A. G. Zhou. Synthesis and thermal stability of two-dimensional carbide MXene Ti_3C_2 . *Material Science Engineering B* 191 (2015) 33-40.
169. H. Ghassemi, W. Harlow, O. Mashtalir, M. Beidaghi, M. R. Lukatskaya, Y. Gogotsi, M. L. Taheri. In situ environmental transmission electron microscopy study of oxidation of two-dimensional Ti_3C_2 and formation of carbon supported TiO_2 . *Journal of Material Chemistry A* 2 (2014) 14339-14343.
170. C. Si, J. Zhou, Z. Sun. Half-metallic Ferromagnetism and surface functionalization-induced metal-insulator transition in graphene-like two-dimensional Cr_2C crystals. *ACS Applied Materials and Interfaces* 7 (2015) 17510-17515.

171. N.J. Lane, M.W. Barsoum, J.M. Rondinelli. Correlation effects and spin orbit interactions in two-dimensional hexagonal 5d transition metal carbides $Ta_{n+1}C_n$ ($n = 1,2,3$). *Europhysics Letters* 101 (2013) 57004.
172. A. Bandyopadhyay, D. Ghosh, S.K. Pati. Effects of point defects on the magnetoelectronic structures of MXenes from first principles. *Physical Chemistry Chemical Physics* 20 (2018) 4012-4019.
173. J.R. Ran, G.P. Gao, F.T. Li, T.Y. Ma, A.J. Du, S.Z. Qiao. Ti_3C_2 MXene co-catalyst on metal sulfide photo-absorbers for enhanced visible-light photocatalytic hydrogen production. *Nature Communication* 8 (2017) 13907.
174. G.R. Berdiyrov. Optical properties of functionalized $Ti_3C_2T_2$ ($T = F, O, OH$) MXene: First-principles calculations. *AIP Advances* 6 (2016) 055105.
175. Y. Bai, K. Zhou, N. Srikanth, J.H.L. Pang, X. He, R. Wang. Dependence of elastic and optical properties on surface terminated groups in two-dimensional MXene monolayers: a first-principles study. *RSC Advances* 6 (2016) 35731-35739.
176. H. Zhang, G. Yang, X. Zuo, H. Tang, Q. Yang, G. Li. Computational studies on the structural, electronic and optical properties of graphene-like MXenes (M_2CT_2 , $M = Ti, Zr, Hf$; $T = O, F, OH$) and their potential applications as visible-light driven photocatalysts. *Journal Material Chemistry A* 4 (2016) 12913-12920.
177. J. Guo, Y. Sun, B. Liu, Q. Zhang, Q. Peng. Two-dimensional scandium-based carbides (MXene): Band gap modulation and optical properties. *Journal of Alloys and Compounds* 712 (2017) 752-759.
178. A. Chandrasekaran, A. Mishra, A.K. Singh. Ferroelectricity, antiferroelectricity, and ultrathin 2D electron/hole gas in multifunctional monolayer MXene. *Nano Letters* 17 (2017) 3290-3296.
179. K. Hantanasirisakul, Y. Gogotsi. Electronic and optical properties of 2D transition metal carbides and nitrides (MXenes). *Advanced Materials* 30 (2018) 1804779.
180. M. Khazaei, M. Arai, T. Sasaki, A. Ranjbar, Y. Liang, S. Yunoki. OH-terminated two-dimensional transition metal carbides and nitrides as ultralow work function materials. *Physical Review B* 92 (2015) 075411.
181. M. Khazaei, A. Ranjbar, M. Ghorbani-Asl, M. Arai, T. Sasaki, Y. Liang, S. Yunoki. Nearly free electron states in MXenes. *Physical Review B* 93 (2016) 205125.
182. H. Lashgari, M. R. Abolhassani, A. Boochani, S. M. Elahi, and J. Khodadadi. Electronic and optical properties of 2D graphene-like compounds titanium carbides and nitrides: DFT calculations. *Solid State Communications* 195 (2014) 61-69.
183. Q. Tang, Z. Zhou, and P. W. Shen. Are MXenes promising anode materials for Li ion batteries? Computational studies on electronic properties and Li storage capability of Ti_3C_2 and $Ti_3C_2X_2$ ($X = F, OH$) monolayer. *Journal of American Chemical Society* 134 (2012) 16909-16916.

184. A. N. Enyashin, A. L. Ivanovskii. Structural and electronic properties and stability of MXenes Ti_2C and Ti_3C_2 functionalized by Methoxy groups. *Journal of Physical Chemistry C* 117 (2013) 13637-13643.
185. Y. Lee, S. B. Cho, Y. C. Chung. Tunable indirect to direct band gap transition of monolayer Sc_2CO_2 by the strain effect. *ACS Applied Material Interfaces* 6 (2014) 14724-14728.
186. Y. Lee, Y. Hwang, S. B. Cho, Y.C. Chung. Achieving a direct band gap in oxygen functionalized-monolayer scandium carbide by applying an electric field. *Physical Chemistry Chemical Physics* 16 (2014) 26273-26278.
187. X. Li, Y. Dai, Y. Ma, Q. Liu, B. Huang. Intriguing electronic properties of two-dimensional MoS_2/TM_2CO_2 (TM = Ti, Zr, or Hf) hetero-bilayers: Type-II semiconductors with tunable band gaps. *Nanotechnology* 26 (2015) 135703.
188. C. Chen, X. Ji, K. Xu, B. Zhang, L. Miao, J. Jiang. Prediction of T and H phase two dimensional transition metal carbides/nitrides and their semiconducting metallic phase transition. *ChemPhysChem*, 18 (2017) 1897-1902.
189. S. Wang, J.X. Li, Y.L. Du, C. Cui. First-principles study on structural, electronic and elastic properties of graphene-like hexagonal Ti_2C monolayer. *Computational Material Science* 83 (2014) 290-293.
190. Z. Guo, J. Zhou, C. Si, Z. Sun. Flexible two-dimensional $Ti_{n+1}C_n$ (n=1, 2 and 3) and their functionalized MXenes predicted density functional theories. *Physical Chemistry Chemical Physics* 17 (2015) 15348.
191. V.N. Borysiuk, V. N. Mochalin, Y. Gogotsi. Molecular dynamic study of the mechanical properties of two-dimensional titanium carbides $Ti_{n+1}C_n$ (MXenes). *Nanotechnology* 26 (2015) 265705.
192. A. Lipatov, H. Lu, M. Alhabeab, B. Anasori, A. Gruverman, Y. Gogotsi, A. Sinitskii. Elastic properties of 2D $Ti_3C_2T_x$ MXene monolayers and bilayers. *Science Advances* 4 (2018) eaat0491.
193. X.H. Zha, K. Luo, Q. Li, Q. Huang, J. He, X. Wen, S. Du. Role of the Surface Effect on the Structural, Electronic and Mechanical Properties of the Carbide MXenes. *Europhysics Letters* 111 (2015) 26007.
194. Z. Fu, Q. Zhang, D. Legut, C. Si, T. Germann, T. Lookman, S. Du, J. Francisco, R. Zhang. Stabilization and strengthening effects of functional groups in two-dimensional titanium carbide. *Physical Review B* 94 (2016) 104103.
195. L. Feng, X.H. Zha, K. Luo, Q. Huang, J. He, Y.J. Liu, W. Deng, S.Y. Du. Structures and mechanical and electronic properties of the Ti_2CO_2 MXene incorporated with neighboring elements (Sc, V, B and N). *Journal of Electronic Materials* 46 (2017) 2460-2466.
196. Z. Fu, H. Zhang, C. Si, D. Legut, T.C. Germann, Q. Zhang, S. Du, J.S. Francisco, R. Zhang. Mechanistic quantification of thermodynamic stability and mechanical strength for

- two-dimensional transition-metal carbides. *Journal of Physical Chemistry C* 122 (2018) 4710-4722.
197. G. Plummer, B. Anasori, Y. Gogotsi, G. Tucker. Nanoindentation of monolayer $Ti_{n+1}C_nT_x$ MXenes via atomistic simulations: The role of composition and defects on strength. *Computational Materials Science* 157 (2019) 168-174.
198. N. Zhang, Y. Hong, S. Yazdanparast, M.A. Zaeem. Superior structural, elastic and electronic properties of 2D titanium nitride MXenes over carbide MXenes: a comprehensive first principles study. *2D Materials* 5 (2018) 045004.
199. M. Ghidui, S. Kota, V. Drozd, M.W. Barsoum. Pressure-induced shear and interlayer expansion in Ti_3C_2 MXene in the presence of water. *Science Advances* 4 (2018) eaao6850.
200. Z. Ling, C.E. Ren, M.Q. Zhao, J. Yang, J.M. Giammarco, J. Qiu, M.W. Barsoum, Y. Gogotsi. Flexible and conductive MXene films and nanocomposites with high capacitance. *Proceedings of the National Academy of Sciences of the United States of America* 111 (2014) 16676-16681.
201. M. Naguib, T. Saito, S. Lai, M.S. Rager, T. Aytug, M.P. Paranthaman, M.Q. Zhao, Y. Gogotsi. $Ti_3C_2T_x$ (MXene)-polyacrylamide nanocomposite films. *RSC Advances* 6 (2016) 72069-72073.
202. H. Zhang, L. Wang, Q. Chen, P. Li, A. Zhou, X. Cao, Q. Hu. Preparation, mechanical and anti-friction performance of MXene/polymer composites. *Materials and Design* 92 (2016) 682-689.
203. H. Zhang, L. Wang, A. Zhou, C. Shen, Y. Dai, F. Liu, J. Chen, P. Li, Q. Hu. Effects of 2-D transition metal carbide Ti_2CT_x on properties of epoxy composites. *RSC Advances* 6 (2016) 87341-87352.
204. Y.J. Mai, Y.G. Li, S.L. Li, L.Y. Zhang, C.S. Liu, X.H. Jie. Self-lubricating Ti_3C_2 nanosheets/copper composite coatings. *Journal of Alloys and Compound* 770 (2019) 1-5.
205. M. Xue, Z. Wang, F. Yuan, X. Zhang, W. Wei, H. Tang, C. Li. Preparation of $TiO_2/Ti_3C_2T_x$ hybrid nanocomposites and their tribological properties as base oil lubricant additives. *RSC Advances* 7 (8) (2017), pp. 4312-4319.
206. X.H. Zhang, M.Q. Xue, X.H. Yang, Z.P. Wang, G.S. Luo, Z.D. Huang, X.L. Sui, C.S. Li. Preparation and tribological properties of $Ti_3C_2(OH)_2$ nanosheets as additives in base oil. *RSC Advances* 5 (2015) 2762-2767.
207. W. Lian, Y. Mai, C. Liu, L. Zhang, S. LI, X. Jie. Two-dimensional Ti_3C_2 coating as an emerging protective solid lubricant for tribology. *Ceramics International* 44 (2018) 20154-20162.
208. Y. Liu, X.F. Zhang, S.L. Dong, Z.Y. Ye, Y.D. Wei. Synthesis and tribological property of $Ti_3C_2T_{(x)}$ nanosheets. *Journal of Material Science* 52 (2017) 2200-2209.

209. J. Yang, B. Chen, H. Song, H. Tang, C. Li. Synthesis, characterization, and tribological properties of two-dimensional Ti_3C_2 . *Crystal Research and Technology* 49 (2014) 926-932.
210. D. Zhang, M. Ashton, A. Ostadhossein, A.C.T. van Duin, R.G. Hennig, S.B. Sinnott. Computational study of low interlayer friction in $Ti_{n+1}C_n$ ($n=1, 2, \text{ and } 3$) MXene. *ACS Applied Material and Interfaces* 9 (2017) 34467-34479.
211. H. Zhang, Z. H. Fu, D. Legut, T. C. Germann and R. F. Zhang. Stacking stability and sliding mechanism in weakly bonded 2D transition metal carbides by van der Waals force. *RSC Advances* 7 (2017) 55912–55919.
212. C. Eames, M. S. Islam. Ion intercalation into two-dimensional transition-metal carbides: Global screening for new high-capacity battery materials. *Journal of American Chemical Society* 136 (2014) 16270.
213. M. Naguib, J. Come, B. Dyatkin, V. Presser, P. L. Taberna, P. Simon, M. W. Barsoum, Y. Gogotsi. MXene: A promising transition metal carbide anode for lithium-ion batteries. *Electrochemistry Communications* 16 (2012) 61-64.
214. D.D. Sun, M.S. Wang, Z.Y. Li, G.X. Fan, L.Z. Fan, A.G. Zhou. Two-dimensional Ti_3C_2 as anode material for Li-ion batteries. *Electrochemistry Communications* 47 (2014) 80-83.
215. S.J. Zhao, W. Kang, J.M. Xue. Role of strain and concentration on the li adsorption and diffusion properties on Ti_2C layer. *Journal of Physical Chemistry C* 118 (2014) 14983-14990.
216. S. Kajiyama, L. Szabova, K. Sodeyama, H. Iinuma, R. Morita, K. Gotoh, Y. Tateyama, M. Okubo, A. Yamada. Sodium-ion intercalation mechanism in MXene nanosheets. *ACS Nano* 10 (2016) 3334-3341.
217. S.M. Bak, R. Qiao, W. Yang, S. Lee, X. Yu, B. Anasori, H. Lee, Y. Gogotsi, X.Q. Yang. Na-ion intercalation and charge storage mechanism in 2D vanadium carbide. *Advanced Energy Materials* 7 (2017) 1-9.
218. X. Xie, M.Q. Zhao, B. Anasori, K. Maleski, C.E. Ren, J. Li, B.W. Byles, E. Pomerantseva, G. Wang, Y. Gogotsi. Porous heterostructured MXene/carbon nanotube composite paper with high volumetric capacity for sodium-based energy storage devices. *Nano Energy* 26 (2016) 513-523.
219. X. Liang, A. Garsuch, L.F. Naza. Sulfur cathodes based on conductive MXene nanosheets for high-performance lithium–sulfur batteries. *Angewandte Chemie International Edition* 54 (2015) 3907-3911.
220. D. Rao, L. Zhang, Y. Wang, Z. Meng, X. Qian, J. Liu, X. Shen, G. Qiao, R. Lu. Mechanism on the improved performance of lithium sulfur batteries with MXene-based additives. *Journal of Physical Chemistry C* 121 (2017) 11047-11054.
221. M.R. Lukatskaya, O. Mashtalir, C.E. Ren, Y. Dall’Agnese, P. Rozier, P.L. Taberna, M. Naguib, P. Simon, M.W. Barsoum, Y. Gogotsi. Cation intercalation and high volumetric capacitance of two-dimensional titanium carbide. *Science* 341(2013) 1502 – 1505.

222. Y. Dall'Agnes, M.R. Lukatskaya, K.M. Cook, P.L. Taberna, Y. Gogotsi, P. Simon. High capacitance of surface-modified 2D titanium carbide in acidic electrolyte. *Electrochemistry Communications* 48 (2014) 118 - 122.
223. M.Q. Zhao, C.E. Ren, Z. Ling, M.R. Lukatskaya, C. Zhang, K.L. Van Aken, M.W. Barsoum, Y. Gogotsi, Flexible MXene/carbon nanotube composite paper with high volumetric capacitance. *Advanced Materials* 27 (2015) 339 - 345.
224. A. Sinha, Dhanjai, H.M. Zhao, Y.J. Huang, X.B. Lu, J.P. Chen, R. Jain. MXene: an emerging material for sensing and biosensing. *TrAC Trends in Analytical Chemistry* 105 (2018) 424-435.
225. Y. Qing, W. Zhou, F. Luo, D. Zhu. Titanium carbide (MXene) nanosheets as promising microwave absorbers. *Ceramic International* 42 (2016) 16412-16416.
226. Q.K. Hu, D.D. Sun, Q.H. Wu, H.Y. Wang, L.B. Wang, B.Z. Liu, A. Zhou, J. He. MXene: a new family of promising hydrogen storage medium. *Journal of Physical Chemistry A* 117 (2013) 14253-14260.
227. G. Chen, Y. Zhang, H. Cheng, Y. Zhu, L. Li, H. Lin. Effect of two-dimension MXene Ti_3C_2 on hydrogen storage performances of MgH_2 - $LiAlH_4$ composite. *Chemical Physics* 522 (2019) 178-187.
228. M. Khazaei, V. Wang, C. Sevik, A. Ranjbar, M. Arai, S. Yunoki. Electronic structures of iMAX phases and their two-dimensional derivatives: A family of piezoelectric materials. *Physical Review Materials* 2 (2018) 074002.
229. S. Kumar, U. Schwingenschlögl. Thermoelectric performance of functionalized Sc_2C MXenes. *Physical Review B* 94 (2016) 035405.
230. A.N. Gandhi, H.N. Alshareef, U. Schwingenschlögl. Thermoelectric performance of the MXenes M_2CO_2 (M= Ti, Zr, or Hf). *Chemistry of Materials* 28 (2016) 1647-1652.
231. S. Sarikurt, D. Çakir, M. Keçeil, C. Sevik. The influence of surface functionalization on thermal transport and thermoelectric properties of MXene monolayers. *Nanoscale* 10 (2018) 8859-8868.
232. F. Shahzad, M. Alhabeab, C.B. Hatter, B. Anasori, S. Man Hong, C.M. Koo, Y. Gogotsi. Electromagnetic interference shielding with 2D transition metal carbides (MXenes). *Science* 353 (2016) 1137– 1140.
233. J. Liu, H.B. Zhang, R. Sun, Y. Liu, Z. Liu, A. Zhou, Z.Z. Yu. Hydrophobic, Flexible, and lightweight MXene foams for high-performance electromagnetic-interference shielding. *Advanced Materials* 29 (2017) 1702367

Chapter III: Experimental Procedure

This chapter discusses the materials used, synthesis methods and consolidation technique. The characterization techniques used for structural, microstructural, mechanical and tribological properties are also discussed.

3.1. Monolithic BNNS Preparation – Spark Plasma Sintering

Two-dimensional boron nitride nanosheet (2D BNNS) is the starting material used for consolidation. The commercial BNNS powder was purchased from pH Matter LLC, Columbus, Ohio. The as-received powder was white in color and have flake-like morphology. BNNS powder surface area was $60 \text{ m}^2/\text{g}$ [1]. The BNNS average powder size was measured from the SEM image of as-received BNNS as shown in Figure 3.1 using ImageJ software. The average powder size was varying from $100 \text{ nm} - 3 \text{ }\mu\text{m}$ with varying nanosheet thickness ($40 - 65 \text{ nm}$).

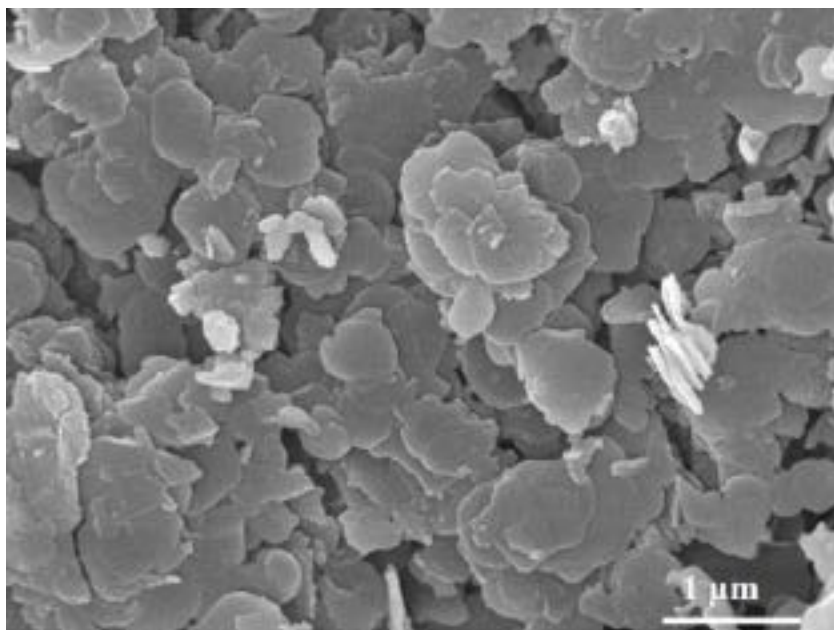


Figure 3.1: SEM image of the as-received BNNS

Spark plasma sintering (SPS, Thermal Technologies model 10–4, LLC, Santa Rosa, CA, USA) technique was followed to consolidate as-received BNNS powder. A cylindrical graphite die of 20 mm diameter was used for consolidation of BNNS owing to graphite's high

thermal and electrical conductivity. The graphite foil was wrapped between the BNNS powder and graphite die to aid electric current concentration during sintering, and to avoid the reaction between die and powder. The temperature of graphite die was monitored by using a pyrometer focused on the predrilled hole of graphite die. As-received BNNS was sintered at 1650 °C for 20 min at the heating rate of 100 °C/min under a uniaxial pressure of 50 MPa. After sintering, the pellet was polished to remove the graphite foil. Sintering parameters for 2D BNNS were optimized based on the literature values reported for spark plasma sintering of h-BN powders. The density of as-received BNNS powders was measured by Helium gas pycnometer (Accupyc 1340, Micrometrics Instrument Corporation, Norcross, GA, USA). For the BNNS SPS pellet, the relative density was measured by Archimedes' method and true density of the pellet was measured by Helium gas pycnometer.

3.2. Synthesis of BCN System

3.2.1. BNNS and GNP Mixing – Ball Milling

BNNS powder details are discussed in section 3.1. Graphene nanoplatelets (xGNP-M-5) were purchased from XG Sciences (Lansing, MI). Figure 3.2 shows SEM images of as-received GNP. The average particle size of GNP was 5 - 10 μm with a thickness of 6 - 8 nm approximately and surface area of as-received GNP varied from 120-150 m^2/g [2]. The individual GNP comprised of 10-20 sheets of graphene and each layer of graphene thickness varied from 0.35 nm to 0.37 nm [3, 4]. For BCN synthesis, initially the powder mixture of two-dimensional boron nitride nanosheet and graphene nanoplatelets was prepared by high energy ball milling method. This method was chosen to obtain uniform mixture of BNNS and GNP for the synthesis of BCN phase. In addition, ball milling will break down the agglomerates of starting BNNS and GNP powder.

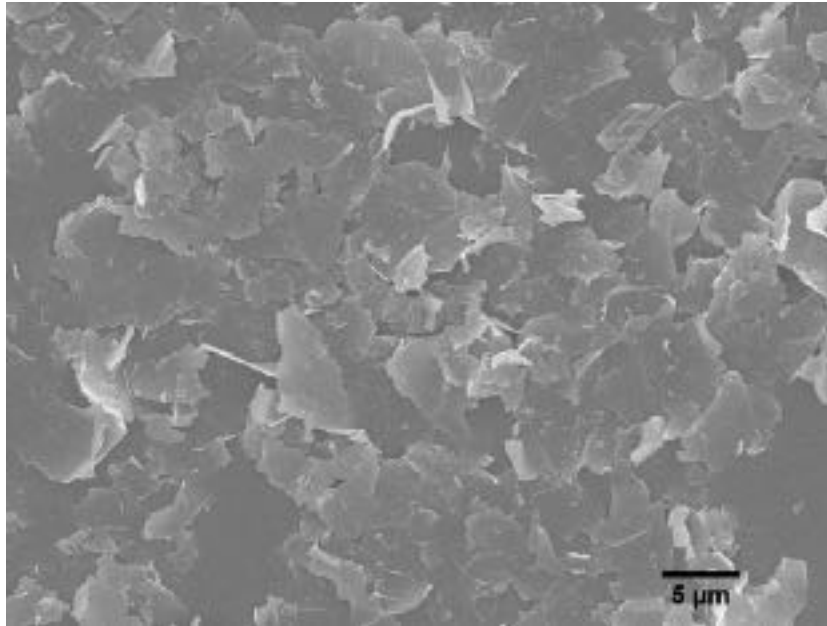


Figure 3.2: SEM image of the as-received GNP

3.2.2. Reaction Synthesis of BNNS and GNP - Spark Plasma Sintering

BCN phase was synthesized using ball milled BNNS and GNP powders by reactive spark plasma sintering method. The amount of mixed powders used for each sintering condition is ~ 3 g. Variable sintering temperature, pressure and holding duration are summarized in Table 3.1. Different parameters were chosen to understand their influence on the BCN phase formation in the compacts by reaction synthesis and their role on the mechanical properties of the synthesized BCN phase. For all the samples, the heating rate of 100 °C/min was used to reach the sintering temperature and holding time. BCN samples of 20 mm diameter and 5 mm thickness were consolidated in argon atmosphere using graphite die and punches.

Table 3.1: Reactive spark plasma sintering conditions for BCN phase

Sample ID	Sintering Temperature (°C)	Sintering Pressure (MPa)	Holding time (min)
BCN-1	1650	50	10
BCN-2	1650	50	30
BCN-3	1750	50	10

3.3. Synthesis of MXene – Hydrofluoric Acid Treatment

MAX phase Ti_2AlC powder was procured from Sandvik Materials Technology, Sweden. The as-received MAX powder showed an irregular particle shape with broad particle size distribution of 100 nm to 20 μm . The MAX powders exhibited lamellar structure with a flake like grains (Fig. 3.3). For MXene synthesis, the as-received Ti_2AlC powder was immersed in 25% hydrofluoric acid (HF) solution for different time intervals (1 h, 2 h, and 4 h) at room temperature [5, 6]. The solution was continuously stirred with a Teflon coated magnetic stirrer at 100 rpm. After HF treatment, powders were washed using de-ionized water and further separated by centrifuge technique. These powders were filtered and dried in the vacuum oven at 80 $^{\circ}C$ for 30 min to 1 h.

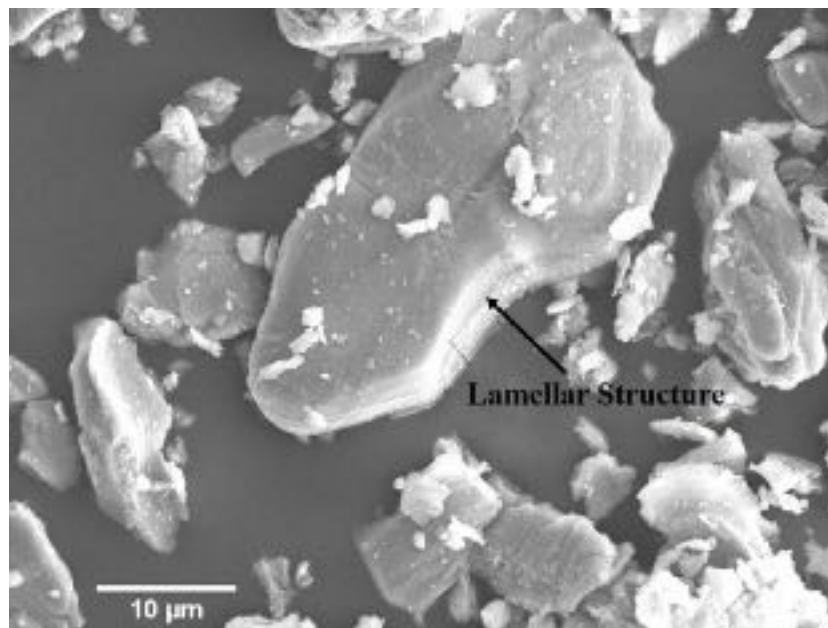


Figure 3.3: SEM image of the as-received MAX (Ti_2AlC) powder

3.4. Structural Characterization

3.4.1. X-ray Diffraction – Phase Analysis

X-ray diffraction (XRD) studies were performed to identify the phases present in the as-received powder (h-BNNS, GNP, MAX), milled powder BCN powders and HF treated MXene powder. Also, the phases present in the spark plasma sintered bulk 2D pellets were

characterized and very important for its property evaluation. The lattice parameters were calculated for the powders and sintered pellets using non-linear least-squares fitting with pseudo Voigt function. XRD was carried out using Siemens D-5000 X-ray diffractometer with Cu K α ($\lambda = 1.542 \text{ \AA}$) radiation. The operating voltage and current were set as 40 kV and 40 mA, respectively. The XRD data were collected in the 2θ range of $10\text{-}90^\circ$, with a scan rate of $0.02^\circ/\text{min}$ and a step size of 0.01° . Using the JCPDS and ICSD standard database, the phases present in the powder and pellet were determined.

3.4.2. Raman Spectroscopy and Fourier Transform Infrared Spectroscopy

Raman spectroscopy studies were performed on the powder and sintered pellets for phase confirmation. Raman spectra shows the type of bonds present in the powder and sintered pellets. Raman measurements were obtained using Ti:Sapphire laser as the excitation source (514 nm) with a power of 18 mW. The model used was 3900S from Spectra Physics, California, USA. The backscattered spectra was detected by holographic imaging spectrograph from Kaiser Optical Systems, Inc (Michigan, USA) equipped with volume transmission grating, charge coupled device detector and holographic notch filter. The Raman spectra were recorded for an exposure time of 300 s with a spectral resolution of 4 cm^{-1} . Similarly for BCN studies, in order to understand the bond formation after sintering, Fourier Transform Infrared Spectroscopy (FTIR, JASCO FT-IR 4100 spectrometer) was used for the analysis.

3.4.3. Crystallographic Texture Analysis

Crystallographic texture studies have garnered significant attention in hexagonal materials over the years. In polycrystalline materials, preferred orientation will have an effect on their physical and mechanical properties. For example are strength, toughness, elastic modulus, electrical and thermal conductivity. Compared to cubic materials, hexagonal based

materials have limited slip systems and activation of twinning [7]. This results in more preferred orientation in hexagonal materials. The crystallographic texture studies were carried out on the top surface and cross-section of monolithic pellets as shown in Figure 3.4. To determine the degree of preferred orientation after sintering. This study was carried out via pole figure measurements using Bruker D8 Discover X-ray diffractometer with Cu K_{α} radiation in Bragg-Brentano geometry and four circle goniometer equipped with automated X-Y-Z movements. The data were collected for 0–360° with a step of 3° in Phi (ϕ) and tilting 0–75° with a step of 3° in the Psi (ψ) range. The measured data were plotted and analyzed using Labotex texture analysis software [8].

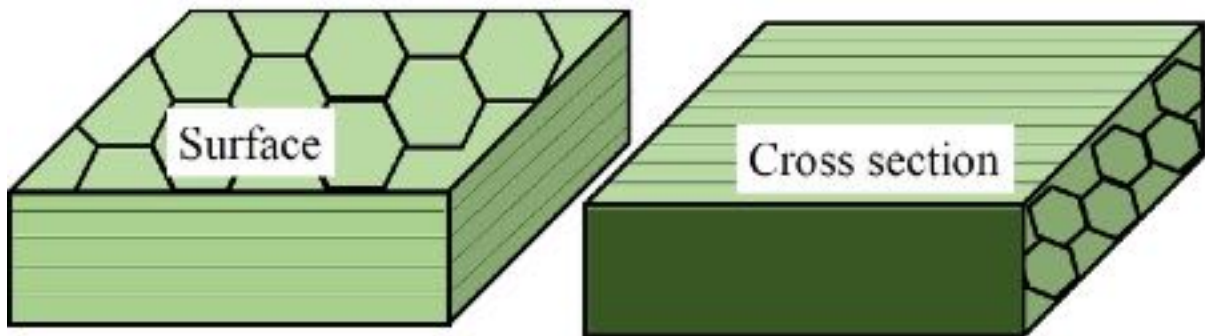


Figure 3.4: Schematic representation of sintered 2D materials, showing the region of interest for texture studies

3.5. Microstructural Characterization

3.5.1. Scanning Electron Microscopy – Fracture Characteristics of Bulk 2D

Field emission scanning electron microscope (FESEM) was used for the microstructural characterization of milled powder BNNS/GNP for BCN synthesis, HF treated MXene powder and sintered pellets. SEM analysis was carried out using JEOL JSM-6330 (JEOL USA, Inc., Peabody, MA) with an operating voltage of 20 kV. Before SEM analysis, samples were sputter coated with gold nanoparticles. Sintered pellets were sectioned using a diamond blade and the sectioned pieces were fractured along the cross-section. The fracture surface of the sintered pellets were observed under SEM to understand the interface of sintered

2D nanosheets, porosity distribution, dense packing and deformation of 2D nanosheets. The elemental analysis of samples were carried out using energy dispersive X-ray spectroscopy (EDS) equipped with SEM.

3.5.2. Transmission Electron Microscopy – Interface Analysis of Bulk 2D Material

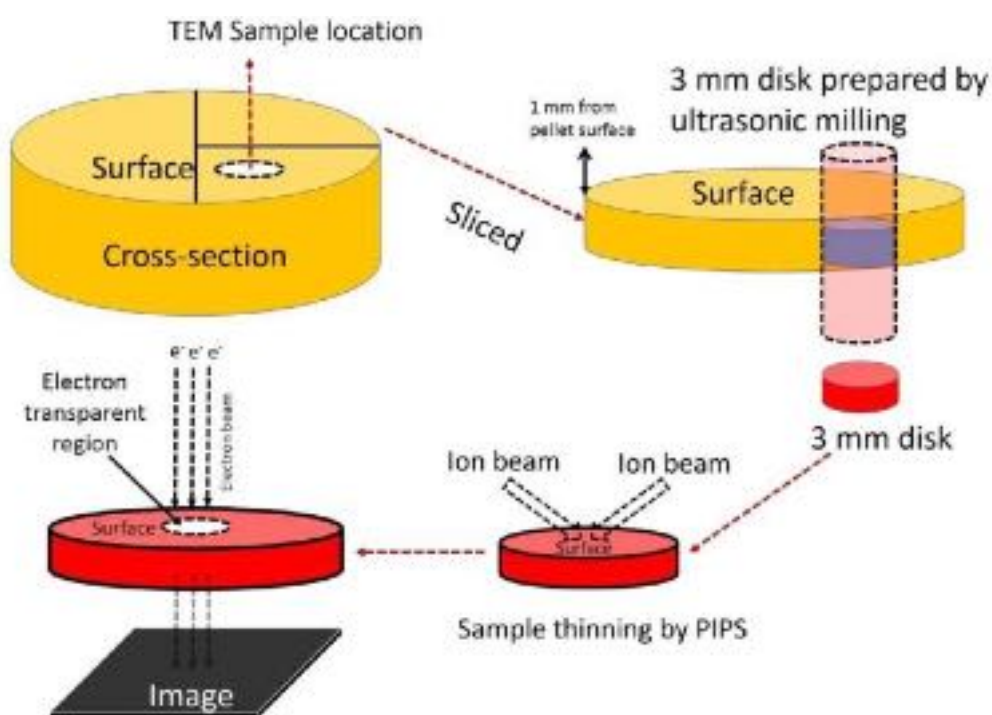


Figure 3.5: Schematic representation of TEM sample preparation of sintered pellet

High resolution transmission electron microscopy (HR-TEM) images along with bright field and dark field imaging experiments of sintered pellets were captured using FEI Tecnai F-30 transmission electron microscope (TEM) equipped with a field emission source at 300 kV operating voltage. HR-TEM image with lattice level resolution was captured to understand the interface of sintered 2D layered materials. The d-spacing (lattice) was measured using the HRTEM images by forward and inverse Fourier transform (FFT & Inverse-FFT) analysis, Gatan, Inc. Digital Micrograph software. The schematic of TEM sample preparation for the sintered pellet is shown in Figure 3.5. A thin sample of 1 mm thickness was sliced from the top surface of the sintered pellet. From this sample, 3 mm disc was prepared by ultrasonic milling.

To achieve the electron transparent region, the sample was milled using precision ion polishing system (PIPS). Before imaging, the electron beam was precisely aligned normal to the thinned sample top surface (basal plane), and then, TEM imaging was carried out.

3.6. Mechanical Properties

3.6.1. Microhardness

Microhardness was measured on the sintered pellets using Vickers microhardness tester at a load of 500 g with a dwell time of 10 s. For BNNS and BCN sintered pellets, the samples were first polished along the top surface and cross-section. The indentations were performed on both the surfaces to compare their effect of orientation on the microhardness values. For each sample, total of 6-8 indentations were performed, where the microhardness value with standard deviations were computed. The microhardness tester used in this study was LECO LM810AT (LECO Corporation, St. Joseph, MI).

3.6.2. Nanoindentation – Hardness and Elastic Modulus

The nanoscale hardness and elastic modulus of BNNS pellet, BCN pellets and HF treated MXene powder were studied by nanoindentation tests. The test were carried out using a Hysitron Triboindenter TI-900 (Hysitron Inc., Minneapolis, MN, USA) with 100 nm Berkovich pyramidal tip. The experiments were performed in the quasi-static indentation mode to measure the elastic modulus and hardness of the polished top surface and cross section of the pellet. During the indentation, the load was increased from 0 to 900 μN in 10 s, with a holding time of 5 s and decreasing the load to 0 N in 10 s. The hardness (H) of the samples was calculated using the equation mentioned below,

$$H = \frac{P_{max}}{A(h_c)} \quad (3.1)$$

where $A(h_c)$ is the area as a function of contact depth measured from tip-area calibration and P_{\max} is the maximum applied load. Standard fused quartz substrate of known modulus (69.6 GPa) was used for tip-area calibration. Using the Oliver-Pharr method, the elastic modulus was computed from the unloading region of the load-displacement curves [9]. Reduced modulus (E_r) of the sample was calculated based on equation 3.2,

$$E_r = \frac{\sqrt{\pi}}{2\sqrt{A(h_c)}} S \quad (3.2)$$

where S is the contact stiffness based on the slope of unloading curve at the maximum load. The sample elastic modulus (E_s) can be calculated using the below equation,

$$\frac{1}{E_r} = \frac{1 - \nu_i^2}{E_i} + \frac{1 - \nu_s^2}{E_s} \quad (3.3)$$

where E_i and ν_i are the elastic modulus (1140 GPa) and Poisson's ratio (0.07) for the indenter, and ν_s is the Poisson's ratio of the sample being indented.

3.6.3. In-situ High Load Indentation – Deformation Behavior of Bulk 2D Material

The in-situ high load indentation tests were carried out using the linear, screw driven micro-load frame (MTI Instruments SEM tester 1000, Albany, NY) as shown in Figure 3.6 [10]. The load capacity of micro-load frame is 4500 N with 0.2 % accuracy and about 20 nm of linear movement resolution. Using MTESTQuattro software (ADMET, Norwood, MA) and an interface, the micro-load frame is controlled. For the high load in-situ indentation studies, the sintered pellets were cut into two pieces. Before indentation, the top-surface and cross-section of the pellet were subjected to ceramographic polishing. The polished sample was loaded across a $1\mu\text{m}$, 120° conospherical diamond tip. This micro-load frame was inserted in a dual-beam focused ion beam/SEM (JEOL JIB-4500) operated in vacuum. Indentation test was performed on the displacement controlled mode at the rate of 0.05 mm/min up to 0.5 mm for loading and the unloading was carried out at the same rate. During testing, the load-

displacement curve was obtained using the MTESTQuattro software and the real time video of the indentations was obtained using SEM. The high resolution real-time imaging with the combination of load-displacement measurements in turn helps to unravel the deformation mechanism of sintered 2D materials.

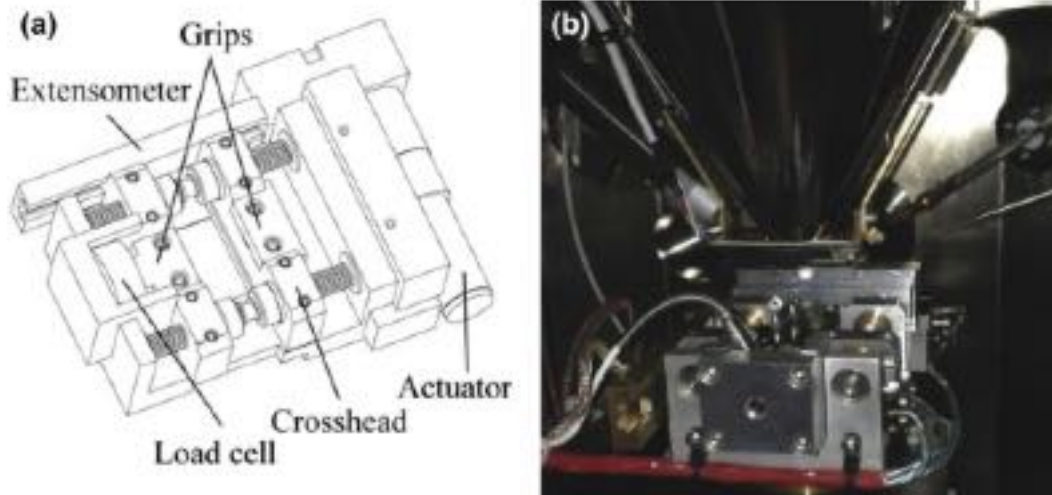


Figure 3.6: In-situ high load indentation micro-load frame (a) Schematic diagram and (b) image of it inside the SEM chamber [10]

3.6.4. Micro- and Nano-scale Damping Studies

Micro-scale (mN load range) damping behavior of 2D materials was studied by stylus impact tests conducted using INNOWEP GmbH Universal Surface Tester (UST, Wurzburg, Germany), to obtain dynamic response for larger displacement range (up to 100 μm). A spherical steel probe of 800 μm diameter was used for these tests. The probe was dropped on the specimen, with the applied loads of 1 and 5 mN. The damped oscillations of the bouncing stylus generates height-time profile (Fig. 3.7) as raw data. This profile is theoretically considered as time-dependent sine wave as shown in equation 3.4,

$$y(t) = Ae^{-\beta t} \sin(\omega t) \quad (3.4)$$

where $y(t)$ is the instantaneous amplitude at a given time t , A is the initial amplitude, β is the damping constant and ω is the angular velocity. From the profile, the logarithmic decrement

will be obtained as the ratio of the heights of two subsequent extrema (y_i and y_{i+1}) as shown by equation 3.5,

$$\Delta = \ln \left| \frac{y_i}{y_{i+1}} \right| \quad (3.5)$$

The loss tangent ($\tan \delta$) will be computed from the logarithmic decrement as shown by equation 3.6,

$$\tan \delta = \frac{\Delta}{\pi} \quad (3.6)$$

Thus the damping characteristics are analyzed by loss tangent ($\tan \delta$), which is a measure of damping capability.

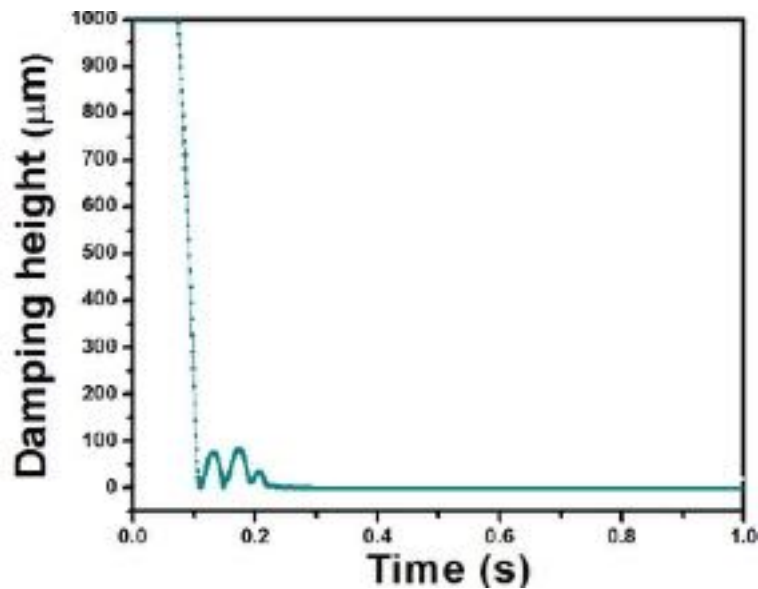


Figure 3.7: Height-time profile of HF treated MXene

Nano-scale dynamic mechanical (nanoDMA, μN load range) tests were carried out on the MAX/ MXene particles using Triboindenter TI 900 (Hysitron Inc., Minneapolis, MN, USA). Berkovich diamond tip of 100 nm diameter was used for this test. For nanoDMA, a dispersion of MAX/ MXene particles in ethanol was produced by ultrasonication. This slurry was poured on the stub. The particle concentration in ethanol was kept very low ($<5 \text{ mg/mL}$) so as to obtain individual particles scattered around the stub as shown in the Figure 3.8. NanoDMA tests were performed on these ‘individual’ MAX/MXene particles. Due to their 2D morphology, the powder particles were oriented such that the indents were made on the top

surface. This was confirmed by optically resolving the particles using an optical microscope attached to the nanoindenter and identified' prior to testing. The nanoDMA tests were conducted for low static loads of 10 and 100 μN , with corresponding dynamic loads of 1 and 10 μN respectively. Damping characteristics are analyzed by determining the loss tangent ($\tan \delta$) over a range of frequencies from 10 Hz to 250 Hz. Also, the nano-dynamic tests were conducted for 50,000 cycles to examine the stability of damping behavior over a large number of loading-unloading cycles. The indentation depths are less than 10% of the particle thickness, as the particles are $\sim 3\text{-}5 \mu\text{m}$ in thickness and $\sim 5\text{-}10 \mu\text{m}$ in width. The average displacements/ depths scale of these nanodynamic tests varies from about 9 nm to about 300 nm.

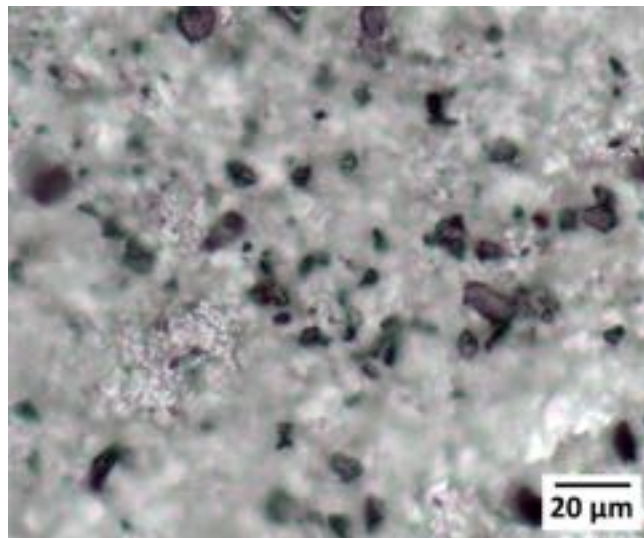


Figure 3.8: Optical image of the dispersed powder particles on the metallic stub. The particles were identified and resolved under the optical microscope to perform dynamic nanoindentations to capture the damping properties of pure MAX and etched particles.

3.7. Tribological Behavior of Bulk 2D Materials

3.7.1. Ball-On-Disk: Macroscale Friction and Wear

Wear and friction properties of the 2D materials were examined using ball-on-disk tribometer, Nanovea, CA. Using Al_2O_3 ball of 3 mm diameter as counterface, the test was performed. During the wear test, the coefficient of friction (COF) was also continuously recorded. After the test, the wear track profiles were scanned by a non-contact optical

profilometer PS50 (Nanovea, CA). Wear depth was obtained from the optical profilometer images using SPIP software (Image Metrology, Denmark). The average cross-section area of the wear track was achieved by integrating the wear track depth profiles using Origin. A total of 5 cross-sectional profiles were used for each calculation. From the 3D wear track profiles, wear volume loss was computed by multiplying the cross-sectional area of the wear track and circumference of the track,

$$\text{Wear volume loss (mm}^3\text{)} = A \times 2\pi R \quad (3.7)$$

Where A - cross-sectional area of the wear track (mm²), R – radius of the wear track (mm). Total of five cross-sections for each 3D wear track profiles were considered for computing average wear volume loss.

3.7.2. Scratch: Micro- and Nano-scale Wear

Micro-scratch tests were performed on top-surface and cross-section of sintered 2D materials using a Universal surface tester (UST) (Innowep GmbH, Wurzburg, Germany) in ramp and constant loading modes. The load applied was in the range between 10-100 mN with a constant velocity of 0.1 mm/sec. Using a 120° diamond tip, 10 mm scratch was made on the polished samples. Scratches were imaged using a field emission scanning electron microscope (JEOL JSM-6330F) to understand the wear mechanism.

Nano-scratch tests were performed on top-surface and cross-section of sintered 2D materials using Hysitron Triboindenter (TI 900 and TI 950, Hysitron Inc., Minneapolis, USA) at a low load of 7000 μN. The scratch tests were conducted using a 60-degree conospherical diamond tip in both constant and ramp loading modes with a scratch length of 10 μm. In-situ scanning probe microscopy was carried out to image the wear tracks, and the images were processed using a 3-D image processing software (SPIP™, version 5.1, Image Metrology A/S, Denmark) and the depth profiles were obtained from these processed images. Wear volume for

nanoscratch was measured (volume of scratch grooves) from the equation mentioned below [11],

$$\text{Wear volume } (\mu\text{m}^3) = \int_{-1/2}^{1/2} A dx \times l \quad (3.8)$$

where 'A' is area of the cross-section (μm^2) and 'l' is the scratch length (μm). Total of five cross-sections for each nanoscratch profiles were considered for computing average wear volume loss.

3.8. References

1. pH Matter LLC. BN-platelets, nano-boron nitride coatings for coating and composites, pH Matter Documentation.
2. xGnP-M_Data-Sheet. 2013, XG Sciences Inc: www.xgsciences.com.
3. W. Choi, I. Lahiri, R. Seelaboyina, Y. Kang. Synthesis of graphene and its applications: a review. *Critical Review in Solid State Material Science* 35 (2010) 52-71.
4. N.A. Kotov. Materials science: Carbon sheet solutions. *Nature* 442 (2006) 254-255.
5. M. Naguib, J. Come, B. Dyatkin, V. Presser, P.L. Taberna, P. Simon, M.W. Barsoum, Y. Gogotsi. MXene: A promising transition metal carbide anode for lithium-ion batteries. *Electrochemistry Communications* 16 (2012) 61-64.
6. J.X. Li, Y.L. Du, C.X. Huo, S. Wang, C. Cui. Thermal stability of two-dimensional Ti_2C nanosheets. *Ceramic International* 41 (2015) 2631-2635.
7. Y.N. Wang, J.C. Huang. Texture analysis in hexagonal materials. *Materials Chemistry and Physics* 81 (2003) 11-26.
8. K. Pawlik, P. Ozga. LaboTex: the texture analysis software. *Göttinger Arb. Geol. Paläontol.*, SB4 (1999).
9. W.C. Oliver, G.M. Pharr. An improved technique for determining hardness and elastic modulus using load and displacement sensing indentation experiments. *Journal of Materials Research* 76 (1992) 1564-1583.
10. C. Rudolf, B. Boesl, A. Agarwal. In situ mechanical testing techniques for real-time materials deformation characterization. *The Journal of the Minerals, Metals and Materials Society* 68 (2016) 136-142.
11. S.R. Bakshi, D. Lahiri, R.R. Patel, A. Agarwal. Nanoscratch behavior of carbon nanotube reinforced aluminum coatings. *Thin Solid Films* 518 (2010) 1703-1711.

Chapter IV: Results and Discussion

4.1. Monolithic BNNS Consolidated by Spark Plasma Sintering

The two-dimensional boron nitride nanosheets were consolidated by spark plasma sintering (SPS) without any sintering aids. The major novelty of this work lies in following facts: (i) using high aspect ratio 2D BNNS as starting powder instead of conventional h-BN which will lead to stronger texture structure and hence, altered mechanical properties and (ii) high load in-situ indentation study inside scanning electron microscope to understand the deformation behavior of highly oriented monolithic 2D BNNS as a function of orientation (parallel and perpendicular) in real time.

4.1.1. As-received BNNS Characterization – Structural and Microstructural Evaluation

The X-ray diffraction (XRD) pattern of the as-received BNNS powder is shown in Figure. 4.1(a). The as-received BNNS powder was indexed to the hexagonal boron nitride (h-BN) structure with space group $P6_3/mmc$ (JCPDS -00-034-0421). The intense diffraction peak of h-BN (002)/(0002) plane was observed along with (100), (101), (102), (004), (110) and (112). The XRD pattern of the as-received powder comprised of B_4C as trace impurity. The lattice parameter calculated from the XRD pattern of the as-received powder was 'a' = 2.506 Å and 'c' = 6.728 Å. Scanning electron microscopy (SEM) was used to observe the BNNS morphology for the as-received powder. As-received powder shows faceted disk shaped 2D BNNS platelets with curved edges (Fig. 4.1(b)). No agglomeration of BNNS powder was observed. The nanosheet size ranges from 100 nm to 3 µm in diameter and the thickness of nanosheet was ~ 40 – 65 nm.

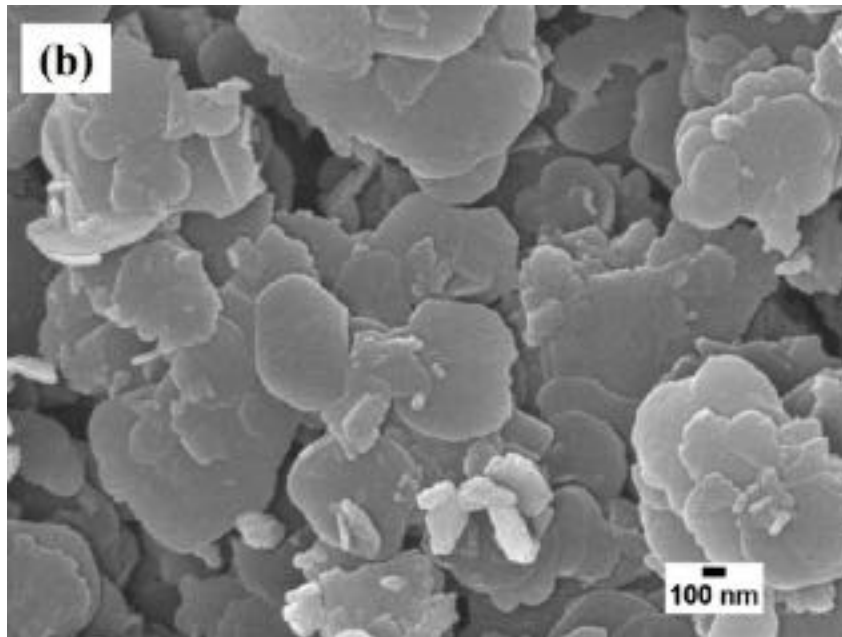
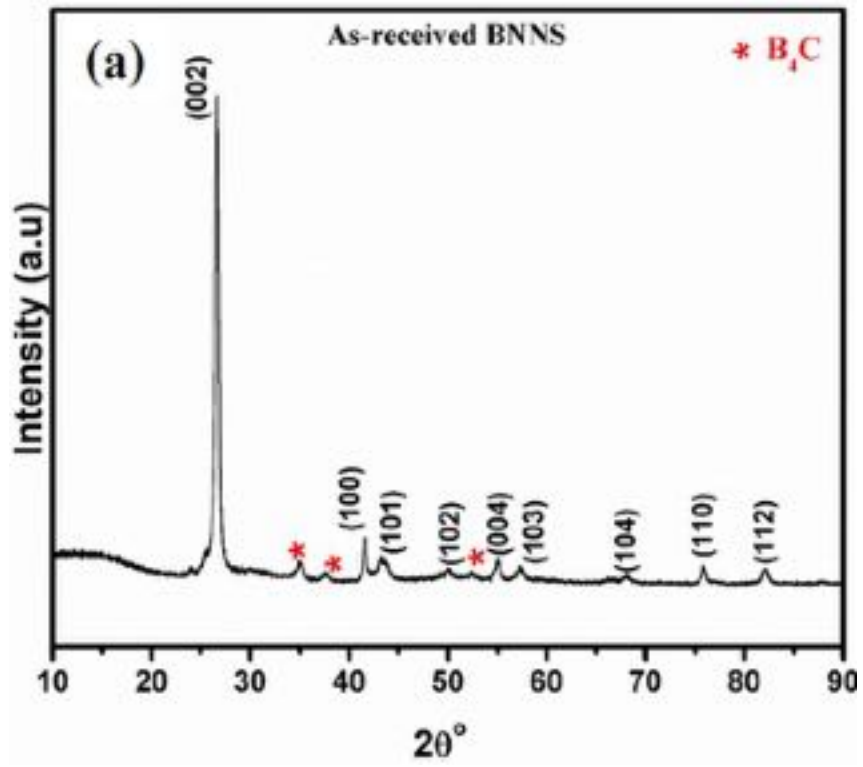


Figure 4.1: (a) X-ray diffraction pattern and (b) SEM image of as-received BNNS powder

4.1.2. Monolithic BNNS – Density, Structural and Microstructural Evaluation

The 2D-BNNS were consolidated in monolithic form using spark plasma sintering at 1650 °C under a pressure of 50 MPa with a heating rate of 100 °C/min and dwell time of 20 minutes. The sintered BNNS pellet was polished to remove the graphite foil, it was circular disk with 20 mm diameter and 3 mm thickness. Using helium pycnometer the density measurements were out for the as-received BNNS powder and the polished monolithic BNNS. The density of as-received BNNS was 2.72 g/cm³, while the density of monolithic BNNS was 2.50 g/cm³. Also the relative density of the monolithic BNNS measured by Archimedes method was ~ 92 %. The densification of h-BNNS is generally difficult due to their structure as they have a strong covalent bonding and anisotropic nature [1].

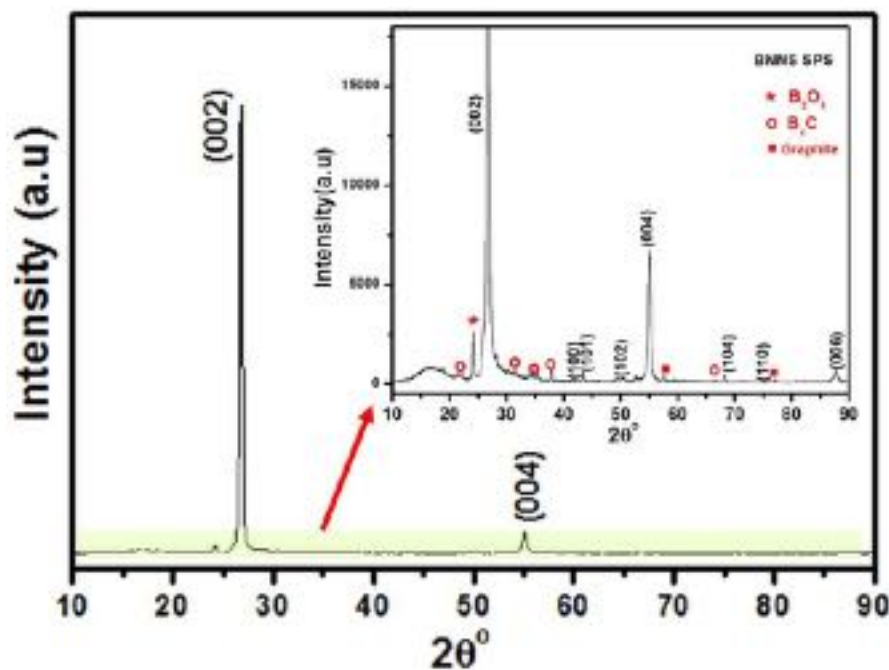


Figure 4.2: X-ray diffraction pattern of sintered BNNS pellet (Inset shows the XRD pattern of sintered BNNS pellet at lower intensity)

After consolidation of BNNS by SPS, monolithic BNNS retained the hexagonal boron nitride structure along with trace of impure phase's boron carbide (B₄C) and B₂O₃ (Fig. 4.2). Lattice parameters of sintered BNNS was calculated from the XRD pattern, where 'c' slightly increased to ~ 6.737 Å and 'a' almost remained the same. Interestingly, the XRD pattern of the

sintered pellet shows an increase in relative intensities of the (002) and (004) planes. This indicates the basal planes preferentially aligned perpendicular to the c-axis, which was also the direction along which the SPS punches applied load during sintering [2].

As a complimentary approach for phase identification, Raman spectroscopy studies were carried out on the sintered pellet in the top surface and cross section as shown in Figure 4.3. The characteristic peak of hexagonal BN was observed for the BNNS SPS pellet on the top surface at $\sim 1366 \text{ cm}^{-1}$ and on the cross-section at $\sim 1366.90 \text{ cm}^{-1}$. This peak position generally correspond to the bulk hexagonal boron nitride. As the layer thickness for the BNNS decreases the peak shifts to slightly higher wavenumber and for the monolayer h-BN, the peak is reported at $\sim 1370 \text{ cm}^{-1}$ [3]. This active Raman peak at $\sim 1366 \text{ cm}^{-1}$ correspond to the high frequency E_{2g} symmetry vibration which occurs because of the in-plane B-N displacements against each other within the basal planes [4, 5]. Figure 4.3 shows that peak intensity of the cross-section decreases significantly compared to the top surface. This is due to the decrease in number of BN layers from which the Raman data was collected along the cross-section compared to the top surface which is more like the bulk h-BN [6, 7]. Raman peak shape for the top surface was slightly narrow and highly symmetric in nature. However, for the cross-section the peak shape was broader and not symmetric. The full width at half maximum (FWHM) for the top surface was $\sim 12 \text{ cm}^{-1}$ and it increased further to $\sim 15 \text{ cm}^{-1}$ for the cross-section. The FWHM corresponding to the E_{2g} band was correlated to the crystal grain size ordering and this band is comparatively less sensitive to strain [5]. Also in general for the crystalline solids, the broadening of Raman peaks is ascribed to scattering which is often related to fine grain size, point defects and stress gradients [8]. From the above understanding, we can conclude the top surface Raman data shows it has larger grain size and lower defect density. Further, the broadening of Raman peak for the cross-section indicate it has poor crystal quality compared to the top surface.

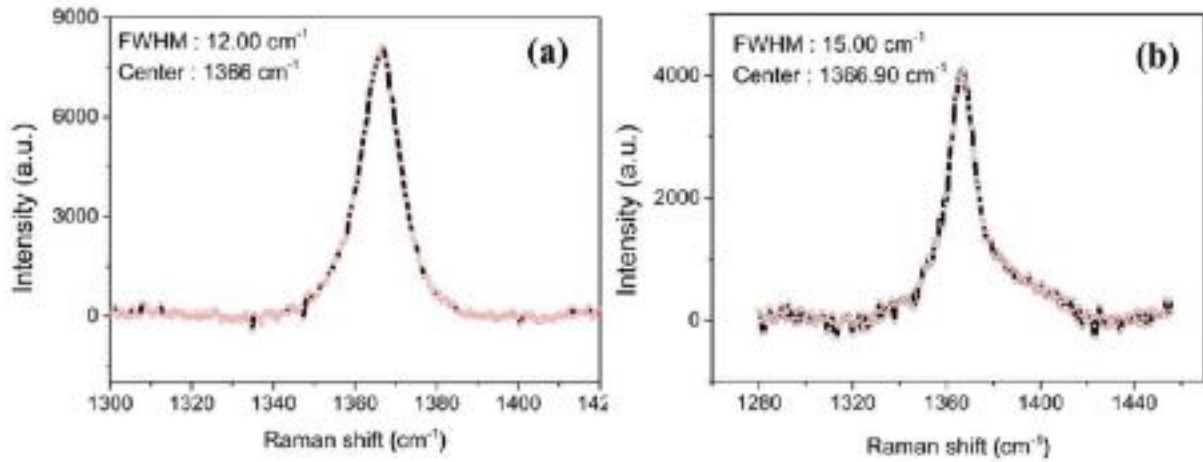


Figure 4.3: Raman spectra of the sintered BNNS from the (a) top surface and (b) cross-section

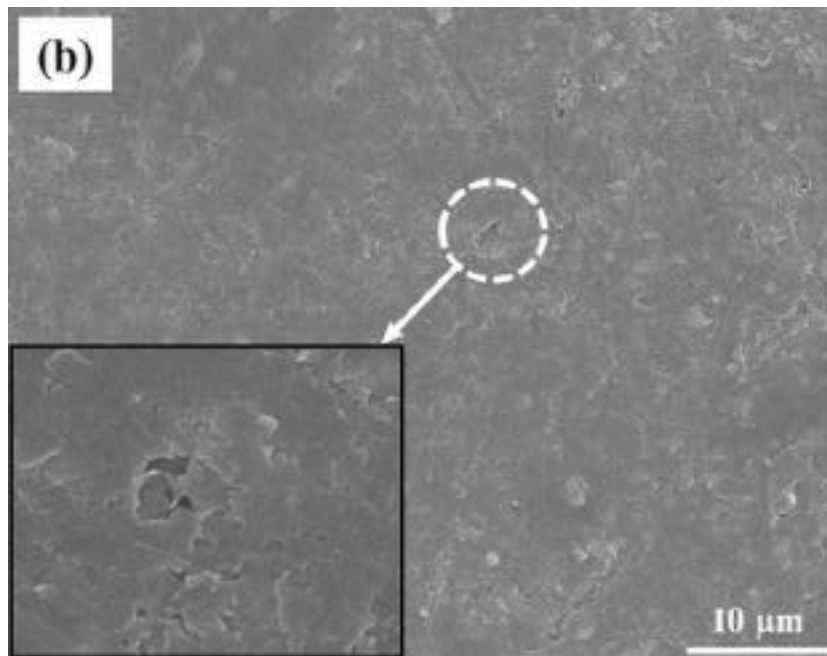


Figure 4.4: SEM image of top surface of sintered BNNS pellet

The microstructure of the polished top surface for the monolithic BNNS pellet was observed using SEM as shown in Figure 4.4. Dense region on the top surface was observed with some fine surface pores observed between the overlapped sintered nanosheets. Microstructure of the sintered BNNS pellet was also studied using high resolution transmission electron microscope (HR-TEM). BNNS sintered pellet surface was imaged along the direction, normal to the basal plane (c-axis was parallel to the electron beam). Bright field TEM image

revealed the microstructure of sintered BNNS with crystalline grains varying in size from 100 nm to 2 μm (Fig. 4.5(a)). Figure 4.5(b) display the high density of multiple twin lamellae present within the grains as indicated by arrowheads. High resolution TEM image displays lattice planes as shown in Figure 4.5(c-d). The two lattice planes with d-spacing of 2.17 \AA each were observed. From the JCPDS file of hexagonal BN, the measured interplanar spacing was verified and this is in good agreement with h-BN ($1\bar{1}0$) and (010) planes, respectively. Additionally, the angle between the measured (hkl) planes with respect to the basal plane can be inferred. As a result, the angle between (0002) vs ($1\bar{1}0$) and (0002) vs (010) was 90° . Further, these two lattice planes ($1\bar{1}0$) and (010) are at an angle of 120° with respect to each other. The Fast Fourier Transform generated diffraction patterns from the HR-TEM image displays a set of hexagonal spots (inset in Figure 4.5(c-d)). Sharp diffraction spots indicate the highly crystalline nature of sintered BNNS. Streaked reflections were also observed in the diffraction, which is related to the basal plane defects such as stacking faults, twinning or Frank dislocations [9, 10]. Twinning is one of the common defects observed in h-BN. Twinning could possibly occur due to the deformation of h-BNNS during sintering at high temperature and pressure. Typically, stresses developed because of the imbalance in the orientation of planes are relieved by slip. However, hexagonal system have scarcity of slip systems and consequently, the stresses were relieved by the twin formation. This corroborates the presence of twin features observed in the BNNS pellet. The deformation twin elements commonly reported in literature for hexagonal boron nitride are (0002) twinning plane and $[11\bar{2}0]$ twinning direction [10], which was in agreement with our observations.

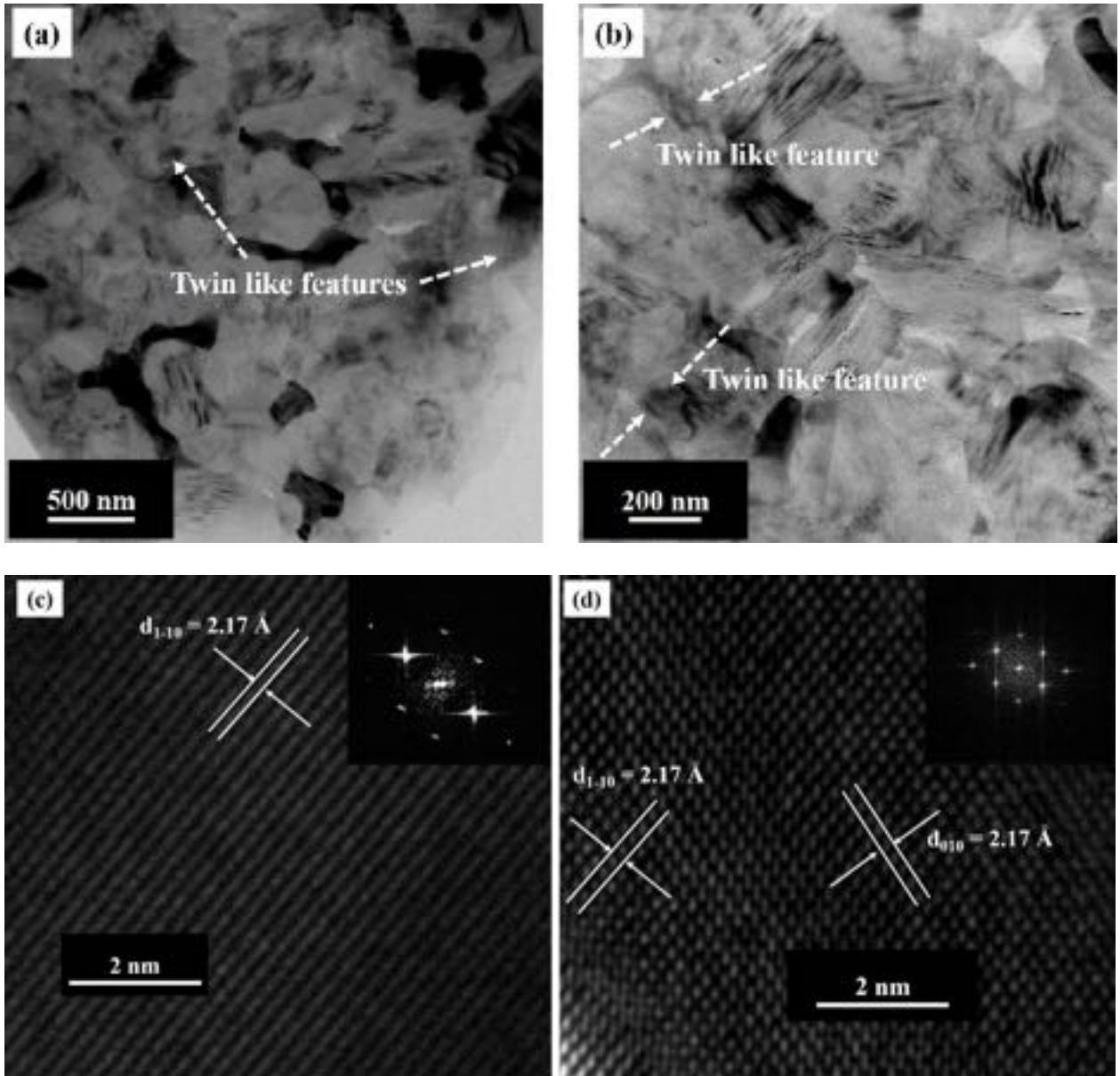


Figure 4.5: HRTEM image of the sintered BNNS showing (a-b) bright field image showing nano-sized grains and twins, (c-d) lattice planes with the inset showing corresponding diffraction pattern

4.1.3. Fracture Mechanism of Monolithic BNNS

SEM images of the fractured surface for the BNNS SPS pellet are shown in Figure 4.6(a-b). The fracture surface of the sample indicates thick densely packed BNNS layers with interlayer gap (Fig. 4.6(a)), which restricted the overall densification to 92%. Also, it is clearly observed that BNNS are arranged in the lamellar structure and highly aligned in one direction (Fig. 4.6(a)). This microstructure clearly supports the X-ray diffraction result of preferred

orientation in the sintered pellet, where the platelets are oriented perpendicular with respect to the loading direction. The edges of the fractured layers display zig-zag nature as shown in Figure 4.6(b). Zig-zag nature of fracture surface indicates, the crack propagated more along the sheet edges and not through the sheets. This asserts the strong bonding nature within the sheets and relatively weaker bonding between the sheet edges [11].

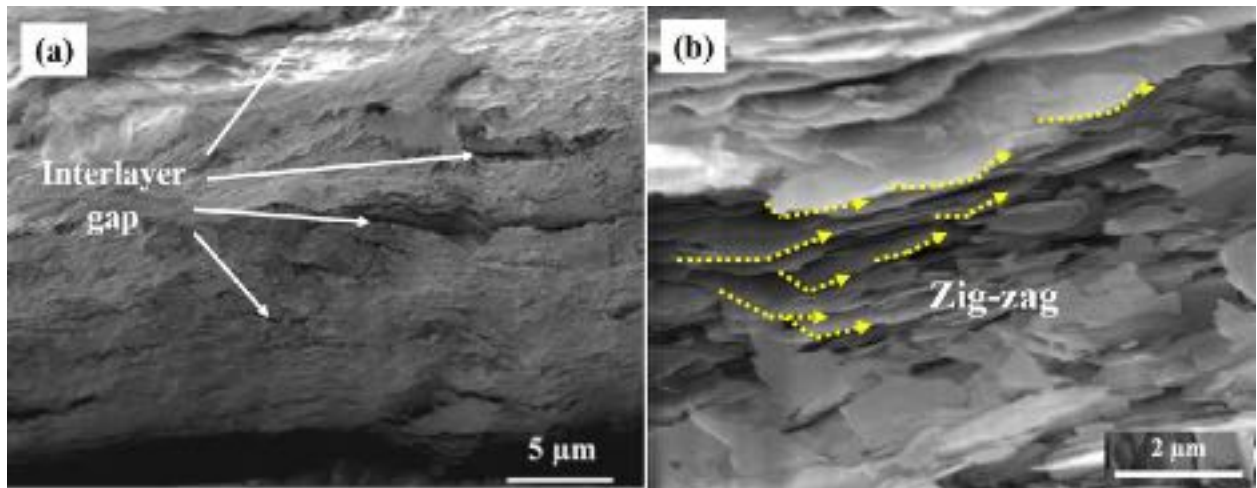


Figure 4.6: SEM images of BNNS pellet (a) fractured surface indicating the lamellar structure and (b) zig-zag fractured surface (yellow dotted arrows indicate the zig-zag edges)

4.1.4. Effect of Texture Orientation of Spark Plasma Sintered BNNS

The X-ray diffraction study on the top surface of the sintered pellet displayed the preferred orientation of the basal plane (0002). Further to understand the orientation in the BNNS sintered pellet along the top surface and cross-section, texture studies were carried out using pole-figure measurements. The pole figures of the top surface are shown in Figure 4.7. Texture analysis clearly show the grains were preferentially aligned along the (0002) basal planes on the top surface of the sintered pellet. Because, at the center of (0002) basal plane pole figure, it displayed concentrated concentric shapes with stronger intensity. The presence of other orientations in the top surface was almost negligible because the pole figures for the $(11\bar{2}0)$ and $(01\bar{1}1)$ planes displayed no intensity at the center. So, the top surface texture results clearly explain the c-axis was oriented in the direction parallel to the loading direction (during

SPS) and ordering of the nanosheets perpendicular to the loading direction. Also, the basal plane $\{0001\}$ texture is most commonly observed in the hexagonal materials [12].

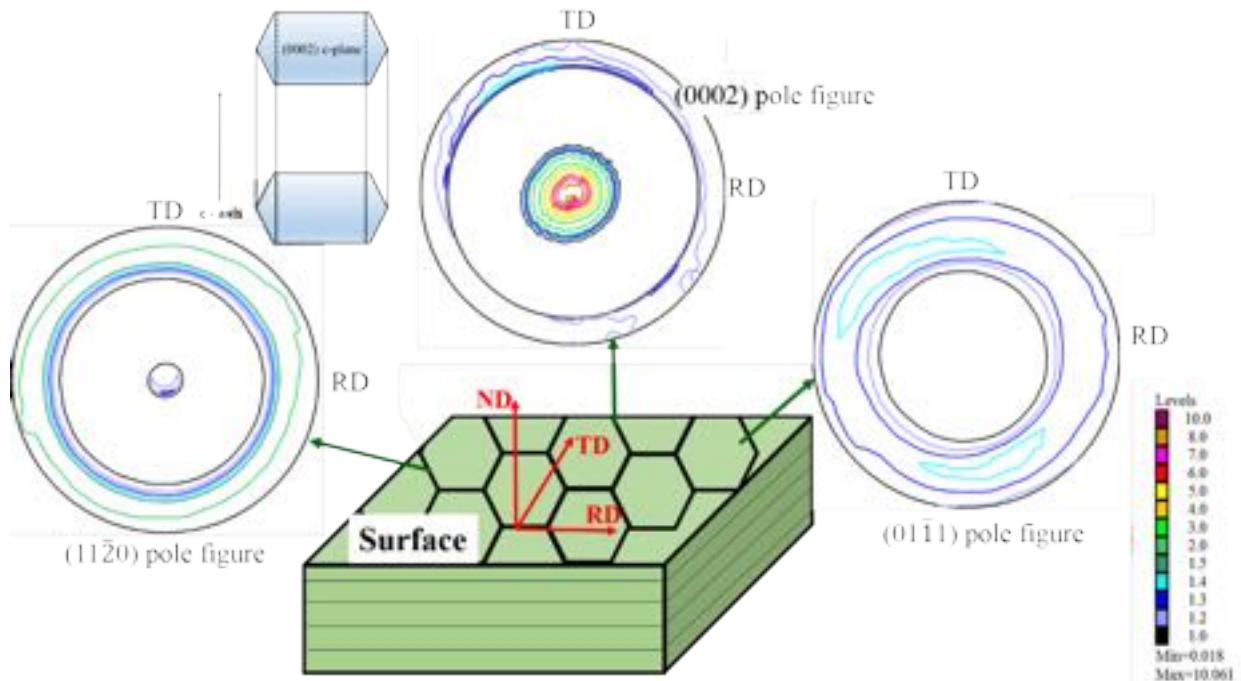


Figure 4.7: Schematic drawing of the sintered BNNS SPS pellet top surface indicating the region of texture studies along with the pole figures of (0002) plane, $(11\bar{2}0)$ plane and $(01\bar{1}1)$ plane. The directions with reference to sample coordinates are defined as normal direction (ND, normal to the sample surface), transverse direction (TD, Y-axis) and reference direction (RD, X-axis)

For the cross-section surface, the pole figures are displayed in Figure 4.8. Along the cross-section of the pellet, a relatively weaker texture was observed. The pole figures of $(11\bar{2}0)$ and $(01\bar{1}1)$ planes showed isolines at the center with less relative intensities, suggesting the preferred orientation is along the prismatic $(11\bar{2}0)$ and pyramidal $(01\bar{1}1)$ planes. There was no trace of texture along the basal planes as there were no isolines observed at the center of (0002) pole figure of the cross-section. Therefore, the texture studies of the sintered pellet display a preferred orientation of the basal plane (0002) perpendicular to the loading direction during sintering. The plausible mechanism for the texture in sintered BNNS is attributed to the uniaxial pressure in the pressing direction and to accommodate this axial strain, the high aspect ratio

nanosheets would have resulted in rotation with basal planes aligned perpendicular to the loading direction.

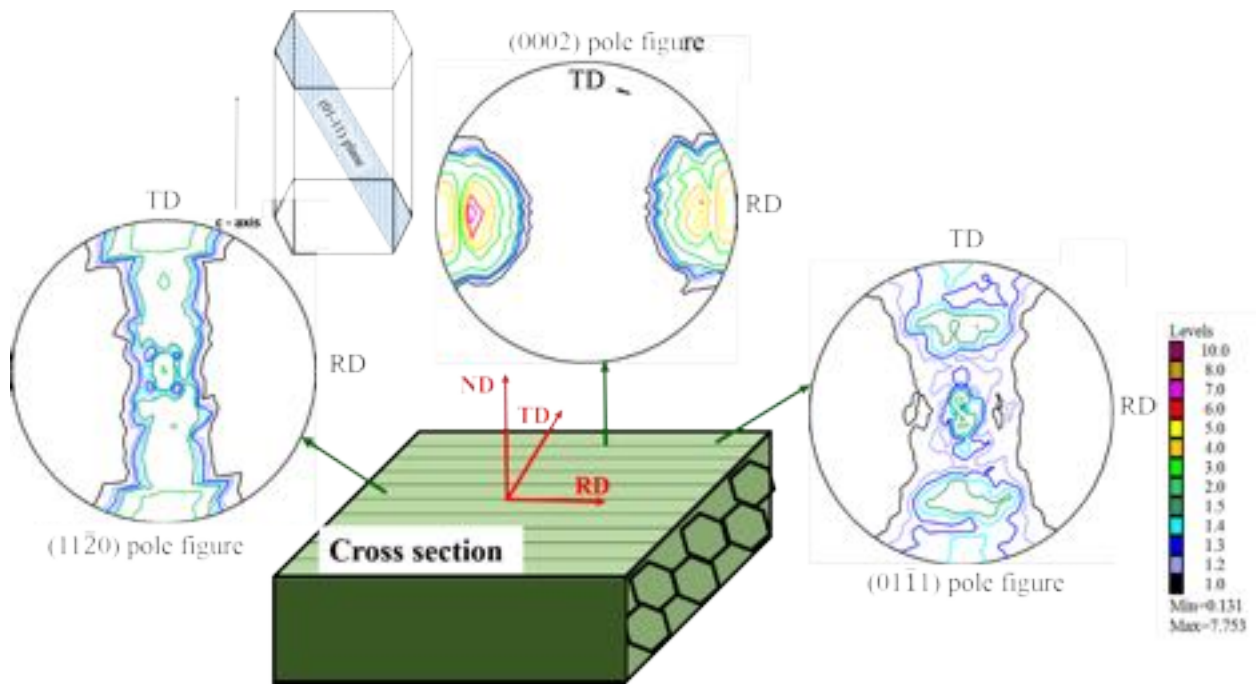


Figure 4.8: Schematic drawing of the sintered BNNS SPS pellet cross-section indicating the region of texture studies along with the pole figures of (0002) plane, $(11\bar{2}0)$ plane and $(01\bar{1}1)$ plane. The directions with reference to sample coordinates are defined as normal direction (ND, normal to the sample surface), transverse direction (TD, Y-axis) and reference direction (RD, X-axis)

4.1.5. Mechanical Properties of Monolithic BNNS

4.1.5.1. Microhardness of Monolithic BNNS

The microhardness of the sintered BNNS pellet was measured using Vickers hardness method. Five indentations were made on the top surface and cross-section of the sintered BNNS pellet to obtain the average microhardness. The microhardness of the top surface is 0.49 ± 0.02 GPa and for the cross-section is 0.28 ± 0.03 GPa. The hardness of the top surface was 74% higher than cross-section due to their strong covalent bonding nature between the boron and nitrogen atoms within the plane along the top surface [13].

4.1.5.2. Nanomechanical Properties: Elastic Modulus and Hardness of Monolithic BNNS

Using nanoindentation, the elastic modulus and hardness of the BNNS SPS pellet was measured. Figure 4.9 shows the typical load vs displacement curves of the top surface and cross-section for the pellet obtained by the nanoindentation test. From the test, the reduced elastic modulus (E_r) of the BNNS is obtained and from this, the sample elastic modulus (E_s) can be calculated using the below equation,

$$\frac{1}{E_r} = \frac{1 - \nu_i^2}{E_i} + \frac{1 - \nu_s^2}{E_s} \quad (4.1)$$

Where E_i and ν_i are the elastic modulus (1140 GPa) and Poisson's ratio (0.07) for the indenter. From the literature, BN nanosheet Poisson's ratio is 0.211 [14]. The top surface elastic modulus of the BNNS pellet is 28.49 ± 5 GPa and hardness is 1.15 ± 0.17 GPa. For the cross-section, the measured elastic modulus is 40.79 ± 11.09 GPa and hardness is 0.609 ± 0.12 GPa. For the top surface, low indentation depth was observed compared to the cross section indent. The cross-section has higher elastic modulus compared to the top surface because of the high in-plane properties of the BNNS [13]. Also, the layered structure of sintered BNNS pellet contribute further to the in plane property and this in turn results in high elastic modulus along the cross-section. Lower elastic modulus was observed for the top surface due to the out of plane strength with respect to the BNNS. The hardness on the top surface was high because of the preferred orientation of the basal planes and the strong bonding nature within the planes. This strong bonding nature results in resistance to deformation and in turn increases the hardness along the top surface. The weak Van der Waals force between the hexagonal layers results in low hardness along the cross-section of sintered BNNS pellet, because this weak force will result in cracking and fracturing between the layers.

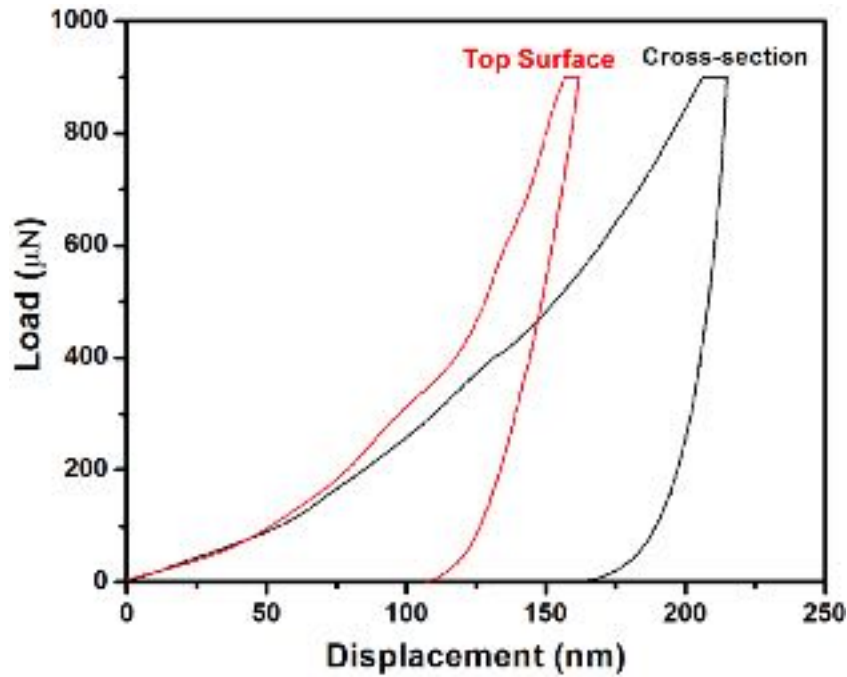


Figure 4.9: Load vs displacement curve of nanoindentations performed on the polished top surface and cross-section of sintered BNNS pellet

4.1.6. Tribological Behavior of Monolithic BNNS

Ball on disk tribometer was used to determine the room temperature coefficient of friction (COF) for the sintered BNNS pellet. Figure 4.10 shows the room temperature COF at 3 N load for a track radius of 2 mm. The wear test was carried on the top surface of the polished pellet. The average COF for the 2 mm track is 0.145. Using the optical profilometer, the track depths were measured from the optical profiles and the track depth for 2 mm track radius is 45 μm . To elucidate the wear mechanism at room temperature, the wear tracks were observed using SEM. Figure 4.11(a) shows the sliding direction for the 3 mm track radius. Due to the layered nature of BNNS, very smooth surface is observed mostly on the wear track. This could be attributed to the slipping of the layered nanosheets due to the weak van der Waals bond between the layers and this resulted in a lower COF [15]. In the edges of the wear track, layers of sintered BNNS were observed in steps as displayed by Figure 4.11(b). Welding of the BN nanosheets were also observed in the wear track. Also, some loosely agglomerated BN nanosheets and pits were formed on the smooth surface of the wear track as shown in Figure

4.11(c). It could be caused due to the uneven loading on the surface and thus resulting in the stress concentration at the edges of the wear track. In certain locations of the wear track, the bending of the nanosheets were observed as shown in Figure 4.11(d).

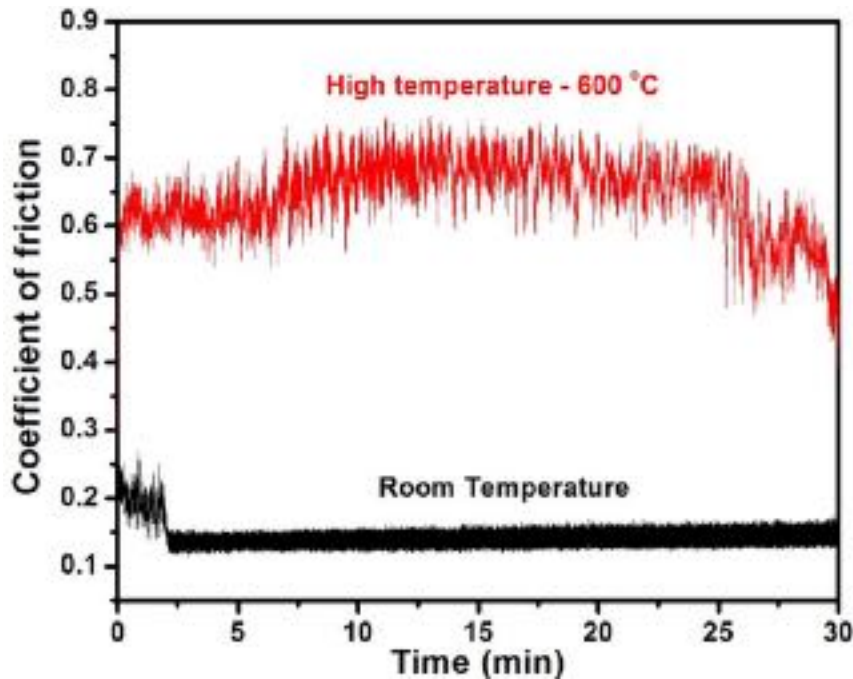


Figure 4.10: Coefficient of friction at 3 N load for the BNNS SPS pellet at room temperature and high temperature for a track radius of 2 mm

To understand the wear nature of the sintered BNNS at high temperature and the BNNS can withstand at high temperature compared to graphene, tribology studies were carried out at a selected high temperature based on the outcome of thermogravimetric (TG) studies for as-received BNNS powders. The weight loss was observed to be minimum around ~450 to 800 °C and this indicated the BNNS are more stable in this temperature region. After 800 °C, significant increase in weight was observed, due to the oxidation of BNNS. As a result, boron oxide would be formed on the surface [16]. Based on the TG results, ~ 600 °C was identified to be the ideal temperature to conduct the high temperature wear test. The high temperature COF at 3 N load for a track radius of 2 mm is shown in Figure 4.10. The average COF for the 2 mm track is 0.646. The coefficient of friction has increased significantly for high temperature wear test compared to the room temperature COF. During the high temperature wear test, the

adhesion of BNNS on to the surface of alumina ball could have resulted an increase in the coefficient of friction. The track depth for the high temperature wear tracks were estimated from the optical profiles and the track depth for the 2 mm track radius is $\sim 175 \mu\text{m}$.

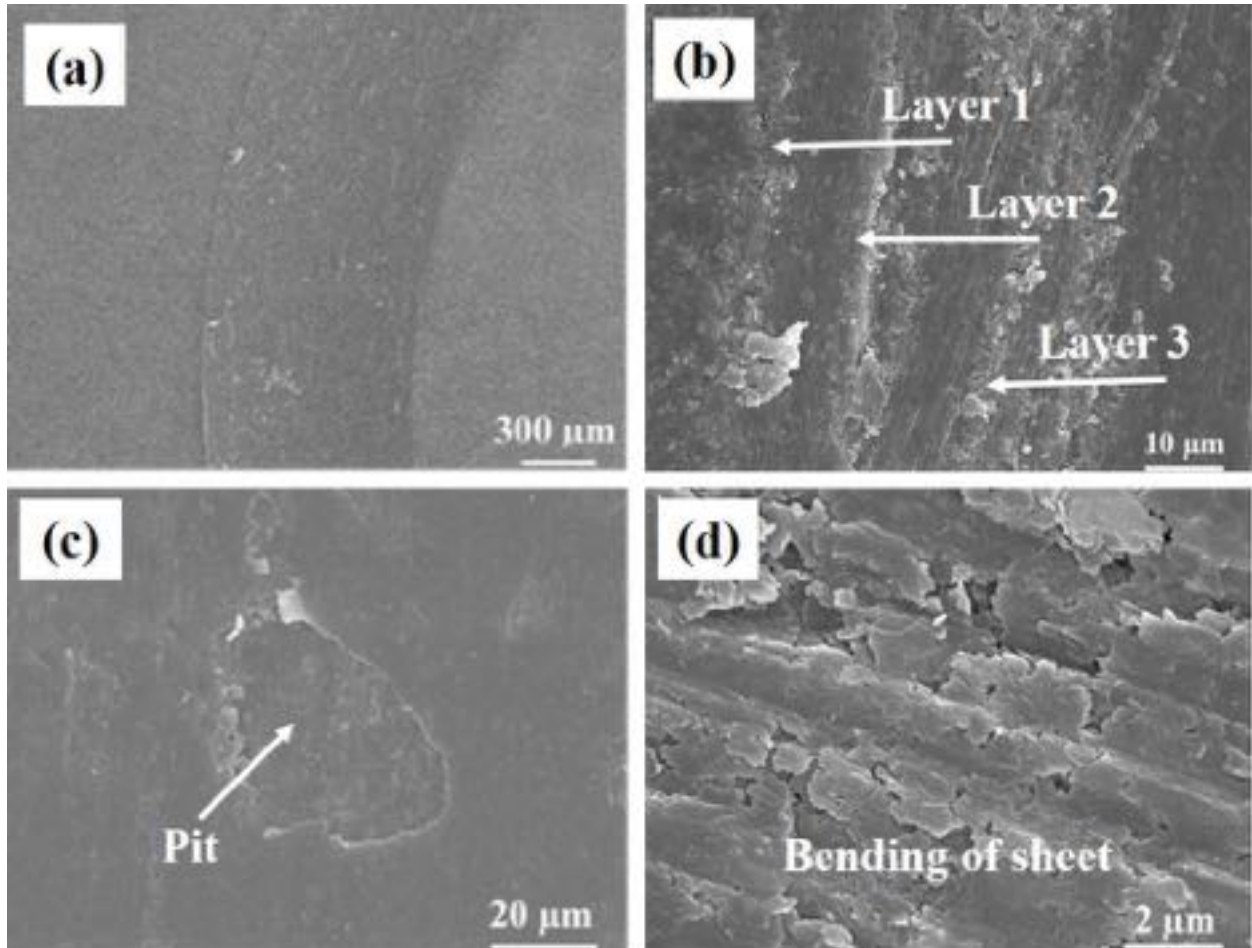


Figure 4.11: SEM images of the wear track for the room temperature test shows (a) direction of the wear track, (b) multiple BNNS layer at the edges of wear track, (c) pit formation and (d) bending of nanosheets

Figure 4.12 shows the surface of the wear track observed using SEM for the high temperature wear test BNNS pellet. For the high temperature studies, the 2 mm track radius test was performed first. The surface of the wear track was extremely smooth as shown in Figure 4.11(a). At certain places of the wear track, pile up of the BNNS wear debris was observed (Figure 4.12(b)). Delamination of the sintered layers were observed in the wear track. Due to this, the crack formation was identified on the delaminated surface as shown in Figure 4.12(c). Also, the adhesion of BNNS layers were observed in the wear track. On comparing

the room temperature and high temperature coefficient of friction, the high temperature COE has increased compared to the room temperature COE. The major observation in the high temperature wear test is more delaminated nanosheets were observed in the wear track compared to the low temperature wear track. So, these delaminated nanosheets would have adhered to alumina ball surface and resulted an increase in the coefficient of friction at high temperature.

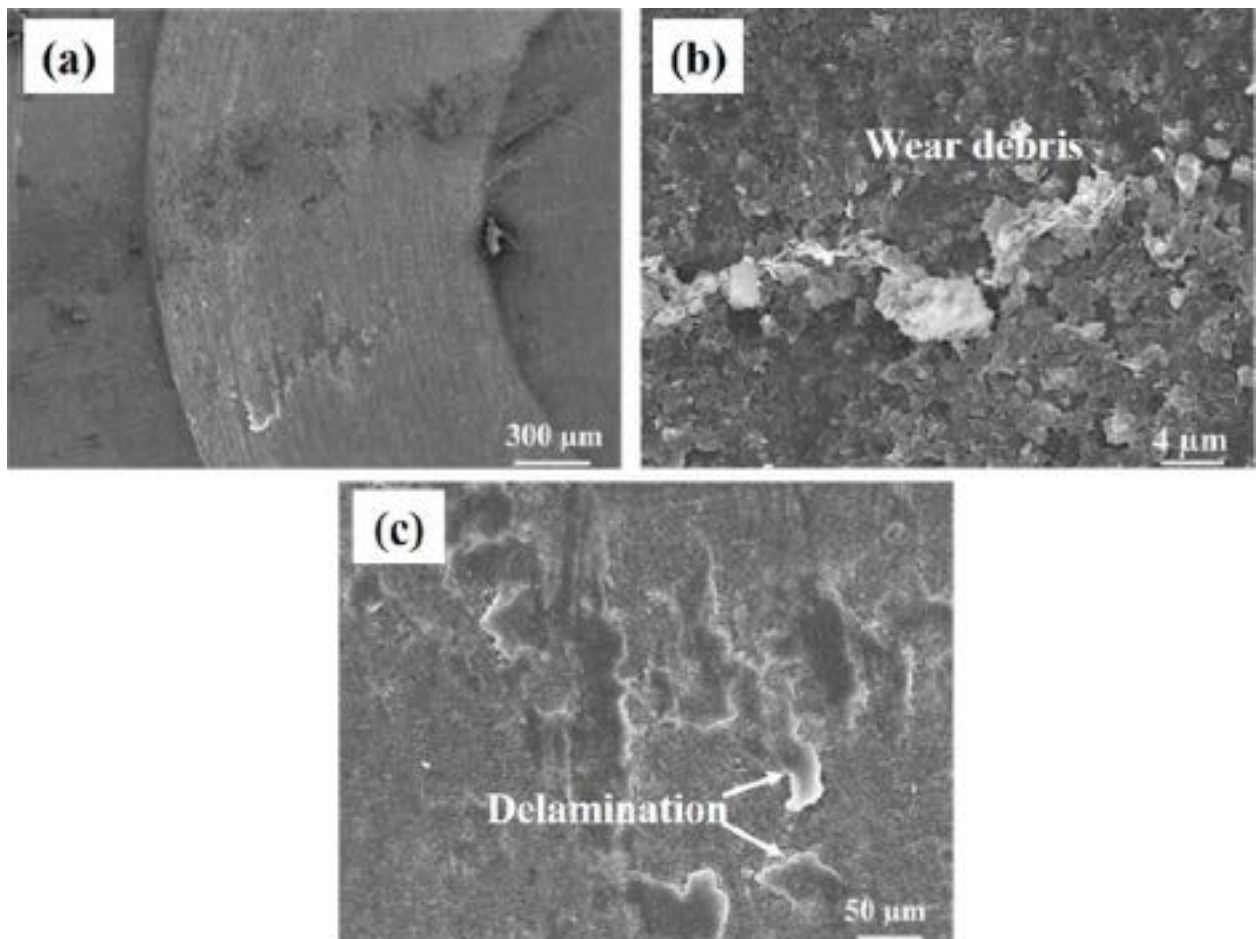


Figure 4.12: SEM images of the wear track at the high temperature indicating (a) smooth wear track, (b) material pile up and (c) delamination and crack propagation

4.1.7. High Load In-situ Indentation Behavior of Monolithic BNNS

In-situ indentation on the top surface and cross-section of the sintered and polished BNNS pellet was carried out using displacement controlled mode with maximum displacement of 0.5 mm. The preferred orientation of the BNNS after sintering has a significant role in the mechanical properties which is apparent from the load-displacement curves. To reach a fixed

displacement of 0.5 mm, the maximum load required was ~370.3 N for top surface (Fig. 4.13(a)) whereas cross-section required a lower load of ~231.3 N (Fig. 4.14(a)). This was in accordance with the higher nanohardness (1.15 ± 0.17 GPa) obtained for top surface from nanoindentation as compared to cross-sectional surface (0.61 ± 0.12 GPa).

4.1.7.1. Deformation along Monolithic BNNS Top Surface

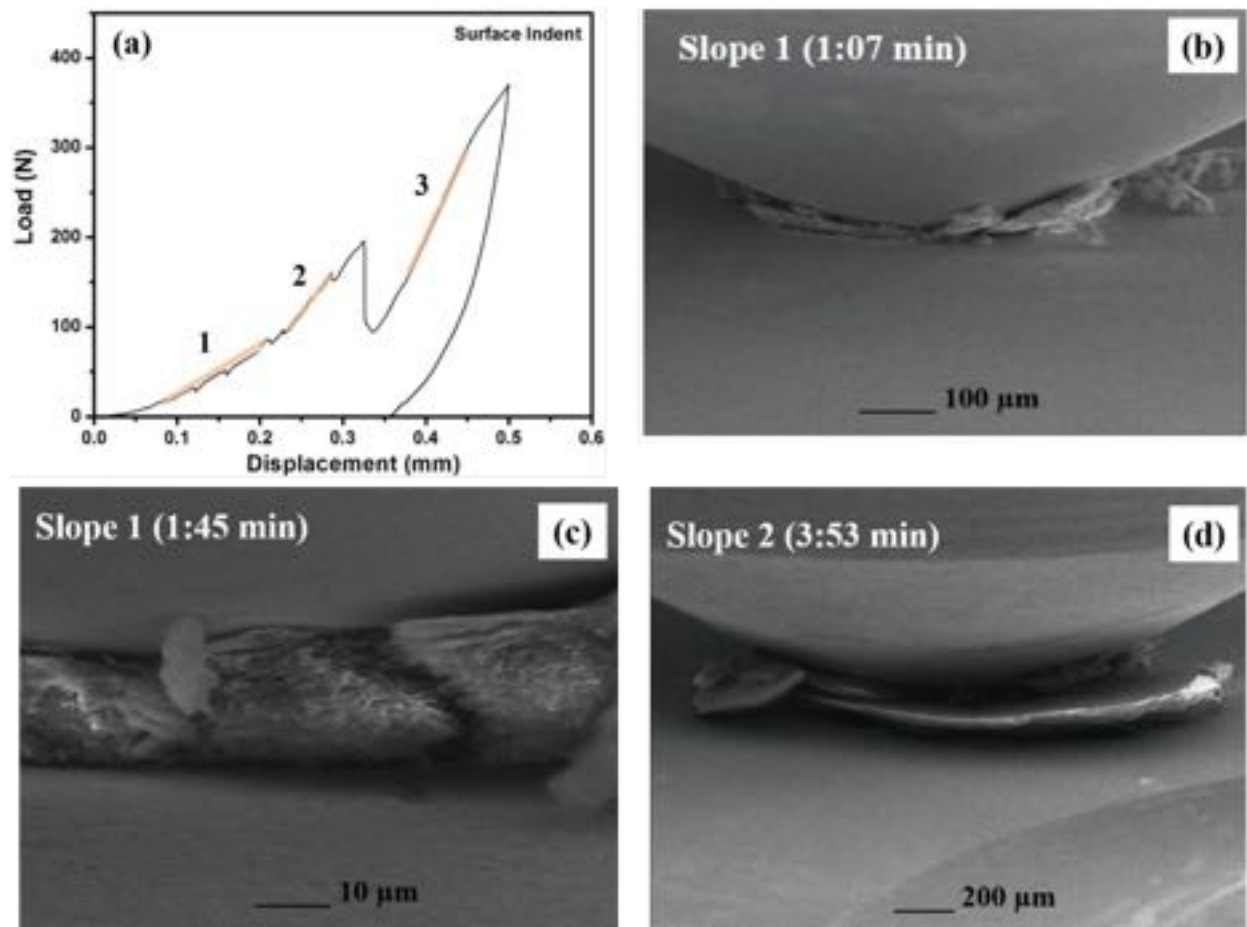


Figure 4.13: Top surface indent load-displacement curve and SEM images of deformation event at different stage of loading

The load-displacement curve for the top surface high load indent is shown in Figure 4.13(a). From the loading curve, three significant slopes were observed. For each slope, the corresponding normalized associated energy was computed by extrapolating the displacement range from 0 mm to 0.5 mm (i.e. total displacement). The work of indentation can be related

to the normalized associated energy, when the slope remains uniform over the complete displacement range. The dominant deformation mechanism can be identified by comparing the normalized energy dissipated from each region and observing the deformation phenomenon at that instant from the video. Small drops in load were also observed in the slope 1 and slope 2 regions. Using the recorded real time video, the slope, time interval from the video, normalized associated energy for each slope and the corresponding deformation mechanism are listed in Table 4.1 for the top surface indent.

Table 4.1: Deformation mechanism observed during top surface indentation with respect to the slope and the corresponding time duration from the video

Slope	Time range in video (min)	Normalized associated energy (mJ)	Specific Time in Video (min)	Deformation mechanism
1	0.05 – 3.38	54.83	0.05	(i) Compression of the sheets
			0.07-3.38	(ii) Delamination of the sintered sheets (Fig. 4.13(b))
			0.32	(iii) Bending of delaminated sheets
			1.10	(iv) Pile up
			1.42	(v) Fracture of delaminated sheets (Fig. 4.13(c))
			2.30	(vi) Sliding
2	3.40 – 4.50	110.85	-	Delamination and fracture of underlying new surface (Fig. 4.13(d))
3	5.05 – 6.48	205.9	-	Mechanisms repeats along the depth with crack observed at the bottom (Fig. 4.14(d))

For the slope 1 region, in the beginning of indentation, compression of sheets was observed. Gradually, delamination of the sheets near the indenter surface (Fig. 4.13(b)), bending and sliding of these delaminated sheets were observed. Pile up of these delaminated sheets occurred. In the middle of slope 1 region, fracture of the delaminated sheet (Fig. 4.13(c)) and sliding of the sheets were observed. As the displacement proceeds further (at the end of slope 1), next layer of sheets was delaminated and the pile up of these sheets occurred. In the whole slope 1 region, there are small drops in load observed at different displacement points and this is related to the layered breakage in the BNNS SPS pellet. The fracture surface of sintered BNNS SPS pellet (Fig. 4.6(c)) clearly reveals the region of dense layers followed by lamellar voids at different locations. These lamellar voids would have resulted in the drop in load as the indentation progressed. The intermediate region between each drop is attributed to delamination of sheets and material pile up. During the slope 2, a big wedge of new surface of layered sheet was delaminated, leading to fracture as shown in Figure 4.13(d). For the slope 3, the tip was engaged and the loading was happening continuously. During this time, the mechanisms repeats along the depth where there was no deformation behavior observed in the video. But from the SEM indentation images after the tip removal, crack propagation was observed at the bottom of fractured indent surface as shown in Figure 4.13(d). The normalized energy calculated for the slopes in top surface showed a two-fold increase in each slope region. Greatest energy dissipation was observed in slope 3 region (205.9 mJ), where it was about 275% and 86% greater than slope 1 and 2 respectively. The deformation mechanism in slope 3 remains to be the dominant deformation mechanism along the top surface.

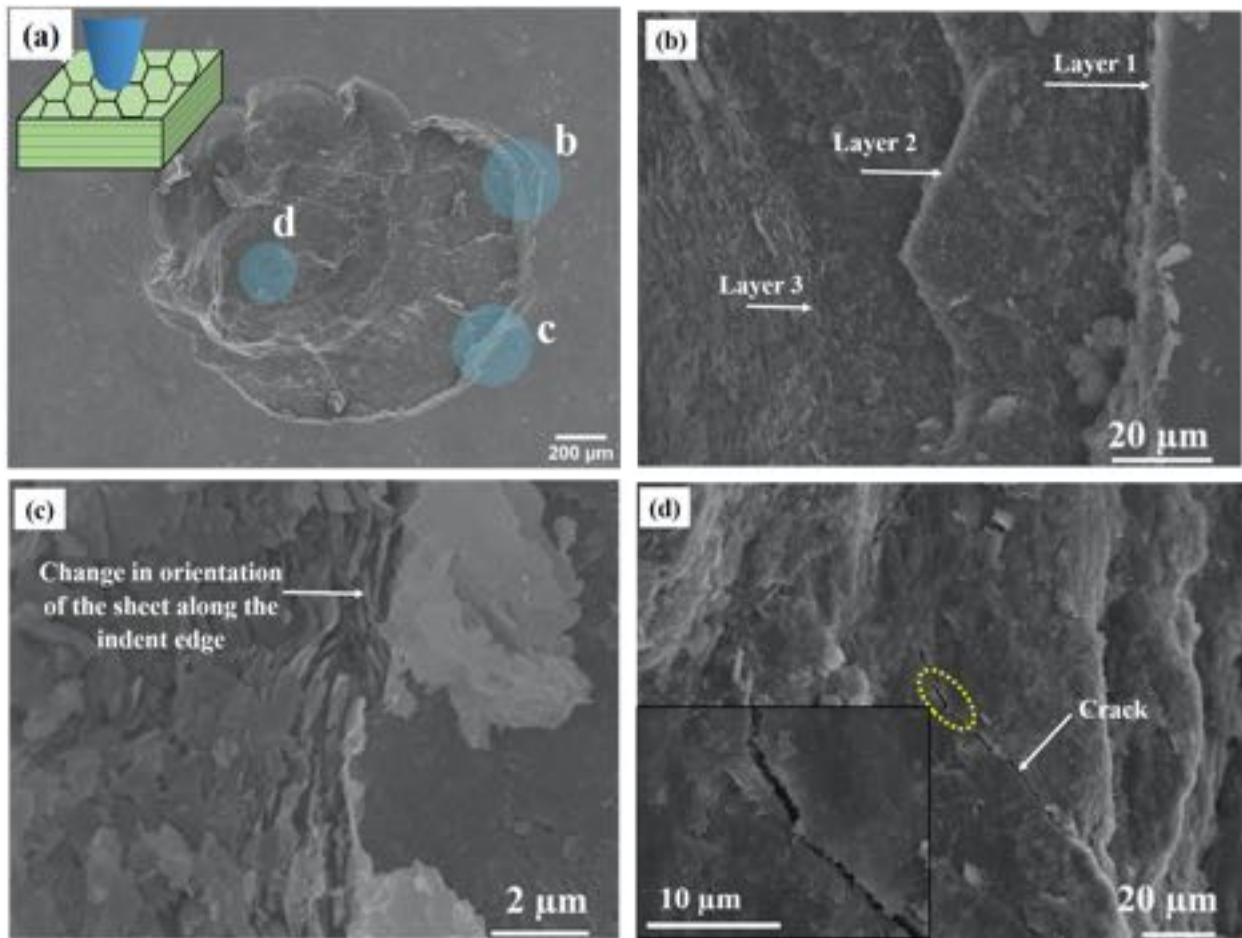


Figure 4.14: SEM images of the top indented surface after the tip removal, (a) lower magnification of the indented surface indicating the regions from where the SEM images b, c and d, were imaged, (b) layered fractured surface, (c) bending of sheets, and (d) crack propagation at the bottom of the indent surface

Figure 4.14(a-d) shows the different locations of the damaged surface in the indent region after the tip removal for the top surface indentation. The delamination of layers has occurred like a wedge forming three different layers/steps until the bottom of the indent as shown in Figure. 4.14(b). This clearly indicates layer-by-layer delamination during indentation. Bending of the layered sheets were observed (Fig. 4.14(c)) at the corner of the indent surface where BNNS have oriented along the height of the step. The fractured regions inside the indented surface clearly indicate the sheets have fractured from the pellet in a zig-zag way. This again confirms the boron nitride sheets fracture along the sheet edges and not through the sheets, and the strong bonding nature of B-N within the planes. Further, at the bottom most -of the indent surface, lateral crack propagation was noticed in Figure 4.14(d). The major

observation from the surface indentation is the sheets have delaminated in layers more in a tapered way and there was no crack propagation observed on the top surface or near the indentation surface as seen in Figure 4.14(a).

4.1.7.2. Deformation along Monolithic BNNS Cross-section

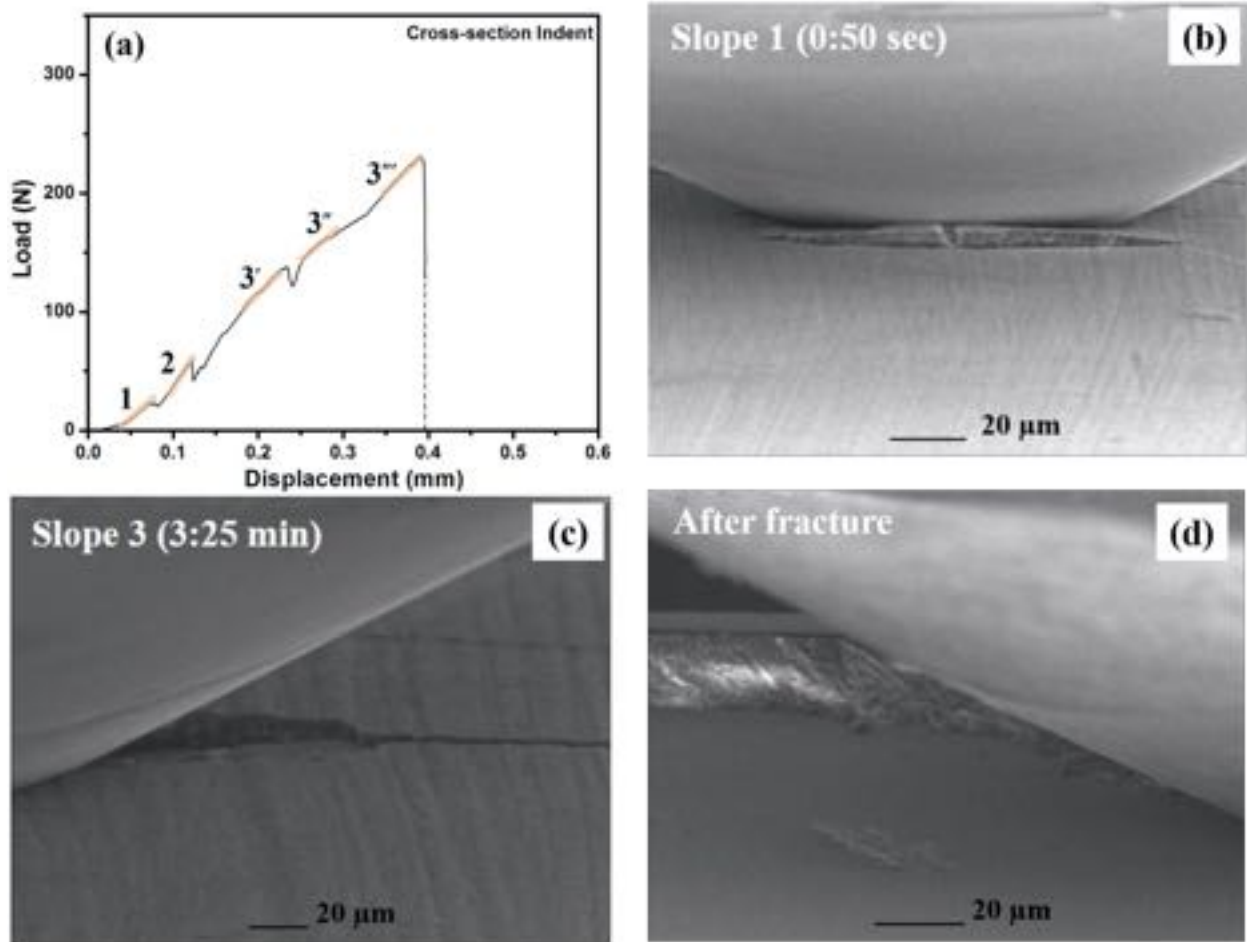


Figure 4.15: Cross-section indent load-displacement curve and SEM images of deformation event at different stage of loading

The load-displacement curve for indentation along the cross-section of the sintered pellet is shown in Figure 4.15 (a). There are three major slope changes observed from the curve during loading. The slope, time range from the video (V2), normalized associated energy for each slope and the corresponding deformation mechanism are given in the Table 4.2. From the load-displacement curve and video V2, the deformation mechanisms observed for the slope 1 sequentially are the compression of sheets, crack initiation, crack propagation, minimal

delamination of sintered sheets followed by the fracture (Fig. 4.15(b)). For the slope 2, bending of delaminated sheets and crack propagation were observed. In the slope 3 region, there is a small drop in load due to pit formation, which results in the evolution of 3 parallel slopes (3', 3'', 3''') in this regime. During the slope 3, the crack propagates further resulting in the fracturing of the sheets at the crack region and due to this, a huge pit is formed near the indenter as shown in Figure 4.15(c). In the displacement range from 0.4 to 0.5 mm, the dominant deformation was fracturing of the cross-sectional layers into two halves with increasing load (Fig. 4.15(d)). In the real time video for this displacement regime, there was continuous engagement of the tip and the loading was happening continuously. During this duration, there was no major deformation observed in the video. This could be attributed to the fracturing of cross-sectional layers with increasing load. In the cross-section, normalized associated energy increased two-fold from slope 1 (55.22 mJ) to slope 2 (103.11 mJ). For the slope 3, the normalized energy remained the same as slope 1. Deformation mechanisms in slope 2 (bending of sheets and crack propagation) are the dominant deformation mechanisms with 87% higher energy of dissipation compared to the slope 1 and 3.

Table 4.2: Deformation mechanism observed during cross-section indentation with respect to the slope and the corresponding time duration from the video

Slope	Time range in video (min)	Normalized associated energy (mJ)	Specific time in video (min)	Deformation mechanism
1	0.30 – 1.01	55.22	0.31	(i) Compression of the sheets
			0.33	(ii) Crack initiation
			0.42	(iii) Crack propagation
			0.45	(iv) Fracture of delaminated sheet (Fig. 4.15(b))
2	1.18 – 1.42	103.11	1.22	(i) Bending of sheets

			1.30	(ii) Crack propagation
3	2.29 – 3.40	54.26	2.30	(i) Pit formation (Fig. 4.15(c))
			3.15	(ii) Crack propagation
-	3.40 – 4.20	-	-	Fracturing into two parts (Fig. 4.15(d))

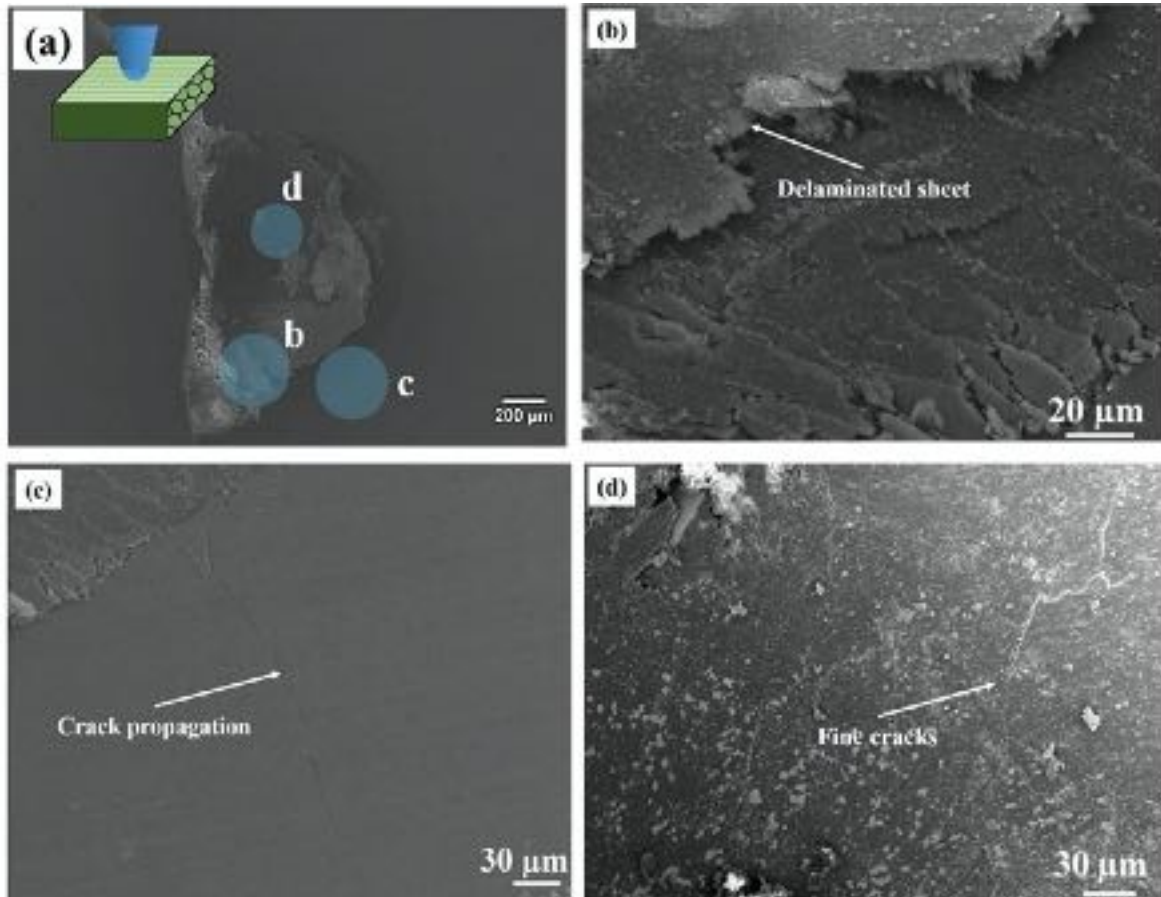


Figure 4.16: SEM images of the cross-section indented surface after the tip removal, (a) low magnification image indicating the regions from where the SEM images b, c, and d, were imaged, (b) delaminated of the sheets, (c) crack propagation from indentation, and (d) fine cracks below the indent surface

After the indentation along the cross-section of BNNS SPS pellet, the indented surfaces were analyzed using SEM as shown in Figure 4.16(a-d). Large delaminated sheets were observed along the edges and inside the indented surface (Fig. 4.16(b)) These BNNS sheets have fine cracks on the surface and were fragmented. Fine multiple cracks merge into one long crack away from the indented region and these cracks were deflected along the edges of the sheet as shown in Figure 4.16 (c). Fine lateral cracks were also formed on the bottommost

center region below the indenter as shown in Figure 4.16(d). Therefore, from the above observations the deformation mechanisms in the cross-section indent are crack initiation, crack propagation, bending and fracturing of the layers which is completely different from top surface indentation behavior.

4.1.7.3. Deformation Mechanism of Monolithic BNNS Pellet with Respect to Different Orientations

The normalized associated energy (mJ) measured from each slope of the top surface and cross-section of load-displacement curves are listed in Tables 4.1 and 4.2. From this quantified normalized associated energy, energy dissipation of the top surface increases four-fold as the displacement occurs and it takes much longer to fail. In the cross-section, the calculated normalized energy goes only two-fold higher and the failure occurs more rapidly as compared to the top surface. This is expected because of the nature of bonding of boron and nitrogen atoms within the plane (top surface), where they exhibit a strong covalent bonding with a bond energy of 3.25 eV and along the cross-section they have a weak Van der Waals bond between BN layers with a bond energy of 0.052 eV [17]. The in-plane bond energy is about ~62.5 times higher than the out-of-plane bond energy, which contributes to higher dissipation of energy along the top surface. Additionally, zig-zag nature of fracture and bending of layered sheets at corner of the indent surface are the distinct top surface fracture mode, by which the dissipation of energy increases along the top surface compared to the cross-section.

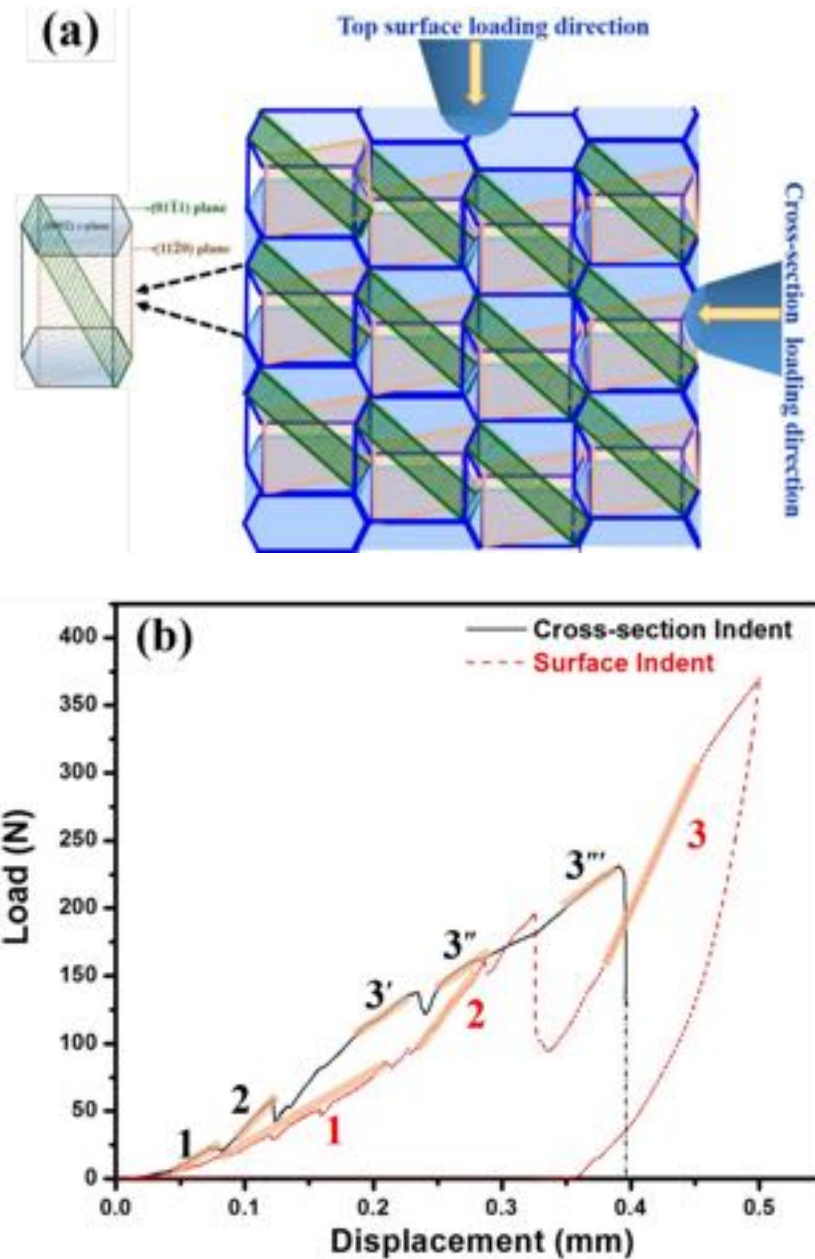


Figure 4.17: (a) Schematic drawing showing the simple hexagonal system marked with the basal plane (0002), prismatic plane (11 $\bar{2}$ 0), pyramidal plane (01 $\bar{1}$ 1) and the schematic of layered BNNS. Also, the loading direction along the top surface and cross-section are marked. (b) Combined load-displacement curve along the top surface and cross-section of sintered BNNS

In-situ indentation behavior along with the texture and TEM results provides a deeper insight about the deformation mechanism of 2D BNNS with respect to the orientation. The most common plastic deformation mechanisms are slip and twinning. Generally, slip occurs in a system, when the critical resolved shear stress (τ_c) reaches a critical value. The critical resolved shear stress, τ_c is given by equation 4.2,

$$\tau_c = \sigma_y * \text{Cos } \phi * \text{Cos } \lambda \quad (4.2)$$

where, σ_y is the yield stress, ϕ is the angle between the tensile axis and slip plane normal, λ is the angle between the tensile axis and slip direction. Schmid factor is given by $\text{Cos } \phi * \text{Cos } \lambda$. A schematic of the hexagonal BNNS system with the planes and loading direction are shown in Figure 4.17(a). The top surface texture studies clearly showed a preferred orientation of basal planes (0002) perpendicular to the direction of pressure during sintering. Also, the TEM studies on the top surface revealed twin like features after sintering. The indentation test was performed in such a way that load was applied in perpendicular direction to the top surface, (i.e.) the loading direction was at 90° to the basal plane. This does not satisfy the Schmid factor to activate the slip along the basal plane because $\text{Cos } \phi$ is 0 and thus $\tau_c = 0$. So, along the top surface, there is no plastic deformation due to slip. Strong bonding between the boron and nitrogen atoms along the basal plane restricts the crack propagation through basal plane. From this understanding, the dominant deformation along the top surface will be delamination of BN sheets. Cross-section textured studies showed a relatively weak texture along the prismatic plane (11 $\bar{2}$ 0) and pyramidal plane (01 $\bar{1}$ 1). During the indentation test on the cross-section, the load was applied at 90° along the prismatic or pyramidal planes. Since, there is no major preferred orientation along the cross-section, the load acting on the surface is compressive in nature and there are possibilities to have compression along different directions. In that case, the compression along the [11 $\bar{2}$ 0], may result in twinning and this will activate the basal slip, (0002)[11 $\bar{2}$ 0]. Further, for the pyramidal plane (01 $\bar{1}$ 1), the $\phi \neq 90^\circ$ and $\lambda \neq 90^\circ$. Therefore, the Schmid factor has a finite non-zero numerical value, thus τ_c has a numerical value and this indicates pyramidal plane is also an active slip plane along the cross-section. These active slip planes may lead to plastic deformation along the cross-section. Nanoindentation studies along the cross-section showed lower hardness compared to the top surface. This clearly corroborates the weak Van der Waals forces between the layers in the h-BN system, resulting in crack

propagation through the grains more easily. Further, this leads to fracture along the cross-section surface. Figure 4.17(b) shows the combined load-displacement curves of top surface and cross-section, higher load was required for the top surface to reach the same displacement compared to the cross-section. Total work of indentation measured from the area under the loading curves was found to be 61.44 mJ and 41.07 mJ for top surface and the cross-section, respectively. Along the top surface about 50% more energy was dissipated compared to the cross-section indicating the top surface has higher toughness comparatively. Therefore, the dominant deformation mechanism observed in the top surface were compression of the layered sheets, delamination and material pile up along with zig-zag fracture. In addition, the deformation of top surface was also dominated by twinning and by inciting the non-basal slip systems. This understanding of in-situ deformation mechanism of sintered BNNS pellet with respect to different orientations, will help to develop and design the structural composite materials comprising of two-dimensional boron nitride nanosheets.

4.1.8. Conclusion of Monolithic BNNS Consolidated by Spark Plasma Sintering

Monolithic BNNS has been successfully consolidated by SPS with 92% density. The sintered BNNS pellet has the h-BN structure, where the nanoscale features of individual nanosheets has been retained in the monolithic BNNS. The preferred orientation of nanosheets in monolithic BNNS had a significant effect on mechanical properties and deformation mechanisms. Total energy dissipation during high-load indentation was higher for top surface (61.44 mJ) compared to cross-section (41.07 mJ). Understanding the arrangement of nanosheets in bulk structure will contribute in the robustness of 3D architecture and design of BNNS based composites.

4.2. Monolithic BCN Consolidated by Spark Plasma Sintering

Two-dimensional graphene nanoplatelets and boron nitride nanosheets were used for reaction synthesis (by spark plasma sintering) to form the ternary 2D boron-carbon-nitride (BCN) system. The novelty of the BCN synthesis: (i) using reactive sintering process of 2D BNNS and 2D GNP powder mixture ($\text{BN} + \text{C} \rightarrow \text{BCN}$) at high temperature (greater than 1600 °C) and the sintered BCN compacts exhibit a strong textured structure; (ii) understanding the friction and wear properties of BCN compacts; and (iii) in-situ high load indentation study on the sintered BCN compacts to identify the deformation mechanisms.

4.2.1. High Energy Ball Milled BNNS and GNP Powder Characterization

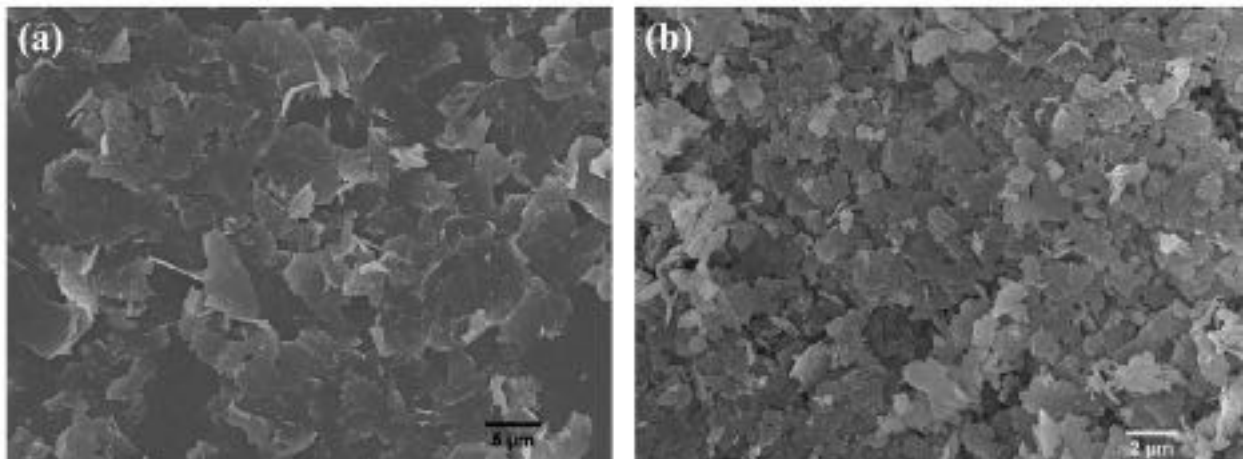


Figure 4.18: SEM images of as-received (a) graphene nanoplatelets and (b) boron nitride nanosheets

Mechanical alloying is an efficient technique for the initial powder preparation, where the BNNS and GNP powders will be mixed together by this method. SEM images of the as-received BNNS and GNP powder are shown in Figure 4.18. As-received GNP particle was in the range of 3-15 μm with thickness of 6-8 nm and as-received BNNS particle was in the range of 100 nm – to 3 μm with thickness of 40-60 nm. As-received BNNS and GNP were ball milled for 1 h in tungsten carbide (WC) vial using WC balls of 8 mm in diameter. The ball to powder ratio chosen for milling was 10:1. The milling was performed for shorter duration, to avoid any

phase formation and the reason for milling was to obtain uniform mixture of BNNS-GNP. Figure 4.19 shows the SEM image of ball milled powders. It clearly shows the uniform mixing of BNNS-GNP, and the nanosheets were not fractured during ball milling. Also, there was no change in morphology and particle size of the ball milled nanosheets.

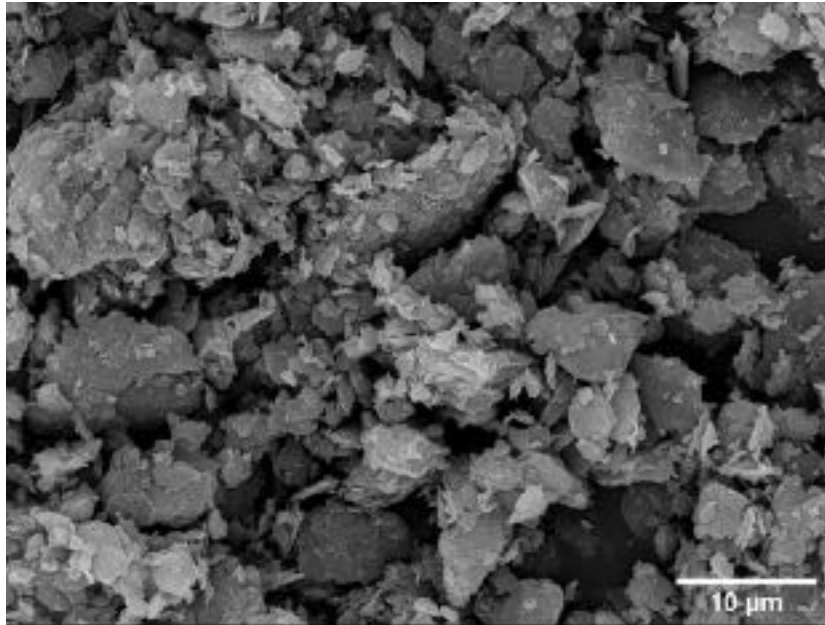


Figure 4.19: SEM image of the ball milled BNNS and GNP

XRD patterns of the as-received GNP, BNNS and ball milled powder are shown in Figure 4.20. The as-received GNP show peaks related to graphene [18] and as-received BNNS show peaks related to hexagonal boron nitride (h-BN) [19] with minor traces of impure boron carbide (B_4C). The XRD pattern of 1 h ball milled powder (BNNS-GNP), shows the individual peaks of BNNS and GNP in the mixed powder. No structure change or phase formation was observed after ball milling. In addition, minor fraction of B_4C was found and there was no contamination of WC from the ball milled vial or balls.

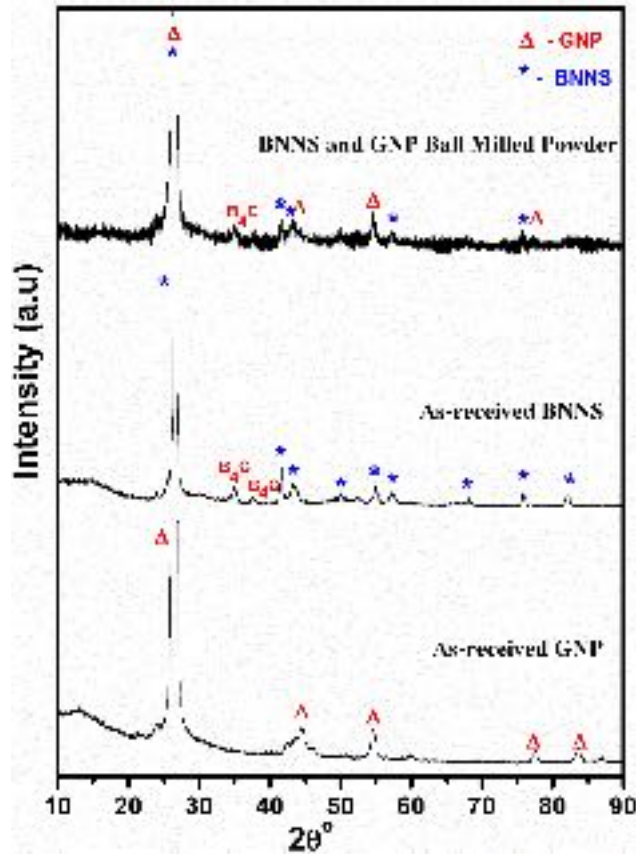


Figure 4.20: XRD patterns of the as-received GNP, as-received BNNS and ball milled BCN powder

4.2.2. Reaction Synthesis BCN System – SPS Parameters

Reactive spark plasma sintering (RSPS) is a reaction synthesis process, where it will form the in-situ synthesized phase with simultaneous densification in a single step. The processing parameters - sintering temperature, dwell time, heating rate and sintering pressure, have a vital role in controlling the microstructure, new phase formation and densification of sample. The reactive SPS process parameters for BCN formation were chosen based on literature and previous research works in our group used for consolidating GNP powder by SPS [20-22]. Also in one of the early studies discussed in Kosolapova *et al.*, BN-C (graphite) was chosen as starting powders for the synthesis to form BCN phase, where the reaction temperature was in a range of 1400 – 2200 °C [23]. The sintering temperature was chosen between 1600 – 1800 °C, dwell time of 10 – 30 min, heating rate of 100 °C/min and sintering pressure of 60 MPa. A systematic approach was applied in this study to discern the effect of

RSPS process parameters. So, the heating rate and sintering pressure were retained uniformly for all the reaction synthesized BCN samples. The RSPS sintering temperature and dwell time were varied and the effect of these parameters were examined methodically. The BCN samples were reaction synthesized at 1650 °C sintering temperature under a pressure of 60 MPa for 10 min (BCN 1) and 30 min (BCN 2) with purpose to analyze the effect of dwell time on the phase formation, properties and densification. The sintering temperature was increased 100 °C from 1650 °C to 1750 °C (BCN 3) for dwell time of 10 min could contribute in increasing the density of BCN sample with in-situ synthesized phase formation. Therefore, the prudent choice of RSPS process parameters will result in synthesizing BCN samples with improved densification and attractive properties.

4.2.2.1. Reactive Sintering Mechanism – BCN Phase Formation

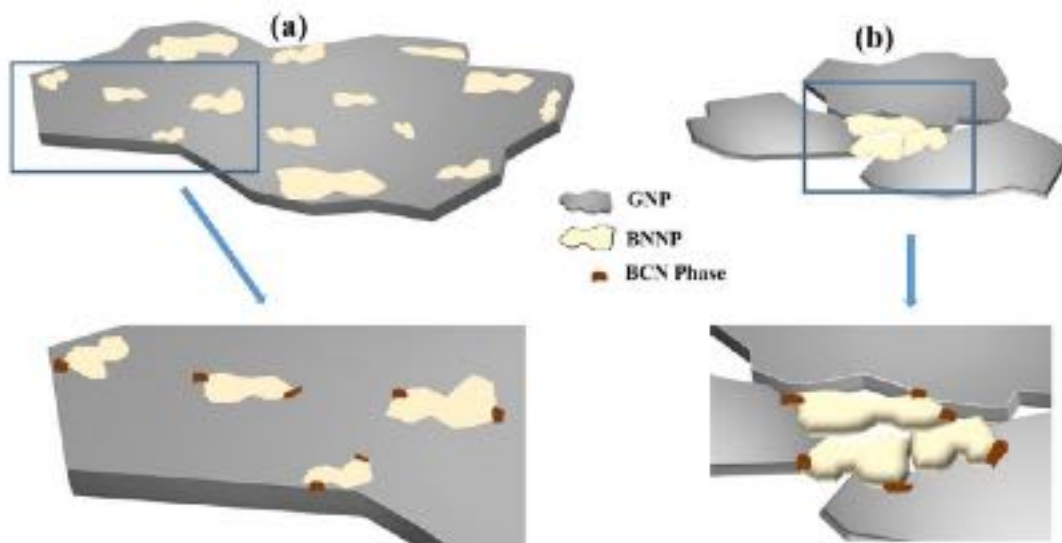


Figure 4.21: BCN phase formation mechanism during reactive spark plasma sintering

The BCN phase formation is achieved by two major steps: (i) high energy ball milling (mechanical activation) and (ii) reactive spark plasma sintering (RSPS). The possible mechanisms of reactive spark plasma sintering process of composite (BNNP and GNP) powders as reactants for BCN phase formation will preferably be controlled by a solid-state

diffusion mechanism in two different ways as shown in Figure 4.21. In this reactive spark plasma sintering process, below is the reaction for BCN phase formation,



The reactant powder mixture of BNNS and GNP were prepared by high energy ball milling method. The initial microstructure and properties of the mixed reactant powders will have a strong impact over the in-situ synthesized phase, microstructure, properties and densification. This method of mixing will contribute in achieving uniform distribution of BNNS/GNP and it will improve the reactivity of composite powders [24, 25]. In this process of mixing, some microdefects would be created in the nanosheets and during RSPS, these defects can contribute in the diffusion of atoms [26]. So, the mechanical activation of reactant mixed powders will aid in BCN phase formation by RSPS. In the RSPS process, the sintering process is initiated by pulsed DC current and the reactant powders electrical conductivity has the ability to control the synthesis reaction rate. As graphene nanoplatelets are highly conductive in nature when mixed with insulator like boron nitride nanosheets, during reactive spark plasma sintering process the pulsed electric current transfers through the BNNS/GNP mixture, localized heating (high temperature spots) will be developed in GNP regions where the reaction will begin and accelerate through the nanosheets if strong interfaces were developed between the nanosheets [27, 28]. Thus, the reaction during RSPS would be self-accelerated because of the GNP existence in the reactant mixed powders. The distribution of BNNS and GNP after ball milling can be of two distinct ways as shown in Figure 4.21. As BNNS are smaller in particle size compared to GNP, initially the BNNS may lie above or decorate the graphene nanosheets (Fig. 4.21(a)) or BNNS may accumulate themselves between the edges of multiple graphene nanosheets (Fig. 4.21(b)). Once the RSPS process was initiated, between the good interfaces of nanosheets localized heating was generated and this will improve the reaction kinetics, trigger the solid-state diffusion and result in the in-situ synthesis of BCN phase at the interface

between the nanosheets. The phase formed would be diffusion-controlled, as the elevated sintering temperature increases the rate of reaction, atoms will have high energy and they will diffuse towards the interface (between nanosheets) to form BCN.

4.2.3. Monolithic BCN – Density, Structure and Microstructure

The ball milled 2D-BNNS and 2D-GNP powders were reaction synthesized using spark plasma sintering to form BCN phase at different temperature and dwell time (Table 4.3) under a pressure of 60 MPa with a heating rate of 100 °C/min. After reaction synthesis, the BCN pellets were polished to remove the graphite foil and the pellets were 20 mm circular disk with 3 mm thickness. The density of the as-received BNNS, GNP and ball milled powder were measured using helium pycnometer. The density of the ball milled mixed powder was 2.386 g/cm³, while the density of reaction synthesized BCN pellets are included in Table 4.3. Using Archimedes method, the relative density of the reaction synthesized BCN pellets were measured. BCN 2 and BCN 3 showed an increase in relative density compared to BCN 1 sample. The increase in relative density of BCN 2 and BCN 3 is attributed to the two major parameters of reactive spark plasma sintering process, namely the increase in reaction synthesis dwell time from 10 min to 30 min at 1650 °C and reaction synthesis temperature from 1650 °C to 1750 °C. Dwell time is one of the important process parameters to be optimized in RSPS, with increase in dwell time the density improved to 93.4% for BCN 2 sample, this is due to the increased surface contact and increased heat flux, which reduces the interlayer gap between the nanosheets. Another important process parameter is the sintering temperature, as the sintering temperature is increased, it will increase the generation of joule heat with enhanced inter-sheet bonding and thermal diffusion of nanosheets. This will contribute in densification of BCN pellet with reduced porosity and in addition, it will enhance the reaction rate during RSPS.

Hence, the density measurements for all three samples demonstrate the importance in selection of RSPS process parameters and their influence in density of sintered BCN pellets.

Table 4.3: Reaction synthesis conditions for SPS and the measured density of reaction synthesized pellets

Sample	Synthesis Temperature (°C)	Dwell time (min)	Density (g/cm ³) (pycnometer)	Relative density (%)
BCN 1	1650	10	2.095	88
BCN 2	1650	30	2.231	93.4
BCN 3	1750	10	2.221	93.2

X-ray diffraction studies on the reactive sintered BCN samples for all the three conditions were performed to confirm the phase formation as shown in Figure 4.22(a). For the BCN 1 sample (1650 °C, 10 min) after reactive sintering showed the strongest diffraction peak at $\sim 26.408^\circ$, it shifted towards lower 2θ angle (Fig. 4.22(b)) and d-spacing calculated for this peak was 3.371 Å. Majorly, the h-BN characteristic peaks were observed. Impure phase B₂O₃, B₄C and carbon were formed after reactive sintering of ball milled powders. The B₄C formation can be related to the BNNS reaction with the graphite foil during SPS. The reactive sintered BCN 2 pellets (1650 °C, 30 min) showed further drift of the strongest diffraction peak at $\sim 26.38^\circ$, towards lower 2θ angle (Fig. 4.22(b)) and d-spacing calculated for this peak was 3.374 Å. The h-BN peaks corresponding to BNNS was observed along with impure phases B₂O₃, B₄C and carbon. The cubic BCN phase formation was observed around $\sim 42.9^\circ$ (Fig. 4.22(c)). The XRD pattern of BCN 3 (1750 °C, 10 min) pellet, shows the existence of h-BN, B₂O₃, B₄C and carbon, which was also observed in the previous sintering conditions. The intense diffraction peak at $\sim 26.106^\circ$ corresponding to (002) plane shifts further to lower angle, where the d-spacing was 3.42 Å. This d-spacing matches the hexagonal BCN (h-BCN) value from the JCPDS file (35-1292). The calculated d-spacing of BCN 3 pellet was larger than the d-spacing of as-received BNNS (3.33 Å) and as-received GNP (3.36 Å). Similar observations were observed in the literature for h-BCN phase formation [29-31]. Similar to BCN 2 (1650 °C, 30

min), cubic BCN ($\sim 42.9^\circ$) phase was also formed for the sample synthesized at 1750°C [31]. Furthermore, the intensity of $\sim 26^\circ$ peak for BCN 2 and BCN 3 pellets was higher compared to mixed reactant powders/BCN 1 pellet, suggesting the increase in crystallinity of newly synthesized phase. This corroborates the ternary B-C-N formation by reactive spark plasma sintering process from the reactant mixture of 2D BNNS/GNP.

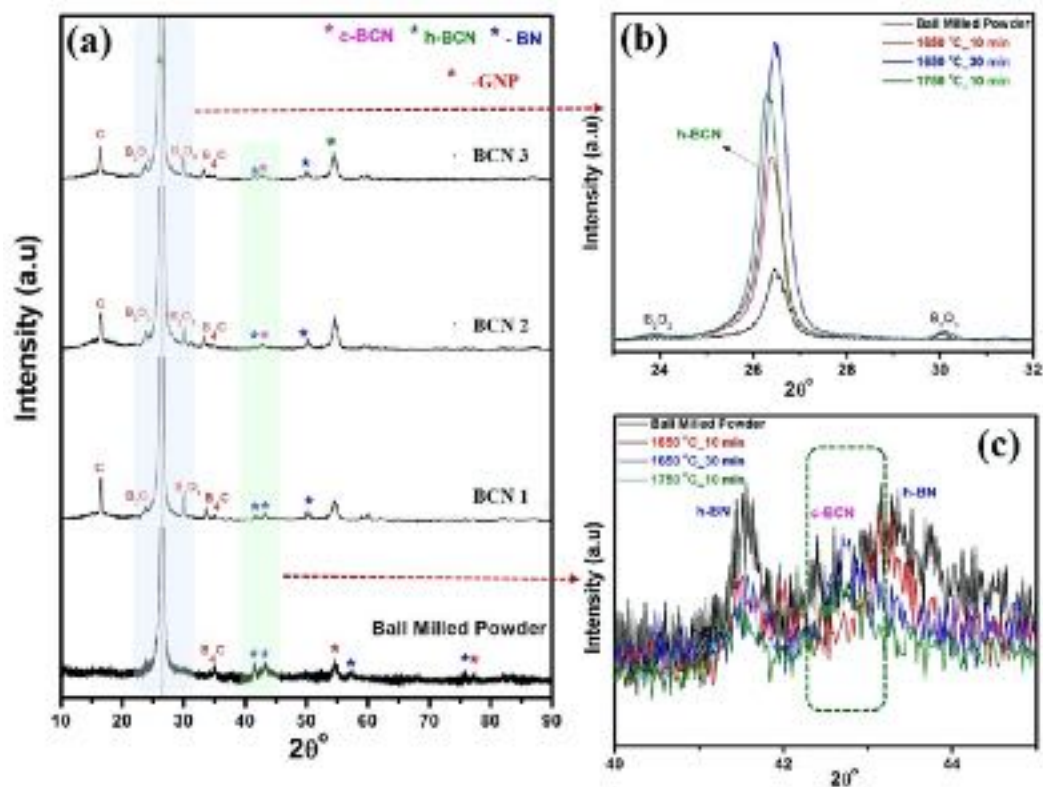


Figure 4.22: XRD patterns of the reaction sintered (a) BCN 1, BCN 2 and BCN 3, (b) and (c) shows the scans in the 2θ range of $23\text{--}32^\circ$ and $40\text{--}45^\circ$ respectively

In addition to understand the nature of chemical bond formed between the BNNS/GNP and to confirm the BCN phase formation after reactive sintering, the Fourier transform infrared (FTIR) spectrum was measured as shown in Figure 4.23. FTIR spectrum of the ball milled powders showed four major peaks 773 , 1015 , 1338 and 1540 cm^{-1} . The 773 and 1338 cm^{-1} peaks were related to the B=N bending and B-N-B stretching in the out-of-plane modes respectively [32]. The peak at 1540 cm^{-1} correspond to the C=C bond [33]. These three characteristic peaks reveal the presence of h-BNNS and GNP. Also, peak corresponding to B-O bond was observed at 1015 cm^{-1} and this confirms presence of boron oxide. The FTIR

spectrum of the reactive sintered BCN 1 pellet shows the two peaks (734 and 1325 cm^{-1}) corresponding to B-N bond, 1006 cm^{-1} corresponding to the B-O bond and 1532 cm^{-1} corresponding to the C=C bond. There was an appearance of new peak at 1147 cm^{-1} which corresponds to B-C [34], suggesting the new phase formation. For BCN 2 pellet, the FTIR spectrum showed the existence of B-N bond (725 and 1323 cm^{-1}) and C-C bond (1525 cm^{-1}). The peak at 979 cm^{-1} correspond to the B-O bond. The B-C and C-N bonds were found at 1141 and 1250 cm^{-1} respectively [34-36]. The existence of bonds B-C, B-N and C-N, indicate the possible BCN phase formation. The FTIR spectrum of BCN 3 pellet revealed the presence of h-BN (723 and 1319 cm^{-1}). The B-O bond of boron oxide was found at 979 cm^{-1} . Peak at 1112 cm^{-1} corresponds to B-C bond. The C-N and C=N bonds were present at 1263 and 1640 cm^{-1} respectively [35, 36]. These two peaks (C-N and C=N) with increase in sintering temperature become intense and prominent. The peaks corresponding to B-N bonds in BCN pellets shift to lower wavenumbers compared to the B-N bond wavenumber in BNNS of mixed powders. This wavenumber shift indicates the carbon substitution in boron nitride nanosheet and h-BCN formation [31]. Based on the above observations, the BCN 2 and BCN 3 reactive sintered pellets confirm the ternary BCN phase formation.

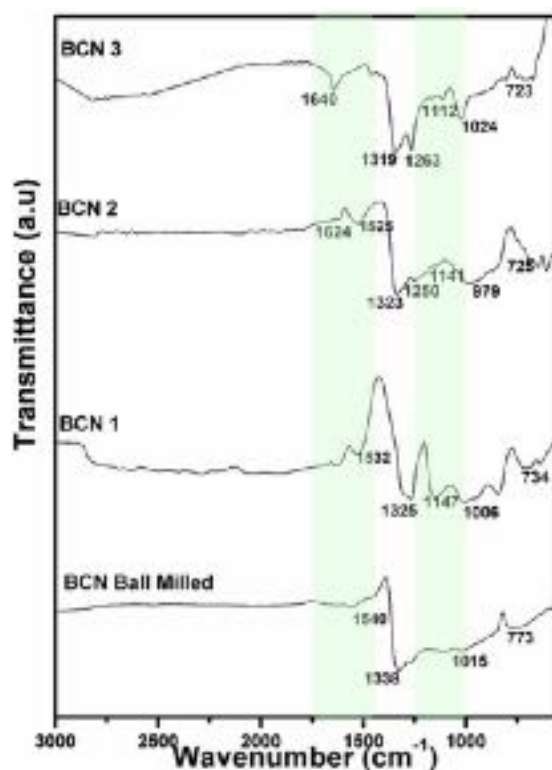


Figure 4.23: FTIR spectra of the ball milled powder and reaction sintered BCN 1, BCN 2 and BCN 3 respectively

The Raman spectra for the reaction synthesized BCN pellets are shown in Figure 4.24. The three dominant and designated peaks of graphitic like structure: D, G, 2D peaks were observed in all the three BCN pellets [37-40]. The D peak is related to the defect induced in graphene structure, such as vacancies, in-plane substitution of atoms or the edges (defect sites in sp^3) [39]. The G peak is related to the graphene first order Raman scattering and from the in-plane vibrations (stretching) of C-C/B-N/B-C/C-N sp^2 bonded pairs [39, 41]. The 2D peak is sometime represented in literature as G' as it is the second most prominent peak of graphene. The 2D peak also arises from the lattice defects, originates from Raman process of double-resonance band and the 2D peak intensity will be higher than G peak intensity for monolayer graphene [42, 43]. In the reaction synthesized BCN 1 pellet, Raman spectrum shows the major D, G, 2D peaks, in addition with traces of small shoulder in G peak which is represented as D* and trace of D+G near the 2D peak. The D* is activated by the weak structural disorder present in the GNP and D+G is also induced by the presence of defects (structural disorder) [39]. The

D peak of the BCN 1 sample is broader than BCN 2 and BCN 3 (Fig. 4.24(a)), due to the existence of both h-BNNS (in-plane B-N vibrational mode) and D peak of GNP [39, 44]. The Raman spectra of BCN 2 and BCN 3 show the dominant three peaks (D, G, 2D), where the D peaks becomes narrow and the intensity of D peak decreases compared to D peak of BCN 1 (Fig. 4.24(a) and (b)). This observation of D peak in BCN 2 and BCN 3 pellets imply the sheets have become more crystalline in nature with less defects. In addition, the shoulder peak D* becomes more prominent peak in the BCN 2 and BCN 3 pellets Raman spectra, indicating the possible B-C-N phase formation. The intensity of D+G peaks also increases for BCN 2 and BCN 3 pellets compared to BCN 1 pellet, most probably due to the diffusion of B/N atoms in GNP [45]. From the intensity ratio of Raman spectra first order D and G peaks, the crystallinity of the sintered BCN pellets can be defined. The change in intensity ratio (R-value) with reactive sintering conditions are shown in Figure 4.24(d). Using Raman spectra, the crystallite size (L_a) can be calculated from the below equation [46],

$$L_a(nm) = \frac{560}{E_{laser}^4} \left(\frac{I_D}{I_G} \right)^{-1} \quad (4.4)$$

where E_{laser}^4 (eV) is the excitation energy, I_D is the intensity of defect D peak and I_G is the intensity of the graphitic peak. The intensity ratio $\frac{I_D}{I_G}$ is inversely proportional to the crystallite size (L_a). The calculated intensity ratio decreased for the BCN pellets with longer holding time (BCN 2 – 1650 °C, 30 min) and increased sintering temperature samples from 1650 °C to 1750 °C (BCN 3 - 1750 °C, 10 min). This measurement shows the enhancement in crystal quality with increase in crystallite size along the nanosheet plane for BCN 2 and BCN 3 pellets. Thus the Raman studies reveal, reaction synthesized BCN 2 and BCN 3 pellets have lower structural defects with bigger nanosized BCN crystals compared to the BCN 1 pellet.

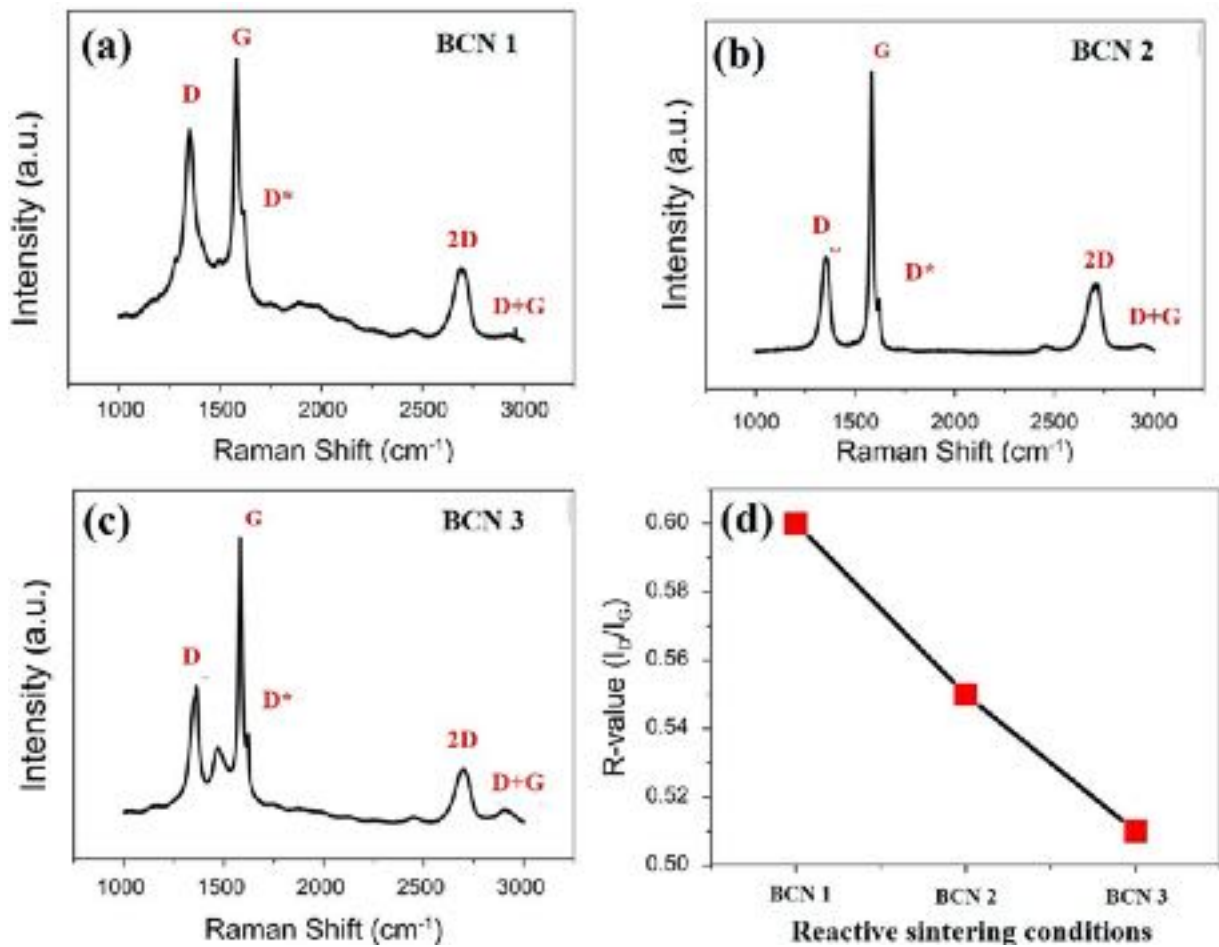
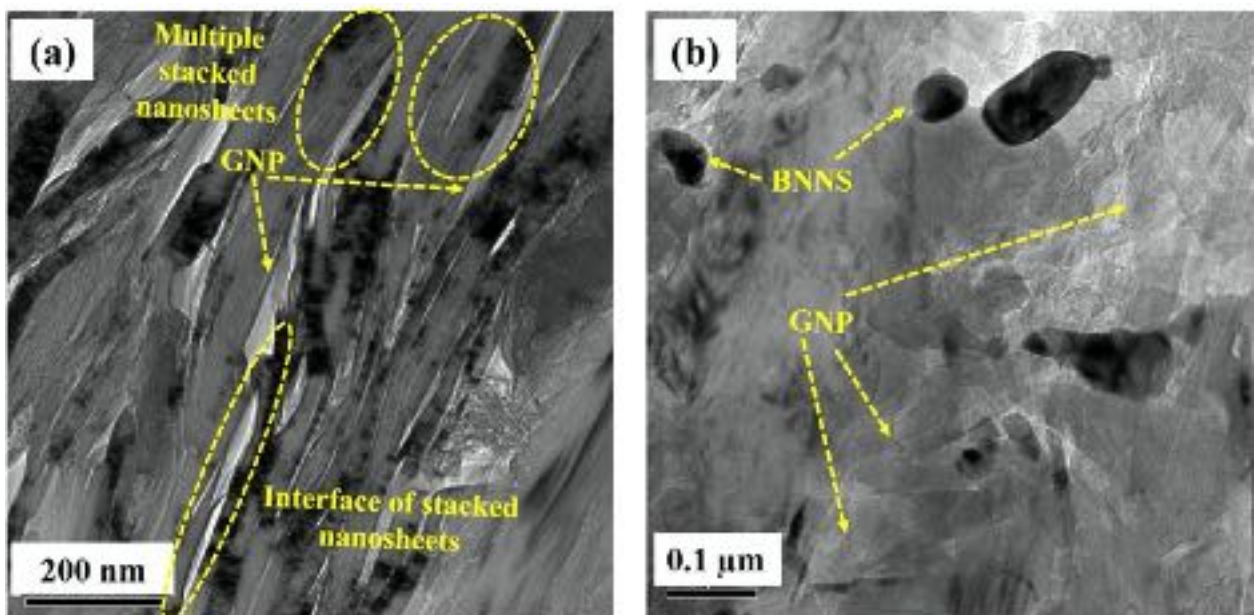


Figure 4.24: Raman spectra of reaction synthesized (a) BCN 1, (b) BCN 2, (c) BCN 3 and (d) change in I_D/I_G value with respect to reactive sintering conditions



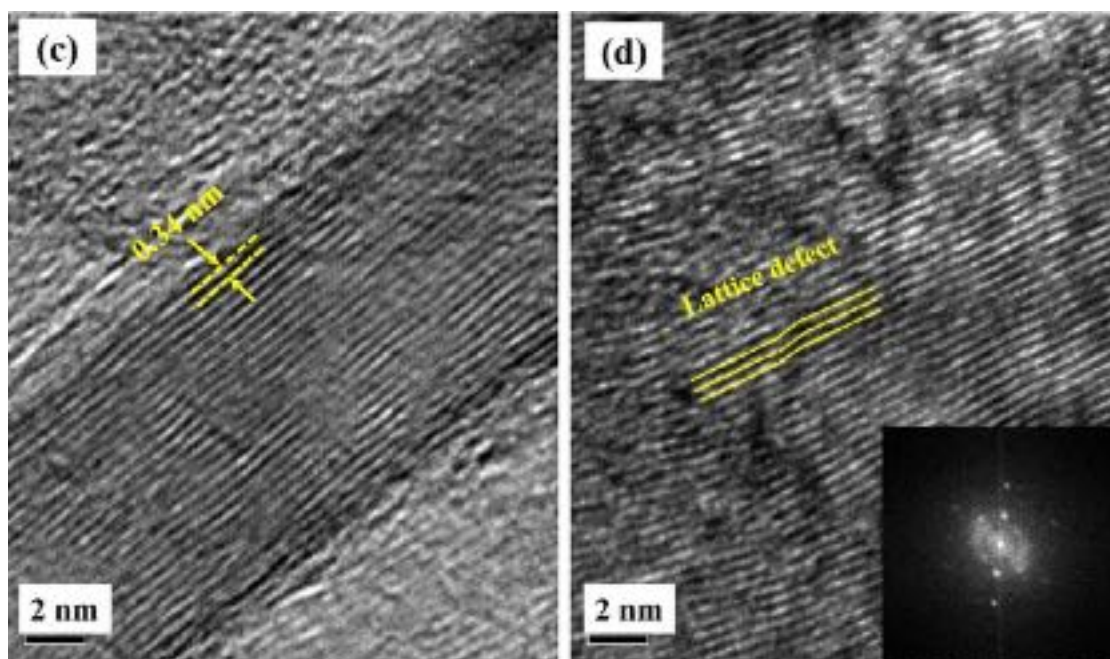
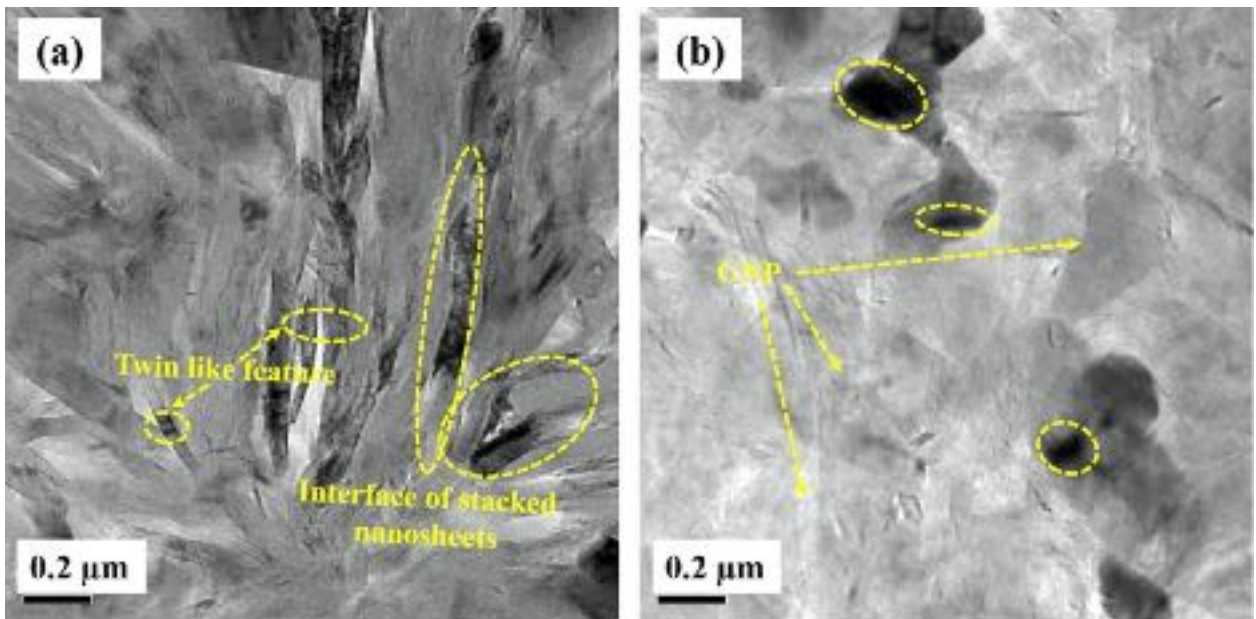


Figure 4.25: HRTEM image of the reaction sintered BCN 1 showing (a-b) bright field image showing GNP/BNNS, (c-d) lattice resolved TEM images with the inset showing corresponding diffraction pattern

High resolution transmission electron microscope was used to study the microstructure of the reaction sintered BCN pellets. As described in section 3.5.2, the BCN pellets were imaged along the direction, normal to the basal plane (c-axis was parallel to the electron beam). Figure 4.25 shows the bright field HRTEM images of reactive sintered BCN 1 pellet. Figure 4.35(a) shows high magnification TEM image of multiple stacked nanosheets sintered together after spark plasma sintering process. Good interface was observed between the sintered nanosheets. The long graphene nanosheets were observed in the stacked nanosheets as shown in Figure 4.25(a). HRTEM image of low magnification (Fig. 4.25(b)) shows regions with nanosheets which are darker and lighter in some places which indicate the presence of multilayered or few layered graphene nanosheets respectively. Mostly rough surface of graphene nanosheet was observed with few folding and some wrinkles were clearly seen in Figure 4.25(b). The low magnification bright field image of BCN 1 pellet displays small flake like nanosheets which are BNNS distributed at multiple spots of graphene nanosheets. Lattice resolved high resolution TEM images of reaction sintered BCN 1 pellet is shown in Figure

4.25(c-d). The lattice resolved HRTEM image (Fig. 4.25(c)) showed lattice spacing of 0.34 nm with typical fringe separation and this lattice spacing corresponds (002) planes of GNP. Lattice defect (atomic arrangement) was observed in the lattice resolved HRTEM image of Figure 4.25(d). Disordered lattice regions were observed at multiple regions. The inset in Figure 4.25(d) shows the Fast Fourier Transform generated diffraction pattern from the HR-TEM image displays a set of diffused hexagonal spots with amorphous ring and the diffractions spots are not well defined. The diffused spot pattern indicates the poor crystalline nature of reaction sintered BCN 1 and streaked diffraction spot were also observed, which is related to the basal plane defects [47, 48]. The microstructure of BCN 1 pellets shows significant amount of unreacted GNP and BNNS, however lattice defects were observed in lattice resolved HRTEM images.



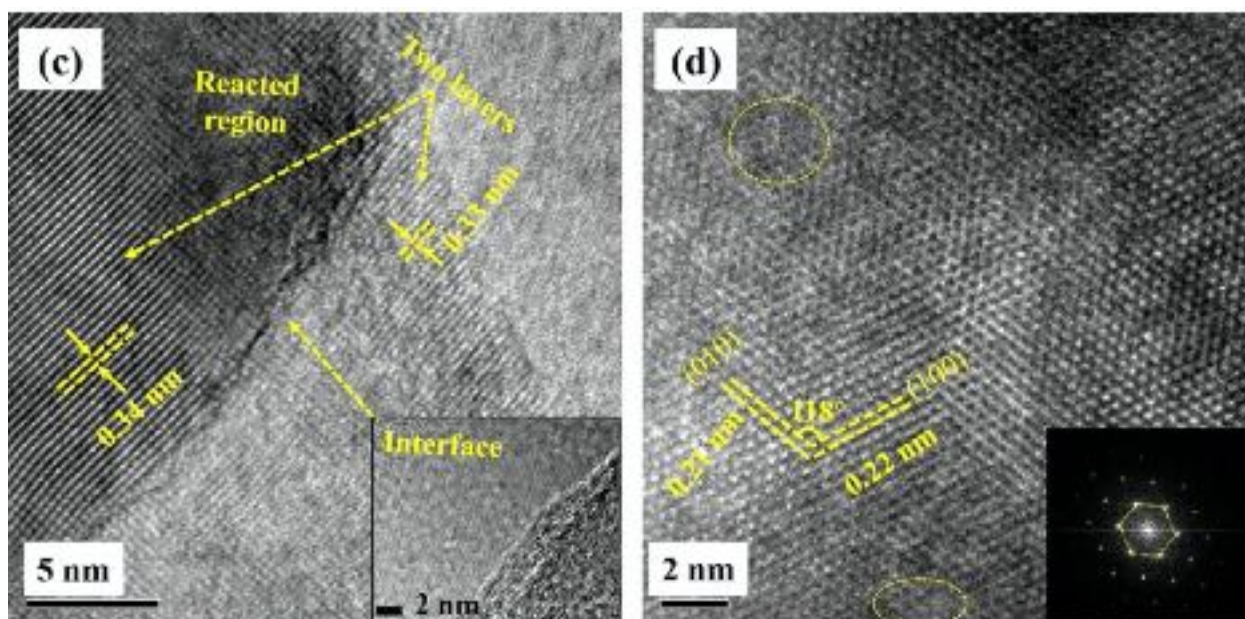


Figure 4.26: HRTEM image of the reaction sintered BCN 2 showing (a-b) bright field image showing GNP/BNNS and reacted BCN region, (c-d) lattice resolved TEM images with the inset showing corresponding diffraction pattern

The bright field HRTEM images of reactive sintered BCN 2 pellet are shown in Figure 4.26. TEM image of BCN 2 pellet (Fig. 4.26(a)) at high magnification displays smooth interface between the stacked nanosheets and the bright field image displays significant amount of contrast in certain regions due to the high density of dislocations developed during the RSPS process. In some regions, twin boundary formation was observed as seen in Figure 4.26(a). Significant amount of ripple formation was developed on the unreacted graphene nanosheets after reactive spark plasma sintering [49]. Figure 4.26(b) displays multilayered graphene nanosheets with some region of the sheets being smooth (free from ripple formation). Most of the sintered graphene nanosheets was folded, wrinkled with few corrugated regions (Fig. 4.26 (b)). Irregular shaped small dark regions (marked in the Fig. 4.26(b) as circles) were observed, indicating the possible reaction product - BCN particles formed between the nanosheets. Figure 4.26(c-d) shows lattice resolved high resolution TEM images of reaction sintered BCN 2 pellet. Two different layers was observed in the Figure 4.26(c), with the lattice spacing of 0.33 nm and 0.34 nm corresponding to BNNS and GNP respectively. Between the BNNS and GNP layers, the reacted region was clearly visible with the change in their lattice arrangement and

orientation. Near the reacted region, some of the places were amorphous. This is ascribed to the distortion of ordered BNNS/GNP lattice, where the incorporation of boron or nitrogen or carbon atoms in the ordered lattice create these amorphous domains [50-52]. The inset in Figure 4.26(c) shows the high magnification of interface between two different sintered layers and the interface is quite smooth. The good bonding at the interface arises from the diffusion of B-N and C atoms during the reactive spark plasma sintering with longer dwell time. The high magnification view of the reacted BCN region displays the lattice image and corresponding Fast Fourier Transform generated diffraction pattern from the HR-TEM image of Figure 4.26(d). The image shows well resolved lattice fringes implying the crystalline nature of synthesized BCN phase with less lattice imperfections (lattice imperfection regions are shown in the dotted circle of Fig. 4.26(d)). Two different lattice spacing of 0.21 nm and 0.22 nm adjacent to each other was observed. The lattice spacing of 0.21 nm correspond to (100) plane and 0.22 nm correspond to (010) plane spacing of BCN [53, 54], while the angle between the two planes was 118° . This observation is similar to 2D boron nitride nanosheets structure, suggesting the observed BCN phase is hexagonal in nature like BNNS [53-55]. The FFT generated diffraction pattern from the TEM image reveals sharp bright diffraction spots with hexagonal symmetry. All the TEM observations of Figure 4.26(c-d) imply the single crystalline nature of reaction synthesized hexagonal BCN phase. The high-angle annular dark field-scanning transmission electron microscope (HAADF-STEM) images of reaction synthesized BCN 2 is shown in Figure 4.27. The STEM image shows two different color contrast, where the grey matrix belong to the nanosheets and the reaction synthesized BCN phase is the bright white nanoparticles. The Figure 4.27(a) shows the nanoparticles are mostly formed between the nanosheets (as marked by yellow arrows). The nanoparticles formed were of varying size from 10 nm to 400 nm. In addition, the particles were of different morphology, the inset in Figure 4.27(b) shows a platelet (layered) shaped, spherical shaped and some irregularly shaped

nanoparticles. The platelet (layered) shaped nanoparticles confirm the h-BCN nanosheet of 2D nature formed after reactive spark plasma sintering.

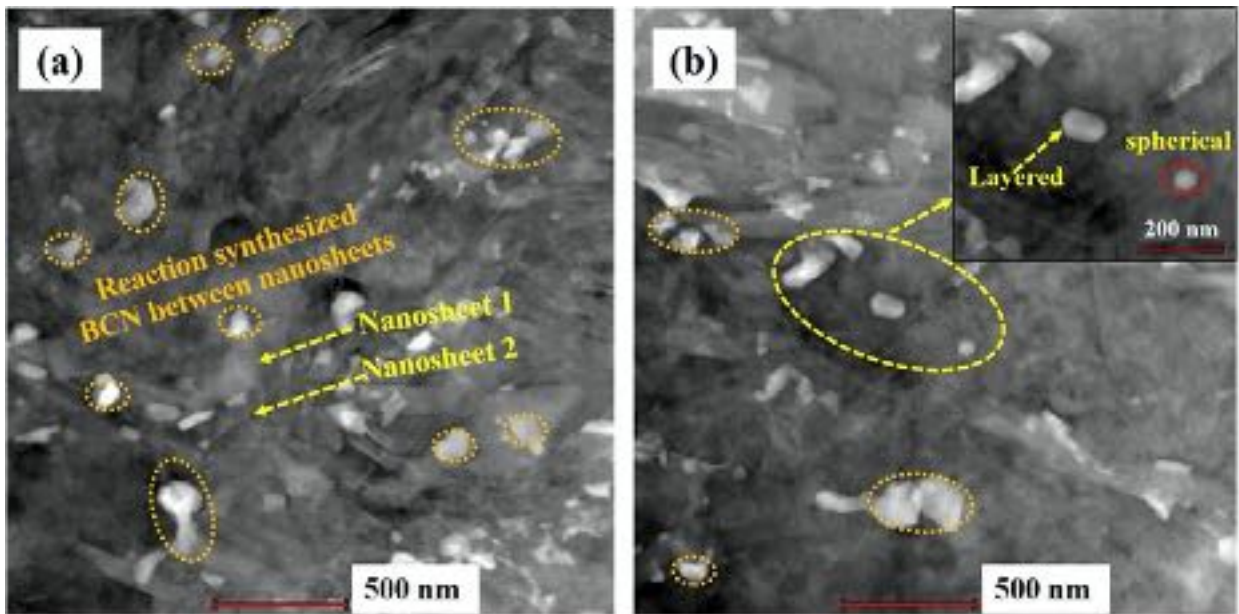
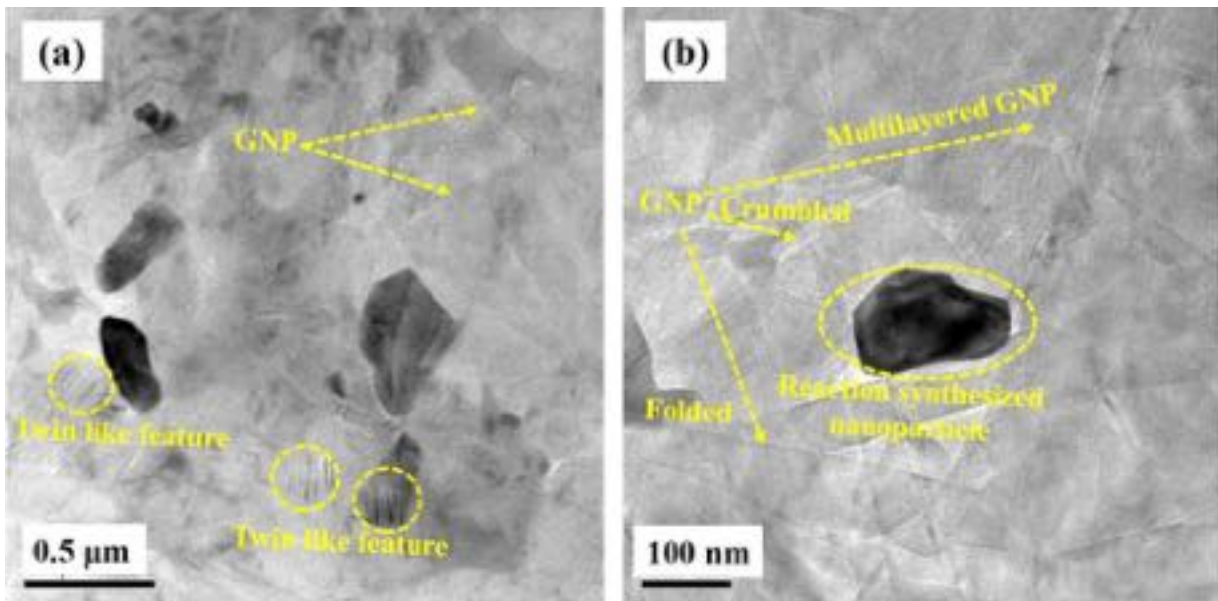


Figure 4.27: HAADF STEM image of reaction synthesized BCN 2

The reactive sintered BCN 3 pellet bright field HRTEM images are shown in Figure 4.28. TEM image of BCN 3 pellet (Fig. 4.28(a)) at high magnification displays smooth interface between the reacted nanosheets. Array of micro-twin formation was observed in some regions as seen in Figure 4.28(a). The ripple formation on the sintered nanosheets has significantly reduced compared to BCN 1 and BCN 2. Multilayered graphene nanosheets with some folds and corrugated regions were seen in Figure 4.28(b). Irregular shaped dark region of 100-120 nm particle (marked in the Fig. 4.28(b) as circle) was observed, indicating the possible reaction product - BCN particles formed between the nanosheets. The high resolution TEM lattice fringes and the corresponding fast Fourier transform (FFT) of reaction sintered BCN 3 pellet are shown in Figure 4.28(c-d). In the Figure 4.28(c), there are two different lattice spacings observed, where 0.348 nm corresponds to (002) plane of hexagonal BCN and 0.209 nm corresponds to (111) plane of cubic BCN. The grain boundary between the two layers are visible and marked by yellow line in Figure 4.28(c). The inset in Figure 4.28(c) corresponds to

the fast Fourier transform pattern from the TEM image and it displays a diffused spotty pattern. This pattern displays a hexagonal symmetry, it is shown by yellow lines in the figure and the diffused pattern arises due to lattice imperfections. Figure 4.28(d) shows the high resolution TEM lattice fringes of BCN 3 and the corresponding fast Fourier transform pattern. This high resolution image displays an ordered atomic arrangement and the crystalline nature of synthesized phase with few lattice imperfections are marked as yellow circles in the Figure 4.28(d). The imperfections observed are amorphous region, missing atoms/vacancies and lattice distortions. The blue boxes (in Fig. 4.28(d)) show the presence of dislocation and stacking faults, arising from the lattice misfit during the BCN phase formation. Lattice spacing values of 0.345 nm and 0.27 nm corresponding to (002) and (100) plane are observed. The FFT pattern shows streaks and this arises from the lattice imperfections – distortions and stacking faults.



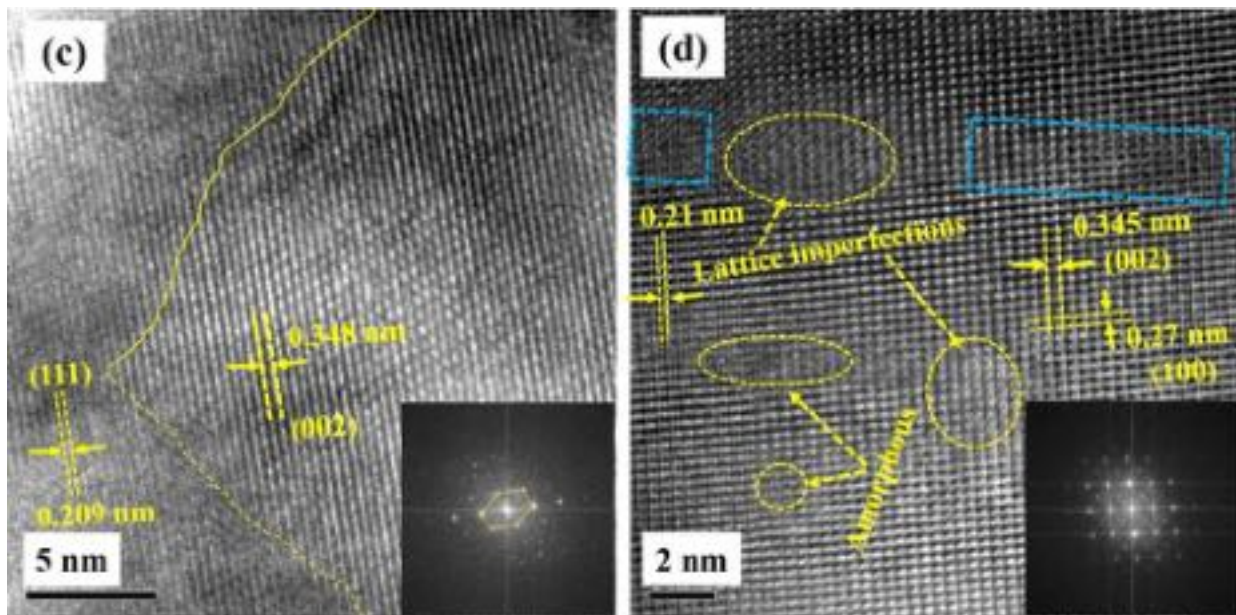


Figure 4.28: HRTEM image of the reaction sintered BCN 3 showing (a-b) bright field image showing GNP/BNNS and reacted BCN region, (c-d) lattice resolved TEM images with the inset showing corresponding fast Fourier transform (FFT) pattern

The HAADF-STEM images of reaction synthesized BCN 3 is shown in Figure 4.29. Three different color contrast was mainly observed in the STEM images, the black colored regions correspond to the porosity in the sintered pellet, the grey matrix belong to the nanosheets and the white colored particles correspond to the reaction synthesized BCN phase. Most of the BCN phase particles were formed between the nanosheets or seen above the nanosheet as shown in Figure 4.29(b) (as marked by big yellow circles). The nanoparticles formed were of varying size from 10 nm to 300 nm. In addition, the particles of different morphology were synthesized, namely platelet (layered) shaped, spherical shaped and some irregularly shaped nanoparticles. The platelet (layered) shaped nanoparticles confirm the h-BCN nanosheet of 2D nature formed after reactive spark plasma sintering. The spherical or irregularly shaped particles correspond to the cubic BCN phase. Compared to BCN 2, the reaction synthesized BCN 3 particles were much smaller in size and more uniformly distributed in the sintered nanosheets, implying the shorter dwell time (10 min) contributed to the fine nanoparticle formation and the increase in sintering temperature from 1650 to 1750 °C intensified the BCN phase formation.

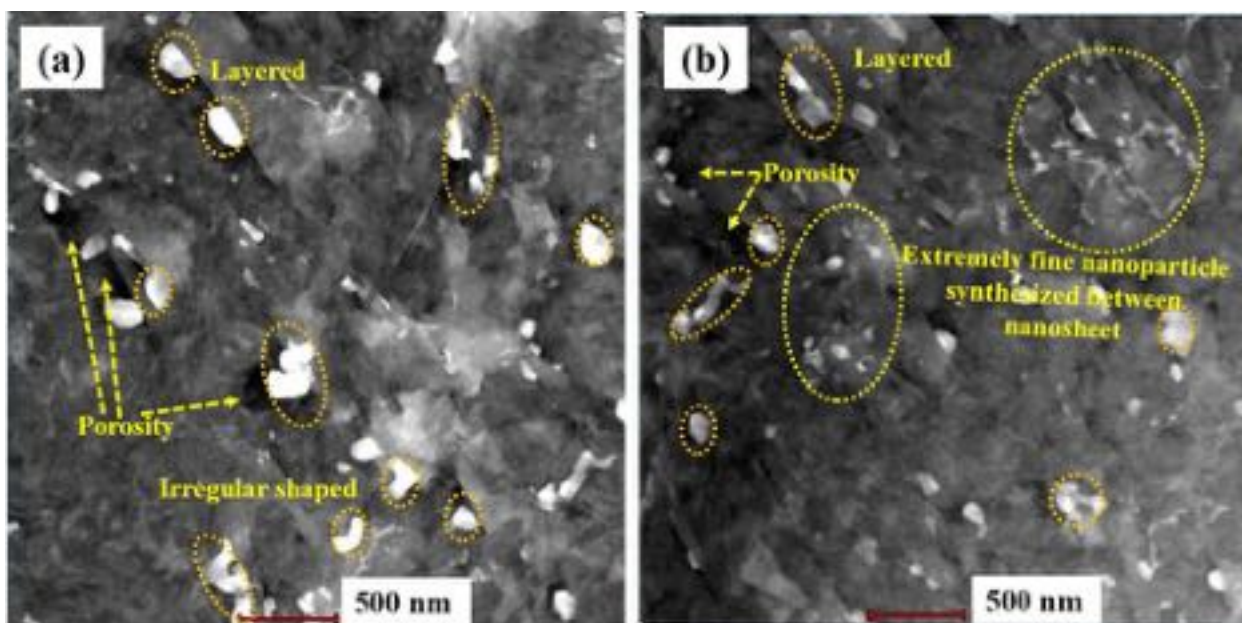


Figure 4.29: HAADF STEM image of reaction synthesized BCN 3

4.2.4. Fracture Mechanism of Monolithic BCN

SEM images of the BCN 1 (1650 °C, 10 min) pellet fractured surface are shown in Figure 4.30. The fracture surface of the reactive sintered pellet shows a poorly reacted 2D BNNS and GNP, where significant amount of porosity (interlayer gap) was observed between sintered layers (Fig. 4.30(a)). This observation clearly confirms the poor densification and reaction of BNNS/GNP at 1650 °C, 10 min. Figure 4.30(b) shows the BCN 1 fracture surface edges to be a combination of zig-zag nature with bending of the nanosheets at some places. The zig-zag nature of the BCN 1 fracture surface shows the crack propagated along the edges of nanosheets due to the poor reaction or bonding between the nanosheets. Mostly, the sintered nanosheets were uniformly aligned as layered structure, this observation shows the preferred orientation of the reaction sintered BCN 1 pellet. At higher magnification, some of the layered nanosheets have folded and kinked (Fig. 4.30(c)). Thus during fracture, the energy dissipation occurs by the above forms of deformation.

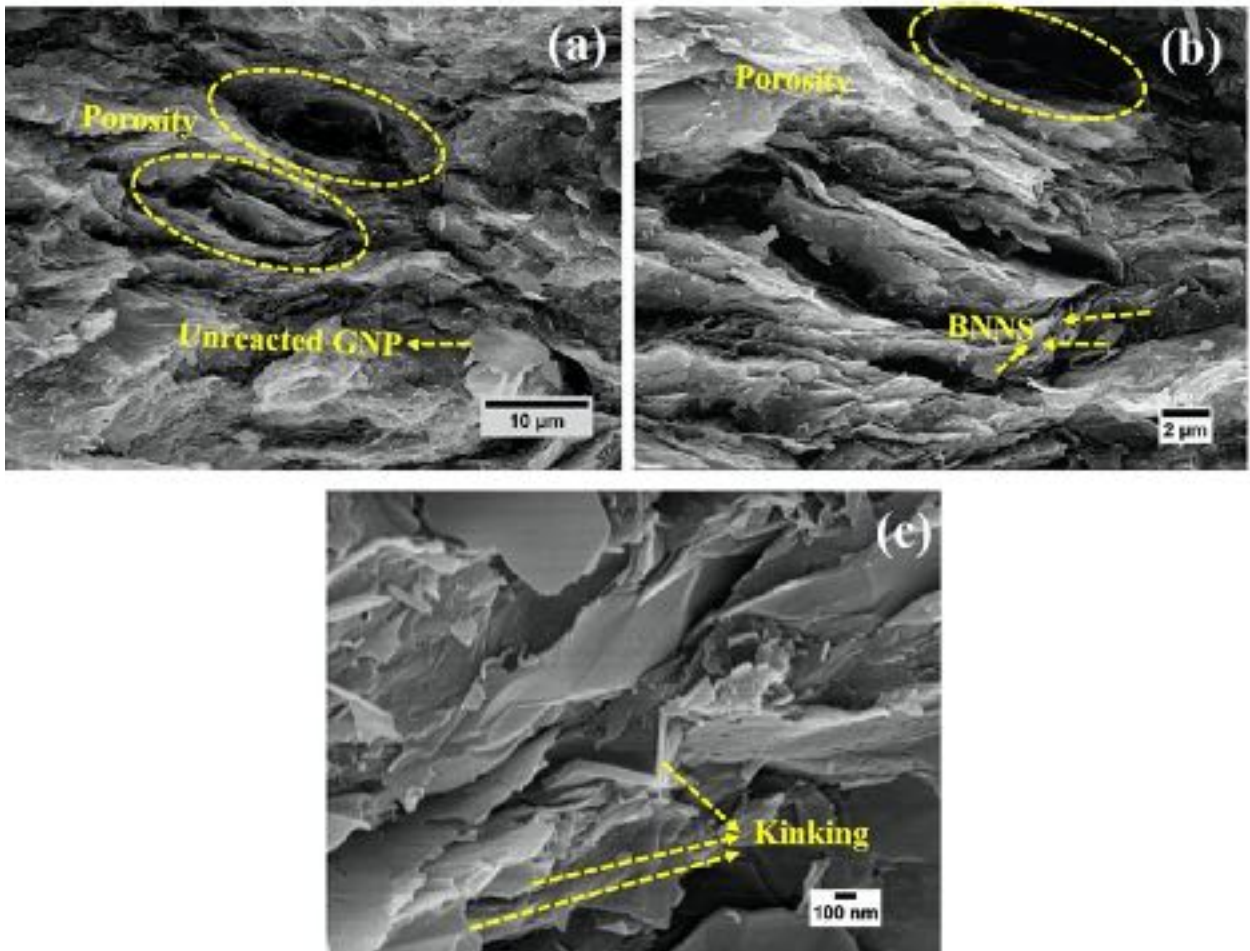


Figure 4.30: SEM images of BCN1 pellet fracture surface indicating (a) unreacted GNP, porosity, (b) unreacted BNNS, zig-zag fracture surface and (c) kinking

Figure 4.31 shows the fracture surface SEM images of BCN 2 (1650 °C, 30 min) pellet. Dense and textured regions were observed in the reactive sintered BCN 2 pellet. This correlates with increase in relative density of the BCN 2 pellet to 93.4% compared to the BCN 1 pellet. The edges of the nanosheets were less zig-zag in nature and the fracture surface was more undulating in nature (Fig. 4.31(a)). Large reacted regions were observed in the fracture surface of BCN 2 pellet. Figure 4.31(b) shows very few regions of unreacted BNNS and GNP compared to the BCN 1 pellet. The sintered nanosheets showed lamellar structure and similar to BCN 1, preferred orientation was observed for the reaction sintered BCN 2 pellet.

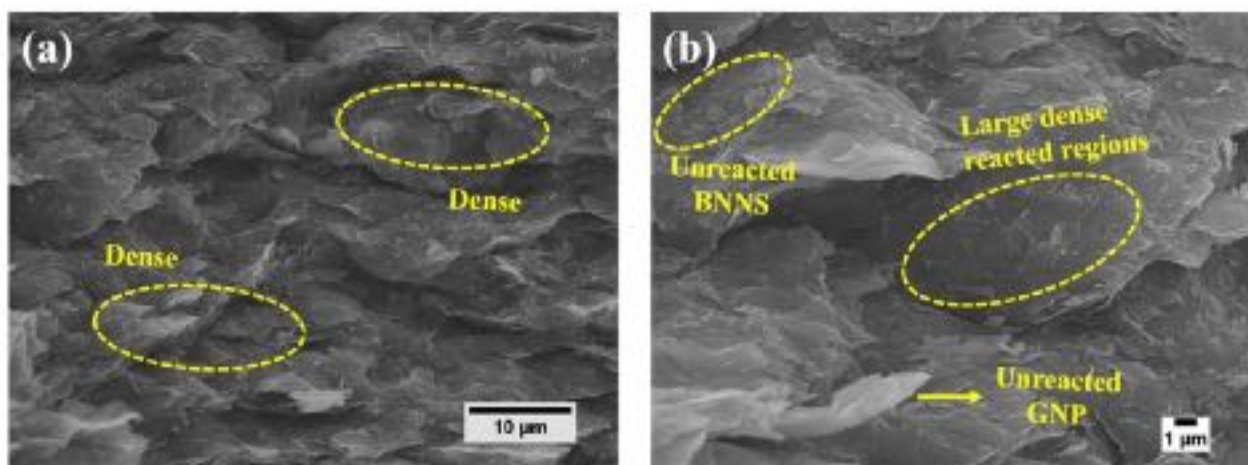


Figure 4.31: SEM images of BCN 2 pellet fracture surface showing (a) dense regions and (b) large reacted regions with few unreacted BNNS and GNP

The fracture surface of BCN 3 (1750 °C, 10 min) pellet are shown in Figure 4.32. The SEM images of the BCN 3 pellet fracture surface displays dense layered structure with a wavy form as shown in Figure 4.32(a). Few interlayer gaps were observed between the sintered sheets, which could be corroborated to the slight decrease in density to 93.2% compared to BCN 2. The increase in sintering temperature to 1750 °C has resulted in large reacted dense regions with few unreacted BNNS/GNP (Fig. 4.32(b)). Also, less bending or folding of nanosheets were observed compared to the BCN 1 fracture surface. Most of the nanosheets were arranged in the layered form. Evidence of reaction sintered multiple nanosheets (Fig. 4.32(c)) were observed at several regions of fracture surface. In addition, the large graphene nanosheets showed regions with reacted and sintered BNNS. These observations were mostly seen in the fracture surface BCN 2 and BCN 3 pellets, suggesting the boron-carbon-nitride phase formation.

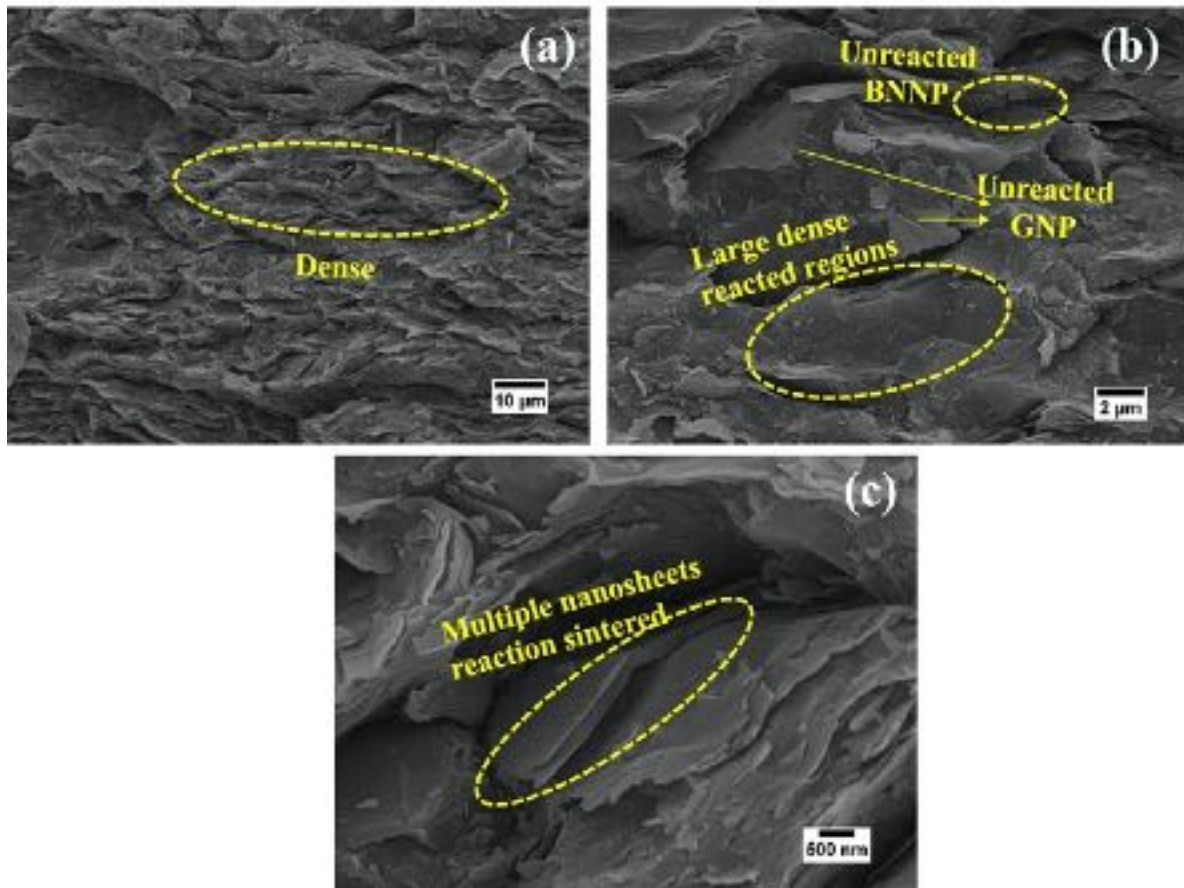


Figure 4.32: SEM images of BCN 3 pellet fracture surface indicating (a) dense regions with lamellar structure, (b) large reacted regions with few unreacted BNNPs and GNPs and (c) multiple nanosheets reaction sintered

4.2.5. Effect of Texture Orientation of Spark Plasma Sintered BCN

In the X-ray diffraction patterns of the reactive sintered BCN pellets, all the three sintering conditions displayed strong intense peak around $\sim 26^\circ$, implying the preferred orientation of nanosheets along the (0002) basal plane. Also, the fracture surface of reactive sintered BCN pellets showed lamellar structure along the top surface. Texture studies were carried out using pole-figure method to discern the role of reactive sintering process on preferred orientation of 2D nanosheets along the top surface and cross-section. The pole figures of BCN 1 (1650 °C, 10 min) pellet top surface and cross-section are shown in Figure 4.33. The concentric shapes with stronger intensity were concentrated at the center of the (0002) basal plane figure as shown in Figure 4.33(a). This clearly explains the nanosheets in the top surface

of reactive sintered BCN 1 pellet were preferentially oriented along the (0002) basal plane and the volume fraction of grains with (0002) plane have increased. The concentration of other orientations, namely $(10\bar{1}1)$ and $(10\bar{1}0)$ planes displayed less concentric shapes with no intensity at the center of pole figures. This study clearly suggest during reactive spark plasma sintering the c-axis of the 2D materials were aligned parallel to the loading direction, where the nanosheets were rotated perpendicular to the loading direction. In hexagonal materials, this preferred orientation of basal plane $\{0001\}$ is most widely observed [56]. The pole figures of the reactive sintered BCN 1 pellet cross-section surface are shown in Figure 4.37 (b). The pole figures of $(10\bar{1}1)$ and $(10\bar{1}0)$ planes showed isolines of very low intensity at the center, comparatively the pole figure of $(10\bar{1}1)$ plane had the isoline concentration slightly more in the center. This demonstrates along the cross-section of the BCN 1 pellet, the preferred orientation was along the $(10\bar{1}1)$ plane. There was no trace of texture along the basal planes as there were no isolines observed at the center of (0002) pole figure of the cross-section. Overall the cross-section has weaker texture compared to top surface of BCN 1 pellet. The top surface pole figures of BCN 2 and BCN 3 pellet (Fig. 4.34(a) and 4.35(a)), demonstrated at the center with highly concentrated concentric lines, insinuating high degree of preferred orientation along the (0002) basal plane and this was similar to the top surface of BCN 1 pellet. Similarly the cross-section of BCN 2 (1650 °C, 30 min) and BCN 3 (1750 °C, 10 min) pellet (Fig. 4.34(b) and 4.35(b)) pole figures showed weak contour lines at the center for $(10\bar{1}1)$ and $(10\bar{1}0)$ planes, and there were no contour lines seen at the center of (0002) pole figures. Thus, cross-section shows slight texturing along the $(10\bar{1}1)$ plane for the BCN 2 and BCN 3 pellet. Overall, the top surface of monolithic BCN pellets texture studies have revealed the dominance of (0002) basal plane texture and the cross-section of monolithic BCN pellets have shown the weak texturing of $(10\bar{1}1)$ pyramidal plane texture (Fig. 4.36). The possible mechanism of the basal plane texturing in the reactive sintered BCN pellet is related to the uniaxial pressure in

the pressing direction, where the high aspect ratio nanosheets rotate and align with basal planes perpendicular to the pressing direction. Further to discern the texturing characteristics of reactive sintered BCN pellets along the top surface and cross-section, from the pole figures of (0002) and (10 $\bar{1}$ 1) planes the relative volume fraction of the textured components for all the three samples were calculated [56, 57]. The relative volume fraction of the textured components are shown in Figure 4.37. The relative volume fraction of (0002) basal plane texture along the top surface increased with longer dwell time (BCN 2) and higher sintering temperature (BCN 3). Likewise, relative volume fraction of (10 $\bar{1}$ 1) pyramidal plane texture along the cross-section increased with longer dwell time (BCN 2) and higher sintering temperature (BCN 3). The degree of preferred orientation for the reactive sintered 2D BCN nanosheets can be improved with higher sintering temperature and longer dwell time. The above observations imply the reactive sintering temperature and dwell time play a significant role in the orientation of 2D nanosheets.

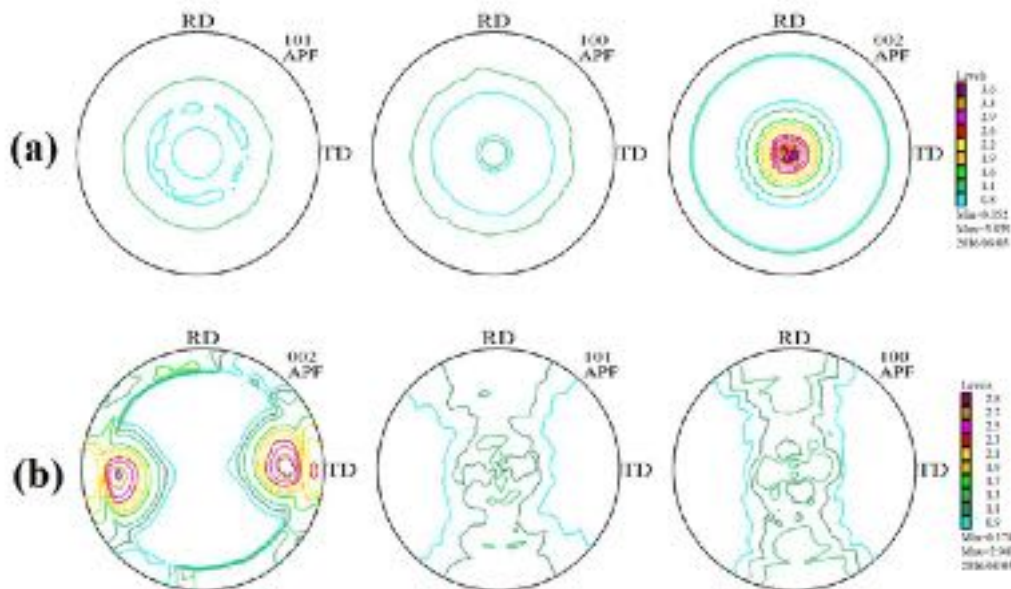


Figure 4.33: Texture studies of reactive sintered BCN 1 (002), (101), (100) pole figures along the (a) top surface and (b) cross-section of the pellet

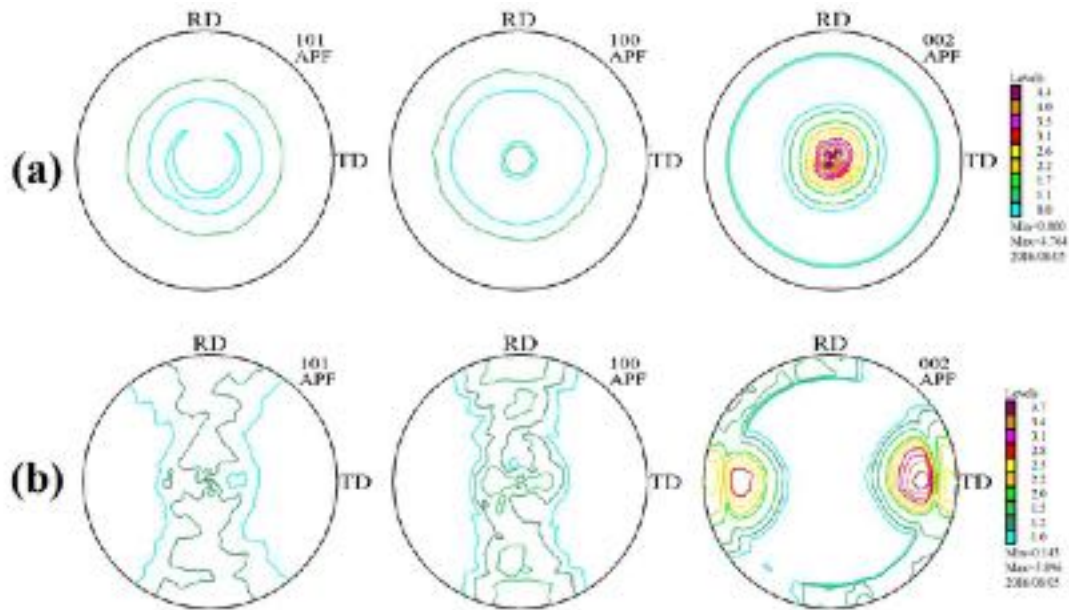


Figure 4.34: Texture studies of reactive sintered BCN 2 (002), (101), (100) pole figures along the (a) top surface and (b) cross-section of the pellet

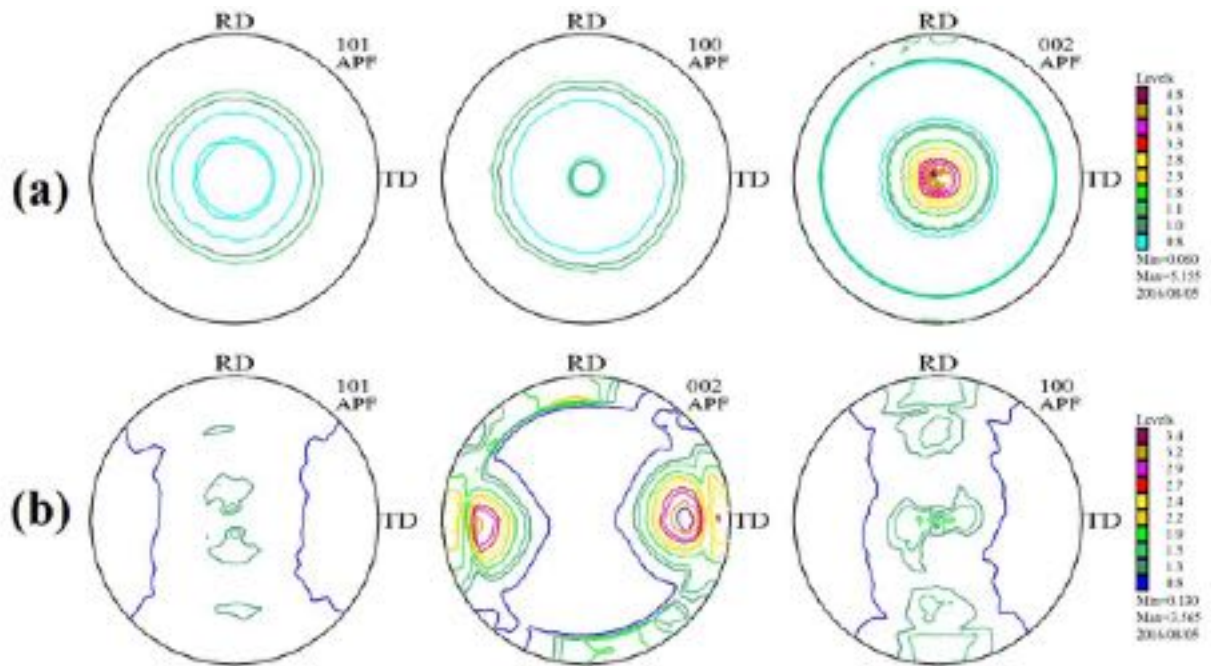


Figure 4.35: Texture studies of reactive sintered BCN 3 (002), (101), (100) pole figures along the (a) top surface and (b) cross-section of the pellet

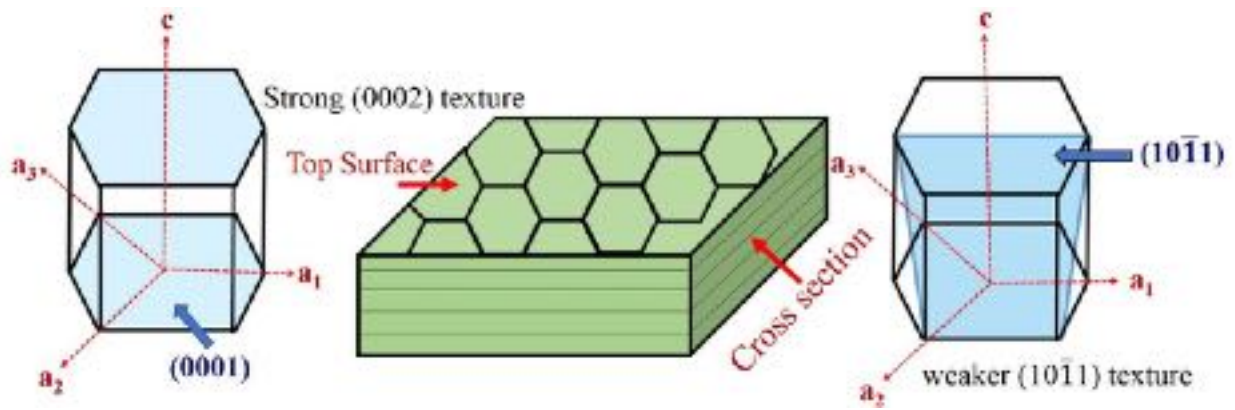


Figure 4.36: Schematic drawing of the sintered BCN pellet indicating the region of texture along top surface and cross-section. Simple hexagonal system is marked with the basal plane (0002) and pyramidal plane (10 $\bar{1}1$)

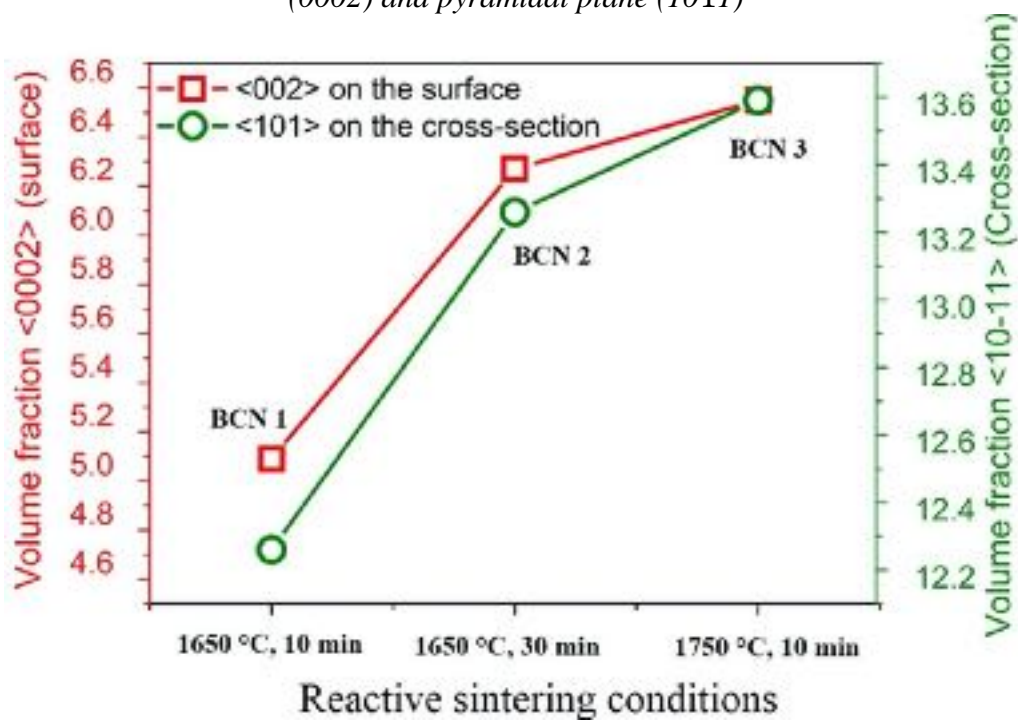


Figure 4.37: Relative volume fraction of textured components for the reactive sintered BCN pellets

4.2.6. Mechanical Properties of Monolithic BCN

4.2.6.1. Microhardness of Monolithic BCN

Using Vickers hardness test, microhardness of the reaction sintered BCN pellets was measured along the polished top surface and cross-section. Five indentations were made on the top surface and cross-section of the BCN pellets to obtain the average microhardness. The measured hardness values are tabulated in Table 4.4. The microhardness of BCN 3 (1750 °C,

10 min) pellet showed about ~16- 23% higher hardness along the top surface compared to BCN 1 and BCN 2 pellets top surface. Along the cross-section, BCN 3 pellet showed about ~2-9% higher hardness compared to BCN 1 and BCN 2 pellets. In comparison to pure BNNS and GNP sintered pellets, BCN 3 pellet demonstrated higher hardness along the top surface and cross-section. The higher hardness of BCN 3 pellet suggest the change in bonding nature of B-N/C-C atoms in the BNNS/GNP and the reaction synthesis process at higher sintering temperature resulted in strong B-C-N bond formation.

Table 4.4: Microhardness of the reaction sintered BCN pellets

Sample	Top Surface (MPa)	Cross-section (MPa)
BCN 1 (1650 °C, 10 min)	413 ± 21	503 ± 35
BCN 2 (1650 °C, 30 min)	438 ± 05	536 ± 14
BCN 3 (1750 °C, 10 min)	509 ± 20	548 ± 19
BNNS SPS	492 ± 20	281 ± 30
GNP SPS	296 ± 12	-

4.2.6.2. Nanomechanical Properties: Reduced Elastic Modulus and Hardness of Monolithic BCN

The reduced elastic modulus and nano-hardness of the reaction sintered BCN pellets were experimentally measured along the top surface and cross-section of the pellet using nanoindentation. Table 4.5 shows the measured hardness and reduced elastic modulus values obtained by nanoindentation test from the reaction sintered BCN pellets. The top surface reduced elastic modulus of the BCN 3 pellet was 17.13 ± 1.55 GPa and hardness was 0.503 ± 0.042 GPa. For the cross-section, the measured reduced elastic modulus was 22.73 ± 2.93 GPa and hardness was 0.458 ± 0.053 GPa. BCN 3 pellet showed higher hardness and reduced elastic modulus compared to the BCN 1 and BCN 2 samples. This is ascribed to the h-BCN, c-BCN phase formation with improved densification for BCN 3 pellet. The hardness on the top surface

of all the three reaction sintered BCN pellets was higher compared to their cross-section, due to their strong texturing along the basal plane and the nature of B-C-N bonding within the basal plane. In addition, the cubic BCN formation in the BCN 2 and BCN 3 pellets will contribute in improving the hardness along the top surface and cross-section compared to BCN 1 pellet. The change in bonding nature of B-N/C-C to B-C-N along the top surface will enhance the resistance to deformation. Along the cross-section of BCN pellets, weak bonding between the sheets (interlayer gap) were observed with weak Van der Waals force between the nanosheets will lower the hardness. The cross-section of the reaction sintered BCN pellets displayed higher elastic modulus compared to the top surface because of the high in-plane properties of the 2D materials [22, 58].

Table 4.5: Nanohardness and reduced elastic modulus of the reaction sintered BCN pellets

Sample	Indentation Direction	Reduced Modulus (GPa)	Hardness (GPa)
BCN 1 (1650 °C, 10 min)	Top Surface	15.22 ± 1.35	0.425 ± 0.031
	Cross Section	20.29 ± 2.71	0.356 ± 0.057
BCN 2 (1650 °C, 30 min)	Top Surface	14.99 ± 2.31	0.443 ± 0.034
	Cross Section	23.52 ± 3.34	0.423 ± 0.06
BCN 3 (1750 °C, 10 min)	Top Surface	17.13 ± 1.55	0.503 ± 0.042
	Cross Section	22.73 ± 2.93	0.458 ± 0.053
BNNS	Top Surface	28.49 ± 5	1.15 ± 0.17
	Cross Section	40.79 ± 11.09	0.609 ± 0.12
GNP [22]	Top Surface	8.7 ± 1.3	0.6 ± 0.13
	Cross Section	10.3 ± 2.9	0.28 ± 0.02

4.2.7. Tribological Behavior of Monolithic BCN

Tribological behavior of the reactive sintered BCN samples for all the three conditions is studied using the ball-on-disk tribometer. The coefficient of friction (COF), wear volume loss and wear resistance are quantified for all the BCN samples at room temperature (25 °C)

and high temperature (600 °C). Figure 4.38 shows the coefficient of friction at room temperature for the reactive sintered BCN samples with normal load of 3 N and 3 mm track radius. The average coefficient of friction of BCN 1 is 0.165, BCN 2 is 0.173 and BCN 3 is 0.189. Compared to the average COF of BCN 1, the COF increased about ~4.85% with increase in holding time (BCN 2) and ~14.55% with increase in sintering temperature (BCN 3). The average COF for all the three BCN samples are higher than COF of bulk BNNS (0.145) and GNP (0.160) of same testing conditions. The increase in COF is ascribed to the formation of new phase – cubic BCN along with hexagonal BCN, h-BNNS and GNP. The cubic BCN is hard phase and the presence of this hard phase in the soft hexagonal matrix results in the increase in COF for BCN 2 and BCN 3.

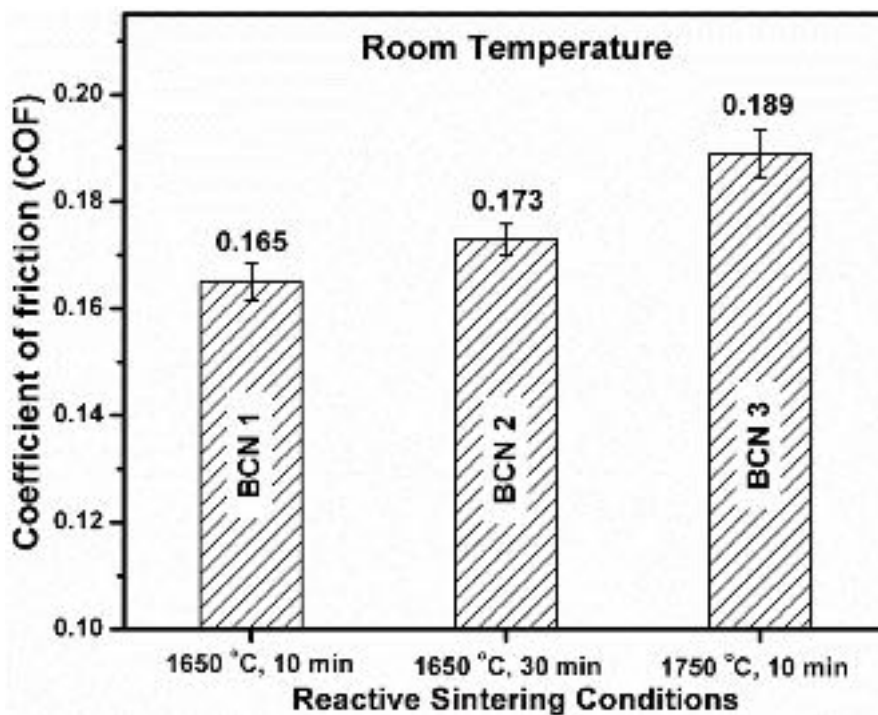


Figure 4.38: Coefficient of friction vs reactive sintering conditions for the bulk BCN pellets at room temperature

From the optical profiles of 3D wear track, the depth of wear track was measured for the reactive sintered BCN pellets as shown in Figure 4.39. The wear depth of BCN 1 pellet is about 17 μm , the depth increases to 24 μm for BCN 2 pellet and 30 μm for BCN 3 pellet. From the average wear depth, the cross-sectional area of the track is calculated and this is multiplied

with the circumference of the track to measure the wear volume loss. The average wear volume loss and wear rate for reactive sintered BCN pellets are tabulated in Table 4.6. Wear volume loss for the BCN 1 pellet is $0.0512 \pm 0.001 \text{ mm}^3$, for BCN 2 pellet is $0.1078 \pm 0.006 \text{ mm}^3$ and BCN 3 pellet is $0.6701 \pm 0.031 \text{ mm}^3$. Compared to BCN 1 pellet, wear volume loss was higher for BCN 2 and BCN 3 pellets. Based on the equation below, wear rate was computed,

$$\text{Wear rate} = V/(P \times S) \quad (\text{mm}^3/\text{Nmm}) \quad (4.5)$$

where the volume loss is represented as $V \text{ (mm}^3\text{)}$, applied load is $P \text{ (N)}$ and sliding distance is $S \text{ (mm)}$. For the reactive sintered BCN pellets, the calculated wear rate values are listed in Table. For BCN 2 and BCN 3, the wear rate increased by 110% and 547% respectively, compared to BCN 1 wear rate. The wear properties of BCN 2 and BCN 3 attenuates compared to BCN 1, this is ascribed to the formation of hard phase cubic BCN (in BCN 2 and BCN 3), resulting in significant delamination of nanosheets in the wear track as shown in the SEM images.

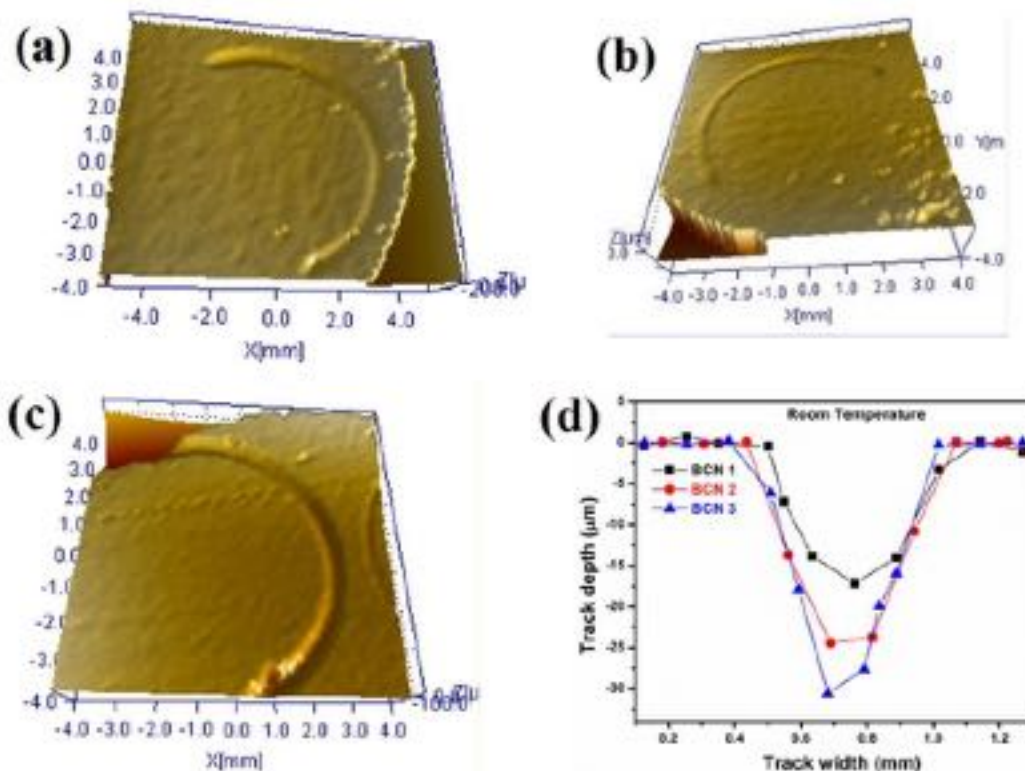


Figure 4.39: Optical profilometer 3D wear track profiles of (a) BCN 1, (b) BCN 2, (c) BCN 3 and (d) two-dimensional line profiles displaying the wear track depth and width of BCN pellets tested at room temperature

Table 4.6: Wear volume loss and wear rate of reactive sintered BCN pellets tested at room temperature

Sample	Volume loss (mm ³)	Wear rate (mm ³ /Nmm)
BCN 1	0.0512 ± 0.001	5.69 X 10 ⁻³
BCN 2	0.1078 ± 0.006	11.98 X 10 ⁻³
BCN 3	0.6701 ± 0.031	36.85 X 10 ⁻³

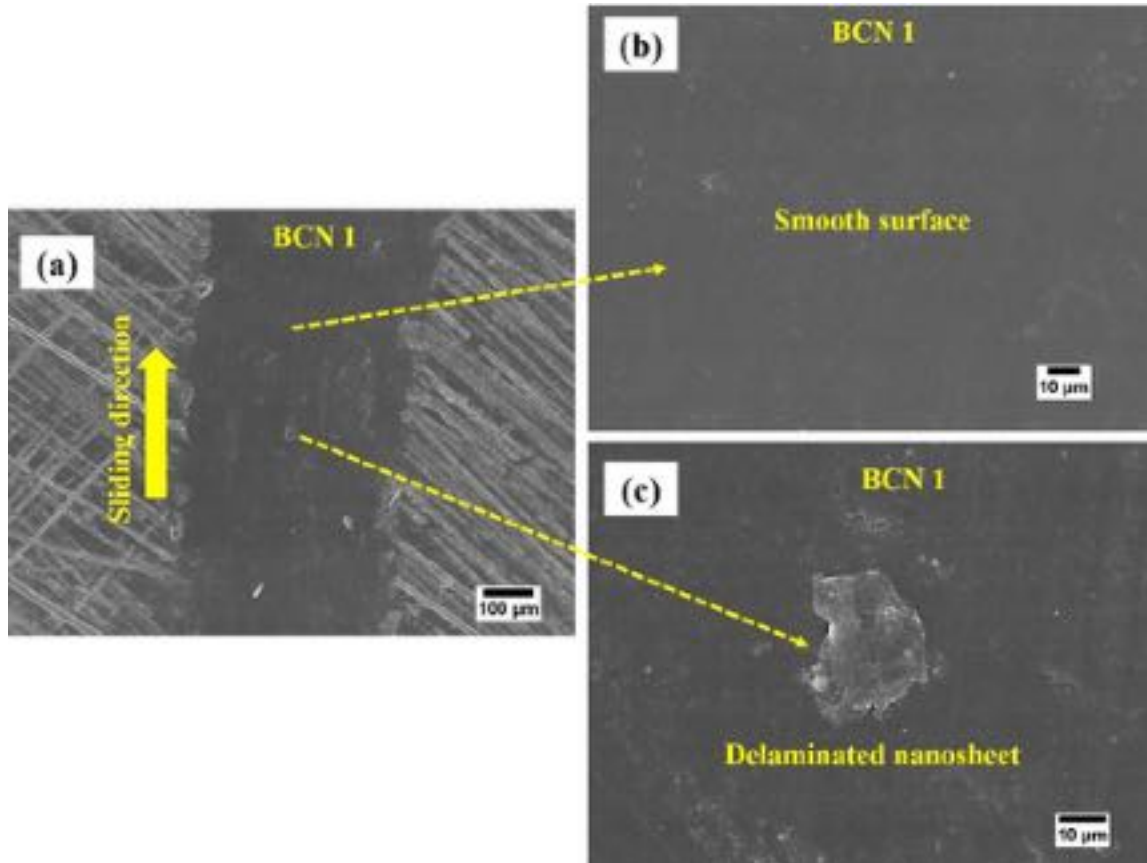


Figure 4.40: SEM micrographs of BCN 1 wear track formed after the wear test at room temperature

To understand the wear mechanism at room temperature of reactive sintered BCN samples, the wear track were examined using SEM. Figure shows the wear track of BCN 1 sample at different magnifications. The sliding direction of the wear track is shown in Figure 4.40(a). The wear track of BCN 1 samples displays a smooth surface with minimum damage or material removed along the track surface (Fig. 4.40(b)). Some regions of the wear track showed fine wear debris attached to the surface. Delamination of nanosheets was observed in the wear track surface of Figure 4.40(c). Due to this, there was pit formation along the wear

track. Overall, less fraction of delamination or pit formation was observed on the wear track surface of reactive sintered BCN 1 samples. The delaminated nanosheets were bend, folded and welded along the wear track surface, which are the typical characteristics of two-dimensional graphene and boron nitride [22]. The lower coefficient of friction and smooth wear track surface of BCN 1 samples are germinated by the shearing of the layered 2D nanosheets and this is due to the weak van der Waals force between the nanosheets [14, 22].

The room temperature test wear track surface of BCN 2 sample at different magnifications are shown in Figure 4.41. The BCN 2 wear track surface and sliding direction at low magnification is shown in Figure 4.41(a). In this sample, the track surface has a combination of smooth and rough surface. The smooth surface is created by the large delaminated nanosheet in the track surface and these nanosheets shear when the ball rotates along the track surface (Fig. 4.41(b)). Few of the nanosheets were found as loose nanosheets on the surface, while some nanosheets were welded along the track. Typical deformation features such as kinking, bending and folding of 2D nanosheets were observed. These features shows the adhesive wear nature of BCN 2 sample. In addition, the wear track surface displayed features related to adhesive wear. The track surface have large and small pits formed by delamination of sintered nanosheets (Fig. 4.41(c)). Since the BCN 2 sample has the presence of hard cubic BCN phase, the track surface should have a combination of both soft and hard material, resulting in abrasive wear. Due to this, the material removed from the track surface during continuous testing will form the fine wear debris along the track. The delamination germinates the micro-crack formation and these cracks propagate. The micro-cracks formed are intergranular in nature (Fig. 4.41(c)). The cracks formed on the track has propagated along the surface and below the surface of BCN 2 sample. This combination of adhesive and abrasive wear causes the increase in coefficient of friction and wear volume loss of BCN 2 compared to BCN 1 sample.

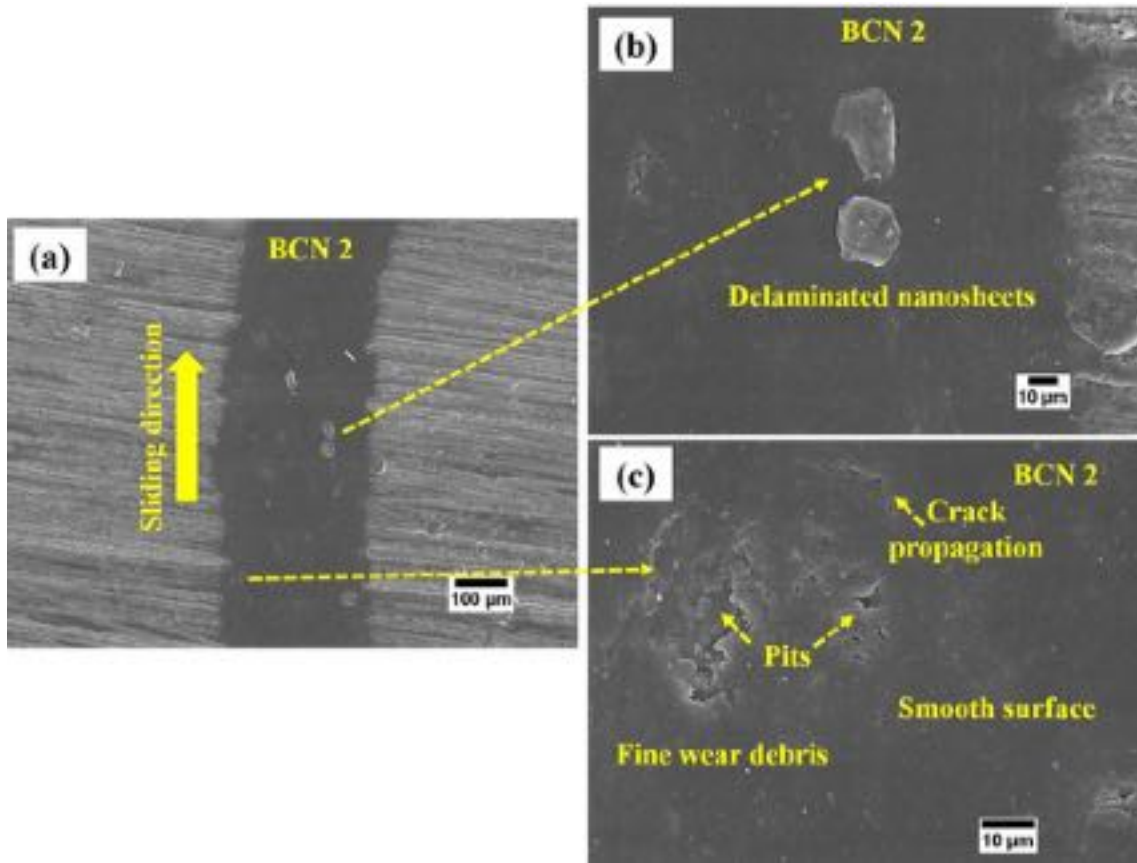


Figure 4.41: SEM micrographs of BCN 2 wear track formed after wear test at room temperature

Reactive sintered BCN 3 sample wear track surface of room temperature test is shown in Figure 4.42. The Figure 4.42(a) shows the low magnification image of BCN 3 wear track and sliding direction. The BCN 3 track surface displays a rough surface with significant amount of visible deformation. Hard cubic BCN phase formation is predominantly observed in XRD and TEM studies, suggesting the hard phase could result in severe wear and deformation in track surface. It can be seen from Figure 4.42(b), the worn surface has delaminated nanosheets, pits, micro-cracks, fragmented wear debris and rough track surface. The delaminated nanosheets of varying size were along the wear track as loose nanosheets and some nanosheets were compacted to the track surface. Upon continuous rolling of counter material during the test, delaminated nanosheets are rolled, bend, folded or crumbled in the track surface, indicating the deformation of nanosheets. Varying size of pits are formed due to delamination and these pits are present on the surface of wear track. Also, the micro-cracks are formed in

succession to delamination of nanosheets. These micro-cracks propagate in the surface and to certain depth of wear track during the wear test. Intergranular type of micro-cracks are formed on the surface (Fig. 4.42(c)). The hard phase removed from the track surface created scratches and grooves along the sliding direction. All these observations, justify the increase in coefficient of friction and wear volume loss for the BCN 3 sample. The dominant wear mechanism for the reactive sintered BCN 3 sample is delamination and abrasive wear. The room temperature wear test of the BCN samples, suggest the change in wear mechanism from shearing of nanosheets/abrasive to adhesive wear mechanism with the emergence of hard cubic BCN phase.

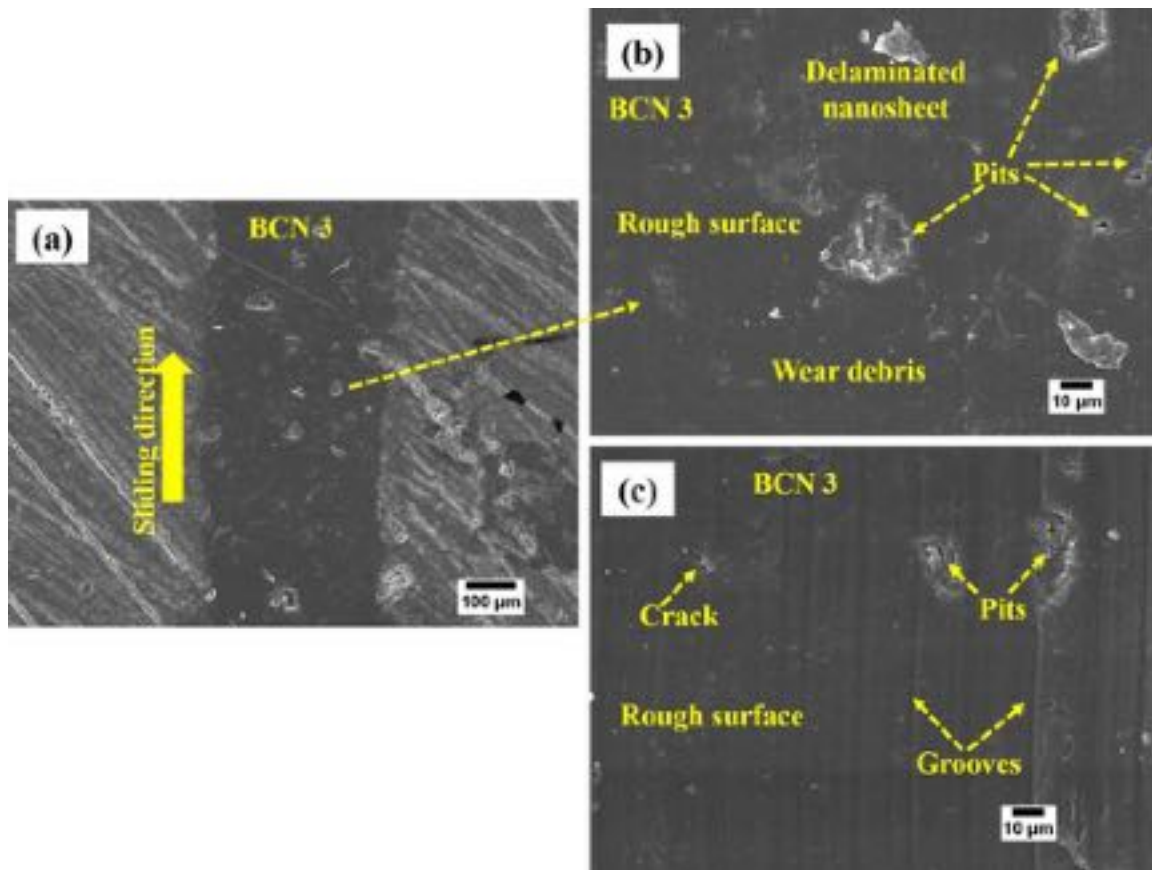


Figure 4.42: SEM micrographs of BCN 3 wear track formed after wear test at room temperature

The high temperature tribological behavior of all three reactive sintered BCN samples were tested at 600 °C. The coefficient of friction at high temperature for BCN samples with normal load of 3 N and 3 mm track radius are shown in Figure 4.43. The high temperature

average coefficient of friction of BCN 1 is 0.131, BCN 2 is 0.121 and BCN 3 is 0.116. For BCN 2 and BCN 3, the coefficient of friction decreased by 7.6% and 11.5% respectively, compared to the BCN 1 friction. Compared to coefficient of friction of room temperature BCN, BNNS and GNP, the coefficient of friction has decreased by ~ for the high temperature BCN samples. In addition, the high temperature BCN coefficient of friction (0.131-0.116) is ~80-82% lower than the high temperature BNNS coefficient of friction (0.656). The decrease in coefficient of friction during high temperature test (600 °C) is attributed to the oxidation of the sintered nanosheets. Though the test temperature is well below the oxidation temperature of BN to form boron oxide, the continuous sliding motion will increase the surface temperature at the point of contact of BCN pellet and this will result in the formation of B₂O₃ along the surface. The B₂O₃ formed on the surface can react with moisture in air to form H₂BO₃. The presence of B₂O₃/H₂BO₃ on the wear track surface will lower the coefficient of friction of BCN pellets during high temperature wear test [59].

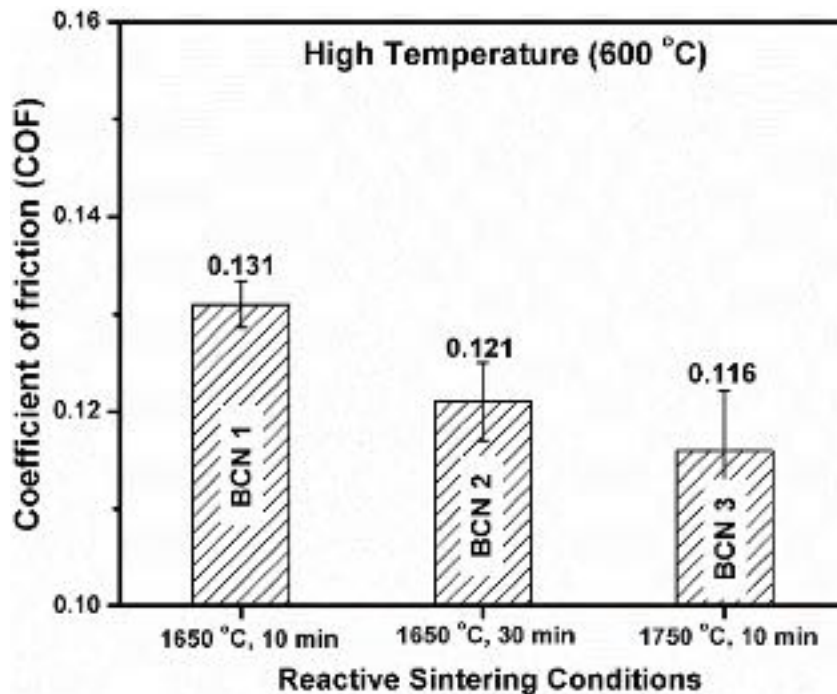


Figure 4.43: Coefficient of friction vs reactive sintering conditions for the bulk BCN pellets at high temperature

Using the 3D wear track optical profiles of reactive sintered BCN pellets high temperature wear test, the wear track depth was measured as shown in Figure 4.44. The high temperature test wear depth of BCN 1 pellet is 17 μm , the depth decreased to 14 μm for BCN 2 pellet and 11 μm for BCN 3 pellet. The average wear volume loss and wear rate for high temperature wear test of reactive sintered BCN pellets are tabulated in Table 4.7. Wear volume loss for the BCN 1 pellet is $0.049 \pm 0.002 \text{ mm}^3$, for BCN 2 pellet is $0.040 \pm 0.015 \text{ mm}^3$ and BCN 3 pellet is $0.034 \pm 0.007 \text{ mm}^3$. Compared to BCN 1 and BCN 3 pellet, wear volume loss was lower for BCN 2 pellet. Using equation (4.5), the wear rate was calculated for high temperature wear test of BCN pellets. The wear rate decreased by 2.5 % for BCN 2 and by 37.5 % for BCN 3, compared to BCN 1 wear rate. This decrease in volume loss and wear rate of BCN 2/BCN 3 are associated with B_2O_3 formation, resulting in smooth wear track as shown in SEM images.

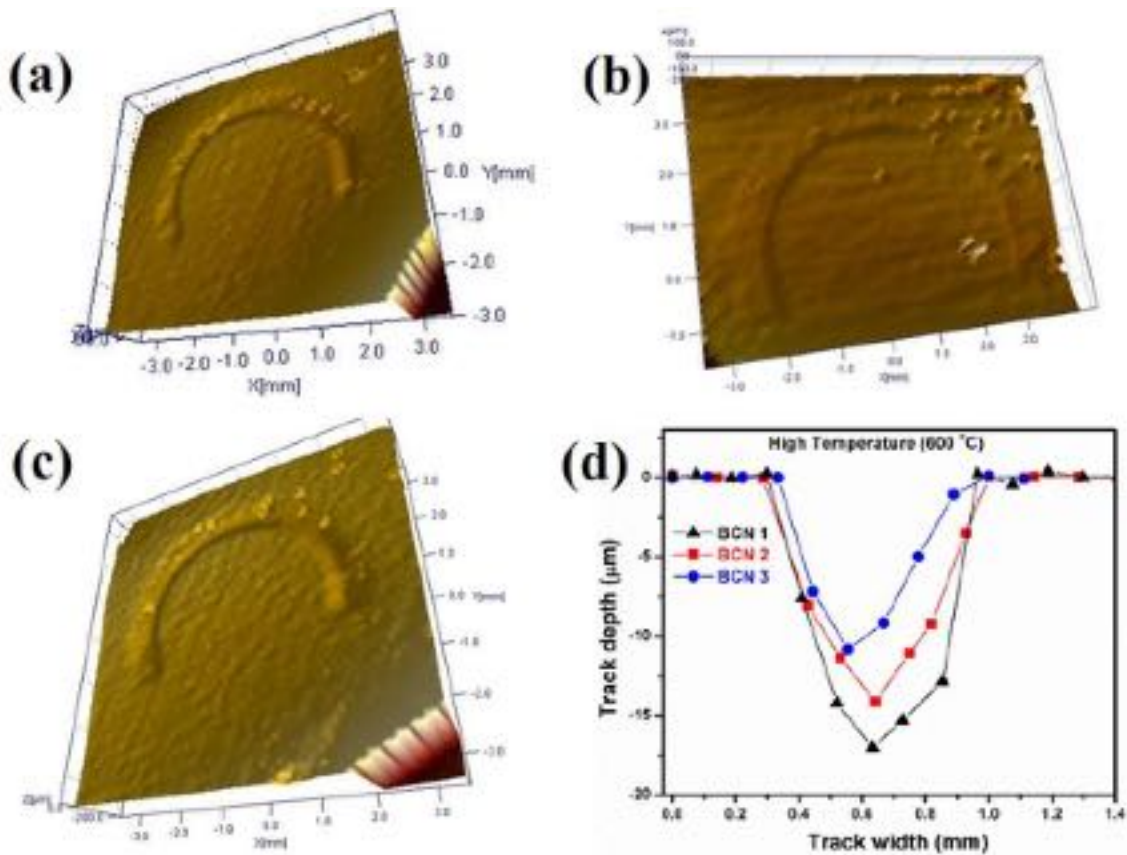


Figure 4.44: Optical profilometer 3D wear track profiles of (a) BCN 1, (b) BCN 2, (c) BCN 3 and (d) two-dimensional line profiles displaying the wear track depth and width of BCN pellets tested at high temperature

Table 4.7: Wear volume loss and wear rate of reactive sintered BCN pellets tested at high temperature

Sample	Volume loss (mm ³)	Wear rate (mm ³ /Nmm)
BCN 1	0.049 ± 0.002	1.73 X 10 ⁻⁶
BCN 2	0.040 ± 0.015	1.69 X 10 ⁻⁶
BCN 3	0.034 ± 0.007	1.08 X 10 ⁻⁶

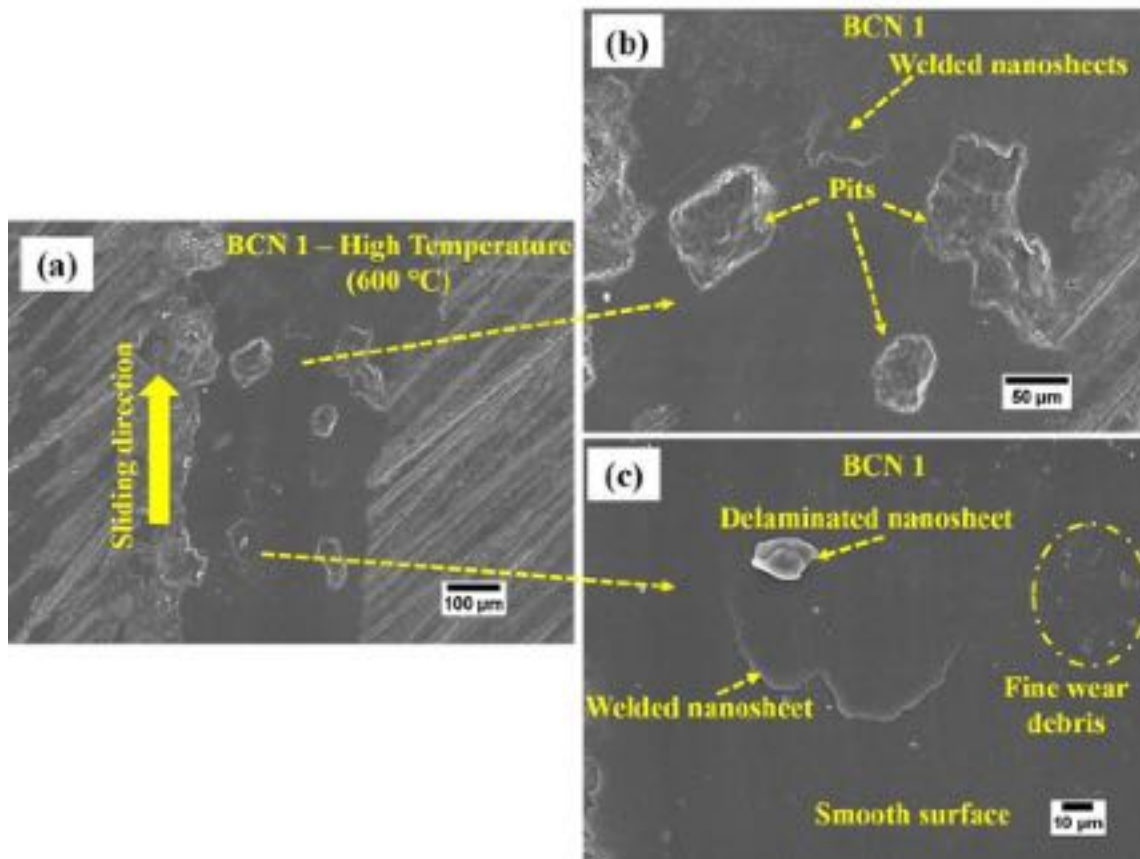


Figure 4.45: SEM micrographs of BCN 1 wear track formed after wear test at high temperature

Using SEM images, the high temperature wear test of reactive sintered BCN samples wear mechanisms are investigated. Figure 4.45 shows the high temperature test wear track of BCN 1 sample at different magnifications. In the Figure 4.45(a), lower magnification of BCN 1 wear track with the sliding direction is shown. The high temperature test wear track for the BCN 1 sample shows large pits, indicating significant material removed from the track surface (Fig. 4.45(a)). Between these pits, the large delaminated nanosheets are welded with the track surface and fine wear debris are spread across the wear track. In additions, the pits are deeper,

this is evident from the layered fracture observed in the pits surface (Fig. 4.45(b)). The delaminated nanosheets from the pits were present on the surface of wear track, in the deformed condition– bend and folded along the track. Smooth track surface is observed between the pits/delaminated nanosheets and this could be due to the tribofilm formation at high temperature (Fig. 4.45(c)). Regardless of pit formation, the track surface is smooth, and the wear debris is fine, these SEM observations support the lower coefficient of friction for BCN 1 high temperature wear test compared to BCN 1 room temperature wear test.

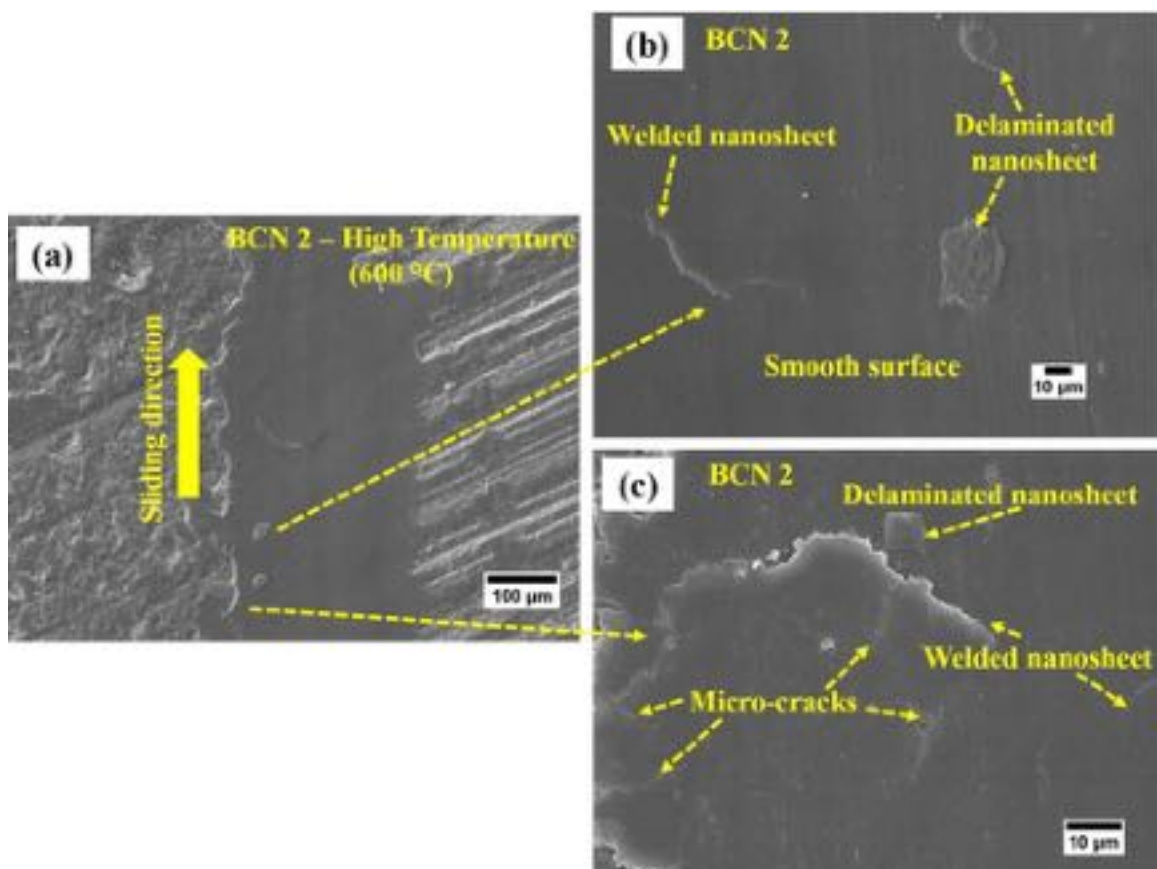


Figure 4.46: SEM micrographs of BCN 2 wear track formed after wear test at high temperature

Figure 4.46 shows the high temperature wear track images of reactive sintered BCN 2 sample at different magnification. The low magnification wear track image and sliding direction during the test are shown in Figure 4.46(a). The wear track surface of this sample is extremely smooth. The smooth surface is accompanied by few delaminated nanosheets. Some of the nanosheets are welded along the track surface as shown in Figure 4.46(b-c). These

welded nanosheets are not deformed by bending or folding. Most of the welded nanosheets are sintered with smooth surface along the wear track (Fig. 4.46(b)) and few other welded nanosheets displayed micro-cracks on the surface as shown in Figure 4.46(c). Few delaminated nanosheets with varying size are loosely present in the wear track and these nanosheets surface are crumbled in nature. In the wear track of BCN 2 high temperature test, there is no pits or wear debris found on the surface. In addition, at high temperature test, the tribofilm formation on the wear track surface will contribute in lowering the coefficient of friction for BCN 2 sample.

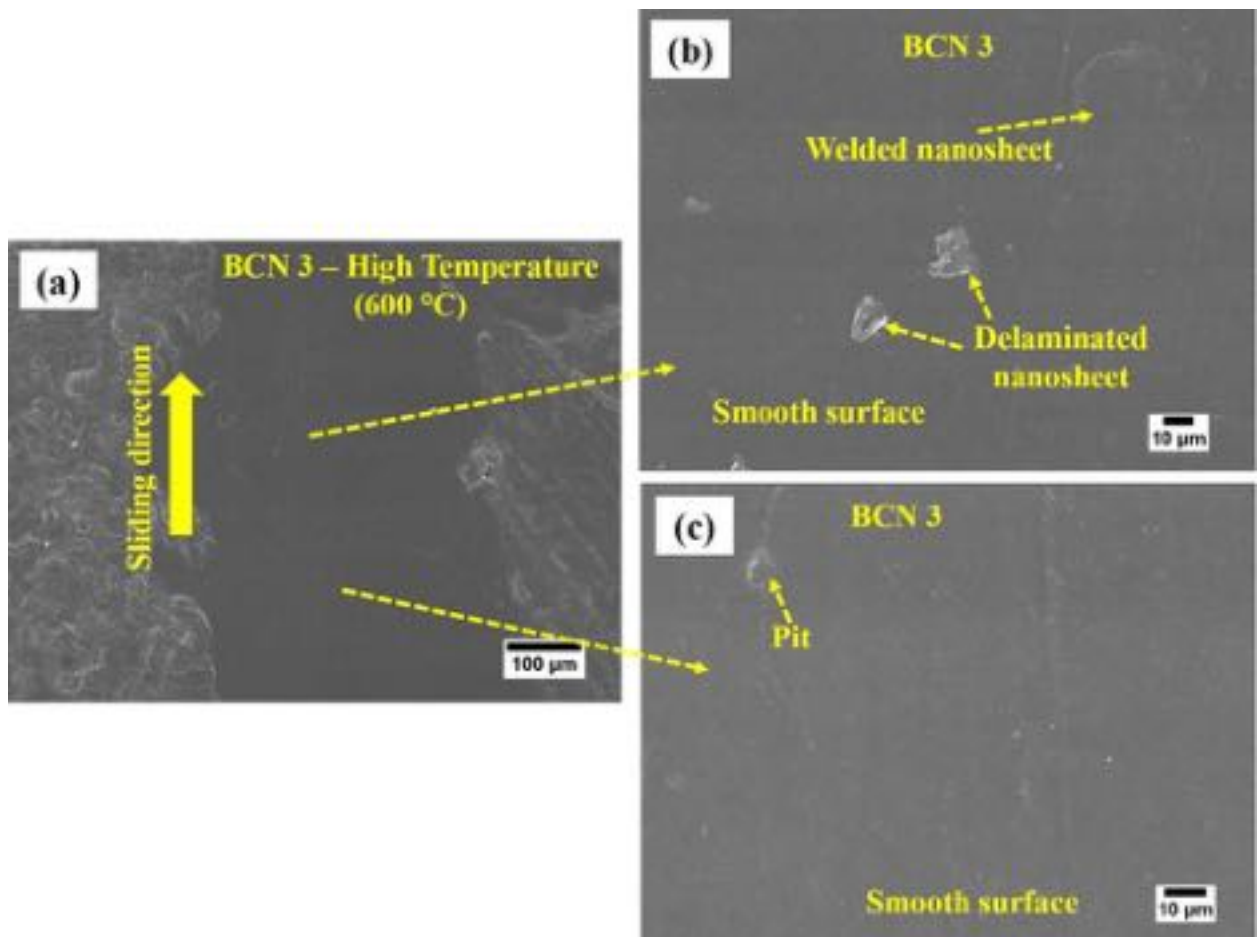


Figure 4.47: SEM micrographs of BCN 3 wear track formed after wear test at high temperature

The wear track surface of high temperature wear test for reactive sintered BCN 3 sample is shown in Figure 4.47. The low magnification image of BCN 3 wear track surface (Fig. 4.47(a)), indicates the sliding direction. The BCN 3 wear track surface is extremely smooth as

shown in high magnification Figure 4.47(b). The track surface has few delaminated nanosheets and these nanosheets are smaller in size, where they are sparsely distributed along the wear track. The delaminated nanosheets are deformed during the test by the continuous rolling of the counter ball, they are crumbled and folded as observed in Figure 4.47(b).

4.2.8. High Load In-situ Indentation Behavior of Monolithic BCN

High load in-situ indentation is performed for the polished bulk BCN pellets top surface. The displacement controlled mode is chosen for the indentation test with 0.5 mm of maximum displacement. The combined load-displacement curve of BCN pellets top surface is shown in Figure 4.48(a). To reach a fixed displacement of 0.5 mm, the maximum load required is 221.6 N for BCN 1, 272.8 N for BCN 2 and 134.2 N for BCN 3. Compared to BCN 1 and BCN 3 samples, higher load of 272.8 N was required for BCN 2 sample to reach the same 0.5 mm displacement. From the top surface high-load indentation loading curve, 5 major distinct slopes are observed for BCN 1 pellet (Fig. 4.48(b)), 3 major distinct slopes were observed for BCN 2 (Fig. 4.48(c)) and BCN 3 (Fig. 4.48(d)) pellets. The slope change in the load-displacement curve indicate, the change in deformation mechanism of the sintered nanosheets as the displacement occurs in the reactive sintered BCN pellets. Based on this, the normalized associated energy for the individual slope can be calculated and this can be related to the work of indentation (where the slope change remained the same over the total displacement range). For the BCN 3 top surface high-load indentation, the real-time video was recorded. By comparing the calculated normalized energy, the dominant deformation mechanism can be chosen based on the deformation mechanisms identified from the recorded video. In the Table 4.8, for the BCN 3 sample, the slope, time interval from the video, normalized associated energy for each slope and the corresponding deformation mechanism are summarized.

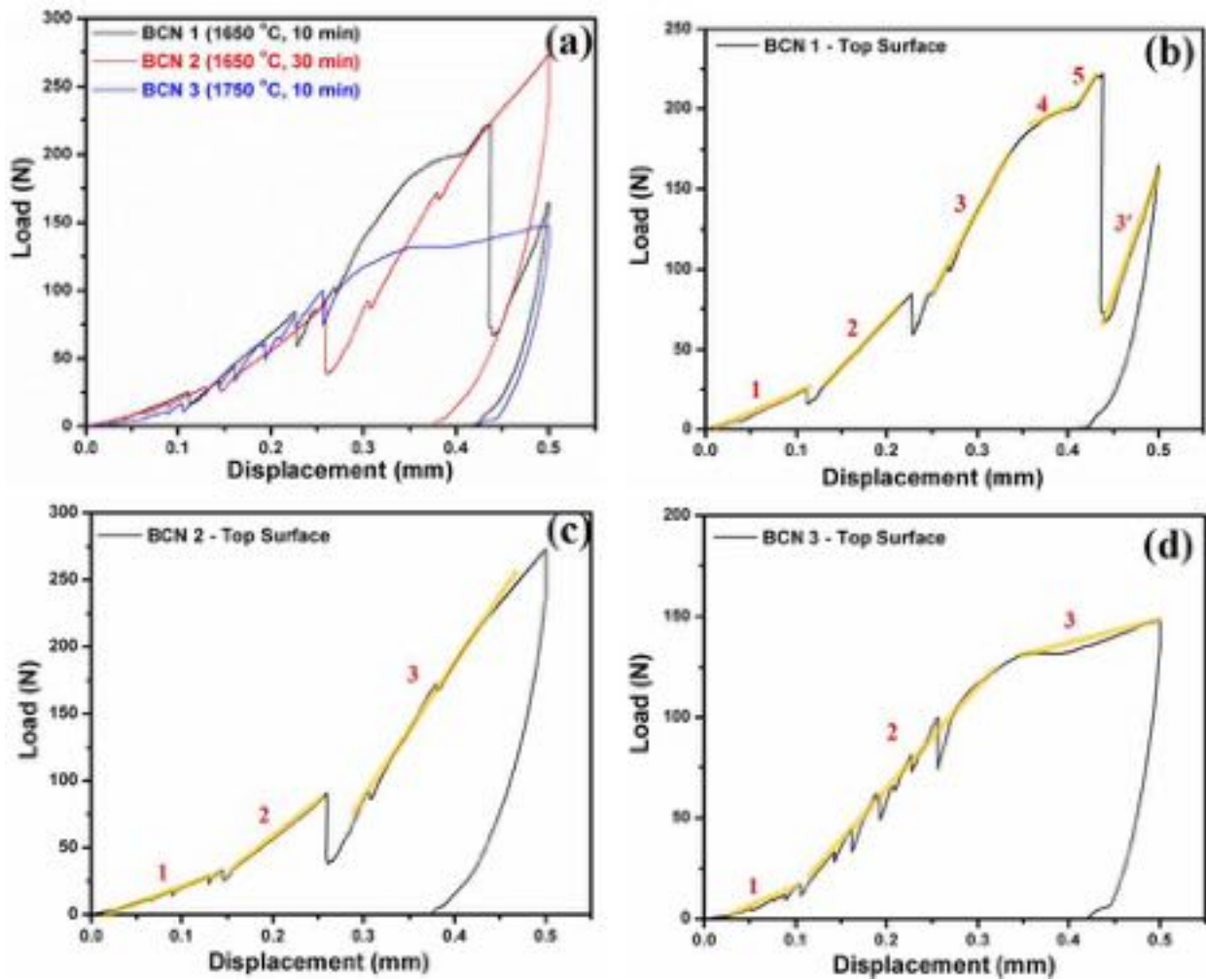


Figure 4.48: Top surface indent load-displacement (a) combined BCN curves, and the individual (b) BCN 1, (c) BCN 2, (c) BCN 3 curves

Table 4.8 presents the time duration, deformation mechanisms and normalized associated energy corresponding to each slope from the load-displacement curve and real time video of BCN 3 top surface indentation. As the indentation started (slope 1 region), the sintered nanosheet are compressed (Fig. 4.49(a)) followed by push out of the nanosheets. Slowly, the nanosheets are delaminated around the indenter region. With further displacement of the indenter on the top surface, the delaminated nanosheets are piled up and started sliding. In the middle of slope 1 regime as the displacements occurred, the nanosheets are continuously pushed out (Fig. 4.49(b)), due to the compression of sintered nanosheets. Delamination of the next layer of nanosheets has been initiated with pile-up of those nanosheets by end of slope 1. From the load-displacement curve of slope 1 region, at several displacement points, small drops

in load are observed. This could be associated to the push out and sliding of the sintered nanosheets. In the slope 2 region, compression of nanosheets was followed by delamination of big portion of sintered nanosheets (Fig. 4.49(c)). These delaminated nanosheets started fracturing with further displacement. After fracturing, the nanosheets have been sliding and pushed out around the indenter. Similar to slope 1, multiple drops in the load are observed in the slope 2 region and this could be due to the fracturing of sintered nanosheets at the bottom of the indent surface. The real-time video of the slope 3 region, did not reveal much of deformation near the indenter surface, except for compression of nanosheets and this is predominantly observed as the displacement occurred. This is also confirmed after the tip removal, as there was no significant damage observed at the bottom of the indent surface. The calculated normalized associated energy for the slopes in the BCN 3 top surface displayed a two-fold increase from slope 1 to slope 2. The normalized energy drops for slope 3 compared to slope 1 and slope 2. The highest dissipation energy is observed in slope 2 region (52.43 mJ), it is about 147% and 338% higher than slope 1 and slope 3 respectively. Hence, the dominant deformation mechanism along the reaction sintered BCN 3 top surface is the deformation mechanisms in slope 2.

Table 4.8: Reactive sintered BCN 3 deformation mechanisms, normalized associated energy and the time range in video observed during the top surface indentation

Slope	Time range in video (min)	Normalized associated energy (mJ)	Specific time in video (min)	Deformation mechanism
1	0.05-2.07	21.22	0.10, 0.31	(i) Compression of the sheets
			0.18, 1.44	(ii) Push out and pile up of the nanosheets
			0.34, 1.12	(iii) Sliding and pile up
			0.38, 0.55, 2.05	(iv) Delamination of the sintered nanosheet
2	2.13-4.15	52.43	2.19	(i) Compression of the sheets
			2.24	(ii) Delamination of the nanosheets
			2.28	(iii) Fracture of the delaminated sheet

			2.35	(iv) Sliding
			2.57	(v) Push out
3	4.69-6.87	11.97	-	Predominantly compression of the sheets was observed

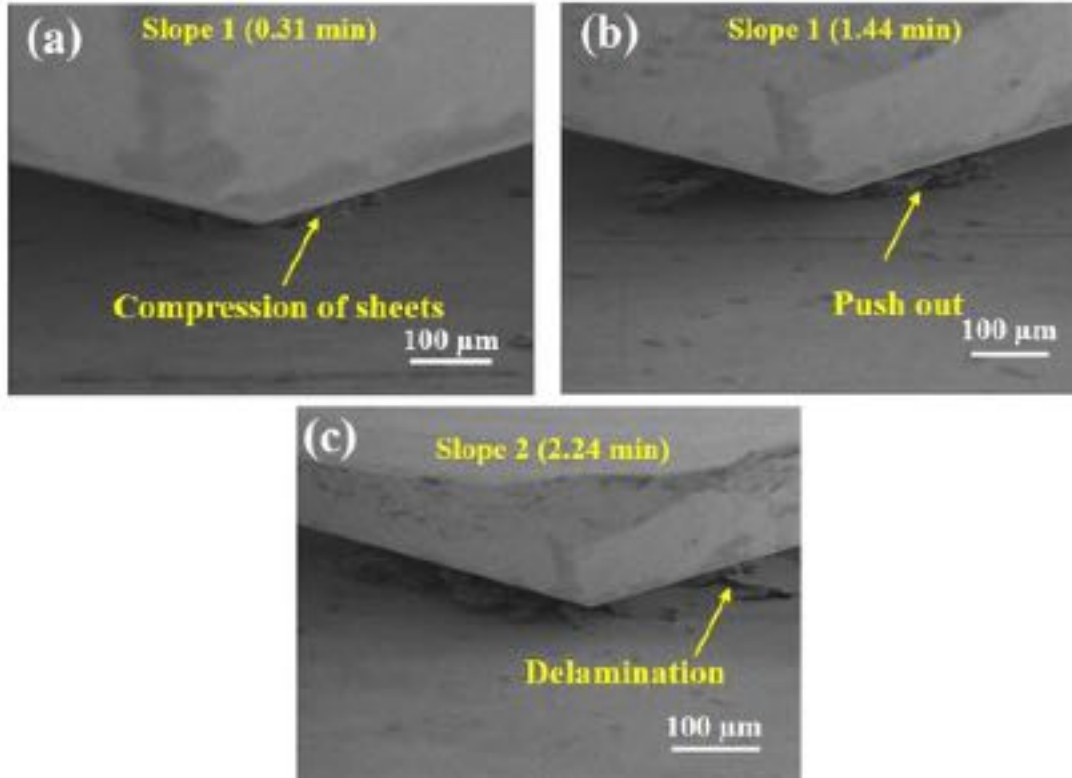


Figure 4.49: SEM images of deformation at different stages of loading from the real-time video

The top surface indent of reaction sintered BCN samples after indentation has been analyzed by SEM. Figure 4.50 shows the SEM images of the BCN 1 top surface indent. The whole indent area of BCN 1 sample is observed at low magnification as shown in Fig. 4.50(a) and the important regions (corresponding to Fig. 4.50(b-d)) are marked by transparent yellow circle in the SEM image. In the Figure 4.50(a), the inset shows the crack propagation at one of the corner of the indent. Inside the indented area, smooth regions in the center is observed with large delaminated and fragmented nanosheets as displayed in Figure 4.50(b). Some regions displayed the sliding of nanosheets, which could be caused by the weak van der Waals forces between the nanosheets. No crack formation has been observed at the bottom of the indented BCN 1 surface. The sintered nanosheets below the indenter tip have been bend, crumpled and wrinkled mostly in the smooth regions. In addition, the high magnification image of the pile-

up of nanosheets (Fig. 4.50(c)) at the bottom of indent surface reveal the weak reaction bonding between the nanosheets and poor densification of BCN 1 pellet. As the displacement occurred on the top surface of BCN 1 pellet, the sintered nanosheets are delaminated layer by layer and this is observed at edges of the indent as shown in Figure 4.50(d). Hence, the deformation mechanism for the reaction sintered BCN 1 pellet are delamination of nanosheets, crack propagation at the corner of indent, bending, crumpling and layer by layer delamination at the edges of indent.

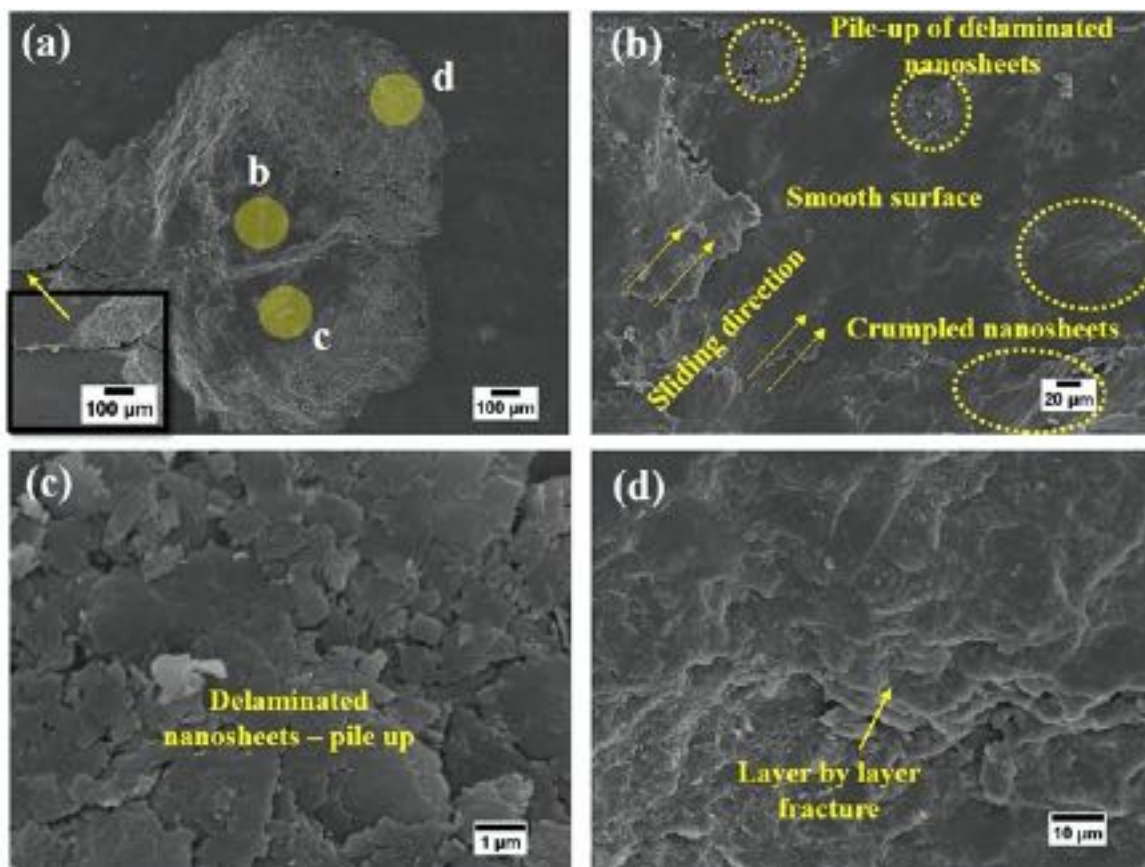


Figure 4.50: SEM images of the reaction sintered BCN 1 top surface indent after the tip removal

Figure 4.51 shows the top surface indent region of reactive sintered BCN 2 pellet after the indenter tip removal. Crack propagation has occurred from all the four corners of indent as shown in Figure 4.51(a-b). At the center of the indented bottom region, display a smooth surface with few delaminated nanosheets (Fig. 4.51(c)). The smooth nanosheet surface display the crumpled features in certain regions of nanosheets. Sliding of the sintered nanosheets are

also observed with some smooth bending of the nanosheets at center of indent region in the BCN 2 pellet. With increase in displacement as the indenter pushed through the top surface, the delamination of nanosheets has occurred in steps till the final 0.5 mm displacement and this shows the layer-by-layer delamination during high load indentation (Fig. 4.51(d)). Few nanosheets have been bend and some nanosheets have undergone zig-zag way of fracture along the corner of the indent surface. This bending or zig-zag type of deformation at the corners is completely dictated by the type of bonding between the nanosheets formed during the reactive spark plasma sintering. The major deformation mechanism observed post indentation for the reaction sintered BCN 2 pellet are crack propagation at all the four corners of indent, layer by layer delamination at the corners of indent with some nanosheet bending, sliding and crumpling at the bottom of the indent surface.

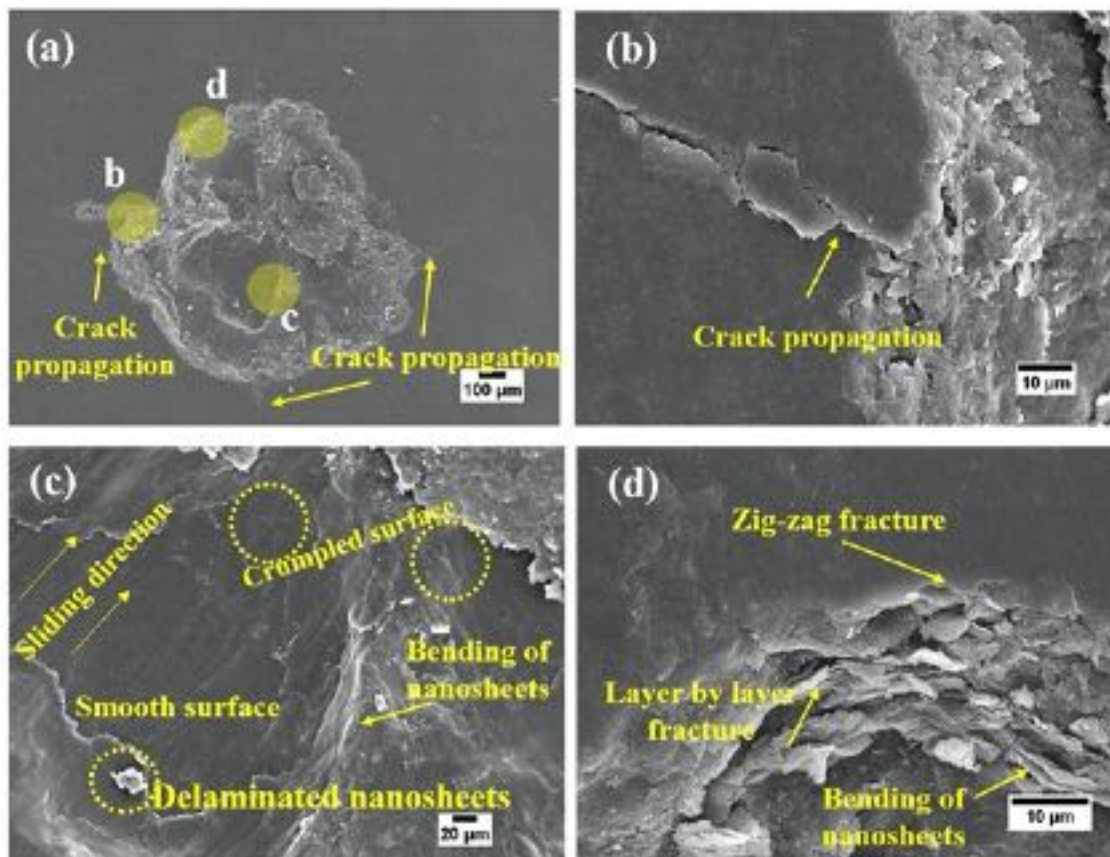


Figure 4.51: SEM images of the reaction sintered BCN2 top surface indent after the tip removal

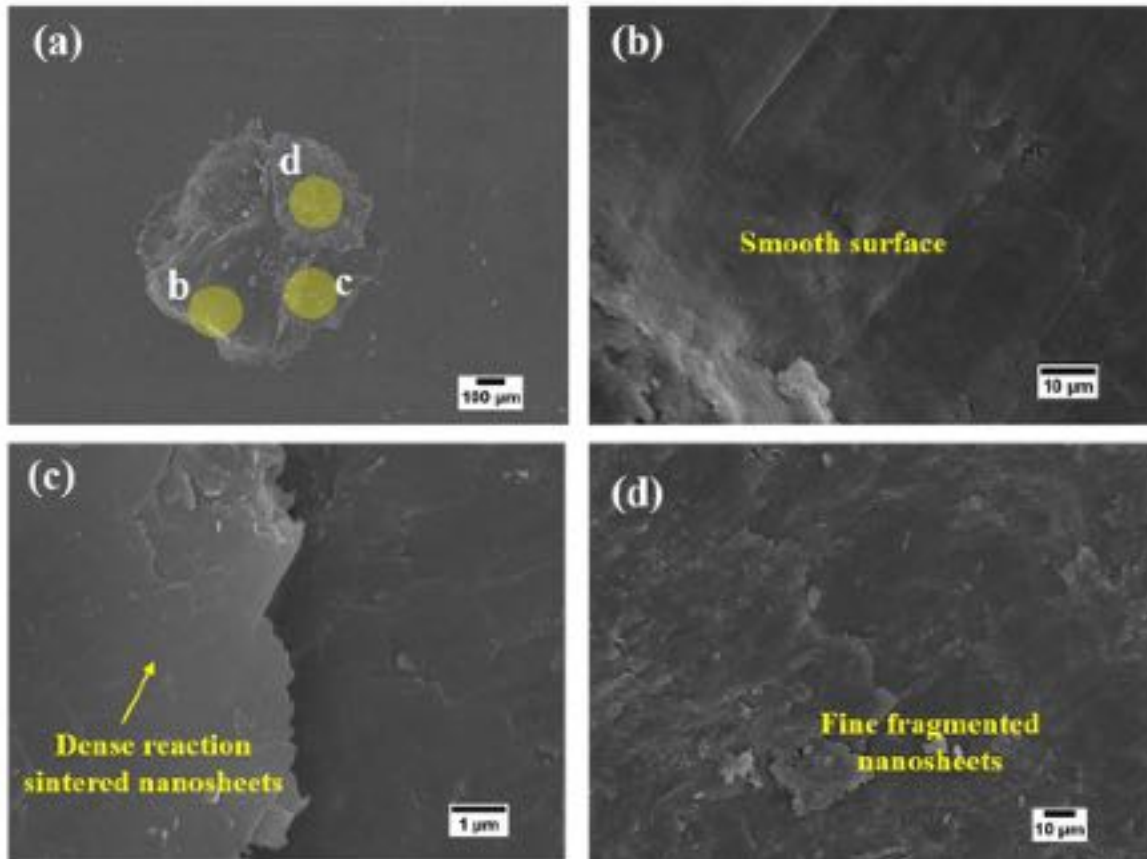


Figure 4.52: SEM images of the reaction sintered BCN 3 top surface indent after the tip removal

Table 4.9: Length of the diagonals from the indent of the BCN high load indentation

Sample	Diagonal Length Measured from SEM (μm)	
	D1	D2
BCN 1	1594	1878
BCN 2	1322	1122
BCN 3	1080	950

For BCN 3 top surface, Figure 4.52 shows the indent region at different magnifications after the indenter tip removal. Figure 4.52(a) shows the low magnification image of the indent and no cracks are formed at the corners of the indent. The high magnification image of the indent surface (Fig. 4.52(b)), display a smooth surface with significant amount of nanosheet sliding and crumpled regions. In addition, the BCN 3 sample looks dense with very few pores and the indent surface was mostly free of large delaminated nanosheet debris. Figure 4.53(c) shows the nanosheets reacted and densely bonded with each other. Few places of the indent

region had fine fragmented nanosheets as shown Figure 4.53(d). All the three high magnification images of BCN 3 indent surface (Fig. 4.53(b-d)), clearly display the nanosheet sliding. Unlike the BCN 1 and BCN 2 pellets, there is no crack formation and layer by layer delamination of nanosheets at the corner of BCN 3 indent surface. There is change in deformation mechanisms for BCN 3 pellet compared to BCN 1/BCN 2. The major deformation mechanisms in BCN 3 indent along the top surface are nanosheet sliding and crumpling with less delamination of nanosheets. In addition, the indent diagonal lengths have decreased for BCN 3 pellet compared to BCN 1 and BCN 2 pellets (Table 4.9).

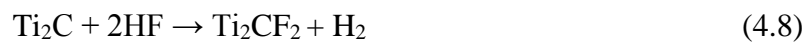
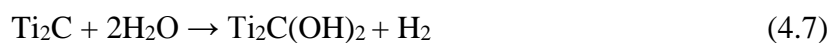
4.2.9. Conclusion of Reaction Synthesized BCN Phase

Boron carbon nitride (BCN) phase is successfully synthesized from 2D GNP and BNNS by reactive spark plasma sintering (SPS) technique from temperature range of 1650 - 1750 °C. Hexagonal BCN phase with minor fraction of cubic BCN phase presence in sintered compacts are confirmed by X-ray diffraction, Fourier transform infrared spectroscopy and transmission electron microscope. Texture study on sintered compacts indicate the preferred orientation of nanosheets (along the (0002) basal plane), perpendicular to the direction of sintering. The coefficient of friction increased with the formation of cubic BCN at room temperature but reduced at 600 °C due to graphitized transfer layer. Room temperature wear rate of BCN synthesized at 1750 °C increased by 500% as compared to BCN synthesized at 1650 °C due to higher level of densification. These results indicate, reaction synthesis temperature plays a vital role in BCN phase formation, mechanical and tribological properties of sintered compact.

4.3. Synthesis and Property Evaluation of 2D MXene

4.3.1. MXene Synthesis – HF Acid Treatment

MAX phase Ti_2AlC powder was used as starting powder for MXene synthesis. Hydrofluoric acid (25%) was added into the de-ionized water to prepare 100 ml of solution in total and Ti_2AlC powder was added into the solution. The solution with MAX powder was continuously stirred using magnetic stirrer, treated for 1 h, 2 h, and 4 h at room temperature [61, 62]. The 2D Ti_2C MXene was successfully synthesized by etching Al layer from the MAX phase Ti_2AlC powder. The synthesized powders were washed 5-10 times with de-ionized water, filtered and separated further by centrifugation technique. These powders were dried in the vacuum oven at 80 °C for 30 min to 1 h. Below, are the possible reactions of Ti_2AlC powder with HF acid and further the synthesized MXene with HF or water during washing [63],



Thus the synthesized 2D Ti_2C MXene will have –OH/-F surface terminations based on the reactions (4.7) and (4.8).

4.3.2. Phase Evolution with HF Acid Treatment

Phase confirmation for the as-received MAX powder and the phase evolution of HF treated powders were studied by X-ray diffraction (XRD). The XRD pattern of the as-received MAX powder shows the major phase to be Ti_2AlC with small amount of TiC phase in Figure 4.53. With HF treatment of MAX powder, the intensity of Ti_2AlC phase decreases with broader peaks indicating the disorder in crystal structure. Emergence of MXene phase was confirmed by shifting of the (002) peak at 12° (Ti_2AlC) to lower angle 9° along with peak broadening [62, 64]. This peak corresponds to Ti_2C formation (Fig. 4.53) with increasing ‘d-spacing’ (d_{002})

or interlayer distance, from 6.75 to 8.45 Å [61, 64, 65]. Also, the peak around 9° was bifurcated for 1 h and 2 h HF treated sample, where both the peaks correspond to Ti₂C indicating MXene sheets have two different interlayer spacing. The interlayer spacing was calculated for all the HF treated MXene samples (Table 4.10). In the bifurcated (002) peaks with increase in HF treatment duration from 1 h to 4 h, the peak intensity at larger d-spacing remains constant with the other peak intensity almost weakens, indicating the increase in interlayer spacing with longer etching time. The new phase formation confirms the etching away of Al from the Ti₂AlC structure. The resulting Ti₂C surfaces could possibly be terminated by -OH, -F and -O surface groups. Intensity of the MXene peaks decrease after 2 h of HF treatment whereas the intensity of TiC remains the same. In addition, the broadening of MXene peak was observed after 4 h of HF treatment. This is ascribed to the slow decrease in degree of structural order.

Table 4.10: Interlayer spacing and FWHM for MAX and HF treated MXene samples

Samples	Interlayer spacing (Å) for (002) plane/ 'd-spacing' (d ₀₀₂)		FWHM	
	Peak 1	Peak 2	Peak 1	Peak 2
MAX	6.75		0.1763	
HF treated – 1 h	8.98	8.45	0.2347	0.1932
HF treated – 2 h	9.12	8.73	0.2366	0.1921
HF treated – 4 h	9.38	8.96	0.2369	0.1940

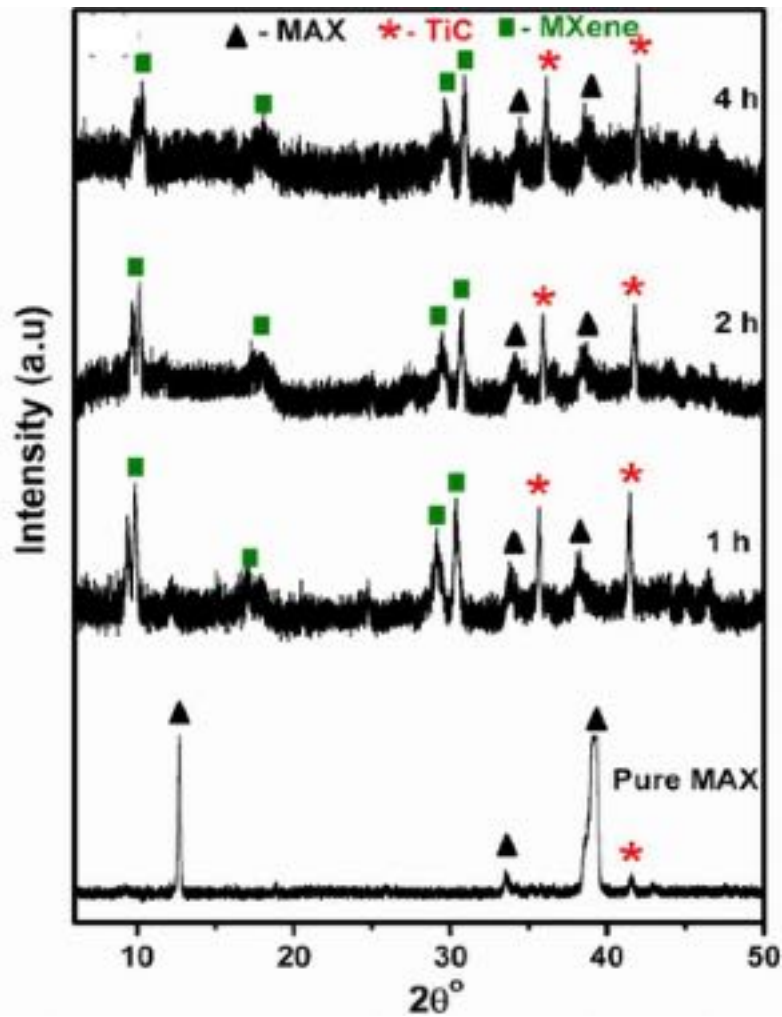


Figure 4.53: X-ray diffraction patterns of MAX and HF-treated MXene powders

4.3.3. Microstructural Evolution with HF Acid Treatment

The morphological changes of Ti_2AlC powder after HF treatment were explored using SEM. Figure 4.54(a) shows the SEM image of the as-received Ti_2AlC powder. It shows a densely packed layered structure. After 1 h of HF treatment, partial separation of the layers was observed (Fig. 4.54(b)). The thickness of the separated layers was 157 ± 20 nm for 1 h of etching. As the HF treatment time was increased to 2 h, further separation of the layers was observed which is caused by the excess removal of Al from Ti_2AlC as shown in Figure 4.54(c). This leads to the formation of thin (100 ± 23 nm) layers, which corresponds to ~ 130 Ti_2C layers. Figure 4.54(d) reveals the HF-treated 4 h powders with evidently separated individual

MXene layers with a reduced thickness of 74 ± 12 nm. The separated MXene layers of 4 h roughly comprises of ~ 96 Ti_2C layers. The visual evidence shows a clean surface for all HF treated powders with no surface oxidation.

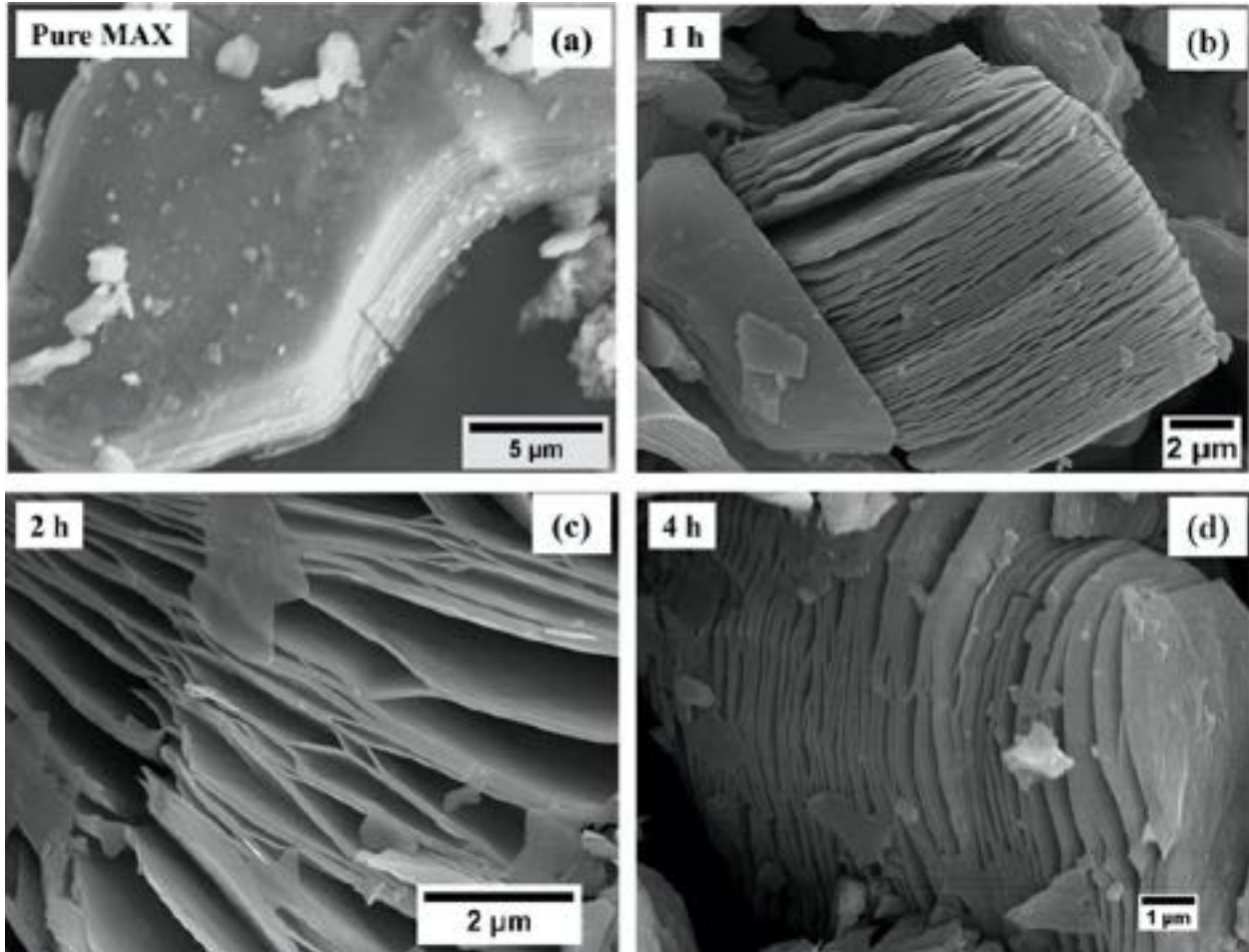


Figure 4.54: SEM images of (a) MAX, (b) 1 h, (c) 2 h and (d) 4 h HF treated MXene powder

4.3.4. Electrical Resistivity of HF Treated MXene

The electrical resistivity of the pure MAX and HF treated samples were measured by four probe technique. For pure MAX phase, electrical resistivity was $0.51 \mu\Omega\text{m}$ indicating the metallic nature and this value is comparable with literature [66]. After HF treatment, the electrical resistivity increased for the 1 h, 2 h, and 4 h. Electrical resistivity of HF treated 1 h was $1.62 \times 10^{-3} \Omega\text{m}$, 2 h was $3.36 \times 10^{-3} \Omega\text{m}$ and 4 h was $8.4 \times 10^{-3} \Omega\text{m}$. The electrical resistivity of HF treated samples up to 2 h are close to literature values [63]. The increase in resistivity

are attributed to the termination of functional groups to the MXene sheets and with increasing HF treatment, there is more defect formation [67].

4.3.5. Tribological Behavior of HF Treated MXene

Using a ball-on-disk tribometer, tribological tests were performed for MAX and HF treated powders by adding them on top of the AISI 1020 carbon steel substrate with 1 N normal load at 100 RPM for 5 min as shown in Figure 4.55. Similar tests were performed using Ti_3C_2 MXene as an additive in ethanol or base oil medium [68-70]. Al_2O_3 ball of 3 mm diameter was used as a counter surface. MAX and HF-treated powders were dispersed in ethanol and ultrasonicated for 10 min. The dispersed powder solution was dropped onto the substrate at an approximate rate of 1 mL/min. The coefficient of friction (COF) value was 0.18 for pure MAX phase powder of 1 N load. The COF significantly decreased to 0.019 for 1 h HF treated powder (1 N), with 2 h and 4 h of HF treatment (1N), the COF increased to 0.021 and 0.079. It should be noted that COF for MXene was 50 – 80% lower than the MAX which ascribed to the interlayer shearing/sliding of MXene sheets due to the weak van der Waals forces between the layers. Further, 1 h HF treated MXene showed superior lubrication properties compared to 2 h and 4 h of HF treatment which is due to the increase in interlayer spacing with more extended HF treatment. Recently, similar behavior of shear-induced slipping of Ti_3C_2 MXene nanosheets under pressure was observed which further substantiates the shearing of Ti_2C sheets in the present work [71].



Figure 4.55: Schematic diagram showing the tribological test and shearing of MXene layers

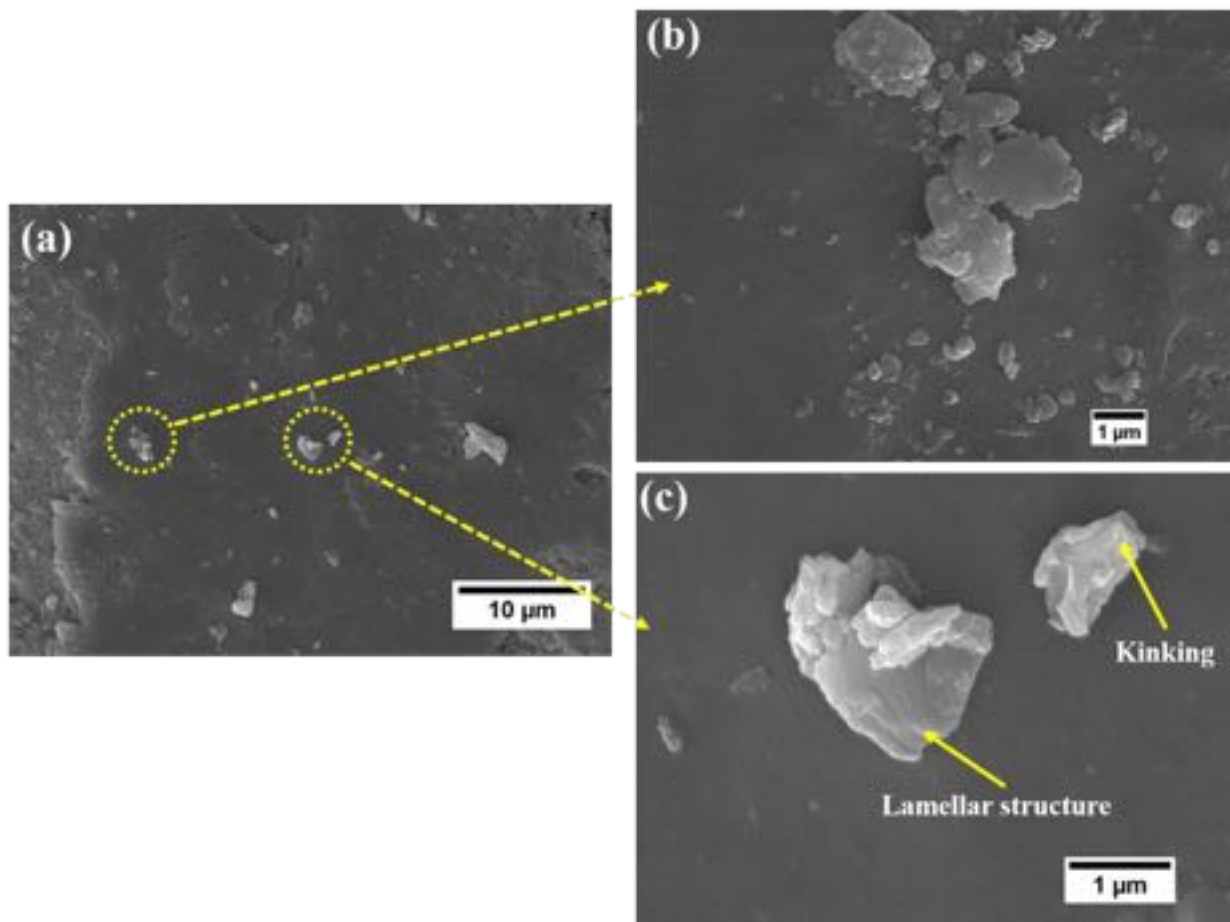


Figure 4.56: Wear track of steel substrate lubricated with pure MAX (Ti_2AlC) powder showing (a) low magnification, (b) pressed MAX powder, (c) lamellar structure and kinking

The coefficient of friction (COF) value was 0.18 for pure MAX phase powder. The COF significantly decreased to 0.019 for 1 h HF treated powder (1 N), with 2 h and 4 h of HF treatment (1N), the COF increased to 0.021 and 0.079. Figure 4.56 show the SEM images of steel substrate lubricated with pure MAX (Ti_2AlC) powder. The wear track surface was smooth with pure MAX powder (0 h) pressed and agglomerated along the track (Fig. 4.56(b)). The large powder particles in the track surface displayed the lamellar structure. Also, there was a deformation of few individual MAX powder by kinking, and this prevented any damage to MAX powders during the test as shown in Figure 4.56(c). In case of 1 h HF treated MXene, SEM images of wear track showed a smooth track surface with a uniform distribution of distinct MXene layers (Fig. 4.57). The separated sheets in the wear track surface were not

folded or damaged, and sheared layers were arranged in steps as shown in Figure 4.57(b). This is due to the cleaving of MXene layers during the test as MXene layers are bonded by weak van der Waal forces (Fig. 4.57(c)). These cleaved MXene layers were separated and slide against each which contributes to lowering the coefficient of friction (COF) of 1 h HF treated MXene compared to pure MAX powders.

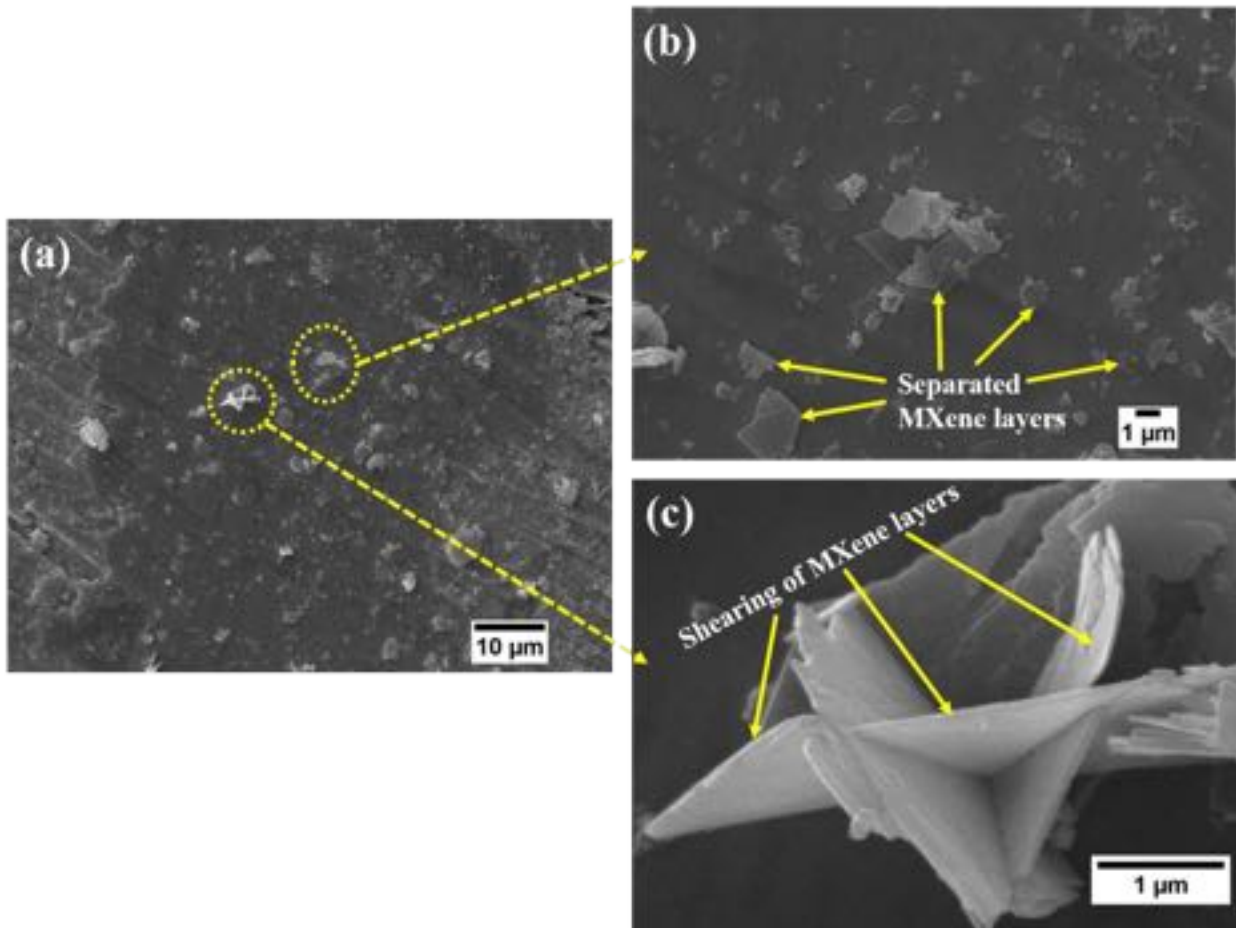


Figure 4.57: Wear track of steel substrate lubricated with 1 h HF treated MXene (Ti_2C) powder showing (a) low magnification, (b) separated MXene layers populated along the track, (c) shearing of MXene layer

4.3.6. Multiscale Damping Behavior of HF Treated MXene

For MAX and HF-treated MXene samples, damping behavior was examined at multiscale level using dynamic mechanical analysis. High load damping tests were performed at impact loads of mN whereas low load tests were conducted at μN which is three orders of magnitude lower. The damping characteristics are analyzed by determining the phase lag (δ)

between the applied force and displacement response. The loss tangent ($\tan \delta$), which is a measure of damping capability, is given by the ratio of loss modulus (E'') to storage modulus (E') [72-75],

$$\tan \delta = \frac{E''}{E'} \quad (4.9)$$

The loss modulus (E'') represents the viscoelastic portion of the material and storage modulus (E') represents the elastic part of the material [14]. Figure 3a shows the $\tan \delta$ values measured at higher loads (mN) applied along the top surface (normal to the basal plane) of all the powders. Loss tangent, $\tan \delta$ value for the MAX phase fluctuates in the range of 0.05 to 0.18. After HF treatment for 1 h, $\tan \delta$ value increases significantly from 0.32 to 0.48. An almost 200% increase in loss tangent was observed as compared to pure MAX, demonstrating enhanced damping behavior, which could be directly correlated to the combination of damping mechanisms present in MAX and MXene phases. The dominant damping mechanisms for MAX phase are the incipient kink bond formation and ripplocations [76-80]. Energy dissipation for MXene can be related to the intralayer bond contracting and interlayer mechanisms due to the weak van der Waals forces between the MXene sheets. Compared to pure MAX, the loss tangent remains to be higher for 2 h (about 98%) and 4 h (40%) of HF treatment. Among MXene samples, loss tangent drops to 38% and 54% respectively for the 2 h, and 4 h HF-treated samples as compared to 1 h HF treatment. It is noted in Figure 4.58 that with increasing load from 1 mN to 5 mN, the loss tangent trends remains same but magnitude drops which is explained later in detail.

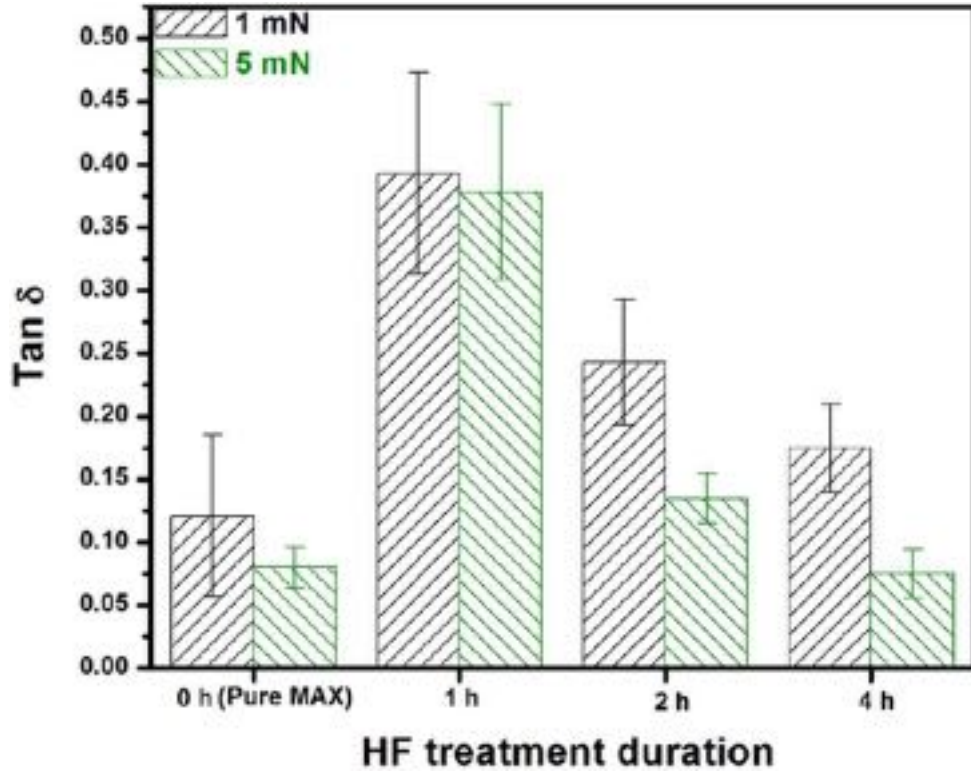


Figure 4.58: Loss tangent values of MAX and HF treated samples at 1 mN and 5 mN load

The height-time profiles of high load (5 mN) damping test for MAX and HF-treated samples are shown in Figure 4.59(a). This profile shows the period required for the amplitude of oscillating stylus to decay through MAX and HF-treated MXene. Pure MAX phase shows the longest decay time of 0.28 s compared to HF treated MXene. The 1 h HF treated sample showed the maximum energy dissipation with the shortest decay time of 0.17 s than 2 h (0.19 s) and 4 h (0.23 s) HF-treated samples. This superior damping behavior of 1 h HF treated is substantiated by measuring the damping constant (β) (fitting the maxima and minima of the height-time profiles with exponential function) and is defined by equation (2) [75],

$$\beta = \frac{1}{\tau} \quad (4.10)$$

Where τ is the relaxation time and describes the time span by which a factor of 'e' decreases the decaying amplitude of oscillating stylus. Figure 4.59(b) shows the damping constant (β) of pure MAX and HF-treated powders for both loads (1 mN and 5 mN). MAX phase has the smallest

damping constant compared to the HF-treated samples, implying MAX phase undergoes slow damping with larger relaxation time. The one hour HF treated sample shows the highest damping displaying rapid damping profiles with smaller relaxation time. Damping constant gradually decreases as the HF treatment duration increases. This trend is similar to the $\tan \delta$ values and is attributed to the decrease in Ti_2C layers with longer etching period. So, the damping behavior changes with the decrease in an array of MXene layers.

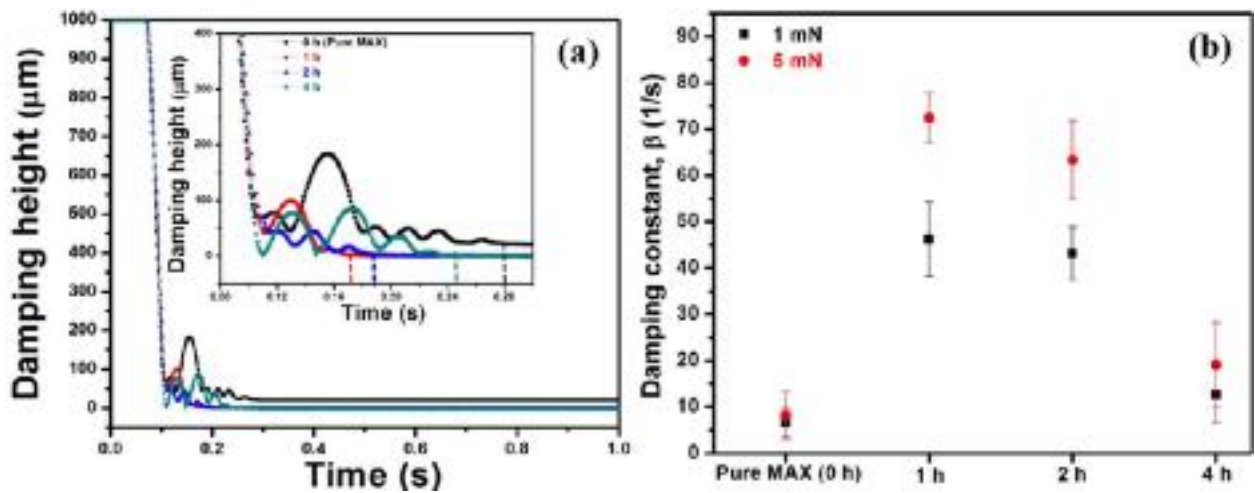


Figure 4.59: (a) damping height-time profiles at 5 mN load and (b) damping constant for pure MAX and HF-treated samples

Nano-dynamic test was performed to probe the *intrinsic* damping behavior of single or few layers of MXene as opposed to high load test which examines the *overall* damping behavior. NanoDMA results for the samples at different loads (1 μN and 10 μN) are shown in Figure 4.60(a) and 4.60(b), where the $\tan \delta$ values (0.015 to 0.10) change with respect to varying frequencies from 0 to 250 Hz. MAX phase displays a continuous increase in $\tan \delta$ values with an increasing frequency for both the dynamic loads. Compared to MXene, the $\tan \delta$ increase in MAX phase was gradual and have plateaued out in the frequency range of 100 – 200 Hz. Similar to high load damping tests, nanoDMA also shows higher $\tan \delta$ values for MXene varying from 0.025 to 0.38 indicating improved damping behavior as compared with pure MAX phase. Among the HF-treated samples for 10 μN (Fig. 4.60(b)), it is observed 1 h has the highest loss tangent of 0.38 compared to the highest loss tangent of 2 h (0.28) and 4 h

(0.15). With increasing frequency for both the dynamic loading condition, the HF-treated samples exhibit an upsurge of $\tan \delta$, with a minimum value of 0.025 to a maximum value of 0.38. Especially for HF treated MXene, there is a gradual increase of $\tan \delta$ up to 125 Hz, and it jumps to a higher value at 150 Hz. After 200 Hz, the 1 h and 2 h HF-treated samples display a gradually decreasing $\tan \delta$ up to 250 Hz. This displays the significant role of frequency in the damping behavior. Regardless of high or low damping loads and frequency, higher $\tan \delta$ values for MXene indicate the synergistic contribution of intralayer and interlayer damping mechanism from the MXene layers.

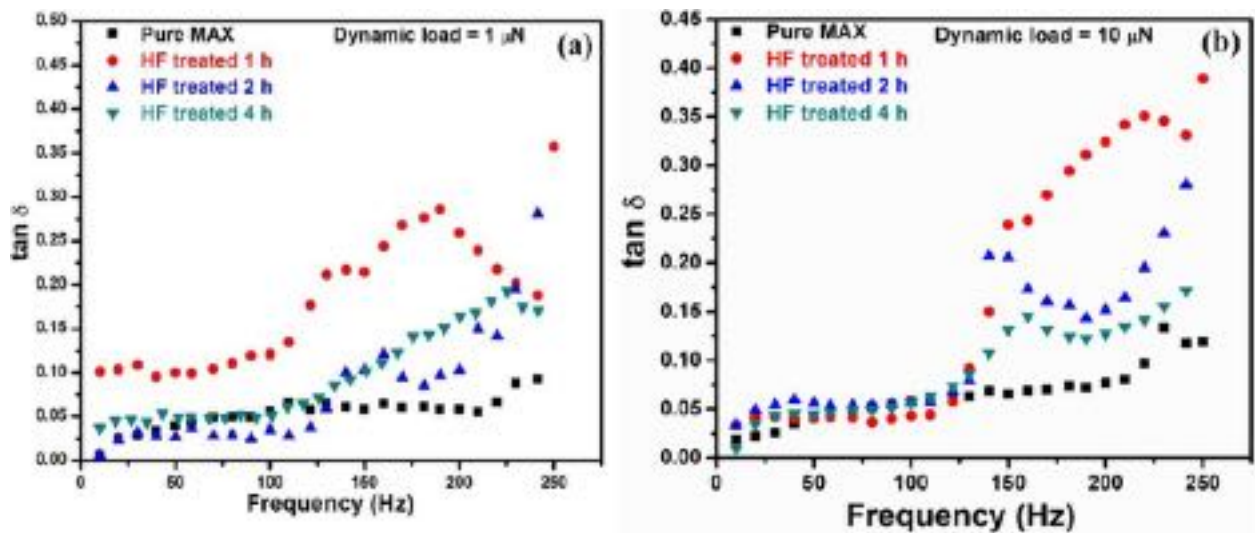


Figure 4.60: Damping behavior of MAX and HF-treated samples at a dynamic loading of (d) 1 μN and (e) 10 μN in the frequency range of 10-250 Hz.

The stability of the nanoscale damping response in MXene samples was studied by subjecting them to a large number of cycles (50000 cycles) at a frequency of 150 Hz for 1 and 10 μN loads. For this study, the frequency of 150 Hz was chosen for both the loads as a significant leap in $\tan \delta$ value was observed during the nano-dynamic tests (Fig. 4.60). Figure 4.61 shows that MXene retains a stable damping behavior. At 1 μN load, $\tan \delta$ remained constant for 1 h sample with small standard deviation indicating the damping process has not degraded the 2D layers after 50000 cycles. For 10 μN load, all the 3 HF treated conditions (1 h, 2 h, 4 h) displayed similar $\tan \delta$ values with a higher standard deviation. This persistent

damping behavior of HF-treated samples after 50000 cycles clearly imply the efficient energy dissipation dictated by MXene upon cyclic loading.

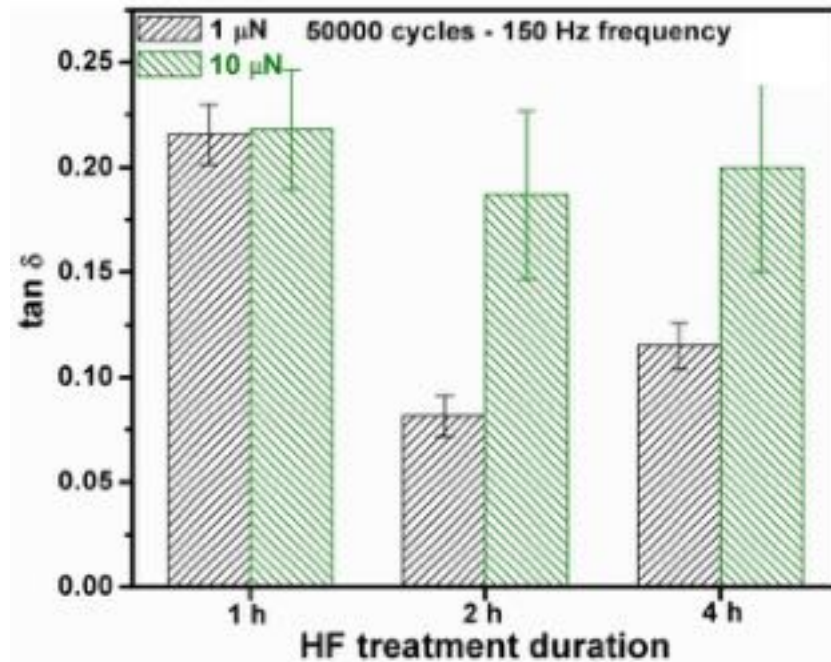


Figure 4.61: Long cycle test for HF-treated samples at loads of 1 μN and 10 μN for a frequency of 150 Hz

4.3.6.1. Damping Mechanisms in MAX and MXene

It is evident from the multiscale damping studies that MXene phase displayed superior damping behavior as compared to pure MAX for both low and higher loads. It is also concluded nanoscale damping behavior is largely stable up to 50,000 cycles. Energy dissipation in MXene can be elucidated by three possible mechanisms, viz.:

- (i) Intralayer – bond contracting within an MXene sheet
- (ii) Interlayer – compression between MXene sheets
- (iii) Interlayer –sliding\shearing between the sheets

(i) Intralayer Bond Contracting: As the load is applied to MXene sheet, covalently bonded Ti-C bond length changes resulting in atomic displacements which could be related to the simple harmonic equation in molecular mechanics [81]. Figure 4.62 illustrates the difference in bond

length of covalently bonded two atoms. The energy (E) required for stretching or contracting is shown by the equation (3),

$$E = k_s(x - x_0)^2 \quad (4.11)$$

Where k_s - spring constant, x_0 – natural bond length between two atoms, x –bond length when stretched. This equation can be further modified for the MXene sheet terminated with surface groups ($-\text{OH}$, $-\text{F}$ or $-\text{O}$) as below,

$$E = k_s(x - (x_0 + y_0))^2 \quad (4.12)$$

Where k_s - spring constant, x_0 –natural bond length between two atoms, y_0 –natural bond length between an atom and a functional group, x –bond length when stretched. The above relationships indicate the energy dissipation along the in-plane direction in MXene sheet when subjected to tensile/compressive loading is due to the bond stretching or contracting between Ti-C and Ti-C-OH/F/O $^-$. This energy is quantified for pure and functionalized Ti₂C from the theoretical bond length and available k_s values from the literature [82, 83]. The bond length change of $-\text{OH}/-\text{F}$ functionalized Ti₂C values are not available in the literature. The change in bond length for pure and oxygen functionalized Ti₂C when subjected to different loading is assumed to increase by 0.05/0.02 Å [84]. The calculated energy (E) values are tabulated in Table 4.11, where the oxygen functionalized Ti₂C requires 80% higher energy for bond contracting than pure Ti₂C.

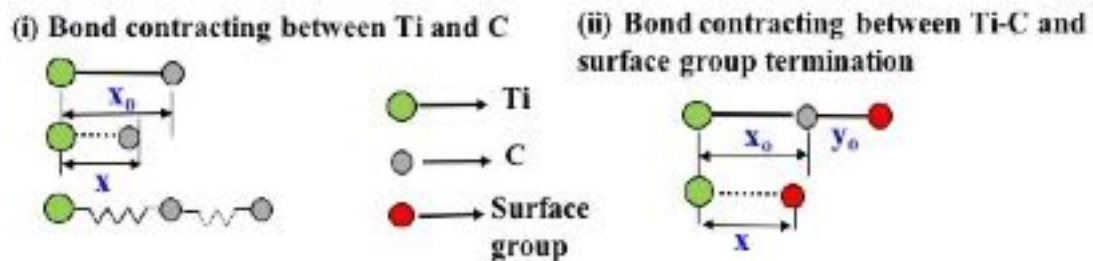


Figure 4.62: Schematic describing the intralayer deformation mechanism

Table 4.11: Calculated energy for bond contracting of pure and functionalized Ti₂C

Composition	Bond length (x ₀ , 10 ⁻¹⁰ m)	Spring constant (k, N/m)	Energy (E, Nm)
MXene (Ti ₂ C) (Ti-C)	2.09	125	0.3125
Ti ₂ CO ₂ (Ti-C)	2.17	227	0.5675
Ti ₂ CO ₂ (Ti-O)	1.96	227	0.0908

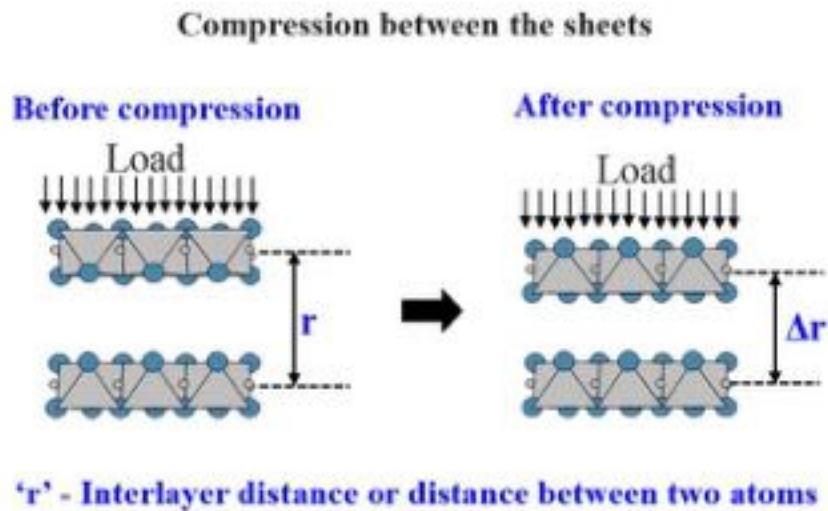


Figure 4.63: Schematic describing the compression between the sheets

(ii) Interlayer – compression between MXene sheets: Ti₂C MXene sheets are loosely held together by weak van der Waals forces and energy dissipation along the interlayer direction could possibly be related to two mechanisms, (i) compression between the sheets and (ii) shearing/sliding between the sheets. Firstly, compression of sheets due to weak van der Waals forces between Ti₂C sheets is discussed as shown in Figure 4.63. This mechanism was confirmed by performing cyclic compressive loading-unloading-reloading of MXene. In the weak van der Waals forces, the attractive force between two atoms is referred as the London dispersion force [85]. From the interaction energy (E) of van der Waals forces of two atoms, the weak interaction force between the atoms were derived and modified by Hamaker as given below,

$$F = \frac{AR}{12r^2} \quad (4.13)$$

where R is the radius of the spheres, r is the distance between two atoms and A is referred to as the Hamaker constant ranging from 10^{-11} to 10^{-13} ergs [85]. The above expression was modified by considering the weak interaction between two flat surfaces and the interaction force (F) was given by,

$$F = \frac{A}{6\pi r^3} \quad (4.11)$$

So, the distance between two flat surfaces, 'r' could be directly correlated to the interlayer distance between the MXene sheets. By differentiating the equation (4.11), energy change can be described as below,

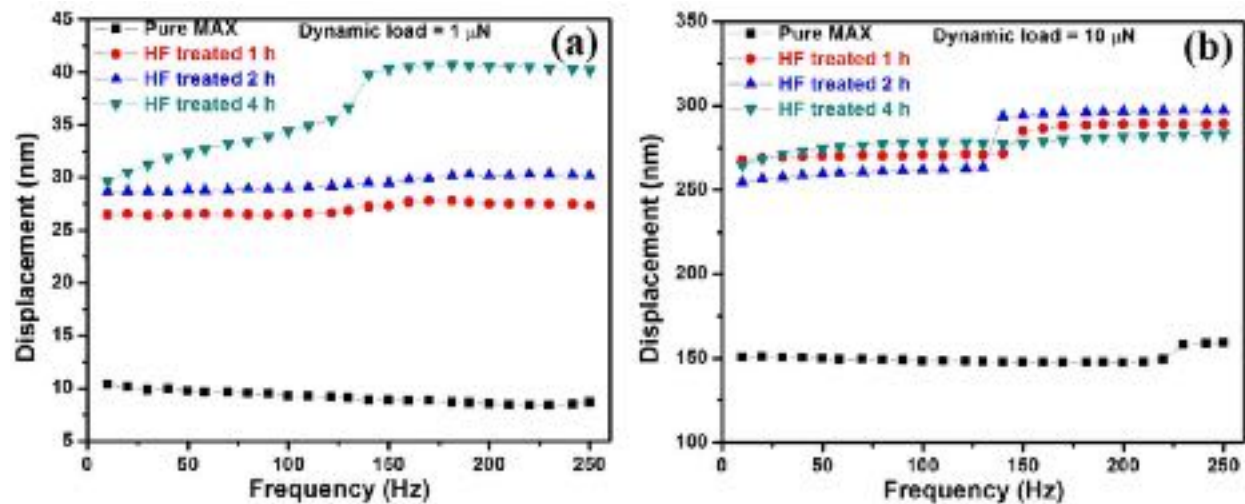
$$E = \frac{A}{2\pi r^4} \quad (4.12)$$

Where energy change is proportional to $1/r^4$. This equation suggests that the energy change increases with decreasing interlayer distance (r). Enhanced energy dissipation results in increased damping effect due to the presence of weak van der Waals forces between the MXene sheets. This energy change was quantified by using the displacement data (Fig. 4.64(a-b)) measured during nanoDMA for both the loads (1 μ N and 10 μ N). Using the theoretical monolayer thickness of Ti₂C and displacement data, the number of Ti₂C monolayer interacted during damping were calculated as shown in Table 4.12 and each monolayer was separated by weak van der Waals forces (an interlayer distance of Ti₂C) [83]. The displacement data was substituted in equation (4.12), and the corresponding energy change are shown in Figure 4.64(c-d). MAX phase was not considered for this energy calculations, as this equation was derived based on the assumptions the sheets were loosely held together by weak van der Waals forces. The energy change during damping (1 μ N load) for the 1 h HF treated sample was 1.25 and 1.5 times higher than 2 h and 4 h HF-treated samples respectively. This observation is in agreement with tan δ values of HF-treated samples, where the 1 h MXene has highest tan δ of 0.35. However, the 10 μ N load energy change for 1 h HF treated sample decreases after a

frequency of 150 Hz and displacement of 270 nm. So, the energy change for 1 h HF treated sample of 10 μN load is not in agreement with $\tan \delta$ value, indicating compression of MXene sheets will not be a dominating mechanism after a specific displacement and high load. With higher load, the dominating mechanism will be interlayer shearing/sliding between the sheets.

Table 4.12: Total number of layers interacted during damping, calculated from the monolayer thickness and average displacement measured during nanoDMA for HF-treated samples

Load (μN)	HF treatment duration (h)	The theoretical thickness of the monolayer (Ti_2C , nm)	Average displacement (nm)	No. of monolayers interacted during damping	Tan δ
1	1	0.231	27	54	0.10-0.35
	2	0.231	30	60	0.01-0.28
	4	0.231	37	74	0.04-0.17
10	1	0.231	278	556	0.06-0.38
	2	0.231	277	554	0.06-0.28
	4	0.231	278	556	0.04-0.15



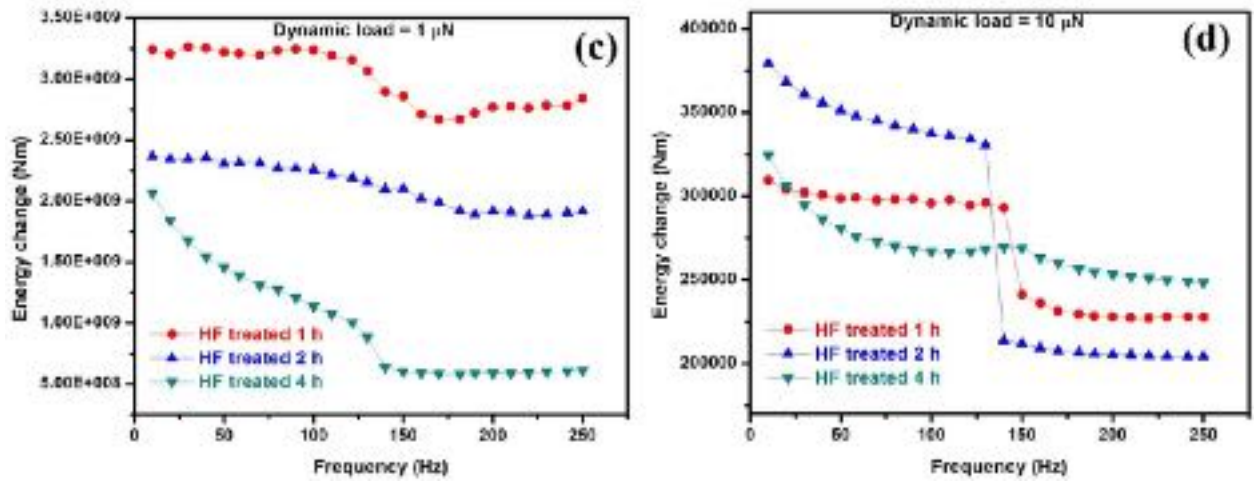


Figure 4.64: Change in displacement with varying frequency upon mechanical loading of (a) 1 μN and (b) 10 μN . Energy change with varying frequency upon mechanical loading of (c) 1 μN and (d) 10 μN

(iii) Out-of-plane – sliding\shearing between the sheets: The second interlayer mechanism due to weak van der Waals forces is the shearing/sliding of MXene sheets. This mechanism is explained based on Cobblestone Model (Fig. 4.65) [86]. It describes that two surfaces slide against each other when subjected to an external load. During sliding, because of the weak van der Waals forces between the surfaces, the layers are separated or attracted to each other. This energy is dissipated in this process of surface separation or attraction. This energy is described as below,

$$Energy = F \times \Delta x \rightarrow F \times \Delta x = 4\Delta\gamma \times A \frac{\Delta r}{r} \quad (4.13)$$

where, γ – Surface energy, A - contact area, r – initial surface separation, Δr – Small surface separation after sliding and $\Delta\gamma = \gamma_{\text{separation}} - \gamma_{\text{attraction}}$. From the above equation, the shear strength (S_c) at the interface can be evaluated by,

$$S_c = \frac{F}{A} \rightarrow S_c = \frac{4 \times \Delta\gamma \times \Delta r}{\Delta x \times r} \rightarrow S_c = \frac{4 \times \gamma \times \epsilon \times \Delta r}{\Delta x \times r} \quad (4.14)$$

Where the coefficient of dissipation, $\epsilon = \Delta\gamma/\gamma$. This ‘r’ could be related to the distance between two atoms which in turn describes the interlayer distance. Also, previous studies have shown with HF treatment; the surface energy increases compared to pure MAX and with surface

functionalization of $-O$, surface energy increases compared to $-OH/-F$ [83, 87]. Coefficient of dissipation, ϵ delineates the fraction of energy loss as the interlayer distance between the MXene sheets increase or decrease. Further, interlayer distance is inversely proportional to shear strength indicating the sliding of layers occurs more as the interlayer distance decreases. So, during damping, the energy could also be dissipated by sliding of MXene sheets. The sliding of MXene sheets was evaluated by conducting sliding tribological test on MAX and MXene (see details in supplementary information). The coefficient of friction (COF) value was 0.18 for pure MAX phase powder of 1 N load. The COF significantly decreased to 0.019 for 1 h HF treated powder (1 N), with 2 h and 4 h of HF treatment (1N), the COF increased to 0.021 and 0.079. It should be noted that COF for MXene was 50 – 80% lower than the MAX which ascribed to the interlayer shearing/sliding of MXene sheets due to the weak van der Waals forces between the layers. Further, 1 h HF treated MXene showed superior lubrication properties compared to 2 h and 4 h of HF treatment which is due to the increase in interlayer spacing with more extended HF treatment. The COF data concurs with damping $\tan \delta$ values, with 1 h demonstrating excellent damping behavior. Recently, similar behavior of shear-induced slipping of Ti_3C_2 MXene nanosheets under pressure was observed which further substantiates the shearing of Ti_2C sheets in the present work [71]. Therefore, the interlayer mechanism – shearing/sliding of MXene sheets for energy dissipation is supported by the tribological study.

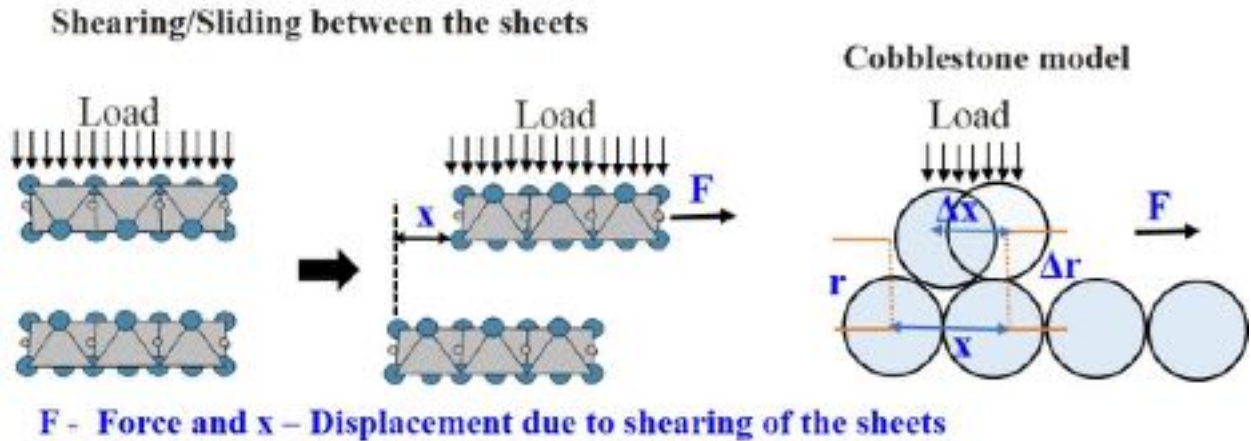


Figure 4.65: Schematic describing the shearing/sliding between the sheets

With increasing HF treatment duration, the array of MXene sheets in the stack decreases which explains the weak van der Waals forces gradually waning between the sheets. So, the intralayer and interlayer mechanism become less active with increasing HF treatment duration. In addition, the defects formed during HF treatment will influence the damping response and the defect concentration will increase with HF treatment duration [88]. From the displacement data measured during nanoDMA (Fig. 4.23), at a low load of 1 μN , the displacement of MXene varied between 26 to 42 nm and based on the calculations from Table 4.6, some MXene sheets interact during damping are well below the thickness of separated layers (70-150 nm). Since the displacement was within the MXene layer, intralayer bond contracting and interlayer compression would be the dominant energy dissipation mechanism at a lower load of 1 μN . With the dynamic load of 10 μN , the displacement was above 250 nm for all the HF-treated samples. This indicates displacement would be higher than 250 nm at the higher loads of 1 and 5 mN. As the load (10 μN /1 mN/5 mN) is applied on the MXene sheets, initially the energy dissipation would be within the layers. With the increase in applied force, the displacement proceeds through the interlayer gap between the MXene sheets, at this stage the energy dissipation occurs through the interlayer compression\sliding between the sheets. So, at larger loads, the dominant energy dissipation will be a combination of all three mechanisms, (i) Intralayer – bond contracting, (ii) Interlayer – compression between MXene

sheets and (iii) Interlayer –sliding\shearing between the sheets. Therefore, the combination of both intralayer and interlayer mechanisms in MXene will surpass the damping behavior of pure MAX phase and emerge as an excellent damping material.

4.3.7. Conclusion of 2D MXene Synthesis and Damping Behavior

In this study, Ti₂C MXene is successfully synthesized as major phase from starting Ti₂AlC MAX and the multiscale damping behavior of MXene is explored. Dynamic loading of multi-layer MXene assembly shows appreciable loss tangent ($\tan \delta$), indicating energy dissipation ability of the material. The $\tan \delta$ value for MXene is recorded to be as high as 0.37, which is about 200% improvement from pure MAX. It is hypothesized there are multi-scale energy loss mechanisms active in the material. While intralayer bond contraction operates in individual MXene sheets, interlayer compression and sliding/shearing mechanisms are active between the stacked layers. The presence of functional groups, van der Waals interactions and low coefficient of friction between the MXene sheets provide MXene with extraordinary energy dissipation ability. Damping behavior is highly stable in MXene for as high as 50,000 cycles, making it extremely promising for advanced applications requiring superior impact resistance, stability against noise, and ability to damp mechanical vibrations.

4.4. References

1. X.M. Duan, D.C. Jia, Z.L. Wu, Z. Tian, Z.H. Yang, S.J. Wang, Y. Zhou. Effect of sintering pressure on the texture of hot-press sintered hexagonal boron nitride composite ceramics. *Scripta Materialia* 68 (2013) 104-107.
2. D.W. Ni, G.J. Zhang, Y.M. Kan, Y. Sakka. Textured h-BN ceramics prepared by slip casting. *Journal of American Ceramic Society* 94 (2011) 1397–1404.
3. J.C. Koepke, J.D. Wood, Y. Chen, S.C. Schmucker, X. Liu, N.N. Chang, L. Nienhaus, J.W. Do, E.A. Carrion, J. Hewaparakrama, A. Rangarajan, I. Datye, R. Mehta, R.T. Haasch, M. Gruebele, G.S. Girolami, E. Pop, J.W. Lyding. Role of pressure in the growth of hexagonal boron nitride thin films from ammonia-borane. *Chemistry of Materials* 28 (2016) 4169-4179.

4. R. Geick, C.H. Perry, G. Rupprecht. Normal modes in hexagonal boron nitride. *Physical Review* 146 (1966) 543-547.
5. R.J. Nemanich, S.A. Solin, R.M. Martin. Light scattering study of boron nitride microcrystals. *Physical Review B* 23 (1981) 6348-6356.
6. R.V. Gorbachev, I. Riaz, R.R. Nair, R. Jalil, L. Britnell, B.D. Belle, E.W. Hill, K.S. Novoselov, K. Watanabe, T. Taniguchi, A.K. Geim, P. Blake. Hunting for monolayer boron nitride: optical and Raman signatures. *Small* 7 (2011) 465-468.
7. S. Yuan, S. Linas, C. Journet, P. Steyer, V. Garnier, G. Bonnefont, A. Brioude, B. Toury. Pure & crystallized 2D boron nitride sheets synthesized via a novel process coupling both PDCs and SPS methods. *Scientific Reports* 6 (2016) 20388.
8. V. Lughì, D.R. Clarke. Defect and stress characterization of AlN films by Raman spectroscopy. *Applied Physics Letter* 89 (2006) 24191.
9. S. Turan, K.M. Knowles. High resolution transmission electron microscopy of the planar defect structure of hexagonal boron nitride. *Physica Status Solidi A* 150 (1995) 227-237.
10. J.Y. Huang, H. Yasuda, H. Mori. HRTEM and EELS Studies on the amorphization of hexagonal boron nitride induced by ball milling. *Journal of American Ceramic Society* 83 (2000) 403-409.
11. X. Duan, M. Wang, D. Jia, N. Jing, Z. Wu, Z. Yang, Z. Tian, S. Wang, P. He, Y. Wang, Y. Zhou. Anisotropic mechanical properties and fracture mechanisms of textured h-BN composite ceramics. *Materials Science and Engineering A* 607 (2014) 38-43.
12. Y.N. Wang, J.C. Huang. Texture analysis in hexagonal materials. *Materials Chemistry and Physics* 81 (2003) 11-26.
13. H. Şahin, S. Cahangirov, M. Topsakal, E. Bekaroglu, E. Akturk, R.T. Senger, S. Ciraci. Monolayer honeycomb structures of group-IV elements and III-V binary compounds: First-principles calculations. *Physical Review B* 80 (2009) 155453.
14. L. Boldrin, F. Scarpa, R. Chowdhury, S. Adhikari. Effective mechanical properties of hexagonal boron nitride nanosheets. *Nanotechnology* 22 (2011) 1-7.
15. T. Saito, F. Honda. Chemical contribution to friction behavior of sintered hexagonal boron nitride in water. *Wear* 237 (2000) 253-260.
16. L.H. Li, J. Cervenka, K. Watanabe, T. Taniguchi, Y. Chen. Strong oxidation resistance of atomically thin boron nitride nanosheets. *Nano Letters* 2 (2014) 1457-1462.
17. M.I. Petrescu, M.G. Balint. Structure and properties modifications in boron nitride. Part I: Direct polymorphic transformations mechanisms. *UPB Science Bulletin Series B* 69 (2007) 35-42.

18. G. Wang, J. Yang, J. Park, X. Gou, B. Wang, H. Liu, J. Yao. Facile synthesis and characterization of graphene nanosheets. *Journal of Physical Chemistry C* 112 (2008) 8192-8195.
19. Y. Xue, L. Qian, G. He, K. Xu, J. Lin, X. Hu, J. Hu. Excellent electrical conductivity of the exfoliated and fluorinated hexagonal boron nitride nanosheets. *Nanoscale Research Letters* 8 (2013) 1-7.
20. X. Luo, J. Zhang, X. Guo, G. Zhang, J. He, D. Yu, Z. Liu, Y. Tian. Synthesis of B–C–N nanocrystalline particle by mechanical alloying and spark plasma sintering. *Journal of Materials Science* 41 (2006) 8352-8355.
21. X.M. Duan, D.C. Jia, Z.L. Wu, Z. Tian, Z.H. Yang, S.J. Wang, Y. Zhou. Effect of sintering pressure on the texture of hot-press sintered hexagonal boron nitride composite ceramics. *Scripta Materialia* 68 (2013) 104-107.
22. A. Nieto, D. Lahiri, A. Agarwal. Synthesis and properties of bulk graphene nanoplatelets consolidated by spark plasma sintering. *Carbon* 50 (2012) 4068-4077.
23. T.Ya. Kosolapova, *Handbook of High Temperature Compounds: Properties, Production, Applications*, pp - 792, 161, Hemisphere Publishing Corp., New York (1990).
24. F. Bernard, E. Gaffet. Mechanical alloying in the SHS research. *International Journal of Self-Propagating High Temperature Synthesis* 10 (2001) 109-132.
25. A.S. Mukasyan, Y.C. Lin, A.S. Rogachev, D.O. Moskovskikh. Direct combustion synthesis of silicon carbide nanopowder from the elements. *Journal of American Ceramic Society* 96 (2013) 111-117.
26. E. Gaffet, G. Le Caër. Mechanical processing for nanomaterials. *Encyclopedia of nanosciences and nanotechnology* (2004).
27. D. Salamon, M. Eriksson, M. Nygren, Z. Shen. Homogeneous TiB₂ ceramics achieved by electric current-assisted self-propagating reaction sintering. *Journal of the American Ceramic Society* 90 (2007) 3303–3306.
28. J. Schmidt, R. Niewa, M. Schmidt, Y. Grin. Spark plasma sintering effect on the decomposition of MgH₂. *Journal of the American Ceramic Society* 88 (2005) 1870–1874.
29. M.A. Mannan, Y. Baba, N. Hirao, T. Kida, M. Nagano, H. Noguchi. Hexagonal nanocrystalline BCN films grown on Si (100) substrate studied by X-ray absorption spectroscopy. *Material Science and Applications* 4 (2013) 11-19.
30. K. Raidongia, A. Nag, K. P. S. S. Hembram, U. V. Waghmare, R. Datta, C. N. R. Rao. BCN: A Graphene Analogue with Remarkable Adsorptive Properties. *Chemistry A European Journal* 16 (2010) 149-157.

31. V.P. Filonenko, V.A. Davydov, I.P. Zibrov, V.N. Agafonov, V.N. Khabashesku. High pressure synthesis of new heterodiamond phase. *Diamond and Related Materials* 19 (2010) 541-544.
32. Y. Liao, K. Tu, X. Han, L. Hu, J.W. Connell, Z. Chen, Y. Lin. Oxidative etching of hexagonal boron nitride toward nanosheets with defined edges and holes. *Scientific Reports* 5 (2015) 14510-1-12.
33. V.S. Tucureanu, A. Matei, A.M. Avram. FTIR spectroscopy for carbon family study. *Critical Reviews in Analytical Chemistry* 46 (2016) 502-520.
34. D.H. Kim, E. Byon, S. Lee, J.K. Kim, H. Ruh. Characterization of ternary boron carbon nitride films synthesized by RF magnetron sputtering. *Thin Solid Films* 447-448 (2004) 192-196.
35. V. Linss, I. Hermann, N. Schwarzer, U. Kreissig, F. Richter. Mechanical properties of thin films in the ternary triangle B-C-N. *Surface and Coatings Technology* 163 (2003) 220-226.
36. H.S. Kim, I.H. Choi, Y.J. Baik. Characteristics of carbon incorporated BN films deposited by radio frequency PACVD. *Surface and Coatings Technology* 133-134 (2000) 473-477.
37. A.C. Ferrari, J.C. Meyer, V. Scardaci, C. Casiraghi, M. Lazzeri, S. Piscanec, D. Jiang, K. S. Novoselov, S. Roth, A. K. Geim. Raman spectrum of graphene and graphene layers. *Physical Review Letters* 97 (2006) 187-401.
38. M.S. Dresselhaus, A. Jorio, M. Hofmann, G. Dresselhaus, R. Saito. Perspectives on carbon nanotubes and graphene Raman spectroscopy. *Nano Letters* 10 (2010) 751-758.
39. L.M. Malard, M.A. Pimenta, G. Dresselhaus, M.S. Dresselhaus. Raman spectroscopy in graphene. *Physics Reports* 473 (5-6) (2009) 51-87.
40. M. Kalbac, H. Farhat, J. Kong, P. Janda, L. Kavan, M.S. Dresselhaus. Raman spectroscopy and in situ Raman spectro electrochemistry of bilayer 12C/13C graphene. *Nano Letters* 11 (2011) 1957-1963.
41. L.G. Cancado, A. Reina, J. Kong, M.S. Dresselhaus. Geometrical approach for the study of G' band in the Raman spectrum of monolayer graphene, bilayer graphene, and bulk graphite. *Physical Review B* 77 (2008) 245408.
42. A.N. Yurkov, N.N. Melnik, V.V. Sychev, V.V. Savrans, D.V. Vlasov, V.I. Konov. Synthesis of carbon films by magnetron sputtering of a graphite target using hydrogen as plasma forming gas. *Bulletin of the Lebedev Physics Institute* 38 (2011) 263-266.
43. C. Thomsen, S. Reich. Doable resonant Raman scattering in graphite. *Physical Review Letters* 85 (2000) 5214-5217.
44. S. Reich, A.C. Ferrari, R. Arenal, A. Loiseau, I. Bello, J. Robertson. Resonant Raman scattering in cubic and hexagonal boron nitride. *Physical Review B* 71 (2005) 205201.

45. C.Y. Zhi, X.D. Bai, E.G. Wang. Raman characterization of boron carbonitride nanotubes. *Applied Physics Letters* 80 (2002) 3590–3592.
46. L. Cancado, K. Takai, T. Enoki, M. Endo, Y. A. Kim, H. Mizusaki, A. Jorio, L. N. Coelho, R. Magalha-es-Paniago, M. A. Pimenta. General equation for the determination of the crystallite size L_a of nano-graphite by Raman spectroscopy. *Applied Physics Letters* 88 (2006) 163106.
47. S. Turan, K.M. Knowles. High resolution transmission electron microscopy of the planar defect structure of hexagonal boron nitride. *Physica Status Solidi A* 150 (1995) 227–237.
48. J.Y. Huang, H. Yasuda, H. Mori. HRTEM and EELS Studies on the amorphization of hexagonal boron nitride induced by ball milling. *Journal of American Ceramic Society* 83 (2000) 403–409.
49. B. Cao, G.N. Yu, C.X. Pan. The ripple's enhancement in graphene sheets by spark plasma sintering. *AIP Advances* 1 (2011) 032170.
50. Z.Z Wu, A. Winter, L. Chen, Y. Sun, A. Turchanin, X. Feng, K.Mullen. Three-dimensional nitrogen and boron co-doped graphene for high-performance all-solid-state supercapacitors. *Advanced Materials* 24 (2012) 5130-5135.
51. G. Bepete, D. Voiry, M. Chhowalla, Z. Chiguvare, N.J. Coville. Incorporation of small BN domains in graphene during CVD using, boric acid and nitrogen gas. *Nanoscale* 5 (2013) 6552–6557.
52. B.J. Matsoso, K. Ranganathan, B.K. Mutuma, T. Lerotholi, G. Jones, N.J. Coville. Single-step synthesis of crystalline h-BN quantum- and nanodots embedded in boron carbon nitride films. *Nanotechnology* 28 (2017) 105602.
53. C.L. Sun, F.K. Ma, L. Cai, A.Z. Wang, Z.Y. Wang, M.W. Zhao, W.S. Yan, X.P Hao. Metal-free ternary BCN nanosheets with synergetic effect of band gap engineering and magnetic properties. *Scientific Reports* 7 (2017) 6617.
54. F. Ma, M. Wang, Y. Shao, L. Wang, Y. Wu, Z. Wang, X. Hao. Thermal substitution for preparing ternary BCN nanosheets with enhanced and controllable nonlinear optical performance. *Journal of Material Chemistry C* 5 (2017) 2559-2565.
55. Q. Li, G. Zhang, F. Liu, K. Han, M.R. Gadinski, C. Xiong, Q. Wang. Solution-processed ferroelectric terpolymer nanocomposites with high breakdown strength and energy density utilizing boron nitride nanosheets. *Energy and Environmental Sciences* 8 (2015) 922-931.
56. Y.N. Wang, J.C. Huang. Texture analysis in hexagonal materials. *Materials Chemistry and Physics* 81 (2003) 11-26.
57. H-R Wenk, V. Houtte. Texture and anisotropy. *Reports on Progress in Physics* 67 (2004) 1367-1428.

58. H. Şahin, S. Cahangirov, M. Topsakal, E. Bekaroglu, E. Akturk, R.T. Senger, S. Ciraci. Monolayer honeycomb structures of group-IV elements and III–V binary compounds: First-principles calculations. *Physical Review B* 80 (2009) 155453.
59. Y.G. Tkachenko, B. Grabchuk, N. Bodnaruk, V. Sychev. Friction and wear of boron carbide at temperatures in the range 20–1500 °C. *Powder Metallurgy and Metal Ceramics* 16 (1977) 541-543.
60. X.H. Zhang, M.Q. Xue, X.H. Yang, Z.P. Wang, G.S. Luo, Z.D. Huang, X.L. Sui, C.S. Li. Preparation and tribological properties of $Ti_3C_2(OH)_2$ nanosheets as additives in base oil. *RSC Advances* 5 (2015) 2762-2767
61. M. Naguib, J. Come, B. Dyatkin, V. Presser, P.L. Taberna, P. Simon, M.W. Barsoum, Y. Gogotsi. MXene: A promising transition metal carbide anode for lithium-ion batteries. *Electrochemistry Communications* 16 (2012) 61-64.
62. J.X. Li, Y.L. Du, C.X. Huo, S. Wang, C. Cui. Thermal stability of two-dimensional Ti_2C nanosheets. *Ceramic International* 41 (2015) 2631-2635.
63. M. Naguib, O. Mashtalir, J. Carle, V. Presser, J. Lu, L. Hultman, Y. Gogotsi, M.W. Barsoum. Two dimensional transition metal carbides. *ACS Nano* 6 (2012) 1322-1331.
64. F. Liu, A. Zhou, J. Chen, H. Zhang, J. Cao, L. Wang, Q. Hu. Preparation and methane adsorption of two-dimensional carbide Ti_2C . *Adsorption* 22 (2016) 915-922.
65. B. Ahmed, D.H. Anjum, M.N. Hedhili, Y. Gogotsi, H.N. Alshareef. H_2O_2 assisted room temperature oxidation of Ti_2C MXene for Li-ion battery anodes. *Nanoscale* 8 (2016) 7580-7587.
66. Y.L. Bai, X.D. He, C.C. Zhu, G.Q. Chen. Microstructures, electrical, thermal, and mechanical properties of bulk Ti_2AlC synthesized by self-propagating high-temperature combustion synthesis with pseudo hot isostatic pressing. *Journal of American Ceramic Society* 95 (2012) 358-364.
67. O. Mashtalir, M. Naguib, B. Dyatkin, Y. Gogotsi, M.W. Barsoum. Kinetics of aluminum extraction from Ti_3AlC_2 in hydrofluoric acid. *Material Chemistry Physics* 139 (2013) 147-152.
68. Y. Liu, X. Zhang, S. Dong, Z. Ye, Y. Wei. Synthesis and tribological property of $Ti_3C_2T_x$ nanosheets. *Journal of Material Science* 52 (2017) 2200-2209.
69. J. Yang, B.B. Chen, H.J. Song, H. Tang, C.S.Li. Synthesis, characterization, and tribological properties of two-dimensional Ti_3C_2 . *Crystal Research Technology* 49 (2014) 926-932.
70. X.H. Zhang, M.Q. Xue, X.H. Yang, Z.P. Wang, G.S. Luo, Z.D. Huang, X.L. Sui, C.S. Li. Preparation and tribological properties of $Ti_3C_2(OH)_2$ nanosheets as additives in base oil. *RSC Advances* 5 (2015) 2762-2767.

71. M. Ghidui, S. Kota, V. Drozd, M.W. Barsoum. Pressure-induced shear and interlayer expansion in Ti_3C_2 MXene in the presence of water. *Science Advances* 4 (2018) eaao6850.
72. P. Nautiyal, L. Embrey, B. Boesl, A. Agarwal. Multi-scale mechanics and electrical transport in a free-standing 3D architecture of graphene and carbon nanotubes fabricated by pressure assisted welding. *Carbon* 122 (2017) 298-306.
73. R. Agrawal, A. Nieto, H. Chen, M. Mora, A. Agarwal. Nanoscale damping characteristics of boron nitride nanotubes and carbon nanotubes reinforced polymer composites. *ACS Applied Materials Interfaces* 5 (2013) 12052-12057.
74. P. Nautiyal, B. Boesl, A. Agarwal. The mechanics of energy dissipation in a three-dimensional graphene foam with macroporous architecture. *Carbon* 132 (2018) 59-64.
75. P. Nautiyal, B. Boesl, A. Agarwal. Harnessing three dimensional anatomy of graphene foam to induce superior damping in hierarchical polyimide nanostructures. *Small* 13 (2017) 1603473.
76. M. Radovic, A. Ganguly, M.W. Barsoum, T. Zhen, P. Finkel, S.R. Kalidindi, E. Lara-Curzio. On the elastic properties and mechanical damping of Ti_3SiC_2 , Ti_3GeC_2 , $\text{Ti}_3\text{Si}_{0.5}\text{Al}_{0.5}\text{C}_2$ and Ti_2AlC in the 300-1573 K temperature range. *Acta Materialia*. 54 (2006) 2757-2767.
77. A.G. Zhou, M.W. Barsoum, S. Basu, S.R. Kalidindi, T. El-Raghy. Incipient and regular kink bands in fully dense and 10 vol% porous Ti_2AlC . *Acta Materialia* 54 (2006) 1631-1639.
78. S. Amini, C. Ni, M.W. Barsoum. Processing, microstructural characterization and mechanical properties of a Ti_2AlC /nanocrystalline Mg-matrix composite. *Composite Science and Technology* 69 (2009) 414-420.
79. J. Gruber, A.C. Lang, J. Griggs, M.L. Taheri, G.J. Tucker, M.W. Barsoum. Evidence for bulk ripplocations in layered solids. *Scientific Reports*. 6 (2016) 33451.
80. M.W. Barsoum, G.J. Tucker. Deformation of layered solids: ripplocations not basal dislocations. *Scripta Materialia* 139 (2017) 166-172.
81. M. Fyta. *Computational Approaches in Physics*, Morgan & Claypool Publishers, San Rafael, CA, USA, 2016.
82. U. Yorulmaz, A. Ozden, N.K. Perkgoz, F. Ay, C. Sevik. Vibrational and mechanical properties of single layer MXene structures: a first-principles investigation. *Nanotechnology* 27 (2016) 335702.
83. Y. Bai, K. Zhou, N. Srikanth, J.H.L. Pang, X. He, R. Wang. Dependence of elastic and optical properties on surface terminated groups in two-dimensional MXene monolayers: a first principles study. *RSC Advances* 6 (2016) 35731-35739.

84. S.A. Khan, B. Amin, L.Y. Gan, I. Ahmad. Strain engineering of electronic structures and photocatalytic responses of MXenes functionalized by oxygen. *Physical Chemistry Chemical Physics* 19 (2017) 14738-14744.
85. D. Lahiri, S. Das, W. Choi, A. Agarwal. Unfolding the damping behavior of multilayer graphene membrane in the low-frequency regime. *ACS Nano* 6 (2012) 3992-4000.
86. Y. Hu, T.B. Ma, H. Wang. Energy dissipation in atomic-scale friction. *Friction* 1 (2013) 24-40.
87. S. Wang, J.X. Li, Y.I. Du, C. Cui. First-principles study on structural, electronic and elastic properties of graphene-like hexagonal Ti_2C monolayer. *Computational Material Science* 83 (2014) 290-293.
88. X. Sang, Y. Xie, M.W. Lin, M. Alhabeb, K.L. Van Aken, Y. Gogotsi, P.R.C. Kent, K. Xiao, R.R. Unocic. Atomic Defects in Monolayer Titanium Carbide (Ti_3C_2Tx) MXene. *ACS Nano* 10 (2016) 9193-9200.

Chapter V: Conclusions

In this dissertation, the mechanical and tribological behavior of sintered bulk 2D BNNS, BCN and for 2D MXene particles are studied in detail. BNNS and BCN (BNNS + GNP) exhibit their potential to withstand the extreme processing conditions during spark plasma sintering at 1650 °C -1850 °C and 50 MPa. In this high temperature process, the 2D materials were able to retain their unique structure/morphology and achieve bulk densification above 90%. After synthesis, structural, microstructural and fundamental deformation mechanisms on spark plasma sintered bulk 2D BNNS, BCN and MXene powders are evaluated. Mechanical properties and the corresponding deformation mechanisms are explored along the in-plane and out-of-plane orientations. The dissipation energy associated with the individual deformation mechanisms are quantified and compared. This chapter comprises of the conclusion from the present work on spark plasma sintered BNNS, BCN and MXene powders. The major conclusion from this dissertation are listed below in terms of (i) BNNS SPS, (ii) BCN SPS and (iii) MXene.

(i) Spark Plasma Sintered BNNS

1. BNNS are successfully consolidated without any sintering aid into a monolithic pellet by spark plasma sintering with the relative density greater than 92%. The monolithic BNNS pellet indicate their potential to retain the 2D nature of BNNS, even at the severe processing conditions of high temperature – 1650 °C and load of 50 MPa.
2. X-ray diffraction study confirmed the h-BN structure after sintering of BNNS along with B₂O₃ and B₄C as trace impurities.
3. Texture studies of sintered BNNS pellet, revealed the preferred orientation of BNNS basal (0002) plane perpendicular to the direction of pressure is observed on the top

surface of the pellet. The cross-section surface of BNNS pellet showed a faint orientation along the $(11\bar{2}0)$ and $(01\bar{1}1)$ planes.

4. Fracture surface of sintered BNNS pellet supports the XRD and texture results of preferred orientation, where the platelets are oriented perpendicular with respect to the loading direction. The fractured layers shows a zig-zag nature, as the propagation of cracks occurred along the edges of nanosheets and not through the nanosheets. Since, the sintered BNNS nanosheets have weak bonding along the edges and strong covalent bonding within the nanosheets.
5. TEM studies on sintered BNNS pellets showed crystalline grains (100 nm – 2 μ m) and high density of multiple twin lamellae. Twin formation resulted from the deformation of hexagonal BNNS during sintering at high temperature and pressure.
6. The coefficient of friction are measured for the sintered BNNS pellet at room temperature (25 °C) and high temperature (600 °C). Room temperature test showed a lower coefficient of friction (0.145) compared to the high temperature test (0.656). This is due to the change in wear mechanism. At room temperature the shearing of the layered sheets occur and it enhances the lubricating effect. During the high temperature test, the BNNS becomes softer resulting in the abrasive wear and this degrades the lubricating effect.
7. High load in-situ indentation studies are carried out in the displacement control mode along the cross-section and top surface of the sintered BNNS pellet. The total energy dissipation, when indenting along the top surface is 61.44 mJ and along the cross-section is 41.07 mJ. So, the energy dissipation is 50% greater during indentation along the top surface compared to the cross-section energy dissipation during indentation. Thus, BNNS has to be arranged in a preferred way (basal planes aligned along the top surface) to increase the toughness when used as a reinforcement in composites.

8. Predominant deformation mechanisms observed on the top surface indentation are compression of the layered sheets, delamination and BNNS pile-up. For the cross-section direction, the key deformation mechanisms are cracking and fracturing with an insignificant delamination. The dominant deformation mechanisms in sintered BNNS pellet are directly related to the preferred orientation of the crystallographic planes. Along the top surface, there is no active slip system. However, twinning was observed. In the cross-section, active pyramidal slip system resulted in a plastic deformation. Additionally, the weak van der Waals forces between the layers caused crack propagation along the cross-section.

(ii) Reaction Synthesized BCN

9. Reaction synthesis of BCN phase using spark plasma sintering are successfully achieved from the powder mixture of BNNS and GNP. The powder mixture are sintered at three different parameters (sintering temperature and time), (i) BCN 1-1650 °C, 10 min, (ii) BCN 2 – 1650 °C, 30 min and (iii) BCN 3 – 1750 °C, 10 min. The reaction synthesized BCN pellets retained the 2D nature of the nanosheets, in spite of their exposure to harsh sintering temperatures.
10. Structural study of the reaction sintered BCN pellets confirmed the h-BCN and c-BCN phase formation in BCN 2/BCN 3 pellet along with other secondary phases (h-BN, B₂O₃, B₄C and carbon) present in the reaction sintered BCN 2/BCN 3.
11. FTIR study also confirmed the BCN phase formation in reaction sintered BCN 2 and BCN 3 pellets. New B-C, C-N and C=N bonds were identified in the FTIR spectra of BCN 2/BCN 3 pellets along with B-N and C-C bonds.

12. Raman studies on the reaction sintered BCN pellets reveal the BCN 2 and BCN 3 pellets have lower structural defects with increase in their crystallite size compared to the BCN 1 pellet.
13. TEM studies on reactive sintered BCN pellets reveal the major hexagonal-BCN phase formation with cubic-BCN phase in the BCN 2 and BCN 3 pellets. The high-angle annular dark field-scanning transmission electron microscopy (HAADF-STEM) study showed the cubic BCN nanoparticles formed between the sintered nanosheets with varying particle size (10 nm – 400 nm).
14. Fracture surface of BCN 2 and BCN 3 pellets showed densely packed nanosheets with minimal interlayer gaps compared to fracture surface of BCN 1 pellet. The fracture surface of all the three samples revealed the preferred orientation of sintered nanosheets with few unreacted BNNS/GNP.
15. Texture studies of reaction sintered BCN pellets revealed the top surface has a preferred orientation of (0002) basal plane texture and the cross-section has shown the weak texturing of (101 $\bar{1}$) pyramidal plane texture. The relative volume fraction of (0002) basal plane and (101 $\bar{1}$) pyramidal plane texture along the top surface and cross-section increased with longer dwell time (BCN 2) and higher sintering temperature (BCN 3).
16. Room temperature tribological studies for the BCN pellets showed an increase in coefficient of friction (COF) by 4.5 % for BCN 2 and 14.5% for BCN 3 sample. This increase in COF is attributed to presence of hard cubic BCN phase, and it is evident from the rough surface of BCN 2/BCN 3 wear tracks. The high temperature tribological studies at 600 °C for the BCN pellets showed a decrease in coefficient of friction (COF) by 7.6 % for BCN 2 and 11.5% for BCN 3 sample. This decrease in COF is attributed to the possible formation of graphitic transfer layer, it is evident from the smooth surface of BCN 2/BCN 3 wear tracks.

17. The high load indentation of BCN top surface, shows the change in energy dissipation mechanisms for BCN 3 pellet compared to BCN 1 and BCN 2 pellets. The energy dissipation mechanism for top surface of BCN 3 are nanosheet sliding, compression with few delamination. This was apparent from the smooth surface at the bottom of BCN 3 indent with no crack formation at the bottom or corner of the indents. The energy dissipated during the nanosheet sliding is the least because of the weak van der Waals forces between the layered nanosheets.

(iii) MXene

18. Two-dimensional Ti_2C MXene with surface terminations ($-OH/-F$) is successfully synthesized from the MAX phase Ti_2AlC powder by HF acid treatment.

19. The structural study using X-ray diffraction confirmed the Ti_2C MXene formation after HF treatment. The Ti_2C MXene phase are present with the remnant MAX phase Ti_2AlC and TiC . The 'd-spacing' (d_{002}) or interlayer distance corresponding to Ti_2C peak increased from 6.75 to 8.45 Å with increase in HF acid treatment.

20. The microstructural studies of HF treated MXene powders revealed no oxidation of nanosheets and thickness of separated MXene layers decreased from 157 ± 20 nm for 1 h to 100 ± 23 nm for 2 h to 74 ± 12 nm for 4 h.

21. Coefficient of friction for pure MAX powder is 0.18, for 1 h HF treated MXene powder COF significantly decreased to 0.019, with 2 h and 4 h of HF treatment, the COF increased to 0.021 and 0.079. The COF of HF treated MXenes are 50 – 80% lower than pure MAX, due to the weak van der Waals forces between the layers, it results in interlayer shearing of MXene sheets.

22. Dynamic loading of multi-layer MXene assembly shows appreciable loss tangent ($\tan \delta$), indicating energy dissipation ability of the material. The $\tan \delta$ value for 1 h HF

treated MXene is recorded to be as high as 0.37, which is about 200% improvement from pure MAX. Multi-scale energy loss mechanisms active in the material are the reason for this enhanced damping behavior of MXene.

23. After 50000 cycles at a frequency of 150 Hz for 1 μN and 10 μN loads, the 1 h HF treated MXene sample displayed stable damping behavior ($\tan \delta - 0.21 \pm 0.014$ (1 μN) and 0.20 ± 0.028 (10 μN)), indicating the excellent energy dissipation behavior of MXene upon cyclic loading.

24. The predominant energy dissipation mechanism in MXene during damping are as follows,

- (i) Intralayer – bond contracting,
- (ii) Interlayer – compression between MXene sheets
- (iii) Interlayer –sliding\shearing between the sheets

25. During damping in a single MXene layer for lower load of 1 μN , the energy dissipation mechanism will be intralayer bond contracting and interlayer compression. Damping in a multilayered MXene for load of 10 μN /1 mN/5 mN, the energy dissipation mechanism will be a combination of intralayer bond contraction, interlayer compression and interlayer sliding/shearing.

Chapter VI: Recommendations for Future Work

The focus of the present research was to explore: (i) the deformation behavior of sintered 2D carbide/nitride ceramics in bulk form concerning their orientation, and (ii) the damping behavior of the synthesized MXene powders. Bulk multilayered 2D carbide/nitride ceramics were prepared by optimizing the synthesis/sintering parameters of SPS and texturing of the multilayered nanosheets was observed. Then, mechanical and tribological properties were evaluated concerning their orientation. The research outcomes from this thesis will establish 2D materials in bulk form for novel applications beyond their conventional applications as reinforcements in composites. In addition to the key findings of this research, future studies are recommended to understand and demonstrate the potential of 2D materials applications.

Current State of the Art	Recommendations
Boron Nitride Nanosheets (BNNS)	
1. In the present research, 2D BNNS was consolidated without any sintering aid to make monolithic BNNS by spark plasma sintering. Mechanical and tribological properties of monolithic BNNS have been studied.	1. In the future study, it is important to consolidate the conventional h-BN powder <i>without any sintering aid</i> under similar spark plasma sintering conditions. Then, the mechanical and tribological properties of monolithic h-BN should be measured and compared with monolithic BNNS properties. Such a comparison will enable us to understand the effect of h-BN vs. BNNS

	morphologies on the properties of sintered compacts.
2. In this study, crystallographic texturing was evaluated along the top surface and cross-section of the BNNS pellet, where BNNS with 100 nm – 3 μm in diameter and 40 – 65 nm thickness were used as the starting powder.	2. It is recommended that the effect of starting BNNS particle size on the texturing should be studied to understand the correlation of particle size on the crystallographic orientation.
3. Mechanical and tribological properties of textured bulk BNNS was explored in the present work. As the conventional h-BN is one of the commonly used thermal conductive fillers (due to high thermal conductivity), it is worthy of investigating the thermal properties of bulk BNNS concerning their orientation.	3. The effect of texturing on thermal properties of bulk BNNS pellet must be explored along the in-plane and out-of-plane direction.
4. The 2D BNNS after SPS consolidation has shown the presence of traces of B ₂ O ₃ phase. B ₂ O ₃ phase can act as a sintering aid and contribute to the densification of bulk BNNS.	4. To nullify the effect of B ₂ O ₃ phase on BNNS consolidation – the as-received 2D BNNS powders should be heat treated before SPS to avoid B ₂ O ₃ formation.

Current State of the Art	Recommendations
Boron-Carbon-Nitride (BCN) System	
<p>1. In this study, hexagonal and cubic BCN phase was successfully synthesized by reactive spark plasma sintering method using BNNS and Graphene as precursors. However, the starting BNNS and graphene phase was still retained with the BCN phase.</p>	<p>1. Reactive spark plasma sintering process parameters (temperature, pressure, time) must be optimized to maximize the BCN phase formation. The optimization of SPS process parameters will also contribute to improving the densification of bulk BCN.</p>
<p>2. Based on the literature, the reaction synthesis temperature to form the BCN phase was chosen in this study. Such experimental study, when coupled with theoretical and thermodynamic calculations can provide useful information to design the experiments with optimal processing parameters.</p>	<p>(i) Thermodynamic modeling should be performed to develop the phase diagram for BNNS-GNP system. This phase diagram will be useful to interpret the initial composition of BNNS and GNP mixture, reaction synthesis temperature for the desired hexagonal BCN/cubic BCN phase formation.</p> <p>(ii) The ab initio calculations should be performed to estimate the energy of formation and enthalpy of mixing for the stable and metastable phases of the BCN system formed from 2D BNNS/GNP. Similarly, the Gibbs energy for the different BCN phases formed should be estimated to identify the stable BCN phase.</p>

<p>3. In the present study, the XRD patterns of reaction synthesized samples have been indexed, and the BCN phase was identified. However, a detailed analysis of the XRD pattern was not performed.</p>	<p>3. The detailed crystal structure information of the synthesized BCN phase has to be probed by Rietveld refinement of the BCN XRD pattern. This study will contribute to quantifying the (i) phase fraction, (ii) lattice parameters, and (iii) the chemical composition of different BCN phase formed by reaction synthesis method.</p>
--	---

Current State of the Art	Recommendations
MXene	
<p>1. In the present work, 2D Ti₂C MXene was successfully synthesized from HF treatment of Ti₂AlC MAX phase. Multiscale damping properties of synthesized MXene nanosheets was explored. Bulk form (e.g., MXene pellet) was not attempted in the current research.</p>	<p>1. Do MXene nanosheets retain their mechanical, electrical and chemical properties in the bulk form such as MXene pellets? This will require consolidation of MXene sheets into a pellet using SPS or other consolidation technique. Such a study will provide the effect of MXene scale length on its properties.</p>

VITA

ARCHANA LOGANATHAN

EDUCATION AND EXPERIENCE:

- July 2003 – June 2007 Bachelor of Engineering (B.E) in Metallurgical Engineering, PSG College of Technology, Coimbatore, Anna university, India
- Jan. 2008 – Dec. 2011 Master of Science (M.S) by Research in Metallurgical and Materials Engineering, Indian Institute of Technology, Madras, India
- Aug. 2015 - Dec. 2019 Doctoral Candidate (Ph.D) in Materials Science and Engineering, Florida International University, Miami, Florida
- Nov. 2006 – April 2007 Undergraduate Research Intern, in Advanced Magnetics Group, Defence Metallurgical Research Laboratory, Hyderabad, India
- June 2012 - Aug. 2015 Research Engineer, Advanced Materials Research in Nissan Research Centre, Renault Nissan Technology and Business Centre, Chennai, India

PUBLICATIONS AND PRESENTATION:

First Authored Articles

1. Archana Loganathan, Pranjali Nautiyal, Benjamin Boesl, Arvind Agarwal. Unravelling the Multiscale Damping Properties of 2D Layered MXene. *Nanomaterials and Energy* 8 (2019) 1-10.
2. Archana Loganathan, Ashutosh Sahu, Chris Rudolf, Cheng Zhang, Sara Rengifo, Tapa Laha, Benjamin Boesl, Arvind Agarwal. Multi-scale Tribological and Nanomechanical Behavior of Cold Sprayed Ti₂AlC MAX Phase Coating. *Surface and Coatings Technology* 334 (2018) 384-393.
3. Archana Loganathan, Amit Sharma, Chris Rudolf, Cheng Zhang, Pranjali Nautiyal, Satyam Suwas, Benjamin Boesl, Arvind Agarwal. In-situ Deformation Mechanism and Orientation Effects in Sintered 2D Boron Nitride Nanosheets. *Materials Science and Engineering A* 708 (2017) 440-450.
4. Archana Loganathan, Sara Rengifo, Alexander Franco Hernandez, Yusuf Emirov, Cheng Zhang, Benjamin Boesl, Jeganathan Karthikeyan, Arvind Agarwal. Effect of 2D WS₂

Addition on Cold-Sprayed Aluminum Coating. *Journal of Thermal Spray Technology* 26 (2017) 1-13.

Co-authored articles

5. Tanaji Paul, Linqi Zhang, Sourabh Biswas, Archana Loganathan, Matthew G Frith, Jan Ilavsky, Ivan Kuzmenko, Jim Puckette, A Kaan Kalkan, Arvind Agarwal, Sandip P Harimkar. Quantification of Thermal Oxidation in Metallic Glass Powder Using Ultra-Small Angle X-ray Scattering. *Scientific Reports* 9 (2019) 6836.
6. Jenniffer Bustillos, Daniela Montero-Zambrano, Archana Loganathan, Benjamin Boesl, Arvind Agarwal (2019). Stereolithography-based 3D Printed Photosensitive Polymer/Boron Nitride Nanoplatelets Composites. *Polymer Composites* 40 (2019) 379-388.
7. Melania Antillon, Pranjal Nautiyal, Archana Loganathan, Benjamin Boesl, Arvind Agarwal. Strengthening in Boron Nitride Nanotube Reinforced Aluminium Composites Prepared by Roll Bonding. *Advanced Engineering Materials* 20 (2018) 1800122.
8. Tony Thomas, Cheng Zhang, Ashutosh Sahu, Pranjal Nautiyal, Archana Loganathan, Tapas Laha, Benjamin Boesl, Arvind Agarwal. Effect of Graphene Reinforcement on the Mechanical Properties of Ti₂AlC Ceramic Fabricated by Spark Plasma Sintering. *Materials Science and Engineering A* 728 (2018) 45-53.
9. Leslie Embrey, Pranjal Nautiyal, Archana Loganathan, Adeyinka Idowu, Benjamin Boesl, Arvind Agarwal. Three-dimensional Graphene Foam Induces Multi-functionality in Epoxy Nanocomposites by Simultaneous Improvement in Mechanical, Thermal and Electrical Properties. *ACS Applied Materials and Interfaces* 9 (2017) 39717-39727.
10. Pranjal Nautiyal, Archana Loganathan, Richa Agarwal, Benjamin Boesl, Chunlei Wang, Arvind Agarwal. Oxidative Unzipping and Transformation of High Aspect Ratio of Boron Nitride Nanotubes into White Graphene Oxide Platelets. *Scientific Reports* 6 (2016) 29498.

(Listed 10 out of 18 published journal articles)

11. Archana Loganathan. Microstructure and Wear Properties of Cold Sprayed Nanodiamond Aluminum Matrix Coating, The Minerals, Metals, and Materials Society (TMS 2019), San Antonio, Texas, 10-14 March 2019.
12. Archana Loganathan. Microstructural and Multiscale Tribological Properties of the Cold sprayed Ti₂AlC MAX Phase Coating, Materials Science and Technology (MS&T 2018), Columbus, Ohio, 14-18 October 2018.

(Listed 2 out of 7 conference presentation, 1 more poster presentations will be given in Oct. 2019 at MS&T 2019, Portland, Oregon)